THERMAL-HYDRO-MECHANICAL MODEL FOR FREEZING AND THAWING OF SOILS

by

Yao Zhang

A dissertation submitted in partial fulfillment
of the requirements for the degree of
Doctor of Philosophy
(Civil Engineering)
in the University of Michigan
2014

Doctoral Committee

Professor Radoslaw L. Michalowski, Chair
Professor Roman D. Hryciw
Professor Wei Lu
Assistant Professor Dimitrios Zekkos

DEDICATION

To my wife Lin Liu and our parents in China

ACKNOWLEDGEMENTS

First of all, I would like to thank my advisor, Professor Radoslaw L. Michalowski, who guided and supported me throughout my doctoral program. He is very generous and knowledgeable in mechanics and geotechnical engineering. Whenever I was confused or got lost, he could always push me in the right direction. He is also very strict and serious in research, therefore has been a role model for me in my academic journey. After five years working with Professor Michalowski, I have not only enriched myself in knowledge and skills, but also built up my way of independent study, critical thinking and serious attitude when dealing with my work.

I would like to thank other committee members, Professor Roman D. Hryciw, Professor Dimitrios Zekkos and Professor Wei Lu for their advice and comments. Great thanks also go to Dr. Ming Zhu, who did a very impressive job in the previous study about modeling the frost heave and helped me in using ABAQUS when I started doing this research.

I would also like to thank all the other faculty members in our geotechnical engineering group Professor Donald Gray, Professor Richard Woods and Professor Adda Athanasopoulos-Zekkos and all my colleagues, especially my officemate Mr. Clinton Carlson, for sharing their knowledge, ideas and experience. I am also grateful to all of my friends in Michigan, the members in “civil-eat” group, especially my housemate Mr. Xiaohu Fan, for their invaluable friendship.

This dissertation was covered by the research carried out at the University of Michigan, Ann Arbor during the period September 2009 to January 2014, and was supported by the funding

from U.S. Army Research Office, Grant No. W911NF-08-1-0376. This financial support is greatly appreciated.

Finally, I would like to express my thankfulness to my parents for their years of encouragement, support and unconditional love; thankfulness to my parents-in-law for their trust, care and understanding. Special gratefulness goes to my wife Lin Liu for her love, patience, understanding and support. We met each other here in Ann Arbor and our love was another achievement of mine in the University of Michigan.

TABLE OF CONTENTS

LIST OF FIGURES

LIST OF TABLES

CHAPTER 1

INTRODUCTION

1.1 Background and Motivation

Cold regions, including permafrost areas and seasonally freezing areas constitute a large portion of Earth's surface. In the northern hemisphere, more than 20% of land surface is occupied by permafrost, whereas more than 50% experiences seasonal freezing and thawing. In cold regions, soils frequently experience frost action.

Frost action in soils involves the processes of freezing and thawing. The resulting phenomena of frost heaving and thaw settlement are commonly seen in seasonal freezing areas, which render the built infrastructure vulnerable to damage. Broken cables, damaged lifelines, broken pipelines, malfunctioning utilities, cracked pavements (Figure 1.1), jacked up foundations (Figure 1.2) and tilted structures, are all examples of damage suffered from frost action. Long-term records indicate an on-going warming of the climate, which has resulted in thawing of portions of the permafrost area. The increase in permafrost temperature leads to thickening of the active layer (upper crust layer where active freezing-thawing cycles occur), leading to extensive settlement of the ground surface causing damage to infrastructure. Understanding how the soil

behaves upon freezing and thawing has the potential of changing the operation practices and design philosophies, and developing methods to alleviate the damages.

Figure 1.1 Cracks and potholes in pavement

Figure 1.2 Jacked up foundation

Artificial ground freezing of soil has long been used as a supporting construction method in geotechnical engineering. By installing freezing pipes and circulating liquid with temperature below the freezing point of water through them, the surrounding soil freezes. An increase in strength and decrease in permeability occurs in freezing soils, thus providing temporary stabilization of soils and hydraulic seal. However, freezing can cause significant changes in soil structure and density which can lead to adverse settlement during thawing. Figure 1.3 shows artificial ground freezing in tunneling. Although widely used, the artificial ground freezing method still needs improvement in areas such as the control of below freezing temperature and the control of deformation of the surrounding soil.

Figure 1.3 Artificial ground freezing in tunneling (Trevi SpA Group)

In order to mitigate the frost damage to infrastructure and to improve the artificial ground freezing method, it is essential to know: firstly, how the soil strength changes with respect to change in temperature, or the evolution of strength of the soil during freezing and thawing; secondly, how the soil deforms when subjected to freezing and thawing. To answer these questions as well as come up with a tool that is capable of predicting the frost action in soils, a comprehensive study has been carried out.

1.1.1 Frost Heave

The cause of frost heave in soil is the formation of ice lenses, rather than the increase in volume of the pore water in soil when it turns into ice upon freezing. This was proven by Taber (1929), who performed experiments on soils with the pore water being replaced by another liquid, benzene. During freezing of the specimen, frost heave still occurred even though the soil was saturated with benzene, which contracts upon freezing. Therefore, the expansion of water when it freezes does not play a key role in frost heave. It is the ice lens formation that causes the frost heave.

Ice lensing is the process of forming and growing of ice lenses. When the temperature of the soil drops below the freezing point of water, ice is produced in the soil pores. Ice lenses nucleate immediately behind the freezing front (referred to as *frozen fringe*) and the free water from surrounding voids and the unfrozen region of the soil is drawn and contributes to the growth of ice lenses. The force that drives the water from nearby areas is called *cryogenic suction*. The ice lenses then grow until the water ceases to move into the freezing zone (frozen fringe). This is caused by the accumulation of ice in the frozen fringe which could decrease soil permeability dramatically. As the freezing front propagates, many ice lenses are generated and

the soil particles are separated. Frost heave is then resulted. Figure 1.4(a) shows the forming of ice lenses in a frost heave test specimen. Figure 1.4(b) illustrates the mechanism of ice lensing and the typical composition of freezing soil in the neighborhood of the frozen fringe.

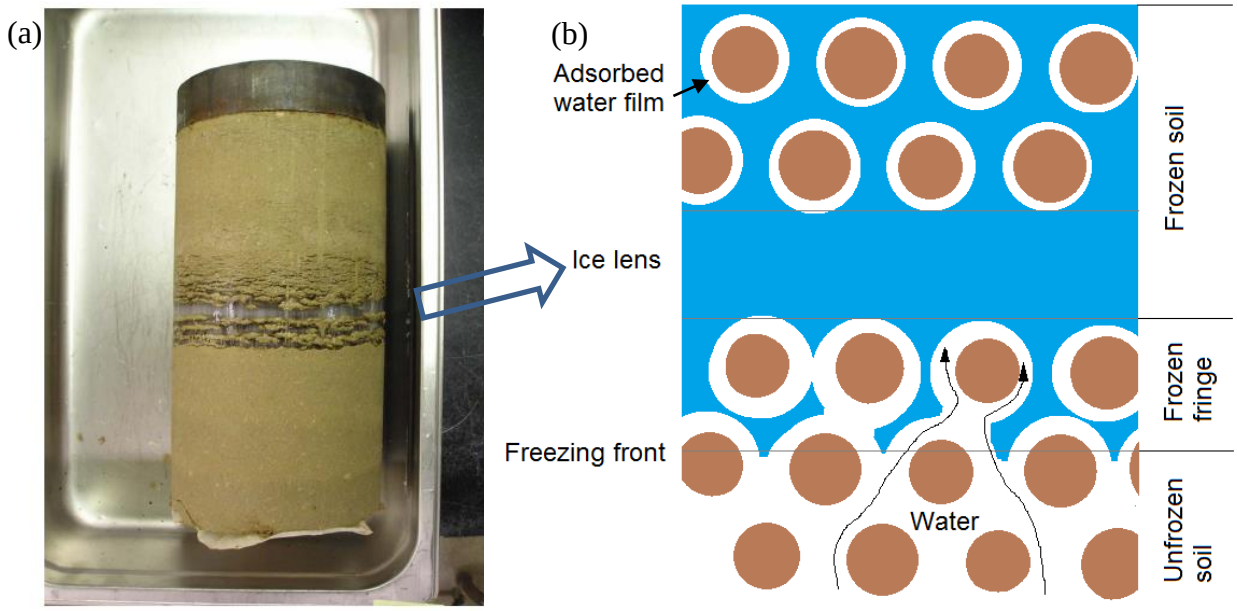

Figure 1.4 Illustration of freezing soil and ice lens (a) Frost heave specimen (Lay, 2005), (b) Illustration of freezing soil

Depending on the speed of the freezing front propagation, a nucleus of an ice lens is formed periodically. Not all ice in the proximity of the freezing front gives rise to an ice lens; much of it remains in pores (*pore ice*) without forming an ice lens. This is often referred to as *freezing in situ*; in situ freezing does not produce frost heave. Ice lensing is a process that is very sensitive to both the duration and the intensity of the freezing temperature. If the temperature drops down very quickly, leading to a fast propagation of the freezing front, ice lenses do not

grow, and all water freezes in situ. A slow rate of cooling, on the other hand, provides sufficient time for water migration, and it favors the growth of ice lenses.

Relatively fine soils that can still provide a good path for the water migration during freezing process are prone to form ice lenses, and they are termed *frost-susceptible soils*. Frost heave will not occur unless the following three requirements are satisfied: (1) presence of frost-susceptible soil, (2) a supply of unfrozen water, and (3) temperature conditions that will cause a freezing front propagation slow enough to allow water transport.

For a *non-frost-susceptible soil*, such as sand or gravel, no ice segregation takes place during freezing. Pore ice will form due to the phase change of the water in the pores. Ice lenses will not form, and the macroscopic deformation (growth) of the soil mixture (mineral, ice, water, air) upon freezing is owed predominantly to expansion of freezing water, but not to water migration. This expansion may be fully accommodated by pores in unsaturated soils, but it will cause macroscopic deformation in saturated soils

1.1.2 Thaw Consolidation and Thaw Settlement

During freezing, a considerable amount of ice could accumulate and the frost heave of a frost-susceptible soil could be more than 20% of the thickness of the frozen layer. When thawing occurs, the ice lenses formed in the freezing process gradually melt. The excess water melted from ice lenses will drain out under its self-weight and/or external loads thus the *thaw consolidation* is taking place. The rate of the thaw consolidation depends on both the melting rate of the ice and the hydraulic conductivity of the soil.

The total *thaw settlement* after consolidation is completed could be larger or smaller than the displacement caused by frost heave (Konrad 1989a). It depends primarily on the history of

loading prior to freezing (whether the soil was normally consolidated, *NC*, or over-consolidated, *OC*), and the number of freeze-thaw cycles. Thawing of a frozen *NC* soil in its first freeze-thaw cycle could cause a settlement larger than the heave induced during the freezing phase. However, some heave could remain in an *OC* soil subjected to its first freeze-thaw cycle. Artificial ground freezing applied in soft soil construction (tunneling, excavations), and pipelines transporting chilled media through unfrozen soil, are examples of circumstances where soil may be subjected to its first freeze-thaw cycle.

Thaw consolidation tests were done by Tsytovich (1960). A compression curve regarding to thaw consolidation in e vs. σ_v plane is illustrated in Figure 1.5. In the figure, e_f denotes the void ratio of frozen soil before thawing starts and e_{th} denotes the void ratio after the soil is completely thawed (e_f and e_{th} are measured under the same stress). The frozen soil sample is placed in an odometer with temperature control. With the temperature maintained constant below freezing, an overburden pressure equivalent to the field stress σ_0 is applied to the specimen. A small decrease in void ratio under this initial loading (A-B). The specimen is then thawed from top down under the constant pressure σ_0 and a large decrease in void ratio takes place (B-C). While the total difference in void ratio between e_f and e_{th} represents the thaw settlement, thaw consolidation (the melting and drainage of excess melted water) is taking place. Rather than consolidating due to additional load, thaw consolidation is thermally induced and occurs under a constant load. After the soil is completely thawed and consolidation under pressure σ_0 is completed, additional pressure $\Delta\sigma$ is applied to the specimen. The process (C-D) represents the classical consolidation of a soil.

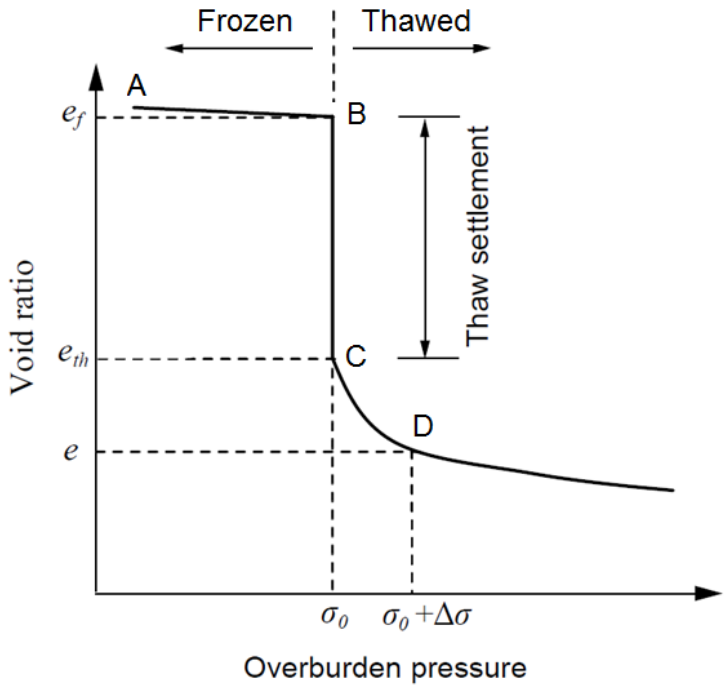

Figure 1.5 Thaw settlement in compression plane (after Tsytovich, 1960)

1.2 Scope and Outline

The purpose of this study is to develop a mathematical description of freezing and thawing soils that could be successfully used in model-based simulations. The emphasis in this dissertation is placed on strengthening in freezing soil and thaw-weakening of soil as well as thermal-hydro-mechanical (multi-physical) description of the freezing and thawing processes in soils.

An elastic-plastic constitutive relationship is presented first. The model is based on hardening plasticity and the critical state framework. Pore ice ratio will be introduced as a principal parameter to govern the hardening and softening of the soil. It describes the strengthening of soil upon freezing, and the weakening and settlement of soil when it is thawing.

Test data is used to calibrate the model. Behaviors of freezing and thawing soil under isotropic and non-isotropic compression are simulated to demonstrate the capacity of the model.

A slightly modified version of a previously proposed porosity rate function is adopted to describe the ice lens formation in freezing frost-susceptible soils (Michalowski 1993, Michalowski and Zhu 2006). The reduction of the rate of ice lensing with respect to the change of soil components (unfrozen water and ice) during the thermal process is considered. A thermal-hydro-mechanical framework is used to capture the multi-physical nature of freezing and thawing processes in soils.

The major contribution of this study is the development of a tool which is capable of simulating frost action in a full freeze-thaw cycle in frost-susceptible soils. The models mentioned above are implemented in a finite element system and calibrated. More complex practical engineering problems with respect to freezing and thawing of soils around a culvert, in front and behind a retaining wall, as well as around a chilled gas pipeline are simulated. The results are promising and the tool is ready to be used in engineering applications.

This dissertation consists of seven chapters. Chapter I introduces the mechanism of frost heave and thaw settlement as well as the motivation of this study. Chapter II presents the literature review of freeze-thaw cycle in soils, constitutive modeling of frozen soils and thermal-hydro-mechanical framework in geotechnical engineering. Chapter III presents the objective of this study. In Chapter IV, the elastic-plastic constitutive model is introduced, calibrated and demonstrated. In Chapter V, the modified porosity rate function is introduced and a thermal-hydro-mechanical framework is adopted. The whole system is then calibrated and used in an example simulation. Chapter VI presents the application of the model in the simulations of complex problems including: freezing and thawing of soils around a culvert; horizontal

movement of a retaining wall caused by frost heaving and thaw weakening; and displacements of the ground surface above a chilled gas pipeline. Chapter VII summarizes the contributions of this study and provides some suggestions for future research.

CHAPTER 2

LITERATURE REVIEW

2.1 Freeze-Thaw Cycle and Thaw Settlement in Frost-Susceptible Soils

Freezing and thawing in frost-susceptible soils (freeze-thaw cycle) may change the structure of the soils due to the cryogenic suction generated in the freezing process as well as the segregation between soil particles caused by the formation of ice lenses. Therefore, after experiencing freeze-thaw cycles, the engineering properties of the soil could be dramatically changed, and the deformation induced by the thermal process differs depending on the soil type and soil history. Experimental studies on soils experiencing cyclic freezing and thawing started in the 1970's.

Chamberlain and Gow (1979) conducted comprehensive research on the effect of freeze-thaw cycles on normally consolidated fine-grained soils using a consolidometer. The soil samples were frozen with free access to water, so that ice lenses could form. Freeze-thaw cycling was repeated until little or no change in void ratio or permeability occurred. The structure and permeability of the tested soils were observed to change after freeze-thaw cycles. The mechanism was interpreted in terms of the size of the mineral fraction of the fine soil, using two highly idealized arrangements shown in Figure 2.1.

For fine soil with less clay minerals, such as clayey silts, the large particles (silt) control the packing, while the clay particles are arranged in packets with a flocculated orientation and free to move in the voids (Figure 2.1(a)). In this case, the coarse-grained particles control the compressibility whereas the clay particles control the permeability. After freeze-thaw cycles, there is little or no change in void ratio since the rearrangement of the coarse grains due to freezing is limited. However, the permeability increases because the freeze-thaw cycles cause the clay packets to collapse to a denser state, but the packets become more dispersed, leaving wider channels for fluid flow.

For fine soil with mostly clay minerals, such as silty clay, the flocculated clay particles form a matrix in which the large grains are floating without being in contact with each other (Figure 2.1(b)). In this case, the clay particles control both the compressibility and the permeability. After freeze-thaw cycles, the clay packets are forced to rearrange into a more dispersed and denser state so that a noticeable decrease in void ratio occurs. However, the densification of the soil does not reduce the permeability, rather the permeability increases because of shrinkage cracks formed after freeze-thaw cycles.

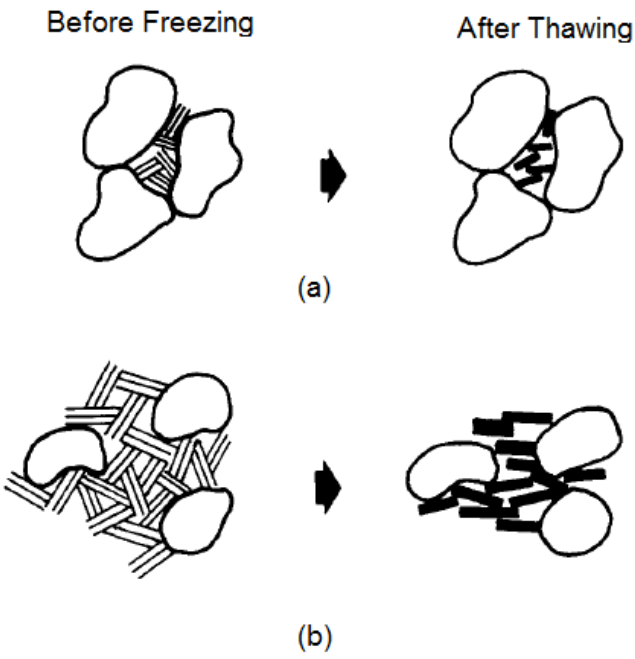

Figure 2.1 Change in void ratio after freeze-thaw cycle: (a) Clayey silts, (b) Silty clay (after Chamberlain and Gow 1979)

Chamberlain and Gow also investigated the mechanism of change in void ratio with respect to freeze-thaw cycle for a normally consolidated soil and interpreted it in the compression plane (e vs. logσ) as is shown in Figure 2.2. In the illustration, a normally consolidated soil at point a is frozen with free access of water under constant total stress state. An increase in void ratio to point b occurs due to the phase change as well as the intake of water and ice lens formation. After thawing, the increased volume due to ice lenses is given away and a further decrease in void ratio to point c takes place as a result of the rearrangement of soil grains and structure changes. However, in terms of effective stress, negative pore pressure (cryogenic suction) generated in the freezing process increases the effective stress between soil particles, and the clay bands end up being consolidated to point b'. Upon thawing, the effective stress drops along the swelling path from b' to point c after the excess pore pressure dissipated.

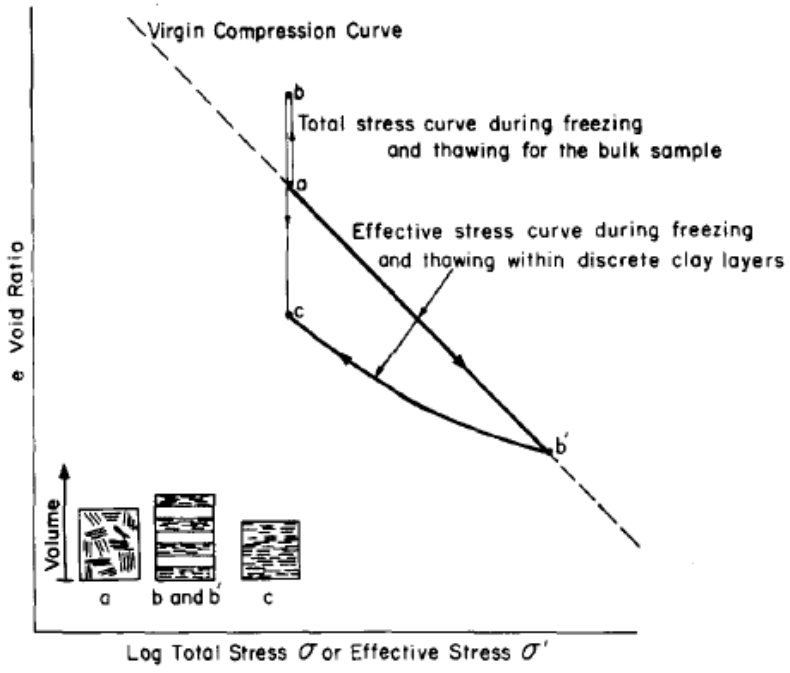

Figure 2.2 Stress paths during freezing and thawing in soil (after Chamberlain and Gow 1979)

Chamberlain (1981) discussed the overconsolidation effect (negative pore pressure) of freezing in soils and developed a method to determine the maximum suction that occurred during freezing process. From the freezing and thawing tests, Chamberlain concluded that the thaw settlement appears to be linearly related to the ratio of the initial water content to the plastic limit, and, after a freeze-thaw cycle, a decrease in volume is observed compared to soil before freezing.

Graham and Au (1984) observed a fissured structure after conducting freezing and thawing tests (close system) on natural Lake Agassiz clay from Winnipeg. Tests of drained and undrained loading along a high stress ratio path in p', q space on both overconsolidated undisturbed soil and soil after freeze-thaw cycles were conducted and compared. The author

concluded from the tests that freeze-thaw cycling produced higher pore water pressure at failure, lower consolidation stiffness and lower strength compared with values for undisturbed clay.

Konrad (1989a) conducted repeated freeze-thaw cycles on clayey silts with various overconsolidation ratios and found out that the void ratio of thawed soil decreased after the cycle in lightly overconsolidated soils (Figure 2.3(a)), but increased in heavily overconsolidated soils (Figure 2.3(b)). Konrad also compared the segregation potential (the potential for ice lens formation) after each freeze-thaw cycle. It was observed that the segregation potential reduced after each freeze-thaw cycle, and most of the changes occurred during the first three cycles. In another report, Konrad (1989b) presented X-ray photographs of the soil specimen experiencing freeze-thaw cycles, which indicated that the soil density changes (therefore the structure) caused by freezing occur in the frozen zone at temperatures below that of the warmest ice lens. The temperature range was between -0.40℃ to -0.57 °C for the clayey silt, dependent on OCR. The tests also showed an increase in hydraulic conductivity after freeze-thaw, which was consistent with the findings of Chamberlain and Gow (1979).

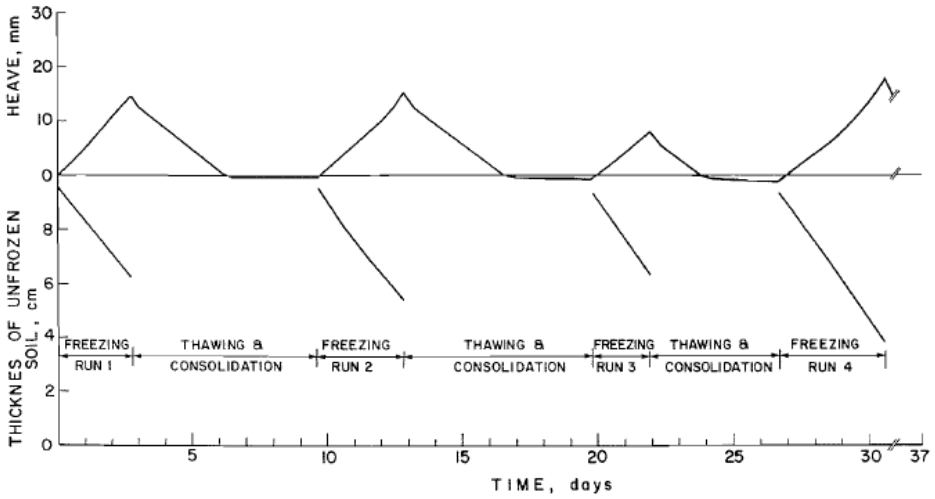

(a)

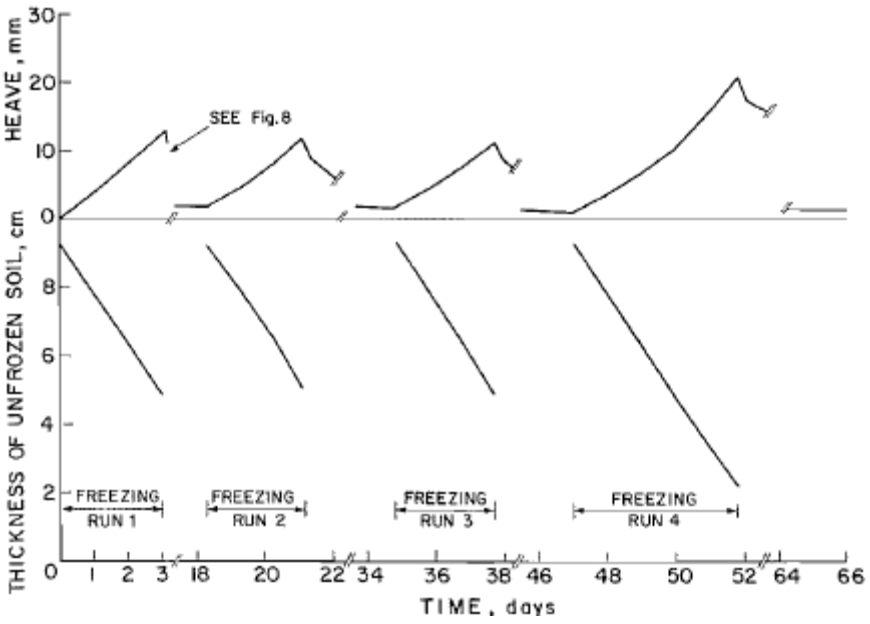

(b)

Figure 2.3 Total frost heave and thaw settlement among freeze-thaw cycles: (a) OCR = 2, (b) OCR = 8 (after Konrad 1989a)

Zou and Boley (2009) carried out open-system freezing-thawing and subsequent compression tests on fine-grained soils using an oedometer. The test results indicated that the slope of the normal consolidation curve for a soil after a freeze-thaw cycle is different than that of the normal consolidation curve and the rebound curve of the soil before freezing. The author explained that it is due to the formation of ice segregation in the frozen zone and the generation of cryogenic suction in unfrozen zone during freezing, which led to large inhomogeneity in soil specimens.

Eigenbrod (1996) performed cyclic one-dimensional open-system freezing and thawing tests on soft fine-grained soils. The volume changes observed could be as much as 30% after thawing, depending on the initial moisture content and plasticity of the clay. A fissured and jointed structure was found in the thawed soil and a large increase in bulk permeability was the

result of it. Eigenbrod et al. (1996) monitored the pore water pressure in one-dimensional freezing and thawing tests on lightly overconsolidated fine-grained soils. The maximum negative pore pressure could be correlated to the compression observed in the soft clay specimen subjected to freezing and thawing, which is often referred to as freeze-thaw consolidation. Stiff clay with water content close to plastic limit did not show freeze-thaw consolidation.

Viklander (1998) conducted a set of freezing and thawing tests on fine-grained non-plastic till, with each experienced eighteen freeze-thaw cycles. The permeability of the soil after the cyclic temperature changes was found to have increased for initially dense specimens, but decreased for initially loose samples. The void ratios decrease for samples with initially high void ratios (e = 0.56), and increase for samples with initially low void ratios (e = 0.25). Residual void ratios ranging from 0.31 to 0.40 were observed for both initially dense and loose soils after 1 to 3 freezing cycles.

Liu and Peng (2009) conducted unconfined compression tests on a thawing soil using a triaxial apparatus with a special temperature controlled system. The tests were performed on soil samples with varying moisture contents and under different freezing and thawing temperatures. The effects of temperature and moisture content on soil strength were investigated and an empirical model describing the stress-strain relationship was proposed.

Qi et al. (2007) conducted tests on a silty soil with one freeze-thaw cycle to investigate changes to the engineering properties of the soil after the process. A critical dry unit weight was found beyond which the soil density, the cohesion and the pre-consolidation pressure will decrease after a freeze-thaw cycle, whereas if the critical dry unit weight is not reached, the three parameters will increase. Yao et al. (2009) concluded that the dependency of soil properties upon freezing and thawing on dry unit weight is related to free energy in soils. The free energy will be

released during thawing in soils with higher dry unit weight, leading to thaw weakening of the soil, whereas the opposite occurs for soils with low dry unit weight.

Proskin et al. (2010) presented laboratory test findings of the effects of freeze-thaw cycle on the behavior of Suncor mature fine tailings (MFT from oil sands mining). A reduced void ratio and compressibility as well as an increased hydraulic conductivity were observed after the MFT experienced freezing and thawing. The results showed a similar trend as for clay soils.

Compared to the experimental studies on the effect of freeze-thaw cycle on soil behavior, very few studies have been conducted on the theoretical description of thaw weakening of frozen soils and corresponding thaw settlement.

Morgenstern and Nixon (1971) formulated the one-dimensional consolidation problem of thawing soil based on heat conduction theory and Terzaghi's consolidation theory. A closed form solution was obtained for a moving thaw boundary in the consolidation problem under the assumption of thawing rate being proportional to the square root of time. It was concluded that excess pore pressures and the degree of consolidation in the thawing soils were dependent on the thaw-consolidation ratio (defined as the ratio of a constant in the solution of heat conduction to the coefficient of consolidation). In order to validate the theory, Morgenstern and Smith (1973) and Nixon and Morgenstern (1973, 1974) conducted one-dimensional thaw consolidation tests on remoulded clays and undisturbed frozen Arctic soils in a special oedometer, in which a sudden constant increase in surface temperature could be applied. The test results showed that the soil behavior could be adequately represented by the theory.

Foriero et al. (1995) formulated a large-strain thaw-consolidation model and used it in finite element simulations. The model was a non-dimensional adaptation of the Gibson et al.

(1981) theory, which considered the variation of permeability and compressibility during consolidation. Non-dimensional design charts were generated using the model to predict thaw-consolidation settlements. A warm oil pipeline in a cold region was simulated and compared with the test data to show the validity of the model. Ming et al. (2012) also used Gibson's large strain consolidation theory along with a moving boundary condition in FEM to simulate the thaw settlement of saturated frozen soil, and obtained reasonable results.

Yao et al. (2012) proposed a large strain thaw consolidation analysis of a thawing frozen soil column. The analysis was performed in finite difference software, FLAC 3D. A moving boundary condition was applied by releasing the fixed nodes when the 0℃ isothermal line was passing by, to simulate the thaw consolidation line. The technique was new and a good way to simulate moving boundary problems (Stephan problems) but needs more effort to be applicable in dealing with complicated boundary value problems.

2.2 Constitutive Models for Freezing and Thawing Soils

When soil is freezing, its strength could be dramatically increased because of the increasing ice component in the soil mixture. The ice in frozen soil can serve as a bonding agent between soil particles, and it increases the cohesive strength of soil considerably. However, when frozen soil is thawing, the melted water (especially in ice-rich soils) can be trapped, leading to large magnitude of excess pore water pressure, thus weakening the soil. In seasonally freezing soils as well as in permafrost regions, the design of transportation infrastructure (highways, bridges, airfields and pipelines) needs to consider the strength and deformation of frozen soil, and knowledge of the stress-strain relationship for freezing and thawing soils is critical.

Unfortunately, few research studies have been devoted in the past to address changes in stress-strain relationship and strength of soils subjected to freezing and thawing.

Zhu et al. (1992) did a number of uniaxial compression tests on frozen soils of different types. They concluded that the stress-strain behavior of frozen soils are dependent on strain rate and temperature and can be classified into 9 categories. Approximate functions describing the stress-strain relationship in each category were given.

Niu et al. (1998) took into account the effect of creep damage on the constitutive relationship for frozen soils. A set of equations including a damage evolution equation, yield criterion and damage growth strain were constructed. Comparison of the model with test results indicated that the model captures the creep properties of frozen soil well.

He et al. (2000) developed a constitutive model for frozen soil based on continuous thermodynamic mechanics and damage mechanics, and can be used to analyze the stress-strain relationship and damage development process. The model was visco-elastic-plastic, in which the rheological behavior was described by introducing a dissipation potential due plastic deformation and damage dissipation. The strengthening and weakening effects of hydrostatic confining pressure on a frozen soil (an increase in soil strength with increasing confining pressure if the pressure is lower than a threshold, but decrease in strength after confining pressure exceeds the threshold) was addressed by Parameswaran and Jones (1981) who included parameters associated with the unfrozen water content in the frozen soil.

Ning and Zhu (2007) developed an elastic constitutive model for frozen sand in which the elastic modulus varied with a proposed freezing parameter. The parameter is a function of the volumetric fraction of ice in the frozen soil, the ultimate strength and the volumetric strain.

Lee et al. (2002) conducted a series of comprehensive tests on Alaskan frozen soils, including hydrostatic compression tests, Brazilian tensile strength tests, unconfined compression tests and triaxial compression tests. A constitutive equation developed by Fossum and Fredrich (2000) was adopted and simplified to describe deformation and failure of frozen soil. The model was strain-rate sensitive and anisotropic in both the elastic and plastic regimes. Model parameters were calibrated using the test data and the prediction carried out was comparable to the test results.

Shoop et al. (2008) adopted a critical state-like modified capped Drucker-Prager plasticity model to describe the behavior of a thawing soil. Triaxial lab tests were conducted to calibrate and validate the model. The model was then implemented into commercial finite element software and successfully used in the simulation of vehicle mobility on thawing soils. Unfortunately, the models were not temperature dependent and could not address the thermal effects on the strength of the soil. Phase transformation in freezing and thawing soils were also not taken into account.

Lai et al. (2009) proposed an elastic-plastic damage constitutive model for frozen sandy soil based on continuum damage theory. The elastic-plastic stress-strain relationship was based on a critical state framework, and the yield surface was chosen to be an ellipse in the p, q plane. Isotropic hardening was adopted and the hardening parameters were chosen to be plastic shear strain, plastic volumetric strain and plastic work. Damage variables were then introduced into the elastic-plastic constitutive relationship, making the elastic modulus dependent on the confining stress and axial strain. With these, the strengthening and weakening effects of confining pressure in frozen soil were successfully addressed. The model was also compared with the Mohr-

Coulomb criteria, and shows its advantages in describing the behavior of frozen soil under high confining pressure.

Li et al. (2011) conducted triaxial creep experiments on frozen soil. Based on the test results, a visco-elastic-plastic constitutive model was developed to describe the creep characteristics of a frozen soil under high confining pressure. The model was then implemented into commercial FE software ADINA, and used in a numerical simulation of a shaft well excavation in artificially frozen ground.

2.3 Critical State and Cam Clay Model

The critical state concept was introduced by Roscoe, Schofield & Wroth (1958) to describe yielding of soils based on the results of tests performed on both sand and clay soils at Cambridge University as well as Imperial College, London. The Cam clay model developed later by Roscoe and Schofield (1963) was among the earliest constitutive models for soils under the critical state framework. Roscoe and Burland (1968) modified the yield condition in the original Cam clay model. This model is often referred to as the Modified Cam clay (MCC) model and it has been widely used in geotechnical engineering for numerical predictions. Later, more constitutive models based on critical state framework were developed, introducing additional state parameters. These models have been proven to be applicable in describing unsaturated soils, undisturbed (structured) soils, and temperature-sensitive soils.

In the field of unsaturated soils, Alonso et al. (1990) developed a constitutive model for partially saturated soils. The model is usually called the Barcelona Basic Model (BBM) and is widely used in the field of unsaturated soil. The model is based on the Modified Cam clay model, and the suction was chosen to be the parameter describing the evolution of the yield

surface due to change in degree of saturation. The increase in tensile strength due to suction was also taken into account by introducing an isotropic tensile yield stress into the yield function. The evolution law of the yield surface was derived in the specific volume versus net mean stress space. It takes the form

$$\left(\frac{p_0}{p^c}\right)=\left(\frac{p_0^*}{p^c}\right)^{[\lambda(0)-\kappa]/[\lambda(s)-\kappa]} \tag{2.1}$$

where p_0 and p_0^* are the pre-consolidation stress for unsaturated soil and saturated soil, respectively. $\lambda(0)$ and $\lambda(s)$ are the slopes for the normal compression line for saturated soil and unsaturated soil, respectively. κ is the slope for unloading reloading line for both saturated and unsaturated soils, p^c is a reference pressure.

Gallipoli et al. (2003) developed an elastic-plastic model for unsaturated soil, which takes explicitly into account the effects of suction as well as its dependence on degree of saturation. First, the author introduced a variable, which could be a measure of the magnitude of the inter-particle bonding due to water menisci to describe the suction effect. $\left(\frac{p_0}{p^c}\right)=\left(\frac{p_0^*}{p^c}\right)^{[\lambda(0)-\kappa]/[\lambda(s)-\kappa]}$ The variable takes the form

$$\xi = f(s)(1-S_r) \tag{2.2}$$

where *f(s)* is a function of suction which accounts for the increase with increasing suction of the stabilizing inter-particle force exerted by a single meniscus; S_r is degree of saturation. Then, a correlation between the variable ξ and the ratio e/e_s was found from the tests and a function was postulated by the author (e and e_s are the void ratios in unsaturated condition and saturated

condition at the same stress state, respectively). With these, the saturated normal compression line and the unsaturated ones are connected and the evolution law was derived using the same procedure as in Alonso et al. (1990), which yields the form

$$\ln(p_0(\xi)) = \frac{\lambda - \kappa}{f(\xi)\lambda - \kappa}\ln(p_0) + \frac{[f(\xi) - 1](1 + \mathrm{N})}{f(\xi)\lambda - \kappa} \tag{2.3}$$

where N is the void ratio at a reference pressure.

In the thermal-mechanical field, Robinet et al. (1996) developed a thermal elastic-plastic model based on the Modified Cam clay model. The model could qualitatively predict the behavior of non-expansive saturated clays under combined heating and loading. The slopes for both NCL and URL are assumed to be independent on temperature; however, the yield condition was defined to be a function of temperature. Therefore, the yield surface is not only changed in the *p', q, v* space as in the Modified Cam clay model, but also changed in the *p', q, T* space by which thermal yielding and thermal irreversible strain ε_{Tv}^{ir} can be addressed. The evolution law was assumed to be related to the thermal irreversible strain, which takes the form

$$p'_{cT} = \left[p'_{c0} \exp\left(\frac{1 + e_0}{\lambda - \kappa} \varepsilon_v^p \right) \right] \exp(\beta_T \varepsilon_{Tv}^{ir}) \tag{2.4}$$

where β_T is a soil constant. The terms in the bracket are the same in the MCC model describing the isotropic strain hardening, whereas the last term is to define the evolution of yield stress due to thermally induced strain. Graham et al. (2001) came up with a similar model. Instead of being constant, the slope for the URL in this model was defined to be decreasing with an increase in temperature. The shift in specific volume due to temperature is defined by the thermal

volumetric strain. The yield condition was the same as in the MCC model, and an associated flow rule was adopted. The evolution law was assumed to be related to the thermal strain, which takes the form

$$P_T' = \frac{P_1'}{\exp\left(\frac{d\varepsilon_v^T}{\lambda}\right)} = \frac{P_1'}{\exp\left(\frac{EdT}{\lambda}\right)} \tag{2.5}$$

where E is a soil constant, λ is the slope for normal consolidation line, $d\varepsilon_v^T$ is the thermal strain.

Abuel-Naga et al. (2007) introduced an isotropic thermo-elastic-plastic model for saturated clays under the framework of MCC model. The thermal evolution of the pre-consolidation pressure took the form:

$$\frac{p_0(T)}{p_0(T_0)} = 1 - \alpha\left[\log\left(\frac{T}{T_0}\right)\right] \tag{2.6}$$

where α is a soil content. Then Abuel-Naga et al. (2009) extended the isotropic model into considering the triaxial stress condition. The yield function for the new model was obtained by introducing an additional parameter into the one used in the MCC model

$$\frac{p}{p_0} = \frac{M^2 + \alpha^2}{M^2 + (\eta - \alpha)^2} \tag{2.7}$$

in which α is a fabric parameter dependent on temperature (other symbols are the same as in the MCC model). The validity of the model was proven by comparing the prediction using the model with the test results.

Hueckel et al. (2009) developed a model to address thermal failure in saturated clays based on the original Cam clay model. The slope for critical state line was adopted as a function of temperature increment. The evolution law for the pre-consolidation pressure took the form

$$p_0^T = p_0 \exp\left(\frac{1+e_0}{\lambda-\kappa}\varepsilon_v^p\right)\left[1-\gamma\log\left(1+\frac{\Delta T}{T_0}\right)\right] \tag{2.8}$$

where γ is a material parameter. With the evolution law, the plastic strain hardening and the thermal softening can be addressed in the model. Various failure modes of saturated clays subjected to temperature changes were captured in the simulation which proves its validity.

The application of the Cam clay framework in undisturbed (structured) soil was first described in Liu and Carter (1999, 2000). The model was formulated by introducing the influence of soil structure into the MCC model, and was often referred to Structured Cam Clay model (SCC). To address the soil structure, an additional term describing the difference in void ratio between the structured soil and the corresponding reconstituted soil at the same stress state during virgin yielding was added to the normal compression line in e, lnp' space (Liu and Carter 2002)

$$e = e_0 - \lambda \ln p' + \Delta e_i \left(\frac{p'_{y,i}}{p_0}\right)^b \tag{2.9}$$

where $p'_{y,i}$ is the value of the mean effective stress at the initial yield point for an isotropic stress state; b is a parameter quantifying the rate of destructuring; Δe_i is the additional void ratio at $p_0 = p'_{y,i}$, where virgin yielding of the structured soil begins. The yield function was the same as in the MCC model, and a non-associated flow rule was adopted. Suebsuk et al. (2010) modified

the SCC model by taking into account the effective stress due to soil structure. Tensile strength due to the soil structure was also added into the yield function.

2.4 Multi-Physical Modeling in Geotechnical Engineering

Multi-physical modeling deals with problems related to more than two of the various physical fields. Such physical fields include: mechanical fields (load and deformation), thermal field (temperature), hydraulic field (fluid pressure and mass flow), bio/chemical field (reactions), and electric/magnetic field (charges, currents, and magnetic circuits).

There are three basic algorithms for multi-physical modeling: one-way coupling, loose coupling, and full coupling (Minkoff et al., 2003). One-way coupling is the earliest manner for multi-physical modeling, in which equations for different fields are solved independently in each step, and the output from one field is passed as input to the other (without information passed back) to solve for the next step. This algorithm is easy to perform, it is computationally less costly, and it is good for problems with one field dominate the process compared to the others. Chances are that physical fields are mutually affected thus considering the effect in only one direction may not reach to an acceptable result. Full coupling method, with all the field variables in one set of equations to be solved simultaneously, provides the most realistic results for such problems. However, the matrix formed from the coupling equations could be huge and the computational cost is significantly large. Loose coupling (sequential coupling) algorithm is in between one-way and full coupling. The equations for different fields are solved independently, but information is passed sequentially between different fields. The results from this algorithm may not as accurate as by the full coupling one, but it is much faster and the results have been proven to be reasonable.

Thermal-hydro-mechanical (THM) modeling deals with multi-physical processes where temperature, hydraulic pressure, and mechanical deformation are simultaneously considered. The mechanisms in a coupled THM system are shown in Figure 2.4. In geotechnical engineering, THM has been widely used in solving porous medium problems in which temperature changes and mass movement are combined, often referred to as thermal consolidation. Such thermally induced consolidation processes could be related to the heating released from a buried nuclear waste, or from a bio-reaction in a solid waste of a landfill.

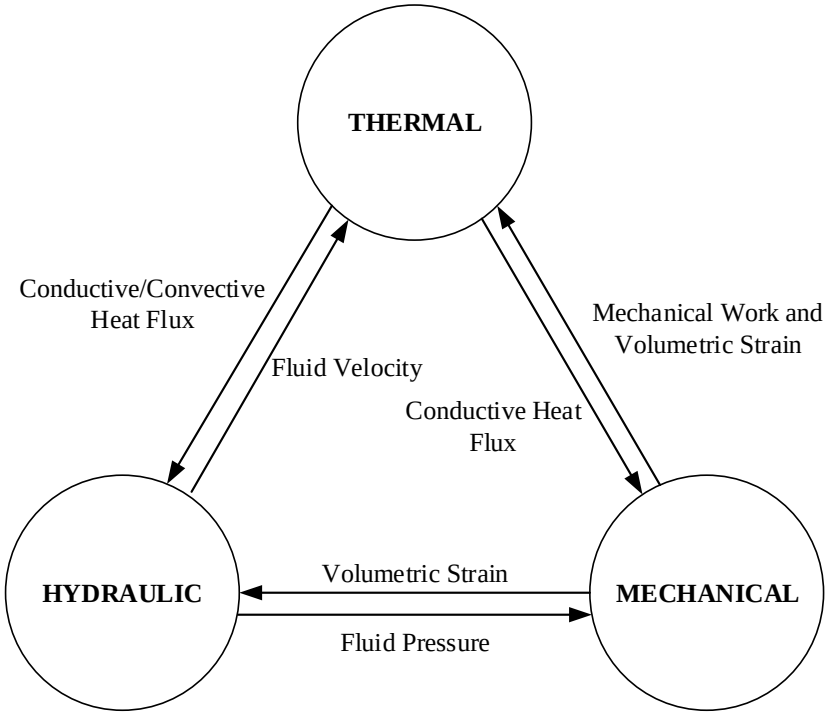

Figure 2.4 The interaction mechanisms in a coupled thermal-mechanical-fluid flow system (after Neaupane et al., 1999)

Application in Porous Medium

Rutqvist et al. (2001a) summarized and compared the assumptions and fundamental equations in the THM models used in four THM finite element codes: ROCMAS, FRACON, THAMES and ABAQUS-CLAY from different research teams. Rutqvist et al. (2001b) compared the results from the heater experiment done in a test pit in Kamaishi Mine with numerical predictions made by the four FEM numerical codes. The results indicated reliable (although advantages in different aspects) predictions of the models for the heat transfer and moisture flow in the thermal consolidation process in rock. However, the capability of the numerical model in prediction of low-stress environment, unsaturated medium were limited. Then as a part of the international DECOVALEX III project, and the European BENCHPAR project, the impact of THM couplings on the performance of a bentonite-back-filled nuclear waste repository in rocks is evaluated using the numerical codes and the results are presented in a series of three companion papers: Chijimatsu et al. (2005), Millard et al. (2005) and Rutqvist et al. (2005).

Chen et al. (2009) created a THM model for unsaturated porous media. The model included a modified Darcy's and Fourier's law to address the fluid and heat flow. The dynamic viscosity of liquid water and void ratio were defined to be dependent on temperature. The influence of liquid flow on temperature gradient (thermo-osmosis), on mass and heat conservation equations, and the influence of heat flow on water pressure gradient and thermal convection were taken into account.

Application in Soils

Missoum et al. (2011) developed a fully coupled THM model considering nonlinear behavior, including temperature dependent dynamic viscosity of liquid and air as well as temperature

gradient dependent liquid and air flow. The partial differential equations in the model were solved using a Galerkin weighted residual approach in the space domain and an implicit integrating scheme in the time domain. The model was successfully used in predicting behavior of unsaturated swelling soils.

Qin et al. (2010) developed a THM model for unsaturated soils based on mixture theory. The dependence of degree of saturation on temperature and stress, the thermal expansion of the soil skeleton, the water and gas flux due to temperature gradient (i.e., the Soret effect), the latent heat of vaporization of water, and the influences of porosity and water content on heat conduction were described in the model. The effect of gas pressure on the phase transition was considered by using thermodynamic restriction relationship based on the vapor chemical potential.

Dumont et al. (2011) proposed a THM model for unsaturated soils by introducing a capillary stress into the effective stress concept. The capillary stress was calculated from the attraction forces due to water menisci on a microstructure level. Thermal softening and desaturation were considered in the model.

Tao et al. (2012) developed a THM model to describe the behavior of methane-containing coal. The model assumed an elastic homogeneous and isotropic body with constant thermal coefficients. The coal was saturated with methane and Darcy's law was used to govern the gas flow. The model was verified by comparing the simulation results of coal and gas outburst using the model with the analytical solution.

Application in Freezing and Thawing in Porous Medium

Some researchers have been trying to use the THM method to address the freezing and thawing process in porous medium e.g. rocks, concrete and soils. Early researchers who used coupling equations in addressing the heat and mass transfer in freezing soils include: Harlan (1973), Guymon and Luthin (1974), Taylor and Luthin (1978), and Jame and Norum (1980). Fundamental governing equations were built and numerical methods were provided to solve the partial differential equations. Due to the lack of computation tools, the application of the methods were limited. As computer technology developed, the THM method became popular again in late 1990's and was widely used in both research and practice.

Neaupane et al. (1999) constructed a THM coupled model to describe the freezing and thawing properties of rocks. A linear thermo-poro-elasticity stress-strain constitutive relationship was adopted. Darcy's law for the fluid flow and the Fourier's law for the heat flux were used in the conservation equations. Neaupane and Yamabe (2001) improved the model by including the thermo-poro-elasto-plasticity constitutive relationship and the Mohr-Coulomb yield condition. An experiment was performed and the measured deformation of rock material upon freezing indicated a good trend in model prediction. Kang et al. (2013) developed THM model for freezing and thawing in rock and implemented the model into the finite difference program FLAC-3D. A simulation of underground low temperature gas storage was performed. Exadaktylos (2006) proposed a coupled model for freezing and thawing of saturated porous medium by making assumptions that freezing and thawing is governed by the theory of thermodynamics of reversible process. Because these models were developed for rocks and concrete, they did not take into account the frost heave and the settlement caused by thaw consolidation.

Corapcioglu and Panday (1995) developed a THM model for unsaturated thawing soil. The model assumed the soil air to be at the atmospheric pressure, other constituents including water, soil grains, and ice were considered to be incompressible. Phase change of water was considered, whereas the evaporation and sublimation of water was neglected.

Zhou and Meschke (2013) proposed a THM model to describe soil freezing. The frost heave was taken into account based on the theory of pre-melting dynamics, in which the contribution of the cryogenic suction was addressed in the coupling equation. The model was verified and successfully used in a simulation of artificial ground freezing in tunnel excavation.

Zhou and Li (2012) differentiated the ice pressure and the water pressure in the equilibrium equation and the Clapeyron equation was used to define the relationship between the two. The fundamental governing equations were introduced with a parameter called "separating void ratio", which played a role as a judge criterion for the formation of ice lenses. By doing this, the frost heave was able to be addressed. The model was then implemented into commercial software COMSOL and a saturated freezing soil column was simulated to show its validity.

Hansson et al. (2004) proposed a TH model for the water flow and heat transfer in frozen soil. A modified Richards's equation considering the effect of both hydraulic and temperature gradient on the water flow was used in the governing equation. The temperature and water content distribution in one-dimensional simulation were close to experimental measurements.

CHAPTER 3

OBJECTIVES

The objective of this research is to advance the modeling of freezing and thawing soils and to demonstrate simulation capabilities of the freezing and thawing process in soils. Changes in stress-strain relationships and strength of soils experiencing freezing and thawing will be considered. The deformation induced by the thermal process, frost heave and thaw consolidation, will be addressed. Specific objectives are as follows:

- To develop a temperature-dependent elastic-plastic stress-strain relationship with evolution of strength for soils experiencing freezing and thawing;
- To revise the porosity rate function to more accurately simulate the amount of frost heave during freezing of frost susceptible soils;
- To build up a comprehensive constitutive model considering the thermal, hydraulic and mechanical processes; describe the evolution of geotechnical engineering properties of soils during freeze-thaw cycles;
- To implement the model in a numerical (finite element) method, and to obtain parameters of the model through calibration using existing laboratory test data;
- To simulate the freezing/thawing processes for infrastructure-related boundary value problems, such as frost heave around culverts and pipelines in seasonal freezing or permafrost regions.

CHAPTER 4

ELASTIC-PLASTIC MODELING FOR FREEZING AND THAWING OF SOILS

The stress-strain relationship and strength are essential to modeling soil behavior upon loading. In general, the difference in stress-strain relationship of soils caused by temperature changes can be neglected. This is due to the fact that for most of the cases, the influence of temperature change on soil structure is very small and the soil behavior does not vary significantly. However, when the soil is under extreme temperatures and the properties or fraction of soil constituents are changing, the stress-strain relationship for the entire soil mixture may be considerably changed. A soil experiencing freezing or thawing is one such example, during which the components of the soil mixture are changing, and so are the stress-strain relationship and soil strength.

In this chapter, an elastic-plastic constitutive model is introduced first, including freezing and thawing, to capture the stress-deformation behavior and strength evolution of the soil subjected to both loading and temperature changes. The model is based on the critical state framework and it is formulated by introducing the influence of fraction of pore ice into the modified Cam Clay model. The elastic-plastic constitutive relationship is then calibrated using

test data. The chapter concludes with some remarks regarding the compression curves corresponding to diverse loading paths.

4.1 Introduction

A soil experiencing freezing and thawing may have dramatically different properties, depending on its thermal state. A thermal process could significantly change the quantitative content of the soil mixture components. For a non-frost-susceptible soil, such as sand or gravel, although no ice segregation will take place during freezing, ice will form in the pores due to the phase change and will co-exist with the pore water. For a frost-susceptible soil, however, such as silt or clay, both pore ice and ice lens will form during freezing.

A soil (both frost-susceptible/non-susceptible) tends to become stronger when it is freezing compared to its room temperature strength and then loses the gained strength when it thaws. Even though there is a lot of interest in thaw-weakening of soils (Henry et al., 2005), little effort was devoted in the past to address changes in strength to soils subjected to freezing and thawing, and no reliable constitutive models have been developed. Recently, some effort was made toward describing elastic-plastic behavior of frozen soils (Lai et al., 2009; Li et al., 2011), but quantitative changes in the soil mixture components upon freezing and thawing, and the corresponding changes in strength, are not addressed by these models. Others tried to exploit an analogy of cryogenic suction in freezing soil to matric suction in unsaturated soils (Nishimura et al., 2009), thus borrowing from the constitutive relationship for unsaturated soils. However, neither the cryogenic suction nor the hydraulic conductivity of frozen soils was evaluated with confidence. Therefore, these efforts did not give rise to computational tools that could be used

reliably in model-based simulations. An elastic-plastic constitutive model is developed to describe the mechanical behavior of a freezing and thawing soil in this chapter.

4.2 Elastic-Plastic Model for Freezing and Thawing Soils

A critical state concept was put forward by Roscoe, Schofield and Wroth in 1958 for describing yielding of soil in simple shear and triaxial tests. It was then proven to be an effective concept dealing with plasticity of saturated clays. Then, the Original Cam Clay Model and the Modified Cam Clay (MCC) Model were developed based on the critical state framework by Schofield and Wroth (1968) and Roscoe and Burland (1968), which have been fundamental constitutive models and widely used in both geotechnical research and engineering practice. In more advanced soil mechanics, additional parameters are added into the Original (Modified) Cam Clay model to make it suitable for specific applications. Such models include the Barcelona Basic Model (BBM) developed by Alonso et al. (1990) to address the effect of suction in unsaturated soil mechanics and the Structured Cam Clay (SCC) Model presented by Liu and Carter (2002) to take into account the influence of soil structure on soil plasticity, etc. In this section, the Modified Cam Clay Model will be used as the fundamental framework. By adding a *pore ice ratio* parameter, the model will be suitable for describing the behavior of freezing and thawing soils.

4.2.1 Pore Ice Ratio

When freezing, soils tend to become stronger compared to soils at room temperature. This is because the water in pores will freeze, and the pore ice will serve as particles/grains cementation or bonding agents, resulting in an increase in strength. The loss of strength will then occur upon thawing when the bonding is released by melting of the pore ice. While other mechanisms inducing strength increase upon freezing may exist, the components fraction changes (the

presence of pore ice) is the chief cause for strengthening of freezing soils. Therefore, the *pore ice ratio* e_{ip} is introduced as a key parameter in the description of the behavior of frozen soils

$$e_{ip} = \frac{V_{ip}}{V_s} \tag{4.1}$$

where V_{ip} is the volume of ice in pores and V_s is the volume of the solid constituent (mineral skeleton) in a given volume of soil.

The pore ice ratio is uniquely related to the unfrozen water content in frozen soils, which is a soil property associated with the freezing process. Because e_{ip} is temperature-dependent, the entire model is dependent on the temperature. As the unfrozen water content can be obtained from laboratory tests, e_{ip} can be assessed from the very same tests.

4.2.2 Unfrozen Water Content Curve (UWCC) in Frozen Soil

In frost susceptible soils, such as silts and clays, not all water freezes at the freezing point due to the existence of surface tension of the water meniscus formed between soil particles. The amount of liquid pore water remaining in frozen soil with respect to freezing temperature is a soil property and the unfrozen water content curve is used to describe this relationship.

A 3-parameter function developed by Michalowski (1993) is adopted here to describe the unfrozen water content curve (UWCC) in the frozen soil. The function takes the following form:

$$w = w^* + (w_0 - w^*)\, e^{a(T - T_0)} \tag{4.2}$$

where a is a parameter defining the rate of decrease in liquid moisture with decreasing temperature, w_0 is the moisture content of unfrozen soil, w^* is the residual unfrozen water content

at some low reference temperature, T_0 is the freezing point of water. The plotted curve for Equation (4.2) and corresponding parameters are illustrated in Figure 4.1. When soil freezes and then thaws, the freezing and thawing UWCCs are not identical, with the primary thawing curve below the primary freezing curve. However, an identical curve for both freezing and thawing is assumed here in simulations due to the lack of data for differentiating them.

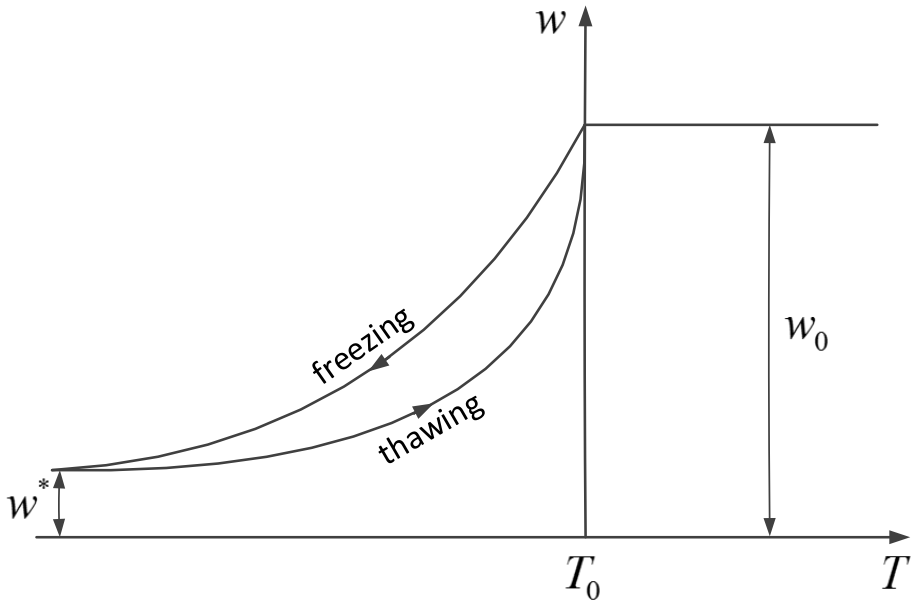

Figure 4.1 Unfrozen water content curve

For saturated soils, all the pore ice is from the phase change of pore water, the volume of pore ice V_{ip} can be calculated from the decrease in liquid water content according to the UWCC. The pore ice ratio e_{ip} in Equation (4.1) can then be calculated as

$$e_{ip} = (w_0 - w) \cdot \frac{\rho_s}{\rho_w} 1.09 \tag{4.3}$$

where ρ_s and ρ_w are the density of the solid mineral and water, respectively. By substituting Equation (4.2) into Equation (4.3), the function can be rewritten as:

$$e_{ip} = \left(w_0 - w^*\right)\left(1 - e^{a(T-T_0)}\right) \cdot \frac{\rho_s}{\rho_w} 1.09 \tag{4.4}$$

Because the unfrozen water content is a function of temperature, so is the pore ice ratio expressed in Equation (4.4).

4.2.3 Critical State Model for Freezing and Thawing Soils

Compression of frozen soils

To describe volumetric changes of the soil, specific volume v is introduced and defined as

$$v = \frac{V}{V_s} = 1 + e \tag{4.5}$$

where V is the total volume of a representative soil element, V_s is the volume of solids in this element, and e is the void ratio. The mean effective stress p' is defined as

$$p' = \frac{1}{3}\sigma'_{kk}, \quad k = 1,2,3 \tag{4.6}$$

where σ'_{kk} is the first invariant of the effective stress tensor.

Compression of both the unfrozen and frozen soil can be represented by the normal compression line (NCL) and the unloading-reloading line (URL) on the plane v vs. $\ln(p'/p^r)$, Figure 4.2(a), where p^r is the reference effective isotropic stress (pressure). The slopes of the

NCL and URL are described by parameters λ and κ (λ_f and κ_f for frozen soil, and both vary with the change in pore ice ratio e_{ip}). The NCL for unfrozen soil is defined by equation

$$v = v_0 - \lambda \ln \frac{p'}{p^r} \tag{4.7}$$

where v_0 is the specific volume at reference pressure p^r. The elastic change of the specific volume in the unloading-reloading regime is given by

$$dv^e = -\kappa_f \frac{dp'}{p'} \tag{4.8}$$

Normal compression lines for an unfrozen and frozen soil are illustrated in Figure 4.2(a, b) along with the unloading-reloading line for the frozen soil. Only one NCL for frozen soil is shown in Figure 4.2(a, b) (for one value of pore ice ratio e_{ip}), but the model accounts for a family of normal consolidation lines dependent on the value of pore ice ratio e_{ip}. The following relationships are postulated for slopes of NCL and URL for frozen soil

$$\lambda_f = \lambda \exp(-\alpha_1 e_{ip}),\ \kappa_f = \kappa \exp(-\alpha_2 e_{ip}) \tag{4.9}$$

where α_1 and α_2 are soil constants (Zhang and Michalowski 2013). Soils tend to become stronger and stiffer when they freeze. This behavior is characterized by an increase of the yield condition (in the stress space), and flatter slopes of NCL and URL for frozen soils (Qi et al. 2010, Lee et al. 2002). The slopes λ and κ for unfrozen soil, and λ_f and κ_f for frozen soil, can be obtained from isotropic compression tests in a triaxial apparatus. Information about a triaxial apparatus designed specifically to test frozen soils can be found elsewhere (Zhao et al. 2013, Re et al. 2003). Having tested the response of soil to isotropic compression, soil constants α_1 and α_2 can

be obtained from fitting the experimental results into the functions in Equation (4.9), with e_{ip} known from the unfrozen water content curve for a given temperature (this will be demonstrated later).

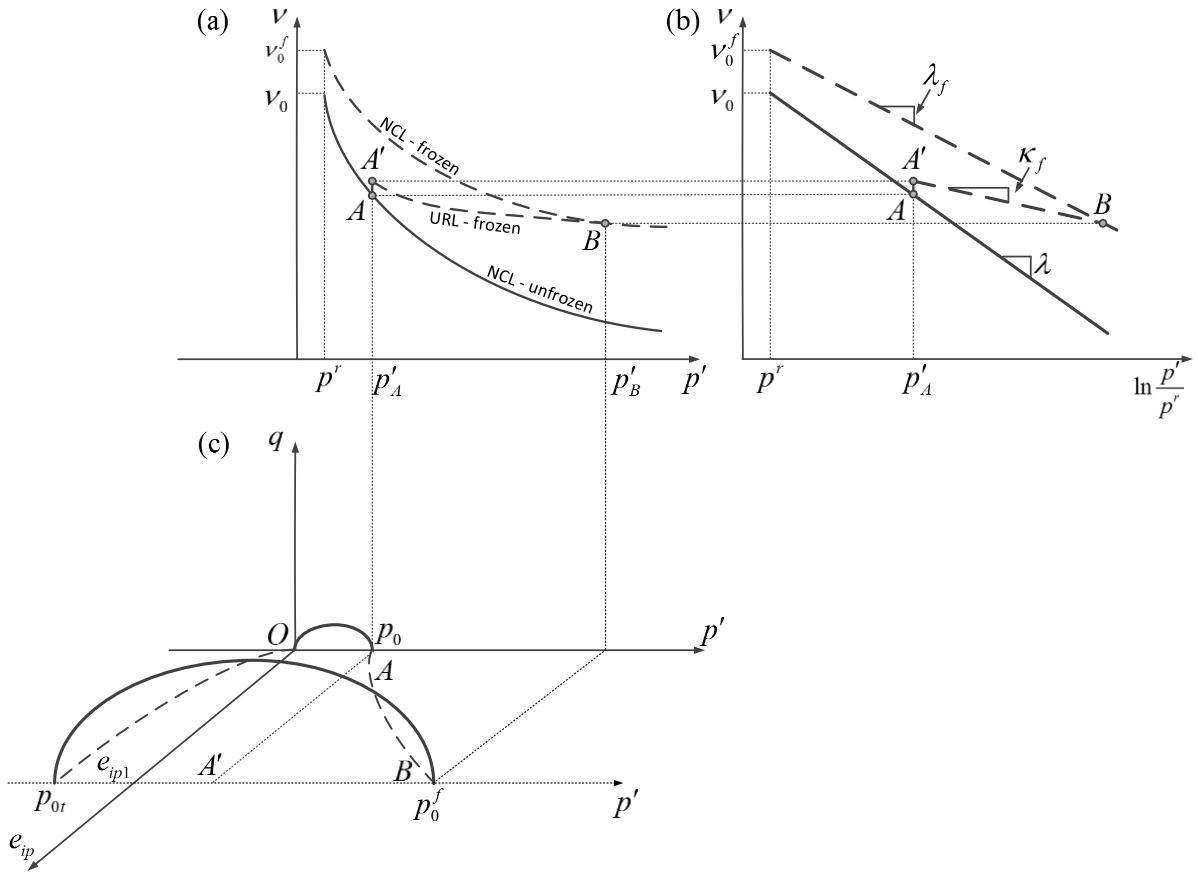

Figure 4.2 (a) Compression curves for freezing soils in *v, p'* space, (b) Compression curves in *v*, $\ln(p'/p^r)$ space, (c) Yield condition for freezing soil

The yield condition

An elliptical yield surface in *q, p'*-plane (deviatoric, effective isotropic stress) is adopted

$$f = q^2 - M^2(p' - p_{0t})(p_0 - p') = 0 \tag{4.10}$$

where p_0 and p_{0t} are the material properties representing yielding in isotropic compression and in isotropic tension, respectively. The ice constituent in the mixture is considered part of the solid, and the effective isotropic pressure p' is the combined stress in the mineral and ice. Yielding stress can change as a result of a compression process; isotropic stress at yielding for unfrozen soil is uniquely related to specific volume *v* and it is referred to as the *pre-consolidation pressure* (p_0). However, the yield pressure can be increased as a result of freezing. For frozen soils, the yielding pressure will be designated by p_0^f, i.e., for frozen soil $p_0 = p_0^f$ in Equation (4.10). p_0^f is a function of both the specific volume and the pore ice ratio e_{ip} (therefore, the temperature). When p_0^f is increased because of freezing, it will be referred to as a *pseudo pre-consolidation pressure*, because the hardening is caused by the phase change and "ice bonding", rather than the normal compression process.

Bonding of particles with pore ice provides the frozen soil with some tensile strength. As the pore ice ratio increases, the isotropic tensile yield strength p_{0t} in Equation (4.10) also increases (but $p_{0t} = 0$ for unfrozen soil). The following evolution law is postulated for the isotropic tensile strength

$$p_{0t} = p_t\left(1 - e^{-\alpha_3 e_{ip}}\right) \tag{4.11}$$

where α_3 is a soil parameter and p_t is an asymptotic bound to the tensile strength of frozen soil with increasing e_{ip} (tensile strength of frozen soil at some low temperature; p_t = -1.0 MPa was used in calculations). Information on tensile strength of frozen soil and ice can be found in Akagawa and Nishisato (2009). The modification to include tensile strength was introduced earlier by Alonso et al. (1990) in the context of unsaturated soils.

The parameter M in Equation (4.10) defines the inclination of the critical state line, as in the modified Cam clay model (Roscoe and Burland 1968, Wood 1990). The inclination of the critical state line is assumed to be independent of the pore ice ratio (also illustrated in Figure 4.3). Plastic deformation of the soil is assumed to be governed by the normality rule.

The evolution of the yield condition during a freezing process is illustrated in Figure 4.2(c) as a function of pore ice ratio e_{ip}. An unfrozen saturated soil at point A on the normal consolidation line (Figure 4.2(a)) is subjected to freezing under a constant isotropic stress p'_A. The volume expansion due to phase change causes the specific volume to increase by a small amount. While the state of the soil is now represented by point A' in Figure 4.2(a), the pseudo pre-consolidation stress increased from p_0 at point A to p_0^f at point B on the normal consolidation line for frozen soil, Figure 4.2(c) as a result of freezing alone. However, the soil is now in the elastic state represented by point A' in Figure 4.2(c). During the freezing process the pore ice ratio increased from 0 for the unfrozen soil to the value of e_{ip1}, and the yield condition increased accordingly. If isotropic loading is now applied under a constant temperature, the specific volume will decrease at the rate of κ_f following the secondary compression line for frozen soil until it reaches the pseudo NCL for frozen soil. This loading process is represented by

path $A'B$ in both Figure 4.2(a) and Figure 4.2(c). During the isothermal loading process, the pore ice ratio remains constant at e_{ip1}.

The evolution law

A procedure is introduced here to define the evolution of the pre-consolidation stress for frozen soil. This evolution law is similar to that introduced by Alonso et al. (1990) for unsaturated soils in terms of matric suction. Here, p_0^f it is the pore ice ratio, in addition to stress, that governs the yield function evolution.

The change in the specific volume $\delta v_{A'B}$ that occurs as the soil is loaded from point A' to point B can be written as

$$\delta v_{A'B} = v_B - v_A - \delta v_{AA'} \tag{4.12}$$

Specific volumes at point A and B are defined by the respective normal consolidation lines (Equation (4.7))

$$v_A = v_0 - \lambda \ln \frac{p'_A}{p^r} = v_0 - \lambda \ln \frac{p_0}{p^r} \tag{4.13}$$

and

$$v_B = v_0^f - \lambda_f \ln \frac{p'_B}{p^r} = v_0^f - \lambda_f \ln \frac{p_0^f}{p^r} \tag{4.14}$$

whereas the change in *v* during elastic loading of the frozen soil along $A'B$, based on Equation (4.8)

$$\delta v_{A'B} = -\kappa_f \ln \frac{p'_B}{p'_A} = -\kappa_f \ln \frac{p_0^f}{p_0} \tag{4.15}$$

Substituting Equations (4.13) through (4.15) into Equation (4.12), one obtains

$$-\kappa_f \ln \frac{p_0^f}{p_0} = \left(v_0^f - \lambda_f \ln \frac{p_0^f}{p^r} \right) - \left(v_0 - \lambda \ln \frac{p_0}{p^r} \right) - 0.09 e_{ip} \tag{4.16}$$

where $0.09e_{ip}$ is the change in specific volume caused by expansion of water due to phase change. Finally, the pseudo pre-consolidation stress for frozen soil becomes

$$\frac{p_0^f}{p^r} = e^{\frac{v_0^f - v_0 - 0.09 e_{ip}}{\lambda_f - \kappa_f}} \left(\frac{p_0}{p^r} \right)^{\frac{\lambda - \kappa_f}{\lambda_f - \kappa_f}} \tag{4.17}$$

with both λ_f and κ_f being functions of pore ice ratio e_{ip}. The pseudo pre-consolidation stress for frozen soil is, of course, a function of e_{ip}. To make the numerical calculations simpler, we postulate the relationship of v_0 to v_0^f as a function of e_{ip}

$$v_0^f - v_0 - 0.09 e_{ip} = \beta e_{ip} \tag{4.18}$$

v_0^f is a function of e_{ip}, and it is indicated in Figure 4.2(a) for one specific value of e_{ip} (if $e_{ip} = 0$, then $v_0^f = v_0$). The calibration (shown later) indicated that taking β as a function of p^r is a reasonable assumption. Therefore, Equation (4.17) can be rewritten as

$$\frac{p_0^f}{p^r} = e^{\frac{\beta e_{ip}}{\lambda_f - \kappa_f}} \left(\frac{p_0}{p^r} \right)^{\frac{\lambda - \kappa_f}{\lambda_f - \kappa_f}} \tag{4.19}$$

Parameter β can be obtained from isotropic compression tests in a triaxial apparatus. Slopes λ, κ and pre-consolidation stress p_0 for unfrozen soil, and slopes λ_f, κ_f and pre-consolidation stresses p_0^f for frozen soils with diverse e_{ip}, can be obtained from the same isotropic compression tests.

An illustration of how the pseudo pre-consolidation stress p_0^f and p_{0t} vary in soil with progressively increasing pore ice ratio e_{ip} is illustrated in Figure 4.3 (the following parameters were used: p_0 = 300 kPa, α_1 = 0.2, α_2 = 0.4, α_3 = 0.6, β = 0.3, λ = 0.35, κ = 0.07, p_t = -1.0 MPa, p^r = 0.1 MPa).

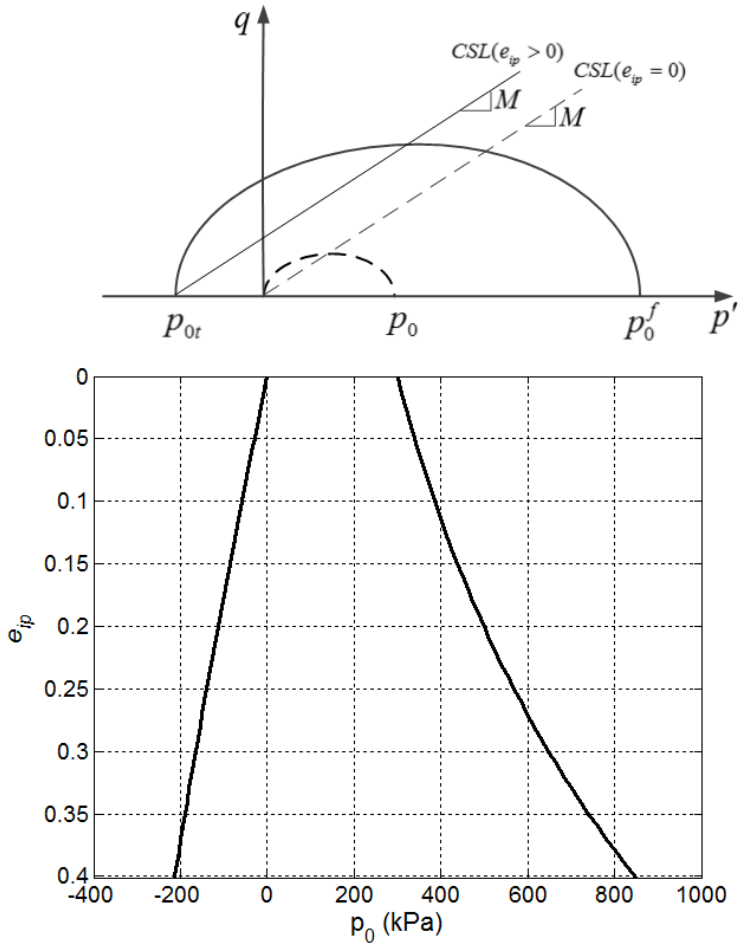

Figure 4.3 Yield surfaces in (p', q, e_{ip}) spaces

Illustration of freezing, loading, unloading and thawing

An illustration of a freeze-thaw and load-unload cycle is shown in Figure 4.4. A saturated soil specimen is pre-consolidated under isotropic compression to reach point A. Now, the freezing process takes place under constant stress, so that the pore ice ratio of the soil increases from zero to e_{ip1}. A small increase in the specific volume is related to expansion of water upon freezing (saturated soil). As the freezing occurs along path AA' (Figure 4.4(b)), the pseudo pre-consolidation pressure of the freezing soil increases to reach p_{0B}^{f}, but the soil remains in an elastic state at A'. The normal consolidation line for the soil with e_{ip1} is marked with the dashed line. The temperature is now maintained, but the isotropic compression is increased from p'_A to reach the normal compression line for frozen soil at B'. The load is then increased and the process continues along the normal consolidation line for frozen soil to reach point C' (with pre-consolidation stress p_{0C}^{f}).

If the soil was to be unloaded at point C' (Figure 4.4(a)), and then thawed to reach point D, the pre-consolidation pressure would decrease from p_{0C}^{f} to p_{0D}, following curve C'D in Figure 4.4(b). This reduction in pre-consolidation pressure can be calculated from Equation (4.20) as

$$\left(\frac{p_0}{p^r}\right) = e^{\frac{-\beta e_{ip}}{\lambda_f - \kappa_f}} \left(\frac{p_0^f}{p^r}\right)^{\frac{\lambda_f - \kappa_f}{\lambda - \kappa_f}} \tag{4.20}$$

which is in the reverse form of Equation (4.19). The pore ice content can be calculated from Equation (4.3) with the liquid moisture content from UWCC in Figure 4.1.

Consider the soil being still at point C', Figure 4.4(b), but it is now subjected to thawing. The process follows path C'C at constant stress p'_C. While the soil is thawing, it cannot sustain the load without yielding. This is because the gradual melting of ice causes the loss of "ice bonding" leading to a decrease in strength. The space between NCL for unfrozen soil (ADC) and that for the frozen soil with e_{ip1} (the dashed line) is occupied by a family of normal consolidation lines for the frozen soil with pore ice ratios between 0 and e_{ip1}. Because the stress p'_C is maintained, a hardening process takes place as the specific volume decreases, causing the pre-consolidation pressure to be constant, but associated with yield conditions with different pore ice ratios as the process progresses from point C' to C, Figure 4.4(a).

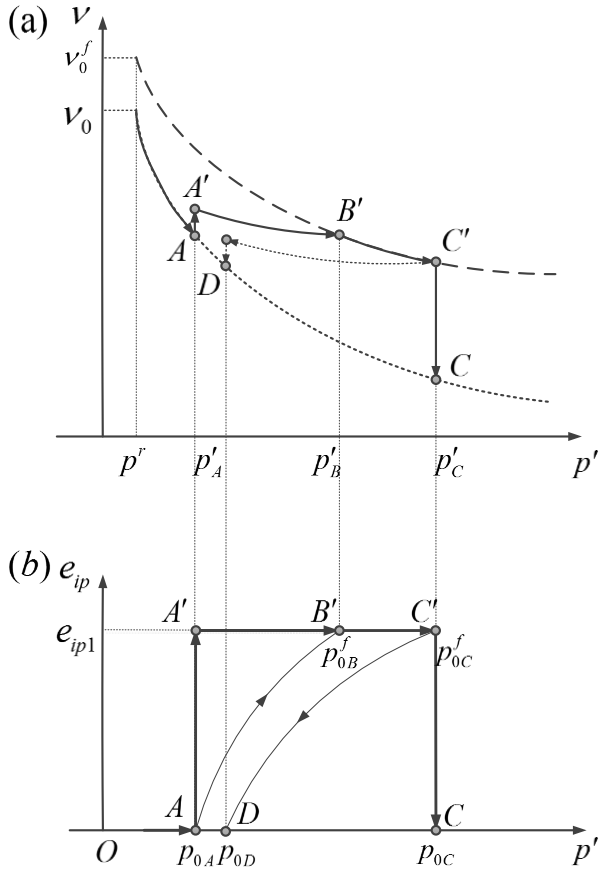

Figure 4.4 Illustration of a freeze-thaw cycle with loading

We now illustrate how to calculate plastic deformation during loading of frozen soil and during thawing. This is needed when calculating thaw settlement. An increment in the specific volume of frozen soil during loading is

$$dv = -\lambda^f \frac{dp'}{p'} \tag{4.21}$$

whereas the elastic portion of it is given in Equation (4.8). Because the volumetric strain increment can be related to the change in the specific volume, in general, as

$$d\varepsilon_v = -\frac{dv}{v} \tag{4.22}$$

The plastic volumetric strain increment caused by mechanical load driving the process from point B' to C' (Figure 4.4(a)) can be derived by subtracting the elastic change in v in Equation (4.8) from the total change in Equation (4.21), and using Equation (4.22)

$$d\varepsilon_v^{pl} = \frac{\lambda_f - \kappa_f}{v} \frac{dp'}{p'} \tag{4.23}$$

and, consequently

$$\varepsilon_v^{pl} = (\lambda_f - \kappa_f) \int_{p_{0B}^f}^{p_{0C}^f} \frac{1}{v} \frac{dp'}{p'} \tag{4.24}$$

The decrease in specific volume in the thawing process C'C is related to the thermally induced yielding, and is equivalent to the drop in specific volume due to the virgin compression of unfrozen soil from D to C (Figure 4.4(a)). Therefore, the irreversible strain ε_v^t due to thaw weakening can be calculated as

$$\varepsilon_{v\_C'C}^{tw} = \varepsilon_{v\_DC}^{pl} = (\lambda - \kappa_f) \int_{p'_D}^{p'_C} \frac{1}{v} \frac{dp'}{p'} \tag{4.25}$$

Soil freezing with ice segregation

The model described defines the strength evolution for a non-segregation freezing and thawing soil. The presence of ice lenses will alter the yield condition and the strength changes are likely to be anisotropic, because of the directional formation of lenses (perpendicular to the heat flow direction). These changes are not included in the model due to a lack of experimental data. Therefore, it is suggested for now that the yield condition described be used for both non-segregation and segregation freezing processes. However, segregation freezing will shift the NCL and URL upward on the plane of specific volume versus $\ln p'$, because the increase in volume caused by growing ice lenses is included in the model as an average growth in porosity.

In a thawing frozen soil with ice segregation, the ice lenses do not start melting until the temperature reaches 0 ℃, whereas the pore ice starts melting earlier, with unfrozen water content consistent with Figure 4.1. Tests performed by Konrad (1989) indicate that if ice lenses formed during freezing, the void ratio after a freeze-thaw cycle will decrease in normally consolidated soils, presumably due to consolidation caused by suction. Consequently, a normally consolidated soil specimen will exhibit settlement after the freeze-thaw cycle(s). However, a small portion of the heave may remain after the freeze-thaw cycle in over-consolidated soils, particularly in soils with large over-consolidation ratio. The model developed and presented in this thesis predicts the settlement after the cycle (due to consolidation caused by suction during freezing), but it does not predict any portion of the heave to remain after thawing in over-consolidated soils.

4.3 Calibration of the Model

The unfrozen water content curve (UWCC) is first calibrated for different types of frost-susceptible soils based on test data. To calibrate the parameters, w_0 and w^* can be directly extracted from test data, whereas the parameter a is obtained from curve fitting. The comparisons of the calibrated curves and the test data are shown in Figure 4.5. In Figure 4.5(a), the calibration curve for a particular clay tested in Fukuda et al. (1997) is shown, and the parameters obtained are $w^* = 0.058$, $w_0 = 0.285$, $T_0 = 0$ ℃, and $a = 0.16$ °C^{-1}. Figure 4.5(b) shows the calibration curve for Fairbanks silt in Alaska (Huang et al. 2004) and the parameters are $w^* = 0.08$, $w_0 = 0.325$, $T_0 = 0$ ℃, and $a = 9.0$ °C^{-1}. By comparing the unfrozen water content curves for clay and silt, one may observe that the UWCC of silt is much steeper than that of clay.

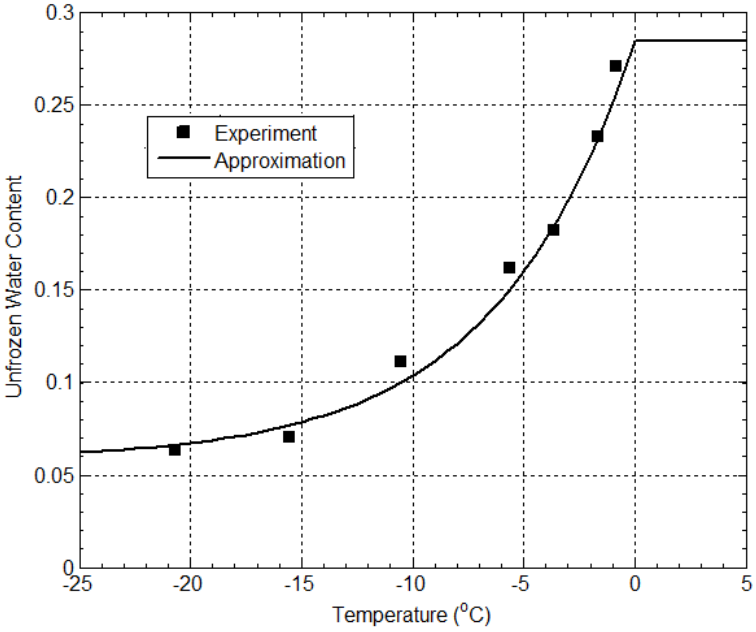

(a)

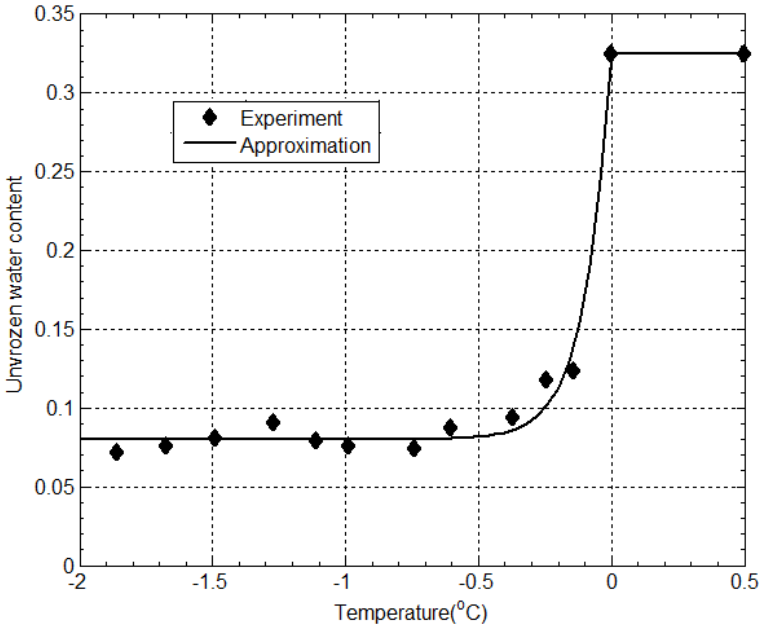

(b)

Figure 4.5 Calibration of unfrozen water content curve: (a) for clay (Fukuda et al., 1997), (b) for silt (Huang et al., 2004)

The elastic-plastic constitutive model was calibrated based on the freezing tests done by Qi, et al. (2010). The pseudo pre-consolidation stress change as a function of freezing temperature is shown in Figure 4.6. The respective parameters obtained from calibration are as follows: λ = 0.35, κ = 0.07, p_0 = 650 kPa, M = 0.7, α_1 = 0.4, α_2 = 1.8, p^r = 100 kPa, β = 0.18.

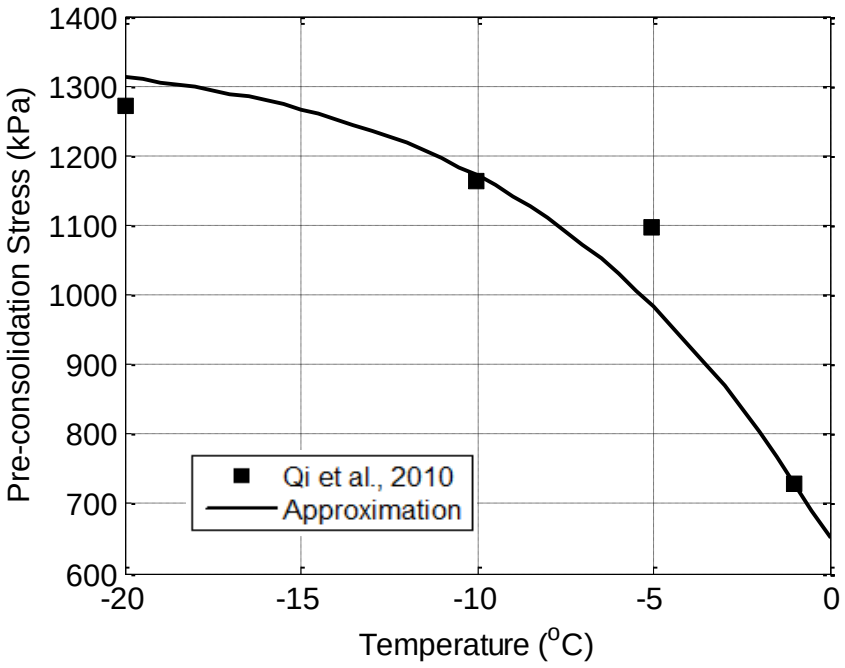

Figure 4.6 Calibration of pseudo-pre-consolidation stress for frozen soil

4.4 Implementation of the Model in Finite Element Method

The elastic-plastic constitutive relationship has been implemented into a commercial finite element software system ABAQUS, using subroutine UMAT which is provided by ABAQUS for users to extend its capability in describing mechanical constitutive behavior of materials.

In order to implement the constitutive relationship, the Jacobian matrix corresponding to the elastic-plastic model needs to be input into the subroutine. As is described in the proposed model, the change in size of the yield surface is dependent on both p_0 and p_{0t} (Equation (4.10)). The change in p_0 is controlled by both plastic volumetric strain ε_v^{pl} (strain hardening) and pore ice ratio e_{ip} (thermal hardening), whereas the change in p_{0t} is related only with the pore ice ratio e_{ip}.

The total elastic-plastic strain increment is a sum of the elastic strain increment and the plastic strain increment:

$$\delta\varepsilon_{ij}^{ep} = \delta\varepsilon_{ij}^{e} + \delta\varepsilon_{ij}^{p} \tag{4.26}$$

The elastic relationship adopted is the same as in the Modified Cam Clay model (Roscoe and Burland 1968, Wood 1990) and the elastic strain increment can be calculated from

$$\begin{bmatrix} \delta\varepsilon_v^e \\ \delta\varepsilon_q^e \end{bmatrix} = \begin{bmatrix} 1/K' & 0 \\ 0 & 1/3G' \end{bmatrix} \begin{bmatrix} \delta p' \\ \delta q \end{bmatrix} \tag{4.27}$$

where $K' = vp'/\kappa$ is the bulk modulus and G' is the shear modulus having the form

$$G' = \frac{3(1-2\upsilon)K'}{2(1+\upsilon)} \tag{4.28}$$

where v is specific volume, κ is the slope for unloading reloading line, and υ is Poisson's ratio. The plastic strain increment caused by compression can be calculated using the same equation as in the Modified Cam Clay model

$$\begin{bmatrix} \delta\varepsilon_v^p \\ \delta\varepsilon_p^q \end{bmatrix} = \frac{(\lambda-\kappa)}{vp'(M^2-\eta^2)} \begin{bmatrix} (M^2-\eta^2) & 2\eta \\ 2\eta & 4\eta^2/(M^2-\eta^2) \end{bmatrix} \begin{bmatrix} \delta p' \\ \delta q \end{bmatrix} \tag{4.29}$$

where $\eta = q/p'$ is the stress ratio.

The finite element implementation of the elastic-plastic constitutive model uses the incremental form of the stress-strain relationship. The procedure has been well developed and can be found in Hadedal (1994) and text books, e.g. Wang (2002). The elastic constitutive relationship is generally expressed as

$$\delta\boldsymbol{\sigma} = \boldsymbol{C}\delta\boldsymbol{\varepsilon}^e = \boldsymbol{C}\left(\delta\boldsymbol{\varepsilon} - \delta\boldsymbol{\varepsilon}^p\right) \tag{4.30}$$

where $\boldsymbol{C}$ is the elastic matrix, $\delta\boldsymbol{\sigma}$ is stress increment, $\delta\boldsymbol{\varepsilon}$ is total strain increment, $\delta\boldsymbol{\varepsilon}^e$ is elastic strain increment and $\delta\boldsymbol{\varepsilon}^p$ is plastic strain increment. The plastic strain increment is related to plastic potential and in a p', q space, it can be written as

$$\delta\varepsilon_v^p = \delta\chi\frac{\partial g}{\partial p'} \tag{4.31a}$$

$$\delta\varepsilon_q^p = \delta\chi\frac{\partial g}{\partial q} \tag{4.31b}$$

where χ is the plastic multiplier, and g is the plastic potential function. The hardening rule is related only to the plastic volumetric strain and is expressed as

$$\delta p_0 = \frac{\partial p_0}{\partial\varepsilon_v^p}\delta\varepsilon_v^p = \frac{vp_0'}{\lambda-\kappa}\delta\chi\frac{\partial g}{\partial p'} \tag{4.32}$$

The differential of the yield condition is (Prager consistency condition)

$$\delta f = \frac{\partial f}{\partial p'}\delta p' + \frac{\partial f}{\partial q}\delta q + \frac{\partial f}{\partial p_0}\delta p_0 = 0 \tag{4.33}$$

So far, the model was expressed in *p'*, *q* space. In order to implement the model into finite element environment in general Cartesian coordinate system, Equation (4.33) is converted into

$$\delta f = \left(\frac{\partial f}{\partial \boldsymbol{\sigma}}\right)^T \delta\boldsymbol{\sigma} + \frac{\partial f}{\partial p_0}\delta p_0 = 0 \tag{4.34}$$

Substituting Equations (4.30 and 4.32) into Equation (4.34), one can obtain the expression for the plastic multiplier increment

$$\delta\chi = \frac{\boldsymbol{C}\left(\frac{\partial f}{\partial \boldsymbol{\sigma}}\right)^T}{A + \left(\frac{\partial f}{\partial \boldsymbol{\sigma}}\right)^T \boldsymbol{C}\left(\frac{\partial g}{\partial \boldsymbol{\sigma}}\right)}\delta\boldsymbol{\varepsilon} \tag{4.35}$$

in which A is hardening modulus and has the following form

$$A = \left(\frac{\partial f}{\partial p_0}\right)\left(\frac{v p_0'}{\lambda - \kappa}\frac{\partial g}{\partial p'}\right) \tag{4.36}$$

An associated flow rule was adopted, $g = f$, and the derivatives of the yield function with respect to the state parameters can be derived from Equation (4.10)

$$\frac{dg}{dp'} = \frac{df}{dp'} = M^2(2p' - p_0 - p_{0t}) \tag{4.37a}$$

$$\frac{dg}{dq} = \frac{df}{dq} = 2q \tag{4.37b}$$

$$\frac{dg}{dp_0} = \frac{df}{dp_0} = M^2(-p' + p_{0t}) \tag{4.37c}$$

$$\frac{dg}{dp_{0t}} = \frac{df}{dp_{0t}} = M^2(-p' + p_0) \tag{4.37d}$$

Substituting Equations (4.23 and 4.37) into Equation (4.36), the hardening modulus can be rewritten as

$$A = M^2(-p' + p_{0t})\frac{(1+e)p_0}{\lambda - \kappa}M^2(2p' - p_0 - p_{0t}) \tag{4.38}$$

By inserting the plastic strain increment

$$\delta\boldsymbol{\varepsilon}^p = \delta\chi\frac{\partial g}{\partial \boldsymbol{\sigma}} \tag{4.39}$$

into the constitutive relation (Equation (4.30)), an elastic-plastic stress-strain relationship can be obtained based on the total strain increment

$$\delta\boldsymbol{\sigma} = \left[\boldsymbol{C} - \frac{\left(\boldsymbol{C}\frac{\partial g}{\partial \boldsymbol{\sigma}}\right)\left(\boldsymbol{C}\frac{\partial f}{\partial \boldsymbol{\sigma}}\right)^T}{A + \left(\frac{\partial f}{\partial \boldsymbol{\sigma}}\right)^T \boldsymbol{C}\left(\frac{\partial g}{\partial \boldsymbol{\sigma}}\right)}\right]\delta\boldsymbol{\varepsilon} = \boldsymbol{C}^{ep}\delta\boldsymbol{\varepsilon} \tag{4.40}$$

where $\boldsymbol{C}^{ep}$ is the elastic-plastic constitute matrix which is coded into the Jacobian matrix in the subroutine.

Boundary value problems can be solved using this model, along with the heat transfer model provided in ABAQUS to explore the mechanical behavior of frozen soils.

4.5 Model Demonstration

A soil specimen subjected to different mechanical loads and thermal processes was simulated to demonstrate the capability of the model. The height of the model specimen (y direction) is 7 cm, and it is divided into 30 finite elements, whereas the width (x direction) is 5 mm (1 element). The temperature and corresponding strength of the soil upon freezing and thawing were monitored during the simulation.

The geometry and boundary condition of the model are shown in Figure 4.7(a). The finite element mesh with the given uniform initial temperature 3°C is shown in Figure 4.7(b), the steady-state temperature distribution after freezing temperature is applied is shown in Figure 4.7(c). The thermal boundary condition for side walls of the model is adiabatic, so that the heat flow only takes place in the vertical direction. The temperature at the bottom boundary was kept constant at 3°C, whereas the top boundary was subjected to freezing and thawing temperatures. The mechanical boundary condition for the left side wall and bottom are such so that they cannot move in the normal direction. The model was initially under an isotropic compressive stress of 20 kPa. The compression changes when the soil specimen is under different steady-state temperatures so that the constitutive behavior of the soil under diverse thermal-mechanical combination can be demonstrated.

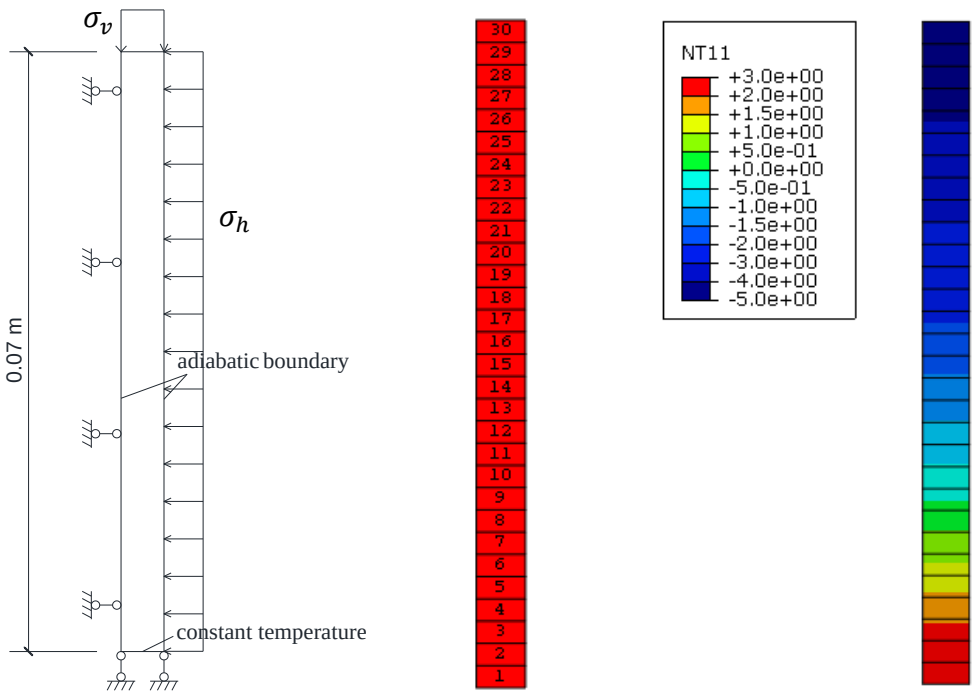

(a) (b) (c)

Figure 4.7 Illustration of finite element specimen: (a) geometry and boundary conditions, (b) mesh and initial temperature 3°C, (c) steady-state temperature distribution

4.5.1 Isotropic Compression

Different combinations of thermal (freeze-thaw cycle) and mechanical load (isotropic loading and unloading, $\sigma_h = \sigma_v$) path were simulated. A freeze-thaw cycle was applied on the top boundary by changing the boundary temperature suddenly from 3°C to -5°C till the whole specimen reaches steady state, then rising it back to 3°C until all the frozen soil thaws. Isotropic compressive loading and unloading were applied on the specimen before freezing, after freezing and after thawing to test the behavior of the constitutive model.

The parameters used in the simulation are listed below: (1) for unfrozen water content, $w^* = 0.08$, $w_0 = 0.325$, $T_0 = 0$ ℃, and $a = 2.0°C^{-1}$; (2) for elastic-plastic model, $\lambda = 0.20$, $\kappa = 0.05$, $p_0 = 80$ kPa, $M = 0.8$, $\alpha_1 = 0.2$, $\alpha_2 = 0$, $\alpha_3 = 0.2$, $p^r = 1.0$ kPa, $\beta = 0.18$, $p_t = -1.0$ MPa; (3) the thermal properties are assumed to be the same for both frozen and unfrozen soil: heat conductivity $\lambda = 1.5$ W/(m· ℃), mass heat capacity c = 2000 J/(kg· ℃). As the heat transfer process is not within the scope of this demonstration simulation, this assumption does not affect the demonstration.

As indicated in Figure 4.7(c), the freezing temperature after reaching steady state at each element are different due to the temperature gradient. The temperature at the center of element #25 is about -4 ℃, whereas at the center of element #10 is about -1 ℃. According to the evolution law presented in the previous section (Equation (4.19)), the soil strength after frozen (represented by the pseudo pre-consolidation pressure) for element #25 is higher than element #10, although they had the same strength (pre-consolidation pressure) before freezing. As a result, the elements may have differnent behavior if they are experiencing loading and unloading after freezing, and after thawing.

The compression curves for three postulated thermal and mechanical proceses are shown from Figure 4.8 to Figure 4.10. In each figure, the results are shown in such order: (a) temperature change scheme at the boundary; (b) mean effective stress change sheme; (c) void ratio vs. mean effective stress (*e* vs. *p'* in log plot) for element #25; (d) void ratio vs. mean effective stress (*e* vs. *p'* in log plot) for element #10.

The "vertical jumps" in the *e* vs. *p'* plot represent the void ratio change in the soil mixture due to freezing and thawing. During freezing, the void ratio increases due to the volume expansion upon phase change of water and ice lens formation, whereas in thawing, the void ratio

has a tendency to decrease. The rate of the changes in void ratio is of course dependent on thermal process for freezing and consolidation process for thawing. These processes, however, will be addressed in the following chapters as they are beyond the scope of this demonstration.

In each case, the void ratio increase during freezing in element #25 is larger than in element #10, because more pore water freezes into pore ice in element #25 (according to the UWCC). Both of the elements underwent the same mechanical loading; however, element #10 experienced yielding under freezing, whereas element #25 behaved elastically.

The implemented model shows its capability giving reasonable results while capturing the characteristics of the mechanical behavior of freezing and thawing in soils under isotropic compression.

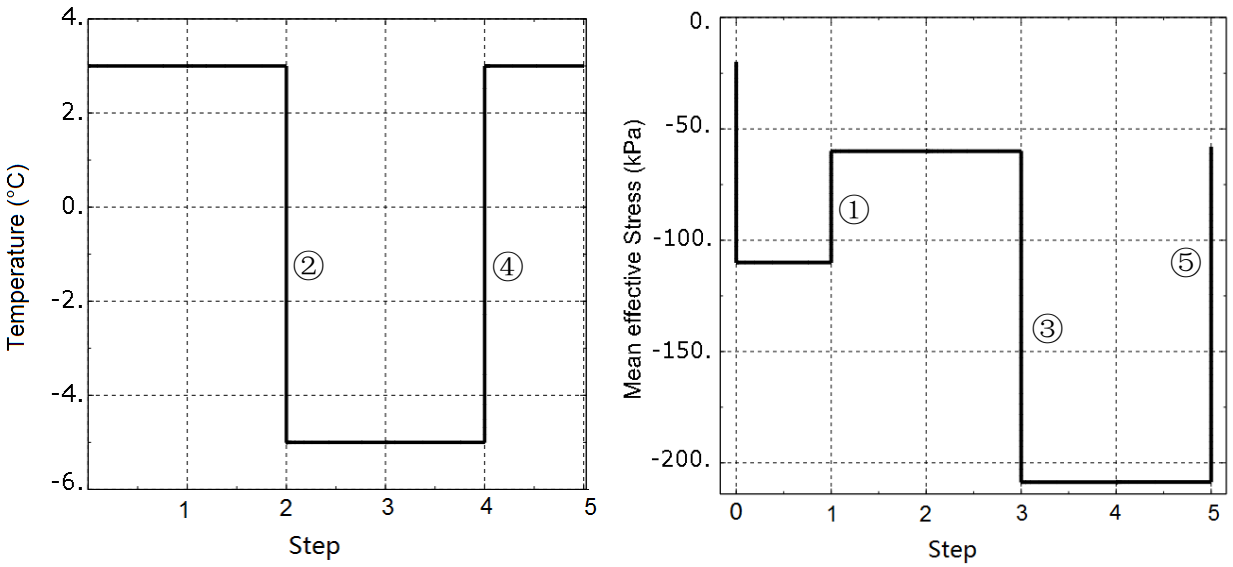

(a) (b)

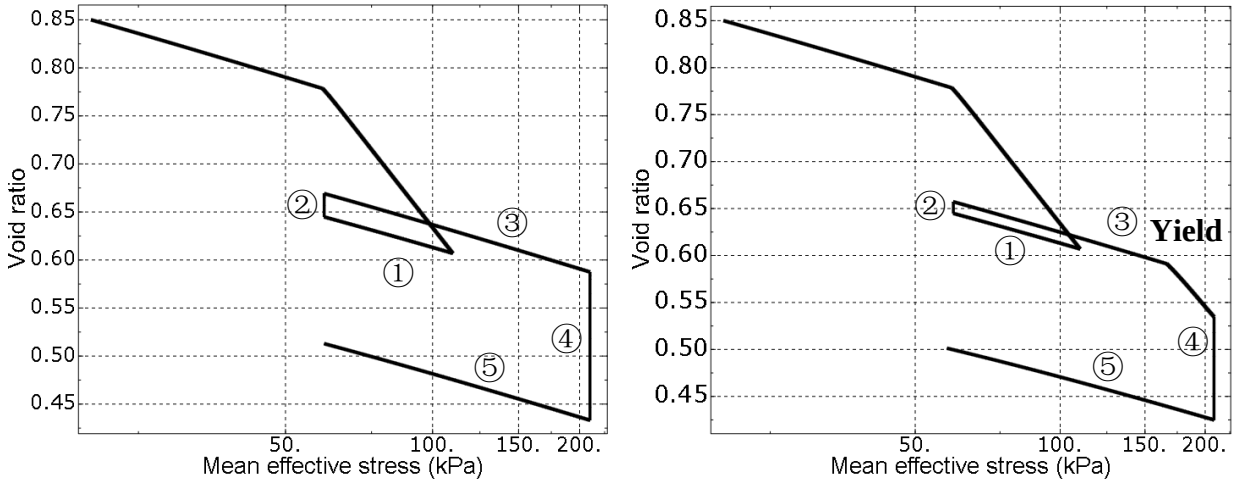

(c) (d)

Figure 4.8 Model demonstration - case 1: (a) top boundary temperature, (b) isotropic compression stress, (c) *e* vs. *p'* curve for element #25, (d) *e* vs. *p'* curve for element #10 (Path: ①unloading-②freezing-③reloading and loading-④thawing-⑤unloading)

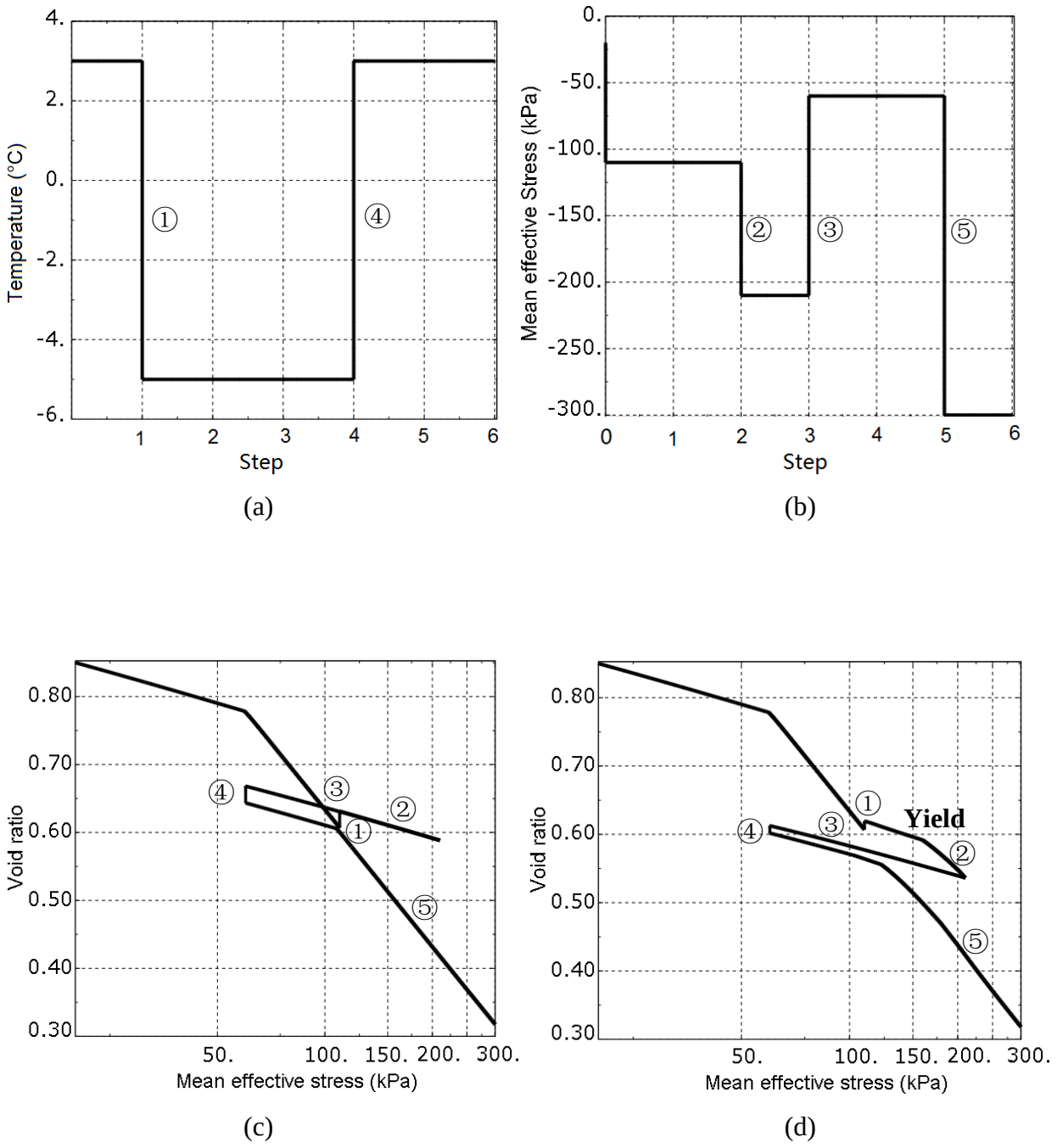

Figure 4.9 Model demonstration case 2: (a) top boundary temperature, (b) isotropic compression stress, (c) *e* vs. *p'* curve for element #25, (d) *e* vs. *p'* curve for element #10 (Path: ①freezing-② further loading-③unloading-④thawing-⑤reloading and loading)

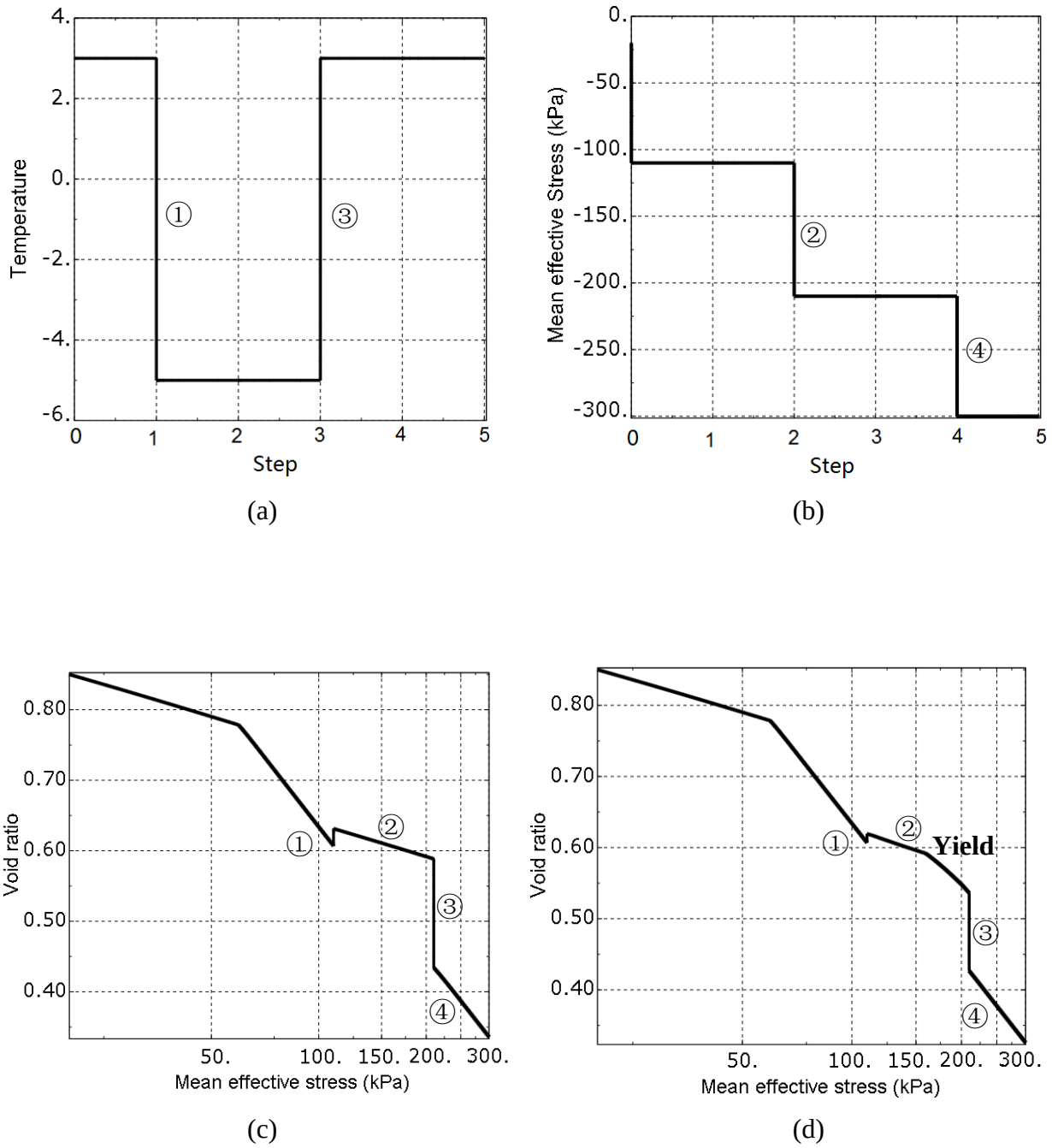

Figure 4.10 Model demonstration case 3: (a) top boundary temperature, (b) isotropic compression stress, (c) *e* vs. *p'* curve for element #25, (d) *e* vs. *p'* curve for element #10 (Path: ①freezing-②further loading-③thawing-④further loading)

4.5.2 Non-Isotropic Compression

The response of the model under both mean stress and deviatoric stress was tested. A compression loading path with deviatoric stress and a freeze-thaw cycle was adopetd. The thermal boundary condition and mechanical loading are shown in Figure 4.11(a) and Figure 4.11(b), respectively.

The model specimen (same as shown in Figure 4.7) was isotropically compressed to 110 kPa in the initial step and unloaded to 80 kPa in step one. Then the horizontal pressure was maintained constant at 80 kPa and the axial (vertical) pressure was increased to 150 kPa in step two. With the stress state unchanged, the temperature was decreased at both top and bottom boundaries to -5°C and the thermal process lasted until the specimen was having a uniform temperature of -5°C in step three. Then the temperature was held constant and the axial pressure was increased to 250 kPa in step four. After that, an increase in temperature was applied at both the top and bottom boundaries to 3°C and the process lasted till the specimen has a uniform temperature in step five. The axial pressure was then descreased to 80 kPa in the final step.

The parameters used in the simulation are: (1) for unfrozen water, $w^* = 0.08$, $w_0 = 0.325$, $T_0 = 0$ ℃, and $a = 2.0°C^{-1}$; (2) for elastic-plastic model, $\lambda = 0.20$, $\kappa = 0.05$, $p_0 = 80$ kPa, $M = 0.8$, $\alpha_1 = 0.2$, $\alpha_2 = 0$, $\alpha_3 = 0.2$, $p^r = 1.0$ kPa, $\beta = 0.18$, $p_t = -1.0$ MPa; (3) the thermal properties are assumed to be the same for both frozen and unfrozen soil: heat conductivity $\lambda = 1.5$ W/(m· ℃), mass heat capacity c = 2000 J/(kg· ℃).

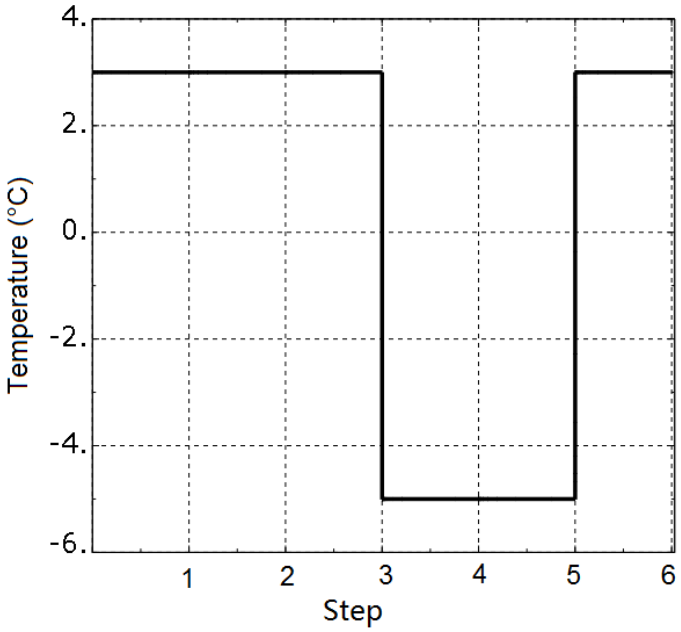

(a)

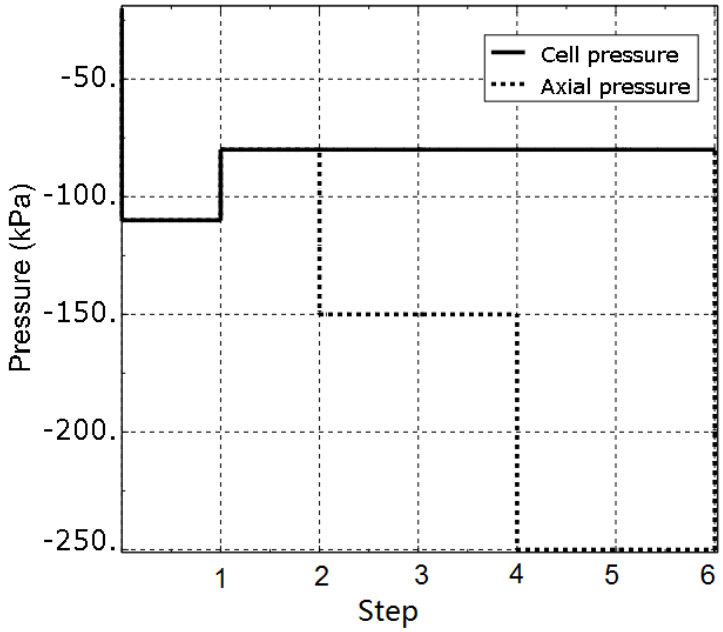

(b)

Figure 4.11 Non-isotropic compression with freeze-thaw cycle: (a) thermal boundary condition, (b) mechanical loading boundary condition

The stress path in *p'*, *q* space and the corresponding yield surface changed during the process are shown in Figure 4.12. The modeled specimen was istropically yielded to 110 kPa (point A) then unloaded to 80 kPa (point B). Then non-isotropic compression occurred and the stress path went along the line with the stress ratio $q/p' = 3$. The loading on the unfrozen soil made the stress state reach the yield surface at point C and moved to point D. The yield surface was pushed outward as well and the corresponding pre-consolidation pressure increased to about 162 kPa. The soil was then frozen and the psuedo pre-consolidaiton pressure increased following the evolution law (Equation (4.19)) proposed in this chapter. The yield surface for the frozen soil expanded and the stress state was left behind in the elastic range. Further loading the specimen makes the stress path go from point D to point F, but is still inside the yield surface for frozen soil. Now, the soil was thawed with the stress state maintained. During thawing, the pre-consoliation pressure would like to decrease following Equation (4.20), leading to the yield surface shrinking to a coresponding position. However, the stress state was kep constant at point F, causing yielding and hardening during thawing, and leading to the yield surface of the thawed soil remain in place (passing through point F). The unloading of axial stress thereafter led the stress path back from point F to point B.

The compression curve in the e, $\ln p'$ space is shown in Figure 4.13. The corresponding points in Figure 4.12 are also shown in Figure 4.13. Note, during freezing process, an increase in void ratio from point D to point E occurred due to phase change; during thawing process, the void ratio drop fom point F to point G was casued by both phase change and thaw weakening.

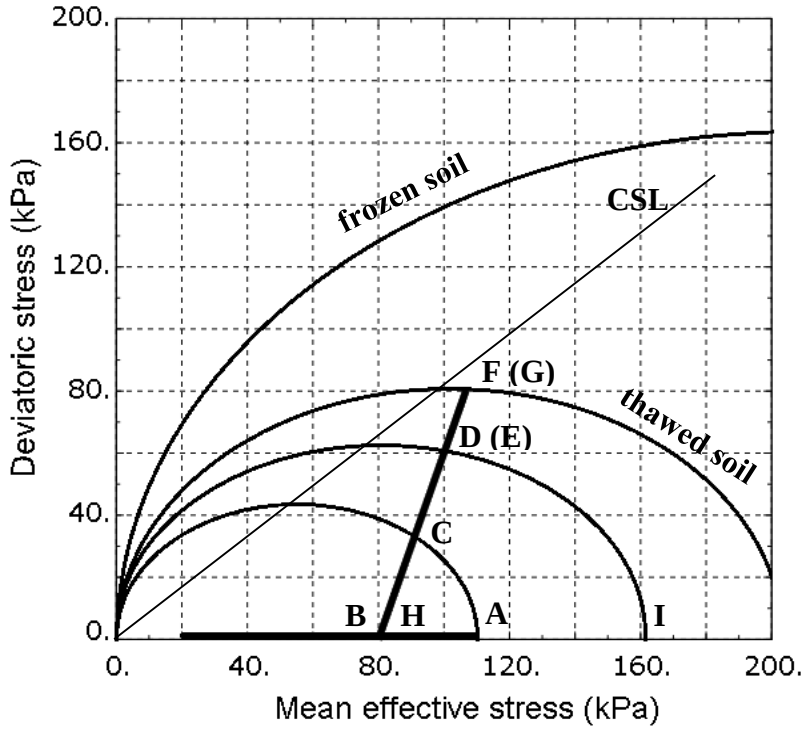

Figure 4.12 Non-isotropic compression: loading path and yield surfaces

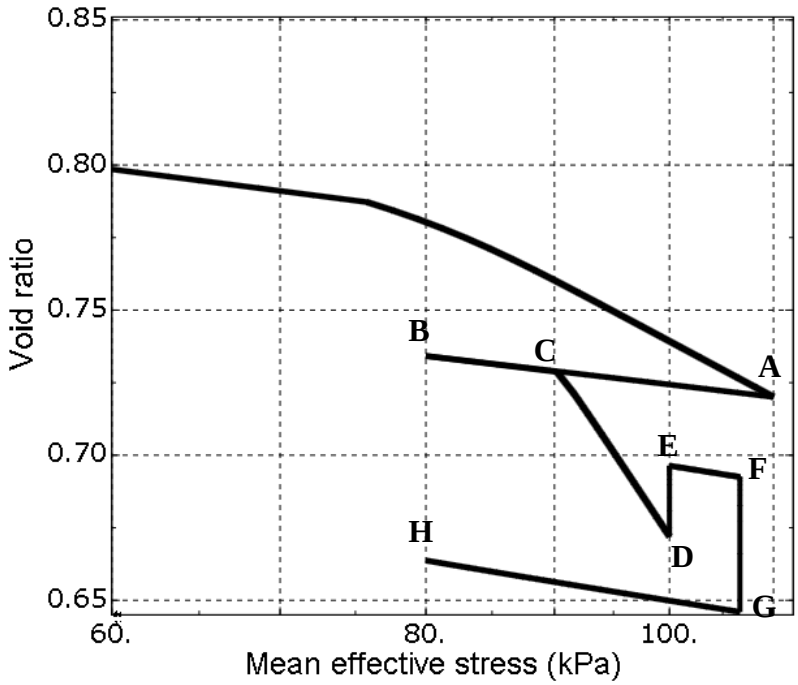

Figure 4.13 Compression curve for non-isotropic compression with freeze-thaw cycle

The normal consolidation line (NCL) and unloading-reloading line (URL) for both unfrozen soil and frozen soil in the non-isotropic compression are shown in Figure 4.14. The dashed lines are for unfrozen (thawed) soil and the dash dot lines are for frozen soil. Point I and point J indicate the pre-consolidation pressure for the unfrozen soil and thawed soil, respectively. Point K indicates the pseudo pre-consolidation pressure for frozen soil.

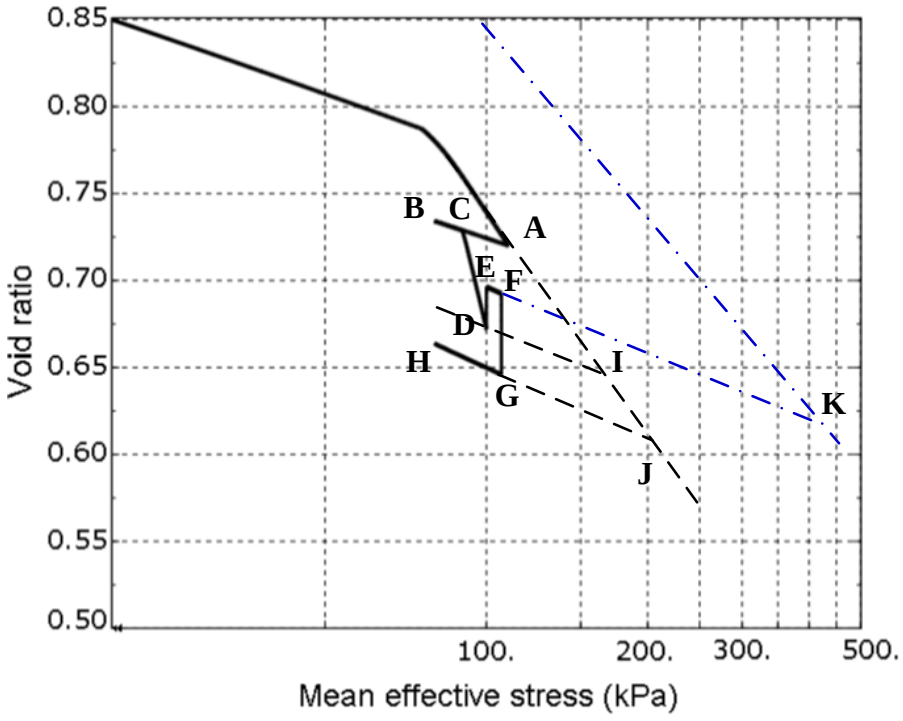

Figure 4.14 NCL and URL in non-isotropic compression process with freeze-thaw cycle

The pre-consolidation pressure (p_0) changes in the process are shown in Figure 4.15. The change of p_0 in step 2, 3 and 5 are due to loading, freezing, and thawing, respectively. The values relelated to points I, K and J can also be identified in Figure 4.14.

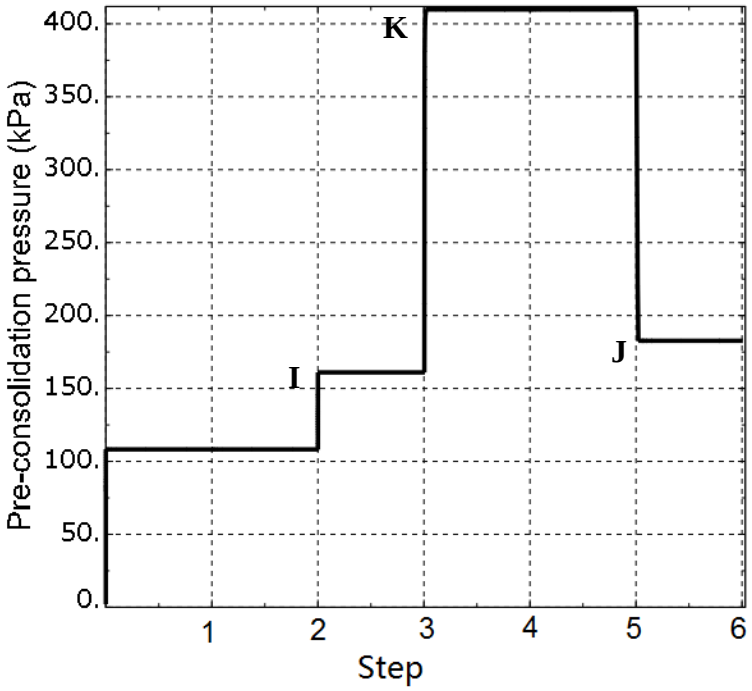

Figure 4.15 Pre-consolidation pressure

This illustration demonstrates that the non-isotropic compression with freeze-thaw cycle can be reasonably described by the implemented model. The model is therefore ready to be used as a tool to solve more complicated boundary value problems in terms of elastic-plastic behavior of soil experiencing freezing and thawing.

4.6 Remarks

An elastic-plastic model has been developed for mechanical behavior in freezing and thawing soils which takes into account the strength and stiffness changes of soils upon freezing and thawing. The model presented is based on hardening plasticity and critical state framework. The model has been implemented into the finite element system to solve boundary value problems. The model behavior demonstration shows that it is capable of capturing the mechanical behavior

in freezing and thawing soils and giving reasonable results of the void ratio changes due to both thermal and mechanical processes. Although no experimental data on such comprehensive thermal and mechanical paths are available for calibration and validation, the model indicates realistic behavior of soil experiencing freezing and thawing, and a capability of solving practical problems.

CHAPTER 5

MULTI-PHYSICAL MODELING OF FROST ACTION

5.1 Introduction

Soil freezing and thawing are multi-physics phenomena, which involve three coupled physical fields: temperature, hydraulic, and the mechanical field, and they are often referred to as thermal-hydro-mechanical (THM) coupled problems. The corresponding issues related to soil freezing and thawing are frost induced heaving, thaw weakening, and settlement. These consequences of freeze-thaw cycles can cause damage to infrastructure in seasonal freezing as well as permafrost areas. Although studies of freezing and thawing soils have been carried out for decades, no models have been developed that can reliably predict changes in strength.

While much research effort has been devoted to the phenomenon of frost heaving, much less attention has been paid to the soil thawing problem and the entire freeze-thaw cycle. Thaw settlement is caused by thermal consolidation under soil self-weight and/or external load, with the rate of it being controlled by the drainage of the melted water. For a frozen frost-susceptible soil, the total amount of thaw settlement depends primarily on the ice-lenses formed during freezing, which distinguishes this process from the conventional consolidation settlement. An elastic-plastic constitutive model has been introduced in the previous chapter, which can be used

to describe the evolution of strength due to the thermally induced changes of quantitative content of the soil mixture components. Now in order to predict the frost action in frost-susceptible soils, the deformation of freezing and thawing soil due to ice lens formation and thaw weakening has to be addressed.

In this chapter, a modified porosity rate function is introduced to describe ice lens formation, thus the frost heave of soil with respect to time in the freezing process can be addressed. Then the function along with the elastic-plastic model will be implemented into the thermal-hydro-mechanical framework in the finite element system ABAQUS. The whole system will be calibrated using test data for the parameters in the porosity rate function and then used as a tool to solve boundary value problems.

5.2 Porosity Rate Function for Frost Heave

The *porosity rate function* (PRF) describes the rate of the average ice growth in a soil volume. This model was found to be very effective in simulations of frost heave. A great advantage of this model is a relatively small number of parameters needed to describe the process of frost heave. The model assumes the soil to be saturated with water (liquid and solid) throughout freezing and thawing.

An early proposal of this function was given in Michalowski (1993), and was modified to be more comprehensive by Michalowski and Zhu (2006) as follows

$$\dot{n} = \dot{n}_m \left(\frac{T - T_0}{T_m} \right)^2 \cdot e^{1 - (\frac{T - T_0}{T_m})^2} \cdot \frac{\left| \frac{\partial T}{\partial l} \right|}{g_T} \cdot e^{- \frac{|\bar{\sigma}'_{kk}|}{\zeta}} \tag{5.1}$$

The core of the PRF is

$$\dot{n} = \dot{n}_m \left(\frac{T - T_0}{T_m} \right)^2 \cdot e^{1 - (\frac{T - T_0}{T_m})^2} \tag{5.2}$$

which was proved to capture well the growth of soil volume due to ice growth. The notations in the function is as follows: $\dot{n}$ is the porosity rate ($\partial n / \partial t$), T is the temperature of the soil mixture (℃), and $\bar{\sigma}'_{kk}$ is the first invariant of the effective stress tensor in the frozen soil (zero if tension). $\dot{n}_m$ is the maximum porosity rate and T_m is the temperature at which $\dot{n}_m$ occurs; T_0 is the freezing temperature of water; g_T is a reference temperature gradient at which $\dot{n}_m$ was determined; ζ is a material parameter defining stress dependency. The quotient $\left| \partial T / \partial l \right| / g_T$ indicates a linear relationship of the porosity rate to the temperature gradient in the heat flow direction. The term $\exp\left(-\left|\bar{\sigma}'_{kk}\right| / \zeta\right)$ is a retardation function to describe the reduction of porosity rate by the stress state (parameter ζ was calibrated for specific clay).

A porosity threshold of 0.75 was introduced, at which heave ceases. This was to indicate that frost heave stops or reduces to an insignificant rate after an intense growth at the stabilized freezing front (Fukuda et al., 1997). An improvement to the model is proposed by substituting this limit with a function of ice and water content. It is believed that the reduction of the rate in ice lensing is related to the increase in the ice content during the heaving process. Therefore, an additional term is imbedded in the porosity rate function

$$\dot{n} = \dot{n}_m \left(\frac{T - T_0}{T_m} \right)^2 \cdot e^{1 - (\frac{T - T_0}{T_m})^2} \cdot \frac{\left| \dfrac{\partial T}{\partial l} \right|}{g_T} \cdot e^{-\frac{|\bar{\sigma}'_{kk}|}{\zeta}} \cdot e^{-\frac{\theta_i}{\theta_w}} \tag{5.3}$$

The term $e^{-\frac{\theta_i}{\theta_w}}$ is to describe the retardation effect on the porosity growth rate as the ice fraction volume θ_i increases (θ_w is the unfrozen water fraction) in the freezing process. This function was selected based on experimental results (Fukuda et al., 1997), and it allowed elimination of the 0.75 ice content threshold used in the previous model for heaving to stop.

5.3 Governing Equations for THM Coupling

Soil freezing and thawing is a multi-physics process in which thermal field, hydraulic field and mechanical behavior are coupled. The soil considered in this model is saturated, and remains saturated during freezing and thawing. The governing equations for each of the thermo-hydro-mechanical (THM) fields are given in the following.

5.3.1 Equilibrium Equations

In this model, the effective stress is the stress averaged over the solid particles and ice, and the total stress σ_{ij} is made up of the effective stress σ'_{ij} and water pressure u

$$\sigma_{ij} = \sigma'_{ij} + u\delta_{ij} \tag{5.4}$$

Substituting this stress into equations of equilibrium

$$\nabla\sigma'_{ij} + F_i = 0 \tag{5.5}$$

one obtains

$$\nabla\sigma'_{ij} + \frac{\partial u}{\partial x_i} + F_i = 0 \tag{5.6}$$

where F_i is the body force.

5.3.2 Conservation of Mass

Volumetric strain ε_v is the result of the void volume change, and in a saturated soil the volumetric strain depends on the changes of the volume of water in the soil mixture; thus ε_v is related to the consolidation process. The mass conservation principle takes the form

$$\frac{\partial \theta_w}{\partial t} + \frac{\rho_i}{\rho_w}\frac{\partial \theta_i}{\partial t} + \nabla q + \frac{\partial \varepsilon_v}{\partial t} = 0 \tag{5.7}$$

where ρ_w and ρ_i are the densities of water and ice, respectively; θ_w and θ_i are the respective volumetric fractions, ε_v is the volumetric strain, and q is the water flux governed by Darcy's law

$$q = -\frac{k}{\rho_w g}\nabla(u + \rho_w g z) \tag{5.8}$$

where k is hydraulic conductivity, g is gravity acceleration and z is elevation.

5.3.3 Conservation of Energy

The energy conservation equation takes the following form

$$C\frac{\partial T}{\partial t} - \nabla(\lambda_m \nabla \mathrm{T}) - L\rho_i \frac{\partial \theta_i}{\partial t} = 0 \tag{5.9}$$

where L is the water latent heat of fusion per unit mass; C is the volumetric heat capacity of soil mixture, and λ_m is the heat conductivity of the soil mixture. To avoid numerical difficulties, the concept of *apparent heat capacity* is introduced and the energy balance equation is rewritten as

$$(C - L\rho_i \frac{\partial \theta_i}{\partial \mathrm{T}}) \frac{\partial T}{\partial t} - \nabla(\lambda_m \nabla \mathrm{T}) = 0 \tag{5.10}$$

where the expression in parenthesis if the apparent heat capacity. The volumetric heat capacity of the soil mixture is

$$C = \rho_w c_w \theta_w + \rho_s c_s \theta_s + \rho_i c_i \theta_i \tag{5.11}$$

and the heat conductivity of the soil mixture is taken as

$$\log \lambda_m = \theta_s \log \lambda_s + \theta_w \log \lambda_w + \theta_i \log \lambda_i \tag{5.12}$$

or

$$\lambda_m = \lambda_s^{\theta_s} \cdot \lambda_w^{\theta_w} \cdot \lambda_i^{\theta_i} \tag{5.13}$$

where c_w, c_i, c_s and $\lambda_w, \lambda_i, \lambda_s$ are mass heat capacity and heat conductivity for water, ice, and soil skeleton, respectively.

5.3.4 Thermal-Hydro-Mechanical Coupling

The coupling effect of thermal, hydraulic and mechanical processes are described in the governing equations through the coupling variables. Such variables include volumetric strain ε_v and excess pore pressure, *u*. A schematic diagram illustrating how the three physical fields are coupled is shown in Figure 5.1.

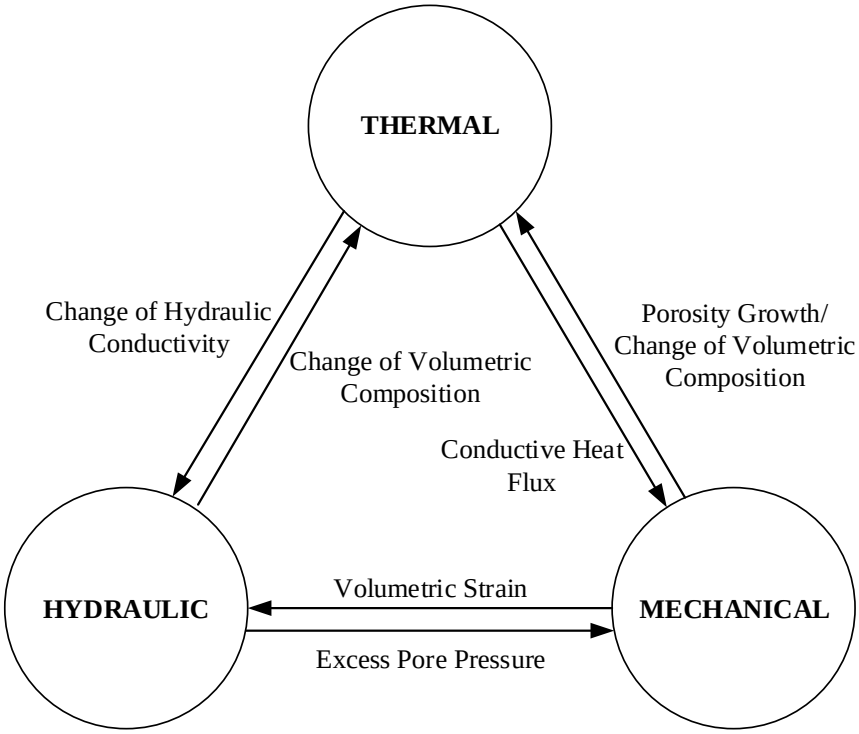

Figure 5.1 Thermal-hydro-mechanical coupling diagram

The heat transfer, the deformation and stress state, and the excess pore pressure in the soil influence one another. Thermal-mechanical coupling (TM): on the one hand, the heat transfer determines the temperature profile of the soil, thus it determines the porosity growth/volumetric expansion in the freezing soil. On the other hand, the porosity growth (ice lens formation) of the soil leads to a change in the fraction of soil components, thus it changes the thermal properties of the soil mixture and affects the following thermal process. The stress field may change too due to constraint as the frost heave occurs, and the change in stress may adversely affect further heaving of the soil through the porosity rate function.

Thermal-hydraulic coupling (TH): the hydraulic conductivity in soil is very sensitive to temperature, especially for freezing and thawing when phase change occurs. In frozen soil, the

hydraulic conductivity may change by orders of magnitude with a slight variation in temperature. Therefore, the hydraulic field is affected by the thermal process, and at the same time it has a reverse influence on the thermal process by changing the thermal properties of the soil mixture as it governs water migration.

Hydraulic-mechanical coupling (HM): the volumetric deformation in soil is related to the void volume change. In a saturated soil, the volumetric strain ε_v determines the potential change in volume of water, the rate of which is controlled by consolidation. If the strain is in compression, the water is being drained out and the generated excess pore water pressure is positive, whereas if the strain is in tension, negative excess pore water pressure is generated and the soil tends to intake water.

5.4 Implementation of the Model in FEM

The thermal behavior of soil and the porosity rate function has been implemented into a commercial finite element software system ABAQUS, using subroutines UMATHT and UEXPAN, which are provided by ABAQUS for users to extend its capability. These implemented models combined with the implemented elastic-plastic stress strain relationship using subroutine UMAT (described in the previous chapter) provide a comprehensive tool to deal with soil behavior upon freezing and thawing. The thermal-hydro-mechanical framework in ABAQUS provides an environment in which the tool can be used to simulate the behavior of freezing and thawing soils in a multi-physical manner.

In ABAQUS, the thermal, hydraulic and mechanical fields are fully coupled with the temperature, displacement (3 components) and excess pore pressure being the degrees of freedom. In each step, ABAQUS solves the conservation of energy (heat transfer) equation in

addition to and in a fully coupled manner with the conservation of mass (continuity equation) and the mechanical equilibrium equations.

The subroutines UMAT, UMATHT and UEXPAN are called in each time increment, at the end of which the state variables are updated at all integration points of the elements. Such state variables include temperature, temperature gradient, stress and components fraction of frozen soil etc., and their values are mutually affected in each time step. For instance, the porosity growth in a current time increment is dependent on the temperature and stresses stored at the end of the previous time increment; at the same time, the growth is reacting to the temperature and stresses through the thermal properties and equilibrium equations.

5.4.1 Implementation of PRF for Porosity Growth

The porosity rate function is implemented into ABAQUS using subroutine UEXPAN, under the assumption that the thermally induced porosity increase (ice lens formation) contributes to the volumetric strain. However, since the $\dot{n}$ is a scalar while the volume growth is anisotropic, a growth tensor $\dot{n}_{ij}$ is introduced to reflect the predominant growth of ice lenses in the direction of heat flow. This growth tensor was described earlier in Michalowski (1993), and it takes the form

$$\dot{n}_{ij} = \dot{n}\alpha_{ij} = \dot{n}\begin{vmatrix} \xi & 0 & 0 \\ 0 & (1-\xi)/2 & 0 \\ 0 & 0 & (1-\xi)/2 \end{vmatrix} \tag{5.14}$$

where α_{ij} is the unit growth tensor; ξ is a dimensionless parameter with values between 0.33 and 1. The growth tensor is specified in the manner that the major principal growth direction coincides with the heat flow direction. When ξ = 0.33, isotropic growth of porosity occurs, whereas ξ = 1 represents one-dimensional growth (only in the heat flow direction), and any

values in between the two indicate certain anisotropic growth. Here, in order to implement the model, the growth tensor is modified so that it could accommodate the finite element system

$$d\varepsilon_{ij}^{g} = d\varepsilon_{v}^{g}\alpha_{ij} \tag{5.15}$$

where $d\varepsilon_{v}^{g}$ is volumetric strain due to ice lens growth. The phase diagram indicating the growth of ice lenses and change of components in pores (water and ice) are shown in Figure 5.2. The incremental change in the porosity can be calculated during each time step by the porosity rate function by

$$dn = \dot{n}dt \tag{5.16}$$

By the phase diagram, the porosity at time *t* and $t + \Delta t$ can be expressed by

$$n_t = \frac{V_v}{V}, \quad n_{t+dt} = \frac{V_v + dV}{V + dV} \tag{5.17}$$

Knowing that the volumetric strain (due to ice lens growth) is

$$d\varepsilon_{v}^{g} = \frac{dV}{V} \tag{5.18}$$

The porosity at time $t + \Delta t$ can then be described by

$$n_{t+dt} = \frac{V_v / V + dV / V}{1 + dV / V} = \frac{n_t + d\varepsilon_{v}^{g}}{1 + d\varepsilon_{v}^{g}} \tag{5.19}$$

Therefore, the volumetric strain can be expressed in the change of porosity by

$$d\varepsilon_v^g = \frac{n_{t+dt} - n_t}{1 - n_{t+dt}} \approx \frac{dn}{1-n} \tag{5.20}$$

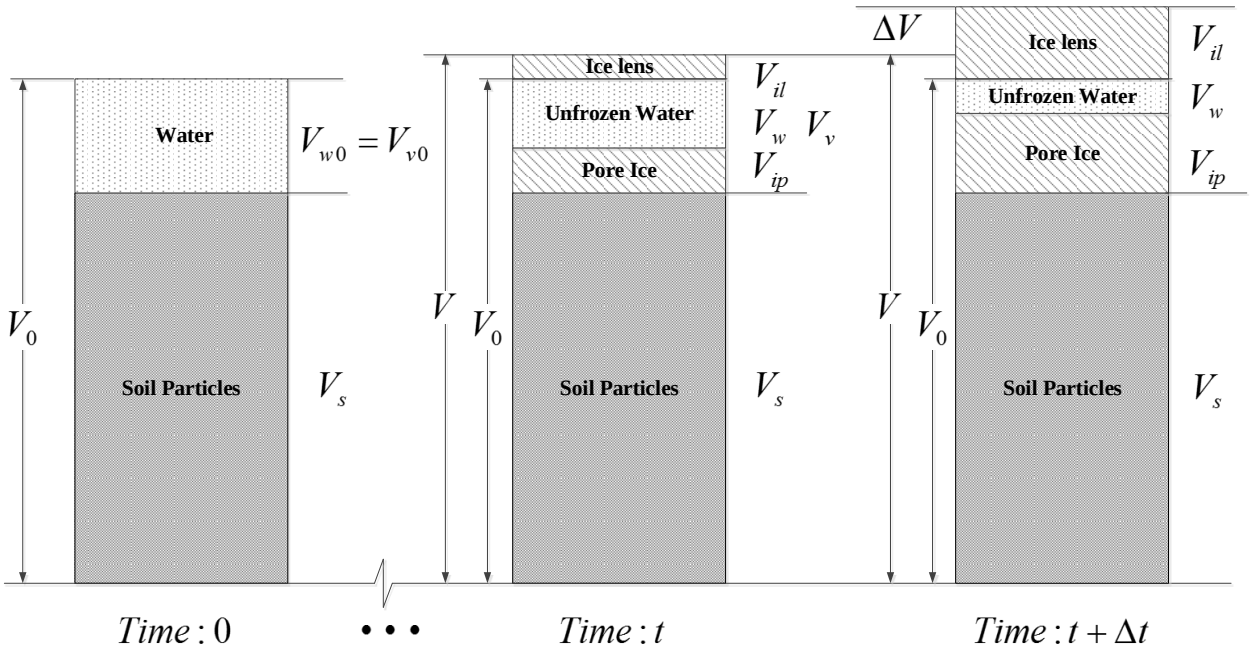

Figure 5.2 Growth of ice lens and volume increment

The total strain could be either induced by loading or by a thermal process. Thus, the increment is composed of the elastic-plastic mechanical increment $d\varepsilon_{ij}^{ep}$ and the thermal porosity growth increment $d\varepsilon_{ij}^{g}$

$$d\varepsilon_{ij} = d\varepsilon_{ij}^{ep} + d\varepsilon_{ij}^{g} \tag{5.21}$$

Since an elastic-plastic relationship is developed and used in this model (described in the previous paragraph), $d\varepsilon_{ij}^{ep}$ is defined and calculated by the constitutive law. The strain increment

caused by porosity growth can be written in the following form by introducing a local coordinate system x_i (i = 1, 2, 3), where x_1 represents the direction of the heat flow (modified from Zhu 2006).

$$\begin{Bmatrix} d\varepsilon_{11}^g \\ d\varepsilon_{22}^g \\ d\varepsilon_{33}^g \end{Bmatrix} = \begin{Bmatrix} \xi \\ \frac{1}{2}(1-\xi) \\ \frac{1}{2}(1-\xi) \end{Bmatrix} d\varepsilon_v^g \approx \begin{Bmatrix} \xi \\ \frac{1}{2}(1-\xi) \\ \frac{1}{2}(1-\xi) \end{Bmatrix} \frac{dn}{1-n} \tag{5.22}$$

Since in the finite element system, an arbitrary coordinate system x, y, z will be used in the computation in which the heat flow direction may not coincide with any of the axes, a growth transformation between the two coordinate system must be performed. In geotechnical engineering, the direction downward into the soil (parallel to the gravity) usually is conventionally chosen as the z direction, whereas x, y are chosen to form the plane that is parallel to the horizontal ground surface. Meanwhile, to reduce the computational cost, most geotechnical problems can be treated as plane problems (plane strain or plane stress), the temperature profile in such cases would be the same in the in-plane direction. The y axis is assumed to be the in-plane direction, and the transformation rule takes the form

$$\begin{Bmatrix} d\varepsilon_x^g \\ d\varepsilon_z^g \\ d\gamma_{xz}^g \end{Bmatrix} = \begin{bmatrix} m^2 & n^2 & -mn \\ n^2 & m^2 & mn \\ 2mn & -2mn & m^2-n^2 \end{bmatrix} \begin{Bmatrix} d\varepsilon_{11}^g \\ d\varepsilon_{33}^g \\ d\gamma_{13}^g \end{Bmatrix} = \begin{Bmatrix} m^2\xi + n^2\frac{1}{2}(1-\xi) \\ n^2\xi + m^2\frac{1}{2}(1-\xi) \\ mn(3\xi-1) \end{Bmatrix} \frac{\dot{n}dt}{1-n} \tag{5.23}$$

where $m = \cos\theta$ and $n = \sin\theta$. θ is the angle made by axis x and heat flow direction and is determined according to the following equation

$$\tan\theta = \left(\frac{\partial T}{\partial z}\right) / \left(\frac{\partial T}{\partial x}\right) = q_z / q_x \tag{5.24}$$

where T is the temperature, q_x and q_z are the heat flux in x and z direction, respectively (modified from Zhu 2006). The coordinate system and the transformation relationship is shown in Figure 5.3. This simplification would fit most of the cases in geotechnical engineering, plus it would tremendously reduce the error in the back calculation (of inverse trigonometric functions dealing with heat flux) in obtaining the heat flow direction.

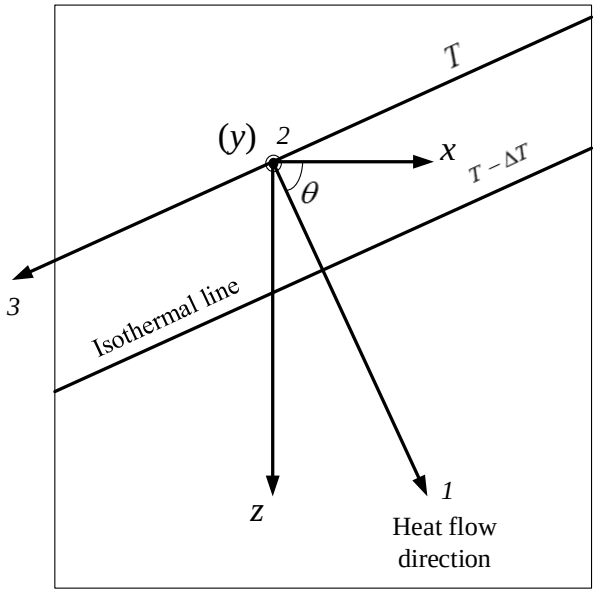

Figure 5.3 Coordinate system (after Zhu 2006)

The volumetric fractions of the three components in soil mixtures can also be calculated after updating the porosity at the end of each time step using the following relationships

$$(\theta_s)_{t+dt} = 1 - n_{t+dt} \tag{5.25a}$$

$$(\theta_w)_{t+dt} = \frac{\rho_s}{\rho_w} w_{t+dt}(1 - n_{t+dt}) \tag{5.25b}$$

$$(\theta_i)_{t+dt} = n_{t+dt} - \frac{\rho_s}{\rho_w} w_{t+dt}(1-n_{t+dt}) \tag{5.25c}$$

5.4.2 Implementation of the Thermal Model with Phase Change

The thermal properties for the soil mixture, the volumetric heat capacity and the effective heat conductivity (as in Equations (5.11 and 5.13)) are implemented in ABAQUS using subroutine UMATHT.

The latent heat in the apparent heat capacity in the conservation of energy equation (Equation (5.10)) needs to be addressed here in detail since the calculation differs for the pore ice and for the ice in the ice lenses. The apparent heat capacity can be rewritten as:

$$C_a = C - L\rho_i \frac{\partial \theta_i}{\partial \mathrm{T}} = C - L\rho_i \frac{\partial(\theta_{ip} + \theta_{il})}{\partial \mathrm{T}} = C - L\rho_i \frac{\partial \theta_{ip}}{\partial \mathrm{T}} - L\rho_i \frac{\partial \theta_{il}}{\partial \mathrm{T}} \tag{5.26}$$

where C_a is the apparent heat capacity, θ_{ip} and θ_{il} are volumetric fraction of pore ice and ice lenses, respectively.

For the latent heat released during *in-situ* freezing and absorbed during thawing, UWCC can be used to track the volumetric fraction variation. Therefore, the second term in Equation (5.26) can be manipulated to yield

$$-L\rho_i \frac{\partial \theta_{ip}}{\partial \mathrm{T}} = L\rho_w \frac{\partial \theta_{wp}}{\partial \mathrm{T}} = L\rho_s(1-n)\frac{\partial w}{\partial \mathrm{T}} \tag{5.27}$$

where θ_{wp} is the volumetric fraction of water in pore, n is the initial porosity of the soil and $\partial w / \partial T$ is the slope of the UWCC (Zhu 2006). Consequently, Equation (5.26) can be rewritten as

$$C_a = C + L\rho_s(1-n)\frac{\partial w}{\partial T} - L\rho_i\frac{\partial \theta_{il}}{\partial T} \tag{5.28}$$

When the latent heat is associated with the formation and melting of ice lenses, different procedures are adopted, because the change in fraction constituents differs for freezing and thawing. In the freezing process, the ice lens formation occurs at a temperature that is below freezing, and its rate follows the porosity rate function described in Equation (5.3). The differentiation of ice lens fraction with respect to temperature (the third term in Equation (5.28)) can be calculated as

$$\frac{\partial \theta_{il}}{\partial T} \approx \frac{\Delta \theta_{il}}{\Delta T} = \frac{(\theta_i - \theta_{ip})_{t+\Delta t} - (\theta_i - \theta_{ip})_t}{\Delta T} \tag{5.29}$$

where θ_i is the total volumetric ice content which can be calculated from Equation (5.25c), and θ_{ip} is fraction of pore ice, which can be related to the pore ice ratio defined in Equation (4.1) by

$$\theta_{ip} = (1-n)e_{ip} \tag{5.30}$$

When it comes to the thawing of soil with ice lenses, the ice lenses will not start melting until the temperature reaches 0°C. Therefore, the precise expression of the change of ice lenses upon thawing should involve the Heaviside function

$$\theta_{il} = \begin{cases} \theta_{ilf}, & T < 0 \\ 0, & T \geq 0 \end{cases} \tag{5.31}$$

where θ_{ilf} is the maximum volumetric fraction of ice lenses that have been accumulated during freezing. However, a difficulty is encountered when trying to obtain the derivative of the

discontinued function. Therefore, an analytic approximation is adopted here to overcome this difficulty. The function is approximated as

$$\theta_{il} = \theta_{ilf} \frac{1}{1+e^{kT}} \tag{5.32}$$

where k is a constant. The derivative of the function with respect to temperature gives

$$\frac{\partial \theta_{il}}{\partial T} = \theta_{ilf} \frac{-k}{(1+e^{kT})^2} e^{kT} \tag{5.33}$$

The plot of the approximated Heaviside function in Equation (5.32) is shown in Figure 5.4 and its derivative to temperature in Equations (5.33) is shown in Figure 5.5, with an arbitrary value of $\theta_{ilf} = 0.6$.

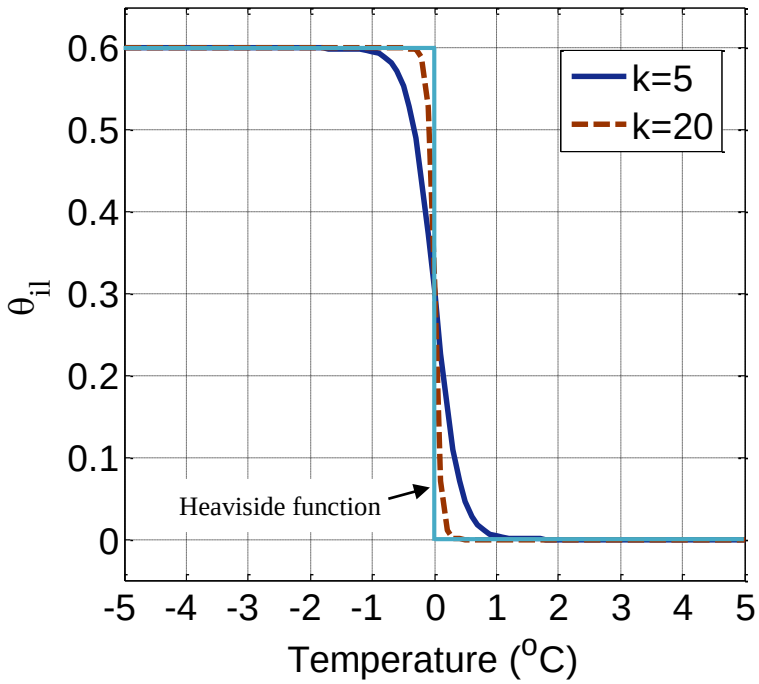

Figure 5.4 Heaviside and approximation functions

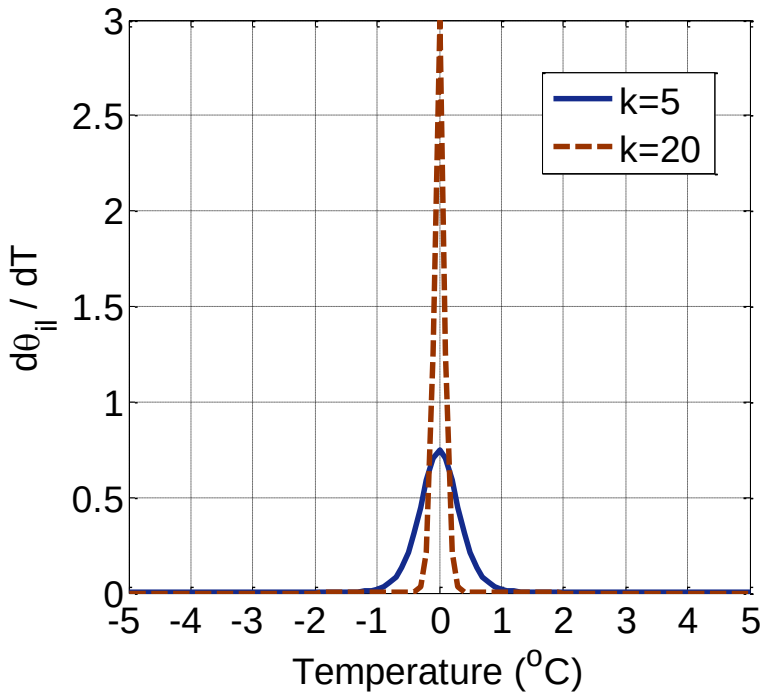

Figure 5.5 Derivative of Heaviside approximation function

It is clear from these plots that the use of the approximation function results in some error compared to the Heaviside function, but the error can be minimized by adopting a higher value of constant *k*. In the following simulation, a value of $k = 10$ is used.

5.5 Calibration

To calibrate the parameters in porosity rate function, the entire THM system was used to simulate a set of soil freezing tests performed by Fukuda et al. (1997). The hydraulic conductivity during freezing was taken as $1.0 \cdot 10^{-7}$ m/s for unfrozen soil and $1.0 \cdot 10^{-12}$ m/s for frozen soil with temperature below -5 ℃; linear interpolation was used for temperatures between 0 ℃ and -5 ℃. A thawing process was also simulated. This was a postulated process, because the Fukuda's test results do not include thawing. The rate of temperature increase in thawing was the

same as the rate of decrease during freezing. To make sure that all parts of the frozen soil are completely thawed, the thawing simulation was carried out until the cold side boundary temperature increased to 1.05 ℃ at t = 119 hours.

The specimens subjected to freezing in Fukuda's tests were cylindrical frost-susceptible clay of 100 mm in diameter and initial height of 70 mm. The initial temperature and the boundary conditions for the tests performed under constant load are listed in Table 5.1 and shown in Figure 5.6. The blue solid line at the bottom represents the temperature change on the cold side (bottom) boundary, whereas the remaining lines indicate the temperature change on the warm side (top) boundary of the specimen for different tests. The initial temperature on the cold side for each specimen was the same; however, the warm side was given different initial temperature to form diverse thermal gradients in specimens. The rate of the temperature change on both sides was kept the same to maintain a constant thermal gradient through the process. An overburden pressure of 25 kPa was applied on top of the specimens. Overburden pressures of 150 kPa, 300 kPa, 400 kPa and 600 kPa were also applied for tests with the thermal gradient of 0.045 (marked purple in Figure 5.6). The porosity rate function was calibrated using the frost heave test data with different overburden pressures and diverse thermal gradients.

Table 5.1. Boundary/initial conditions for freezing tests by Fukuda et al. (1997)

Thermal gradient (dT/dl)	Warm plate (top) (℃)	Cold plate (bottom) (℃)	Overburden pressure (kPa)
0.095	7-0.042t*	-0.042t	25
0.070	5-0.042t	-0.042t	25
0.061	4-0.042t	-0.042t	25
0.045	3-0.042t	-0.042t	25
			150
			300
			400
			600
0.035	2-0.042t	-0.042t	25

*t=time (*in hours*), *total testing time 47hrs.*

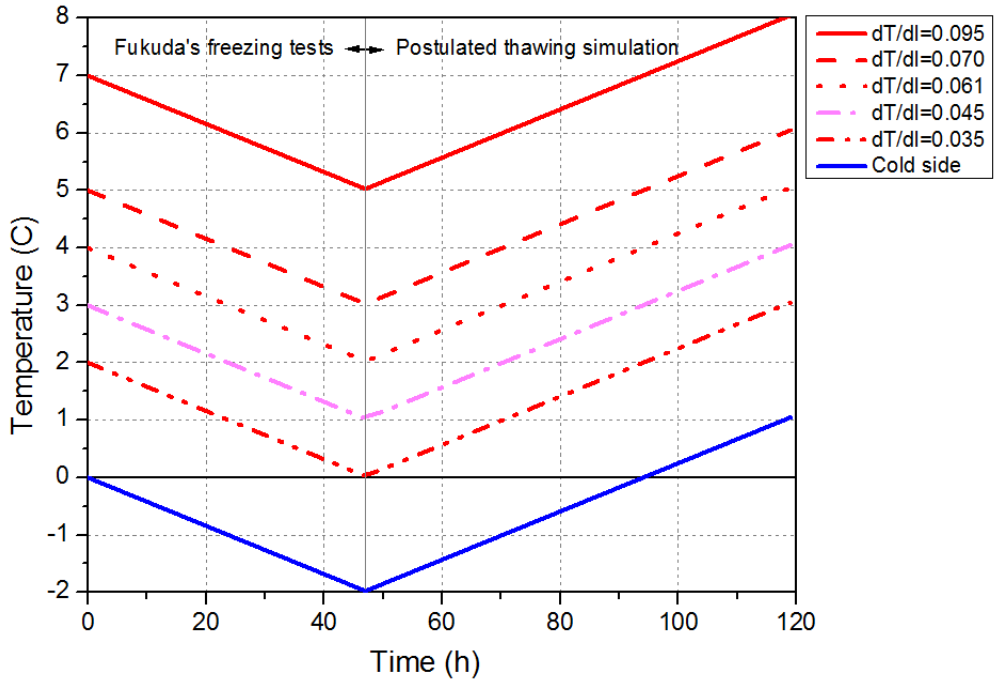

Figure 5.6 Thermal boundary condition for model calibration (freezing process is taken from Fukuda et al., 1997, the thawing part is postulated)

The soil is saturated, with an initial porosity of 0.427, and specific gravity of 2.62. The density of the soil mixture was taken as 1,927 kg/m^3. Typical values of thermal properties for soil particles, water and ice were taken from Williams and Smith (1989) and Selvadurai et al. (1999), and they are listed in Table 5.2.

Table 5.2. Material properties of soil components
(after Williams and Smith, 1989)

	Density	Mass heat capacity	Volumetric heat capacity	Latent heat	Thermal Conductivity
	ρ	c	C	L	λ
	(kg/m^3)	(J/(kg· ℃))	(J/(m^3· ℃))	(J/kg)	(W/m· ℃)
Soil particles (clay mineral)	2620	900	$2.36 \cdot 10^6$	--	1.95
Water	1000	4180	$4.18 \cdot 10^6$	333000	0.56
Ice	917	2000	$1.93 \cdot 10^6$	333000	2.24

These values are also used later in the numerical examples of boundary value problems. By fitting a curve to the test data, the frost heave parameters in the porosity rate function for the particular clay used by Fukuda et al. (1997) were found to be: T_m = -0.82 ℃, $\dot{n}_m$ = $1.98 \cdot 10^{-5}$ s^{-1}, g_T = 100 ℃/*m*, and ζ = 0.73 MPa. The curves for frost heave with respect to time match the test data very well, as shown in Figure 5.7 and Figure 5.8. The curves for the postulated thawing process are also plotted in the same figures.

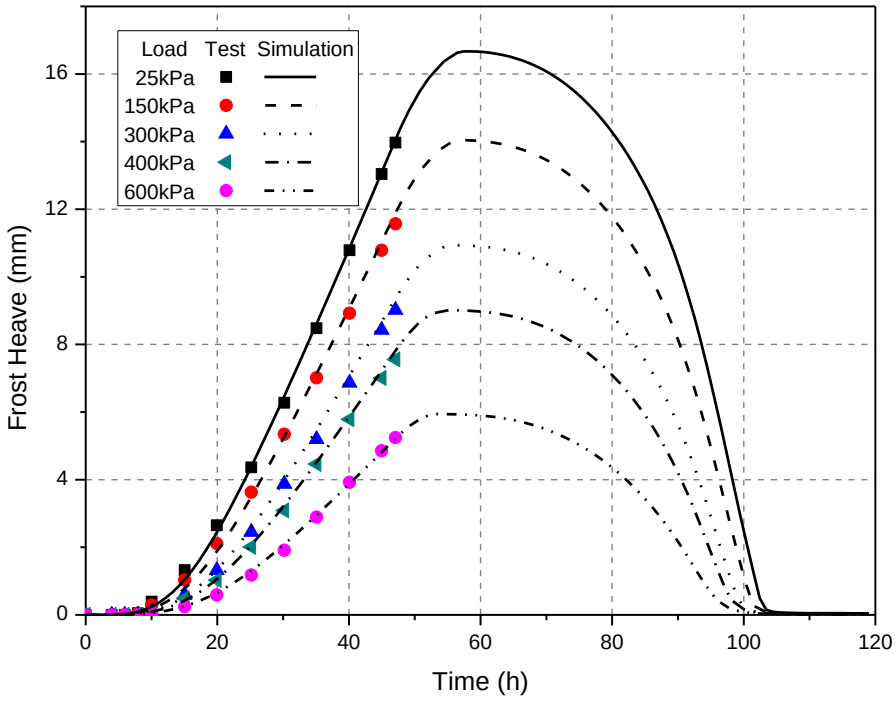

Figure 5.7 Calibration curve of PRF for different overburden pressure

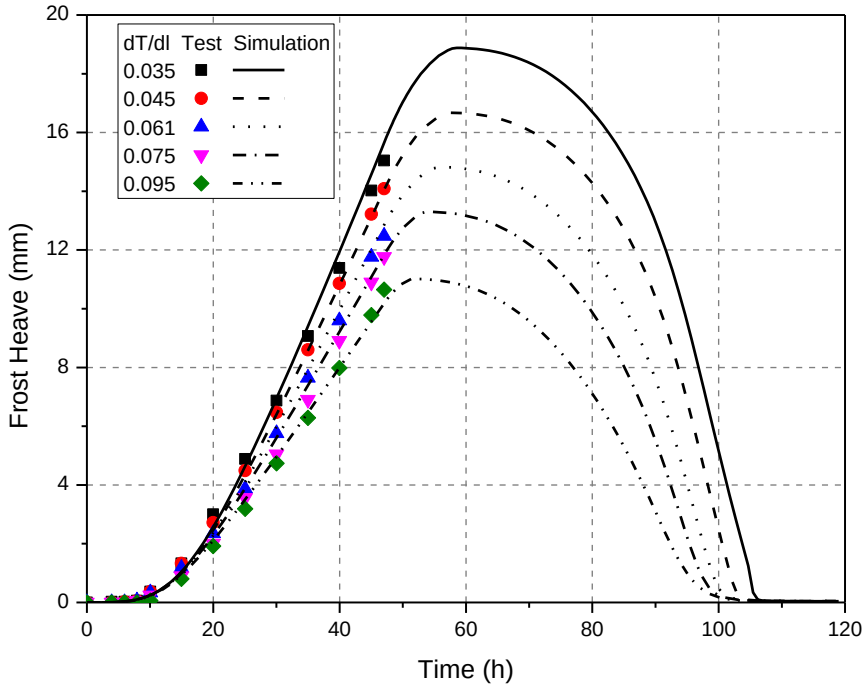

Figure 5.8 Calibration curve of PRF for different temperature gradient

An interesting phenomenon observed in the simulation is that even though the boundary temperature starts increasing after 47 hours, the soil turns out to heave more before settlement occurs. The temperature distribution at different times for samples with thermal gradient of 0.035 is plotted in Figure 5.9. The freezing front propagation can be incurred from the figure.

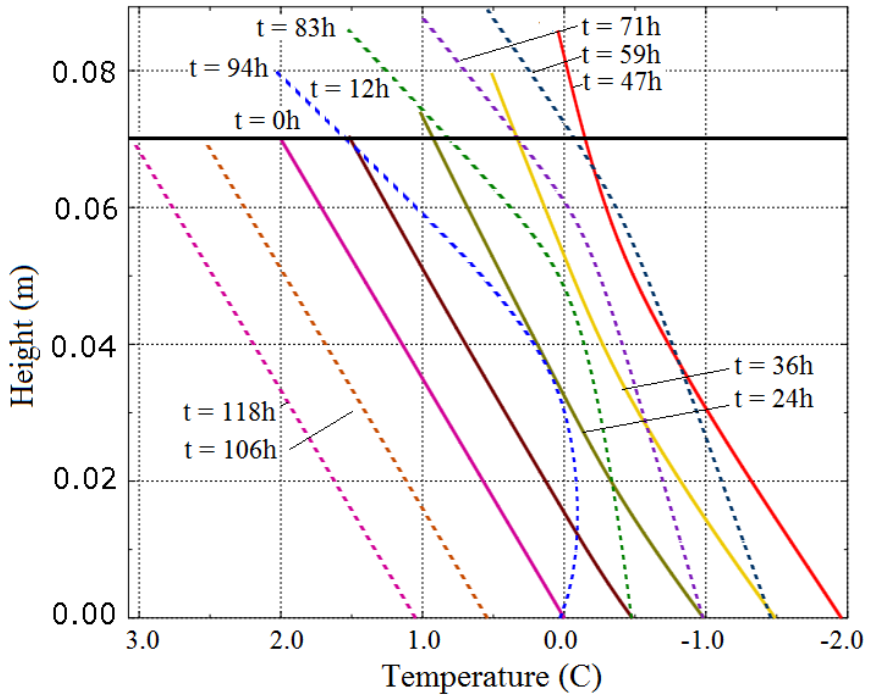

Figure 5.9 Temperature distribution for the sample with initial *dT/dl* = 0.035; solid lines represent temperature during freezing, dashed lines during thawing

The solid lines indicate the temperature profile during freezing, whereas the dashed lines are during thawing. The freezing front propagates fast upwards after freezing starts and only a small portion in the upper part of the column remains unfrozen after 47 hours. From t = 47 h to t = 59 h, even though the boundary temperatures are increasing and the thawing front is moving downward (from 0.082m to 0.072m), the temperature between depth 0.039m and 0.067m still

decreases. This is due to the latent heat which delays the temperature change. Because most of the specimen is still frozen, and the total growth in volume is larger than the reduction in volume in the upper portion of the specimen subjected to thawing zone, the heaving continues to occur for a few more hours.

A change in the temperature gradient occurs in the thermal process. During freezing, the temperature distribution lines curve at a temperature between T_0 = 0 ℃ and T_m = -0.82 ℃ (T_m is the parameter in PRF indicating the temperature at which the maximum porosity rate occurs). This is because of the change in heat conductivity and the release of latent heat (due to both *in-situ* freezing and ice lens formation). In the thawing process, the temperature distribution lines curve in an opposite direction around $T = T_0$. This is because the ice lenses do not start melting until temperature reaches T_0; this is when large amounts of latent heat start being absorbed.

The cryogenic suction that was needed to transfer the water into the frozen fringe to provide for the porosity growth (ice lens formation) can be back-calculated from the THM system using Equation (5.7). Then, during thawing, the excess pore water pressure generated due to thaw consolidation process can be obtained as well. The excess pore water pressure in a freeze-thaw cycle for dT/dl = 0.035 is illustrated in Figure 5.10.

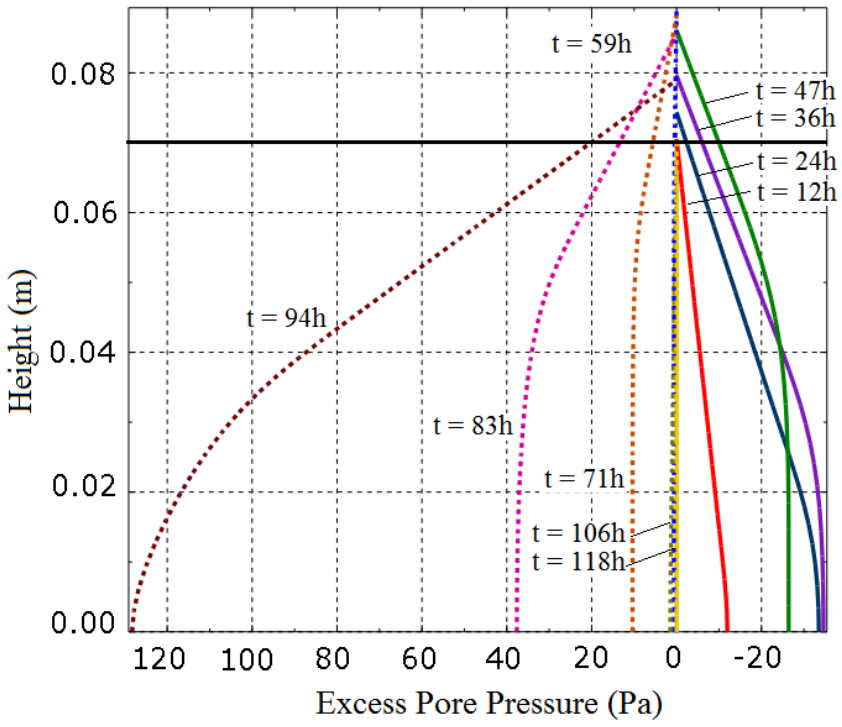

Figure 5.10 Excess pore water pressure distribution for ramp freezing (*dT/dl* = 0.035)

To illustrate the role that the term $e^{-\frac{\theta_i}{\theta_w}}$ plays in the porosity rate function, the distribution of volumetric content of ice, water, and the value of the retardation function in the simulated test (with the thermal gradient of 0.035) are plotted in Figure 5.11 through Figure 5.13. As the ice fraction increases, the term $e^{-\frac{\theta_i}{\theta_w}}$ decreases. This is the effect that allowed elimination of the shut-off porosity threshold from an earlier model.

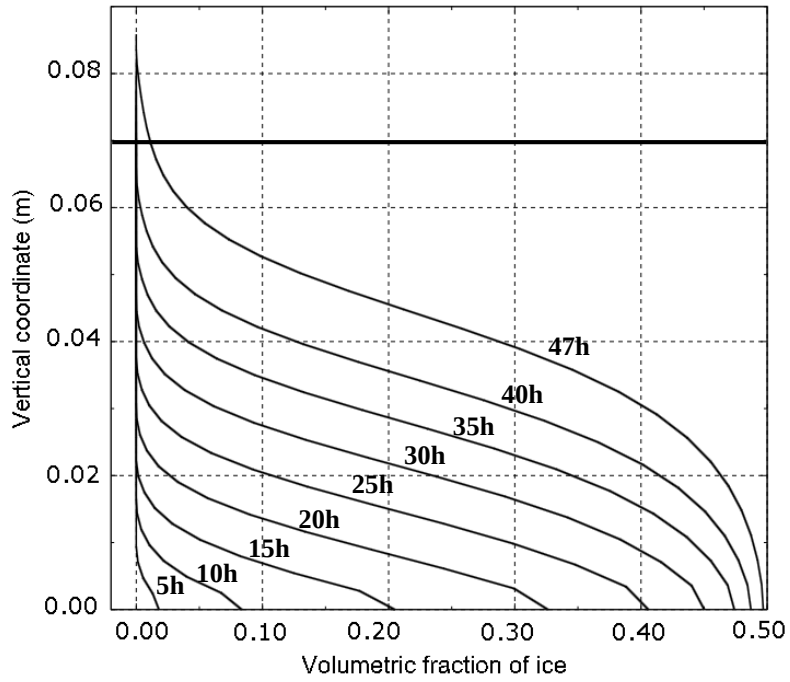

(a) Freezing

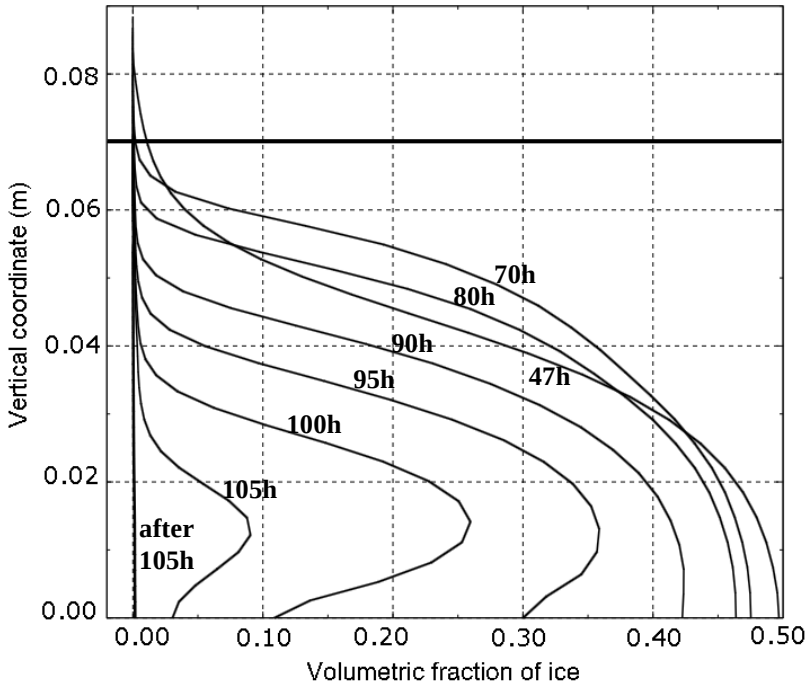

(b) Thawing

Figure 5.11 Distribution of total ice fraction (*dT/dl* = 0.035): (a) Freezing, (b) Thawing

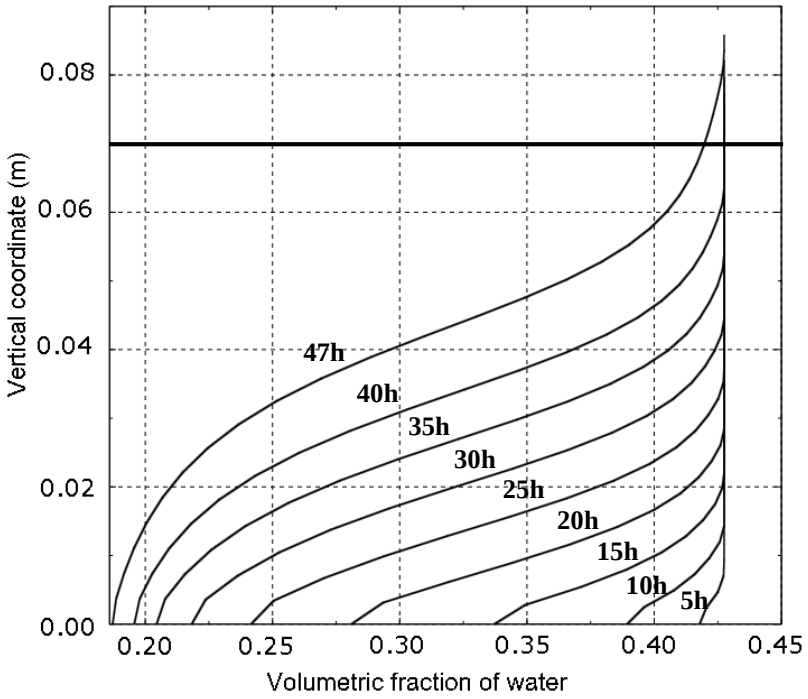

(a) Freezing

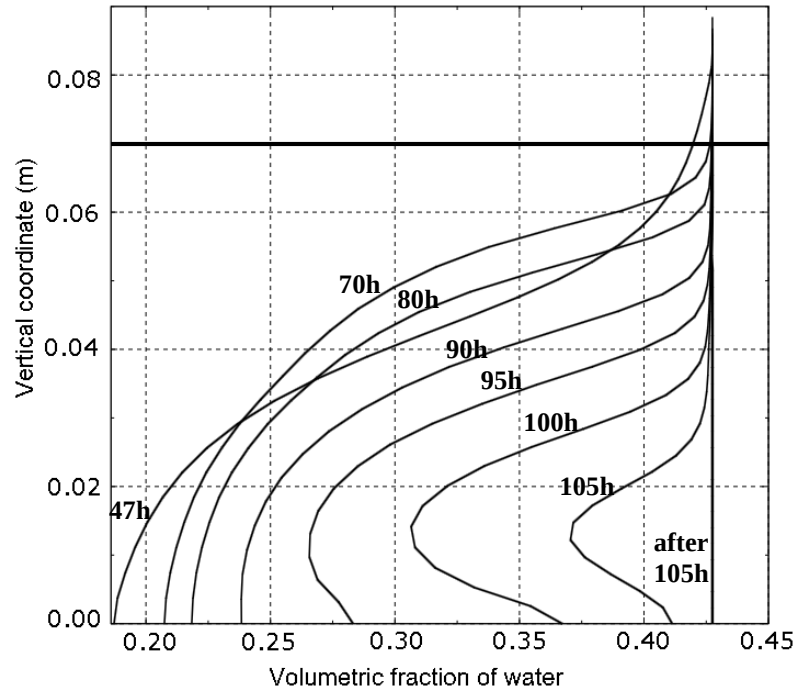

(b) Thawing

Figure 5.12 Distribution of unfrozen water fraction (*dT/dl* = 0.035): (a) Freezing, (b) Thawing

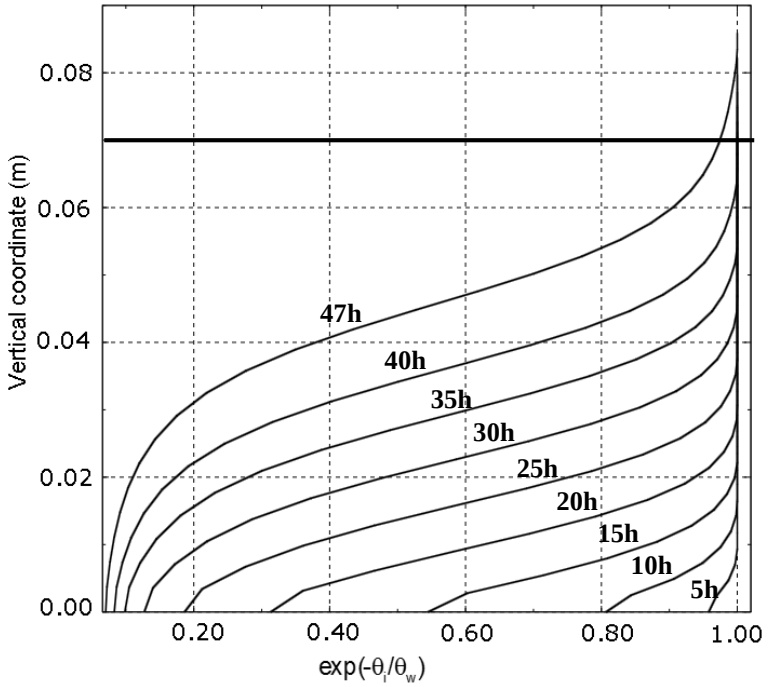

(a) Freezing

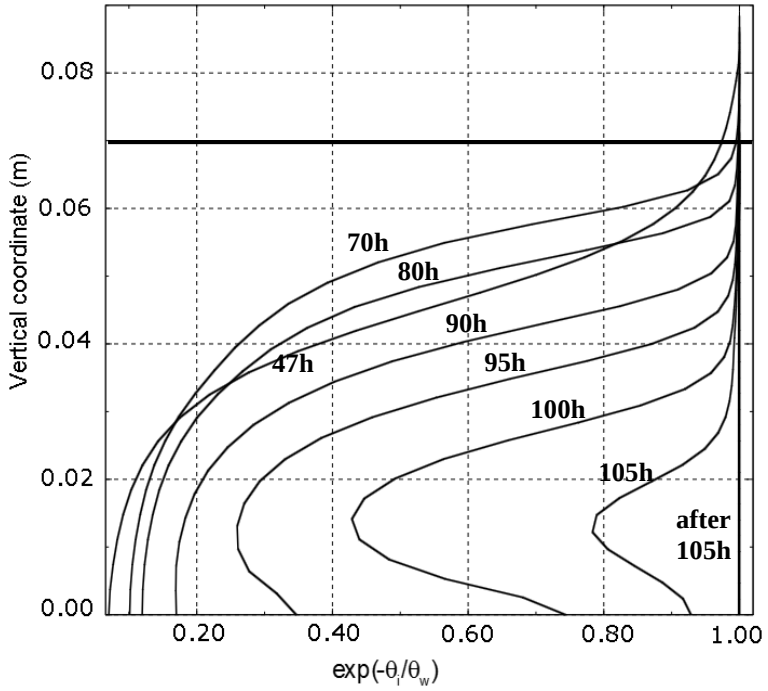

(b) Thawing

Figure 5.13 Distribution of the value for term exp(-θ_i/θ_w) (dT/dl = 0.035): (a) Freezing, (b) Thawing

To investigate the influence of thawing rate on the displacement of the frozen soil, two other temperature boundary conditions were postulated for comparison (shown in Figure 5.14). The solid line represents the boundary temperature rate equal in magnitude but opposite in sign to the freezing rate in Fukuda's test (the same as is shown in Figure 5.6), whereas the dashed line and the dotted line represent a double rate and half the rate, respectively. To assure that the frozen soil completely thawed, the simulations were continued until the cold side temperature reached 1.05 ℃.

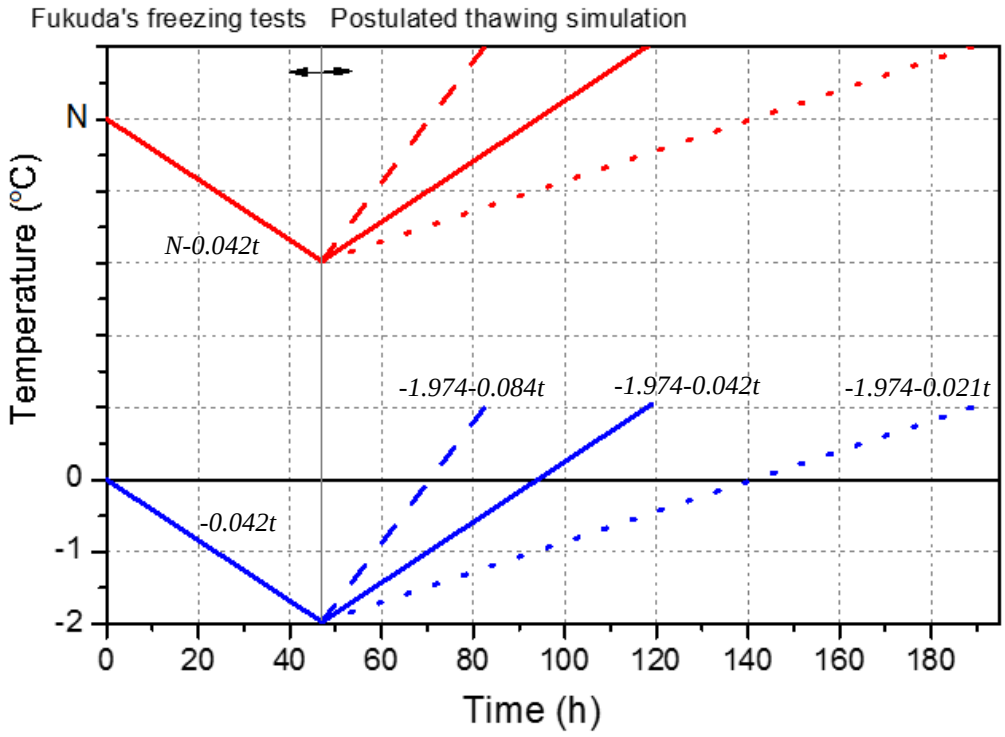

*N = 2, 3, 4, 5 and 7 are the initial warm side temperature in Fukuda's tests.

Figure 5.14 Thermal boundary condition for the thawing process

Other boundary conditions and the parameters used are the same as in the previous simulation. The comparison of the displacement curves are shown in Figure 5.15 and Figure 5.16. Again, during the freeze-thaw process the temperature starts increasing after t = 47 h, but the frost heave does not stop at the same time. Rather, the heave increases further before the thaw settlement takes place. The figures indicate that as the thawing rate increases, further heave decreases. Meanwhile, since the freezing processes are the same for the three cases in which the cryogenic suction was not large enough to yield the frozen soil, the frost heave went back to zero and no further settlement occurred.

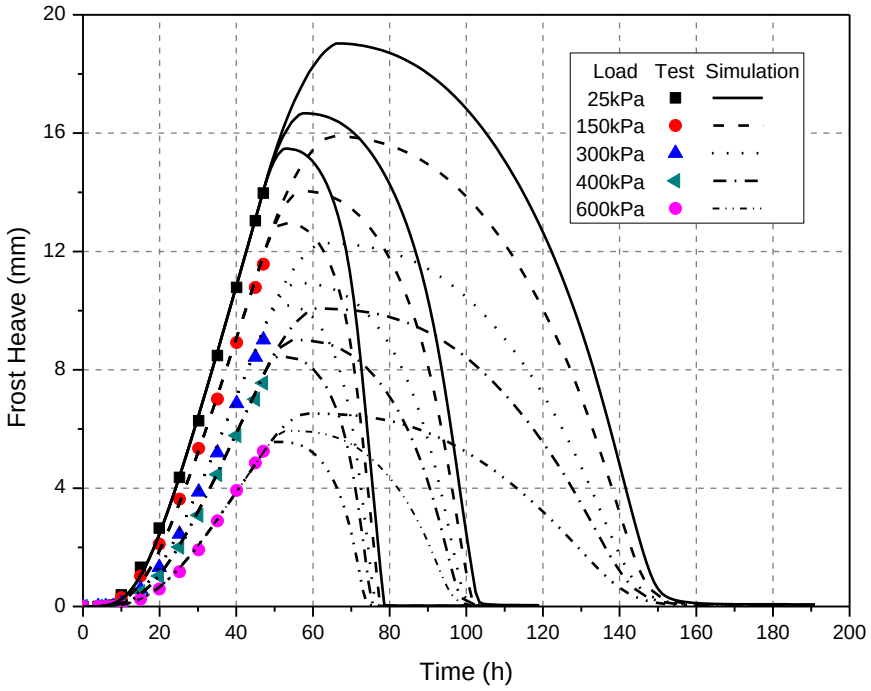

Figure 5.15 Frost heave under the same freezing but diverse thawing rates (different overburden pressure)

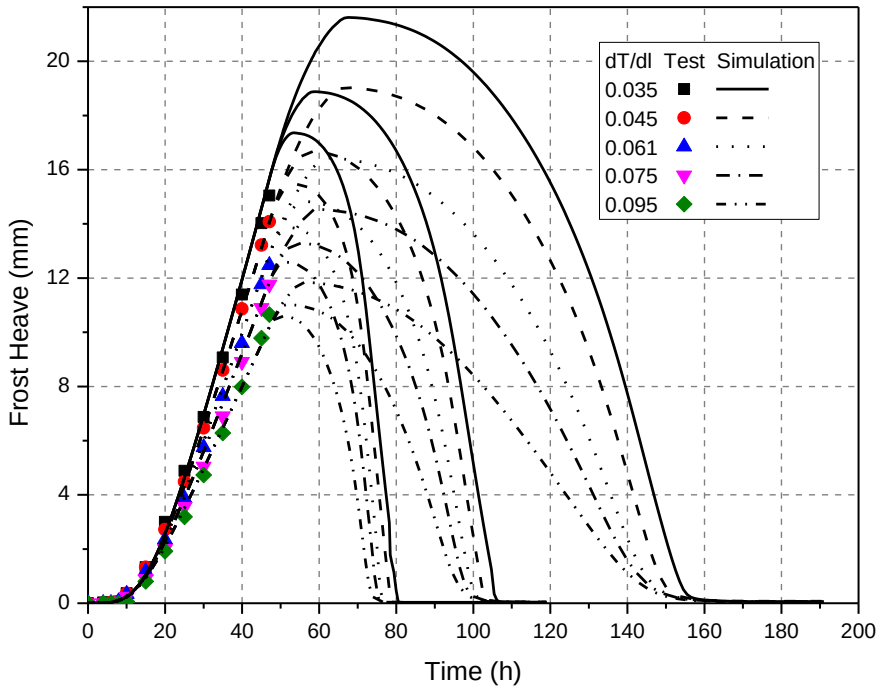

Figure 5.16 Frost heave under the same freezing but diverse thawing rates (different thermal gradients)

5.6 Validation

Validation of the model was carried out using step freeze-thaw measurements of Fukuda et al (1997). The thermal initial/boundary conditions in the step freeze-thaw process were as follows: uniform initial temperature of 5 ℃; at t = 0 the temperature of the bottom plate is reduced to -5 ℃ and continues for 115 hours, whereas the top plate temperature remains at 5 ℃; then the temperature of the bottom increased immediately to 5 ℃ for 10 hours (postulated thawing process in simulation). The simulated frost heave is compared to the test data measured in Fukuda's experiment in Figure 5.17, and it falls very close to the experimental measurements. After the temperature on the cold side of the column increased to 5 °C, the soil thawed very quickly, and the column was completely thawed after 5 hours (no heave measurements for the thawing process were available).

The distribution of excess pore water pressure for the step freeze-thaw cycle is shown in Figure 5.18. The excess pore water pressures generated during the step freezing process were considerably larger than those during the processes with ramped temperatures. The maximum suction was about 1300 Pa, and it occurred at about t = 2 hours at the very bottom of the specimen. When the soil thawed, there were two thawing fronts in the specimen and the thawing process took place rapidly. Because of the rapid thawing and consolidation, an excess pore water pressure of as much as 5500 Pa was generated. The excess pore water pressure dissipated after t = 125 hours.

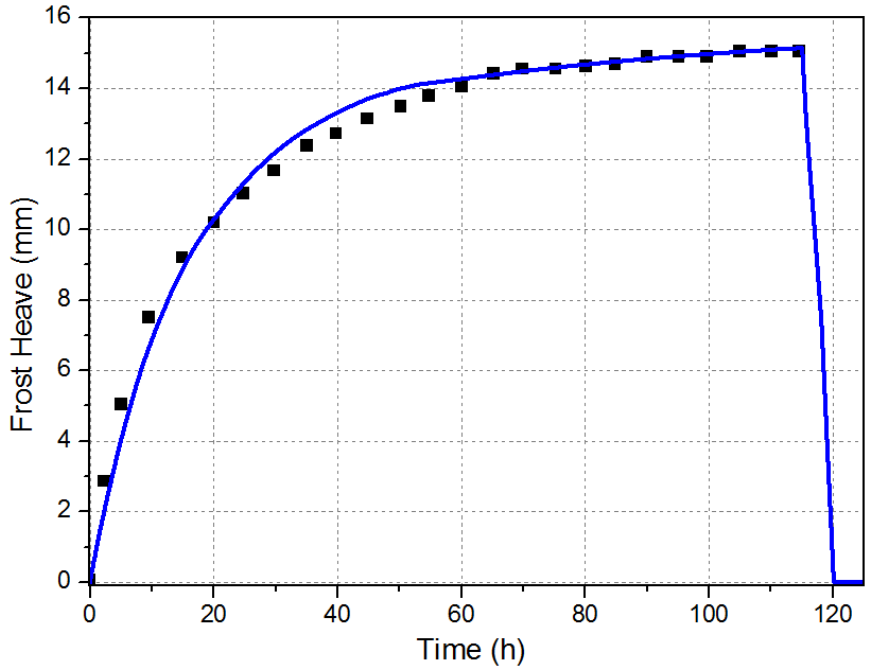

Figure 5.17 Step freezing: comparison of test data and simulated result

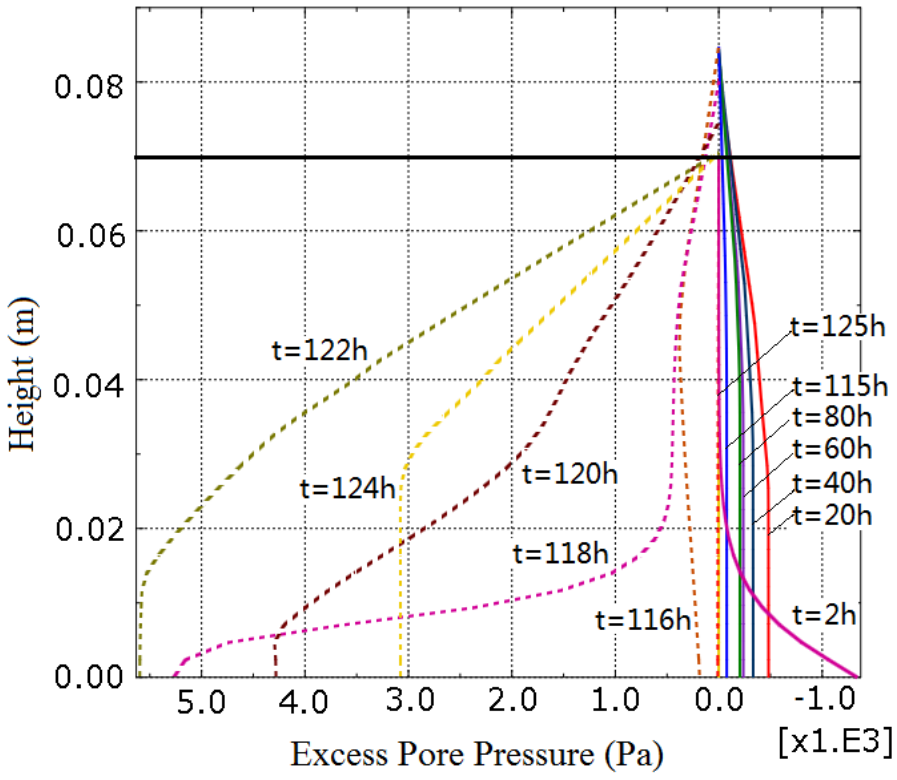

Figure 5.18 Excess pore pressure distribution for step freezing

5.7 Example Simulation: Footing on Frost-Susceptible Soil

A simulation of a footing placed over frost-susceptible soil subjected to a freeze-thaw cycle was performed to illustrate the capability of the model in simulating practical problems.

A continuous footing of a warehouse structure was placed over a frost susceptible soil, as shown in Figure 5.19(a). The initial temperature distribution in the soil profile is shown in Figure 5.19 (b). The ambient temperature inside the warehouse is maintained at 10 ℃, whereas the outside air temperature drops linearly from 5 ℃ to -20 ℃ in 100 days, and at t = 100 days starts rising to reach 25 ℃ at t = 200 days (Figure 5.19(c)). The temperature at the bottom of the model is kept steady at 3 ℃. The heat exchange at the ground surface is affected by the difference in the ambient (air) temperature and the ground temperature, and the Fourier boundary condition was used at the ground surface

$$\lambda_m \nabla T = h_c (T_{air} - T) \tag{5.34}$$

where λ_m is the heat conductivity of the soil mixture, h_c is the convective heat transfer coefficient, T is the soil temperature, and T_{air} is the ambient temperature. A similar boundary condition is used on the masonry wall.

The parameters of the soil used in the simulation are: (1) for unfrozen water content, w^* = 0.058, w_0 = 0.285, T_0 = 0 ℃, and a = 0.16 °C^{-1}; (2) for the elastic-plastic constitutive model, λ = 0.35, κ = 0.07, p_0 = 80 kPa, M = 0.7, α_1 = 0.4, α_2 = 1.8, α_3 = 0.6, p^r = 10 kPa, β = 0.18, p_t = - 1.0 MPa.

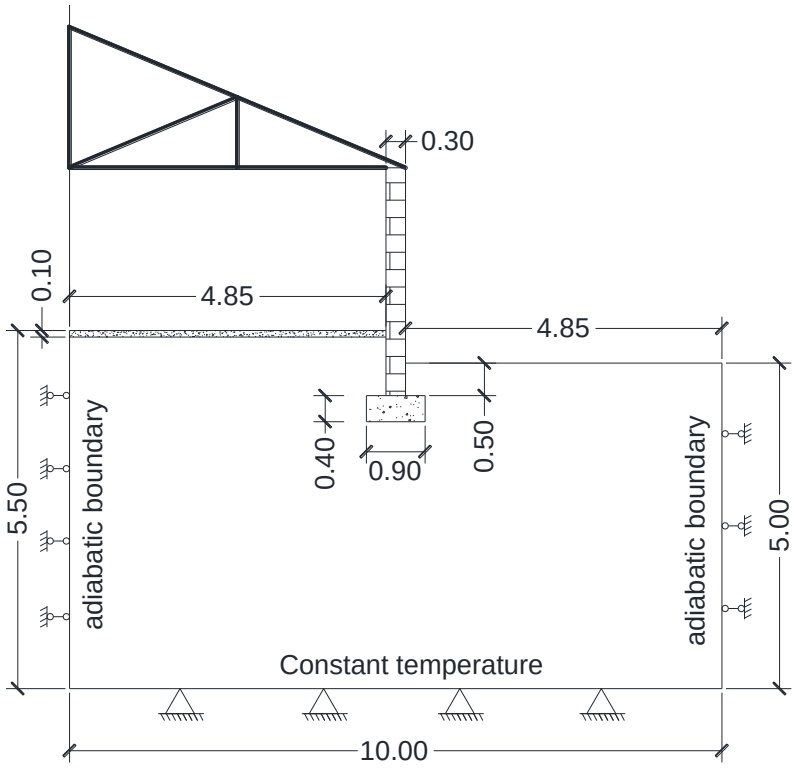
0.30
0.10
4.85
4.85
adiabatic boundary
0.40
0.90
0.50
adiabatic boundary
5.50
5.00
Constant temperature
10.00

(a)

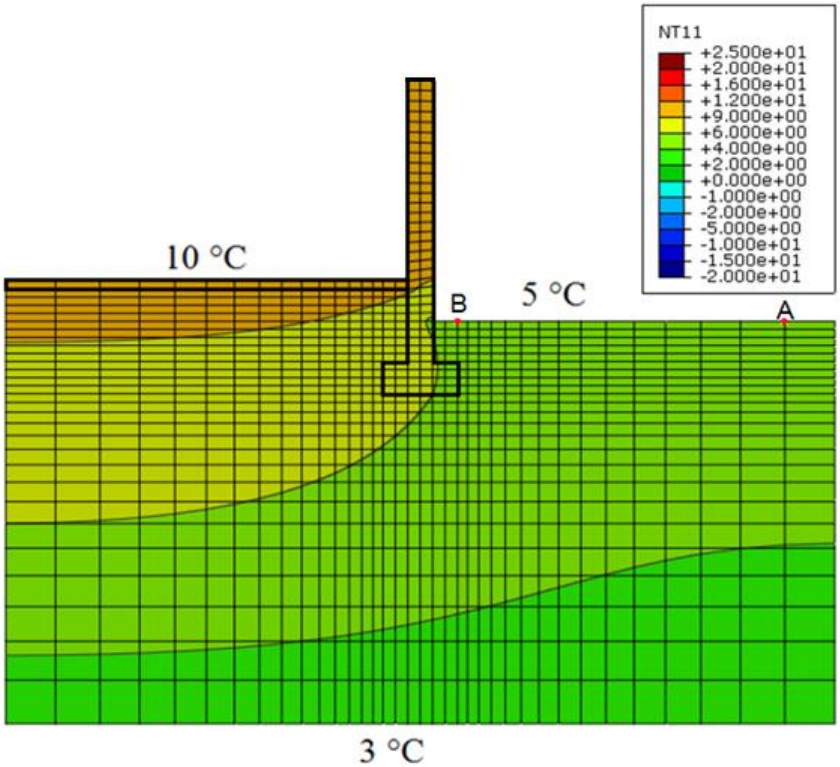
NT11
+2.500e+01
+2.000e+01
+1.600e+01
+1.200e+01
+9.000e+00
+6.000e+00
+4.000e+00
+2.000e+00
+0.000e+00
-1.000e+00
-2.000e+00
-5.000e+00
-1.000e+01
-1.500e+01
-2.000e+01
10 °C
B
5 °C
A
3 °C

(b)

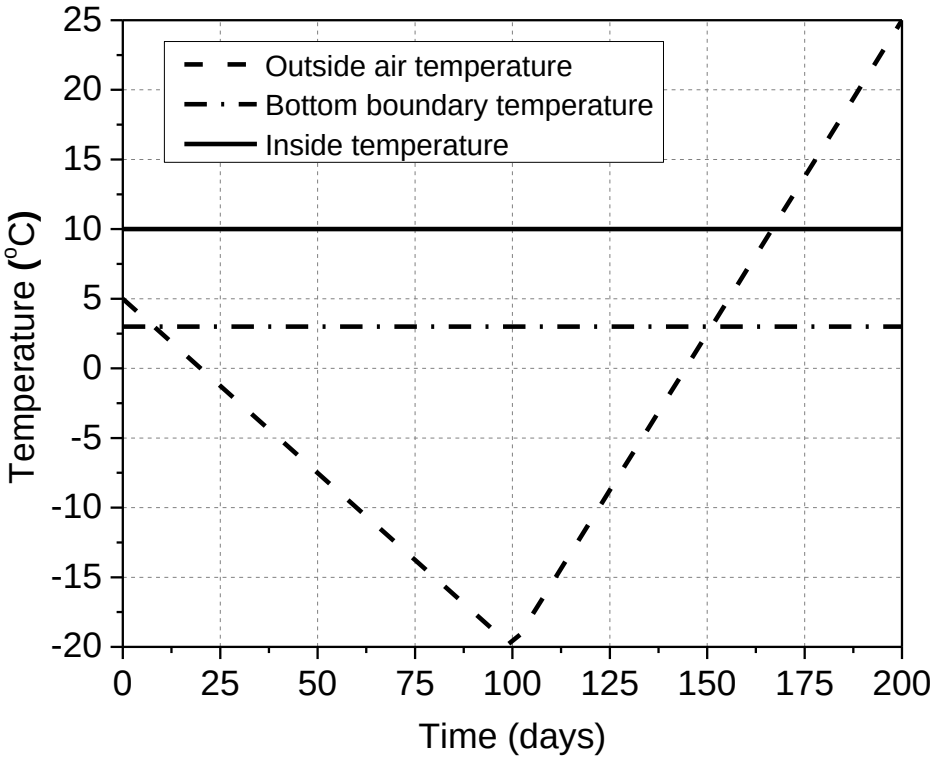

(c)

Figure 5.19 (a) Geometry of continuous footing (in meters), (b) Initial temperature distribution, (c) Thermal boundary condition

The thermal properties adopted for soil constituents in the simulation are the same as those in Table 5.2. The convective coefficient h_c at the soil-air interface is taken as 28 W/(m^2 ℃). The material properties of the masonry wall and concrete footing are listed in Table 5.3. The parameters in the porosity rate function were taken from the calibration and validation section, but the maximum porosity growth rate was reduced tenfold ($\dot{n}_m = 1.98 \cdot 10^{-6}$) to make the soil less frost-susceptible. Because of a lack of comprehensive experimental data for one soil, parameters taken in the simulation come from calibration for two different clays (Fukuda et al., 1997 and Qi et al., 2010).

Table 5.3. Material properties of wall and footing

	Density	Mass heat capacity	Thermal conductivity	Young's modulus	Poisson's ratio	Convective coefficient
	ρ	c	λ	E	υ	h_c
	(kg/m^3)	(J/(kg· ℃))	(W/m· ℃)	(Pa)		W/(m^2 ℃)
Brick	1890	840	1.2	$6.0 \cdot 10^9$	0.15	30
Concrete	2240	970	1.6	$2.0 \cdot 10^{10}$	0.20	90

The hydraulic boundary condition at the ground surface allows drainage, but not intake of water, whereas the bottom boundary is set to be free to drain and intake water. The side boundaries are impermeable, and so is the concrete floor.

The contours of temperature are shown in Figure 5.20 at times t = 60, 136, and 173 days. Displacements are exaggerated by a factor of 3 in all figures that follow.

In the first 60 days the freezing front propagates to about 0.7 m below the open ground surface and starts penetrating into the soil beneath the floor. In the next 40 days the ambient temperature reached the minimum of -20 ℃, and started increasing thereafter, reaching -4 ℃ at t = 136 days. At that moment, the freezing front was located at about 2 m below the open ground surface, and the lower part of the wall, as well as the footing, are at below-freezing temperatures. At 173 days, the air temperature is well above the freezing point and the soil near the ground surface is completely thawed. However, a portion of the soil between 1 to 2 m below the surface is still frozen.

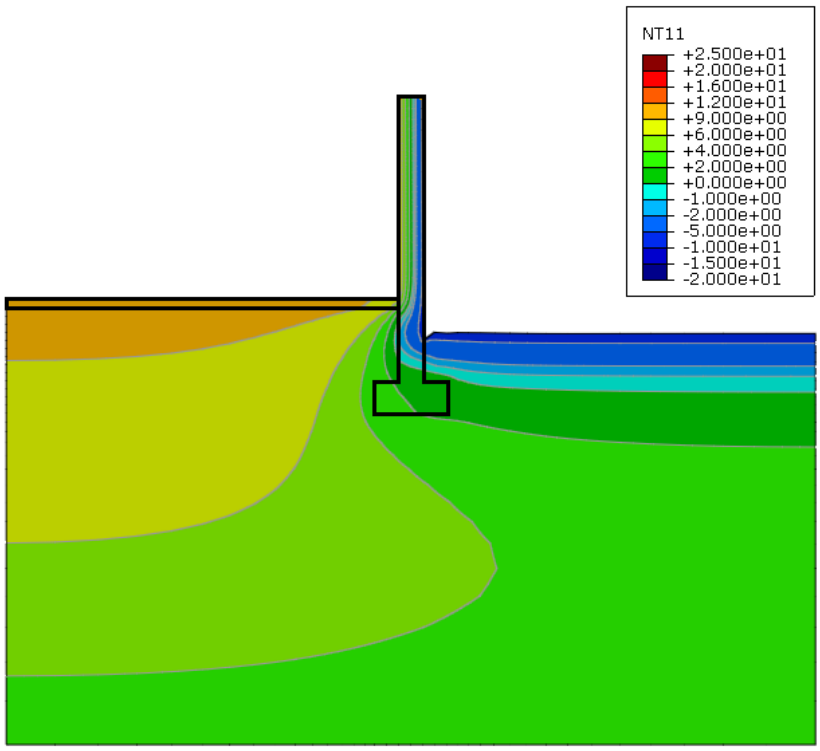
NT11
+2.500e+01
+2.000e+01
+1.600e+01
+1.200e+01
+9.000e+00
+6.000e+00
+4.000e+00
+2.000e+00
+0.000e+00
-1.000e+00
-2.000e+00
-5.000e+00
-1.000e+01
-1.500e+01
-2.000e+01

(a)

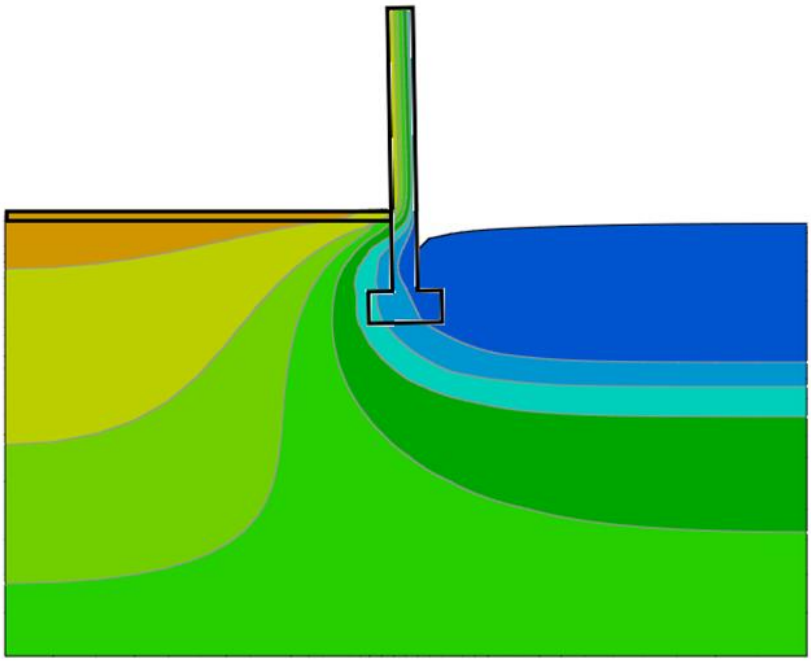

(b)

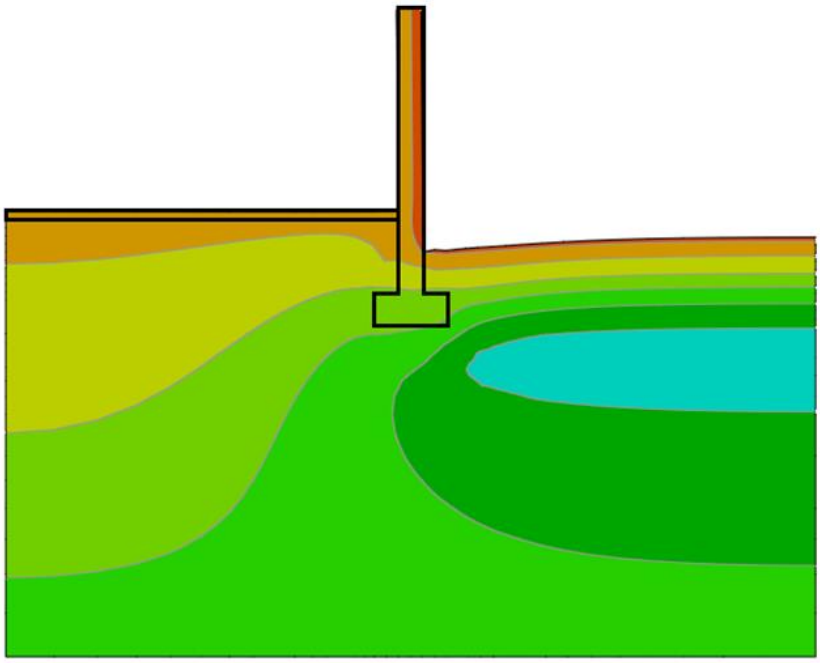

(c)

Figure 5.20 Distribution of temperature (℃): (a) t = 60 days, (b) t = 136 days, (c) t = 173 days (deformation exaggerated by a factor of 3)

The cryogenic suction needed to cause the frost heave, which was predicted by the porosity rate function, was back-calculated for known hydraulic conductivity (given in the section on calibration). Subsequently, the excess pore water pressure generated during the thaw consolidation process was calculated. Figure 5.21 shows the changes in excess pore pressure (suction negative) in the freeze-thaw cycle. After t = 60 days, negative pore pressure is present, with a substantial gradient, causing water transport into the freezing zone. After 136 days, the excess pore pressure below the open ground surface is still negative. Positive pore water pressure occurs on the warm side of the wall, presumably due to tilting of the wall. After 173 days most of the soil has thawed out, and a positive excess pore pressure is generated, which indicates the consolidation process is taking place.

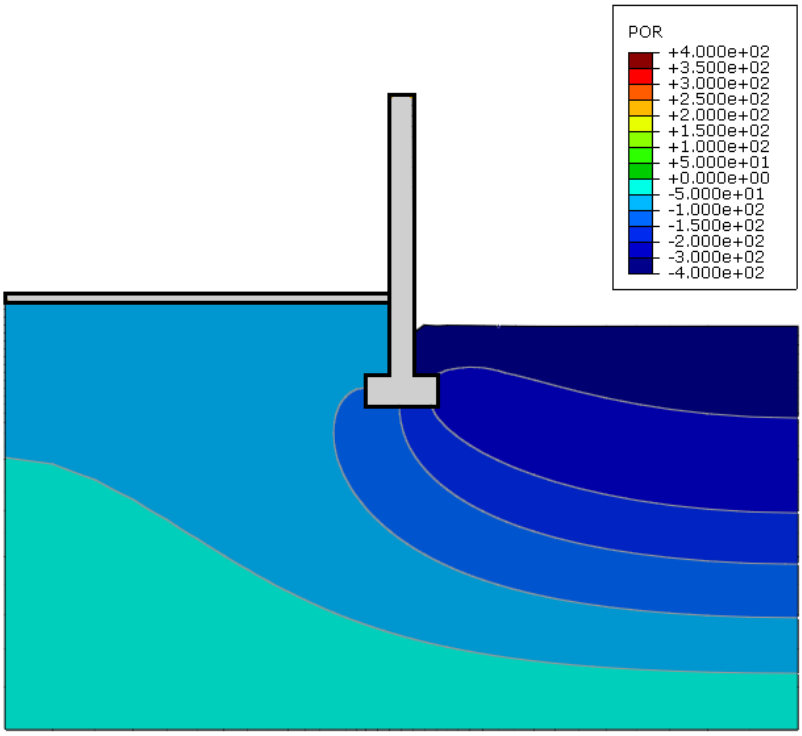
POR
+4.000e+02
+3.500e+02
+3.000e+02
+2.500e+02
+2.000e+02
+1.500e+02
+1.000e+02
+5.000e+01
+0.000e+00
-5.000e+01
-1.000e+02
-1.500e+02
-2.000e+02
-3.000e+02
-4.000e+02

(a)

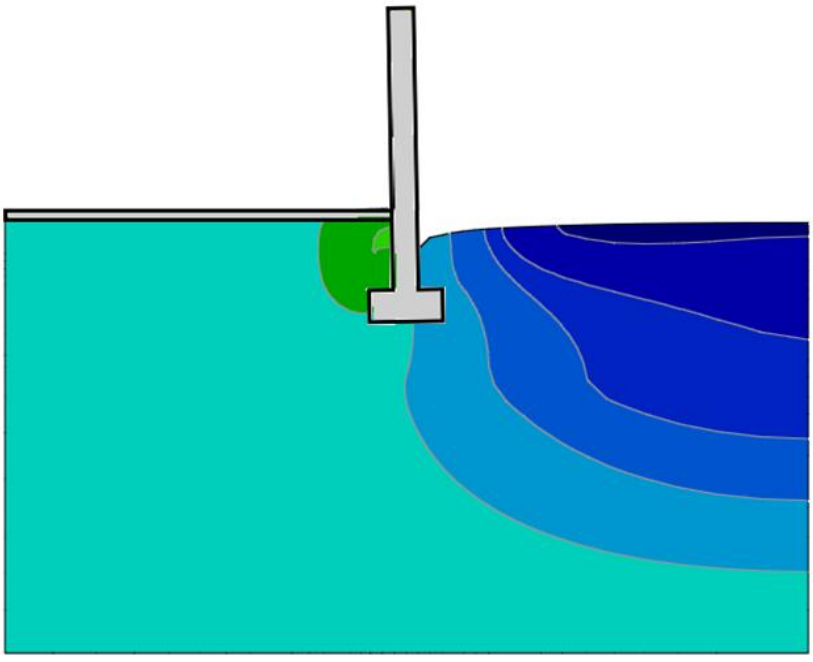

(b)

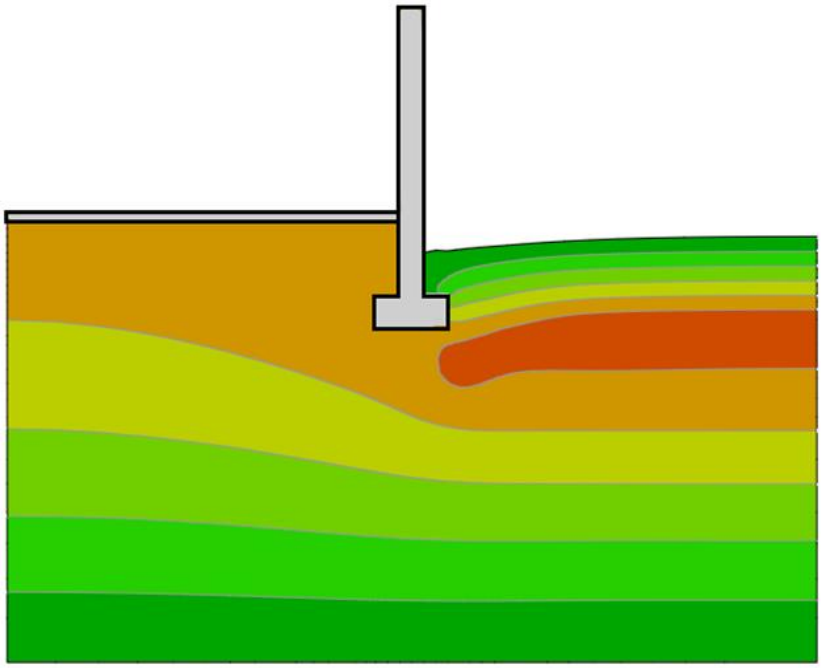

(c)

Figure 5.21 Distribution of excess pore pressure (Pa): (a) t = 60 days, (b) t = 136 days, (c) t = 173 days (deformation exaggerated a by factor of 3)

Vertical displacements caused by frost heave and thaw settlement are shown in Figure 5.22. At t = 60 days, the frost heave is fairly uniform (about 4 cm), except for the immediate proximity of the warehouse wall. After 136 days the maximum ground surface heave is about 14 cm, though it is considerably smaller in the vicinity of the wall of the warehouse. As the freezing front propagated beneath the footing, the growth of ice lenses caused the wall to displace upward by about 2 cm and tilt. At t = 173 days, the soil settled, but has not reached its original level; the thaw consolidation process is not completed yet.

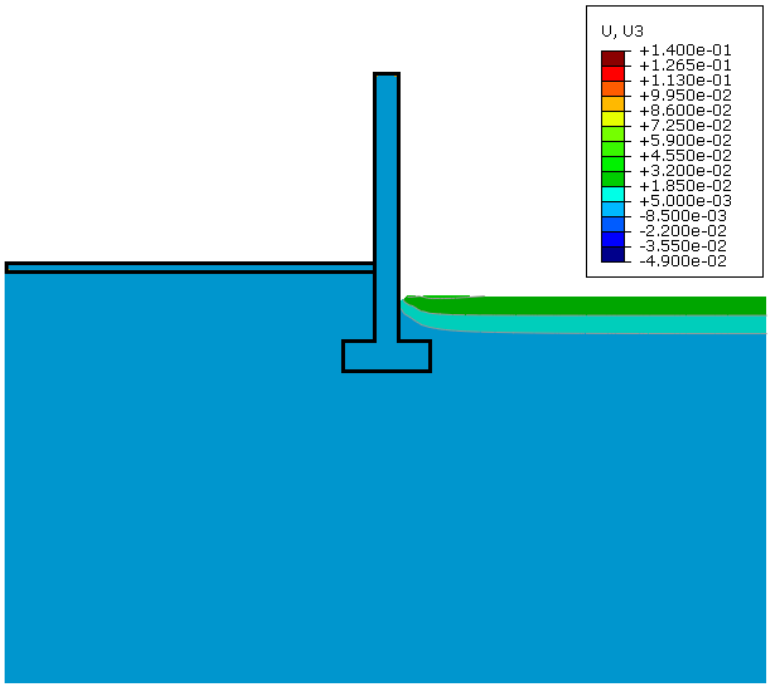
U, U3
+1.400e-01
+1.265e-01
+1.130e-01
+9.950e-02
+8.600e-02
+7.250e-02
+5.900e-02
+4.550e-02
+3.200e-02
+1.850e-02
+5.000e-03
-8.500e-03
-2.200e-02
-3.550e-02
-4.900e-02

(a)

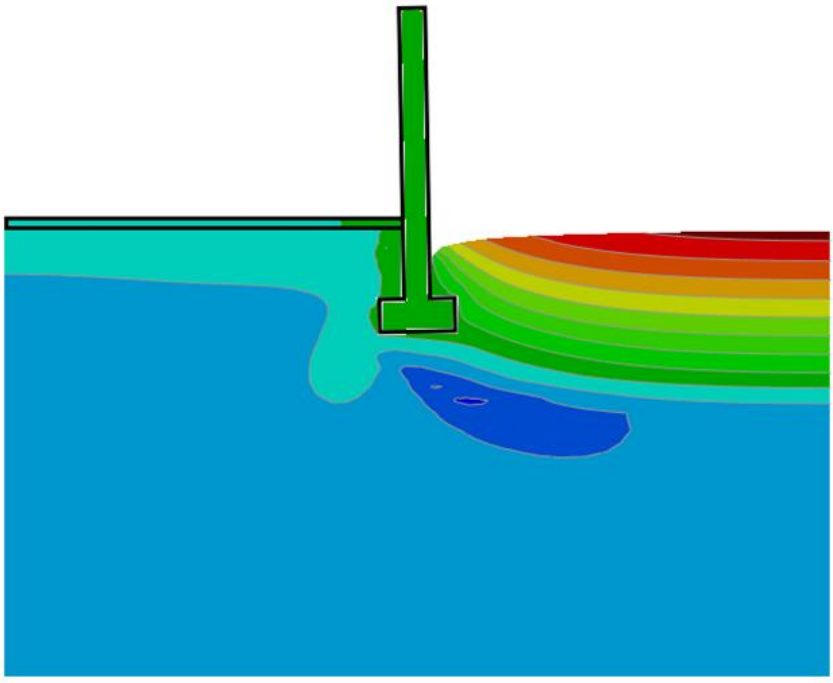

(b)

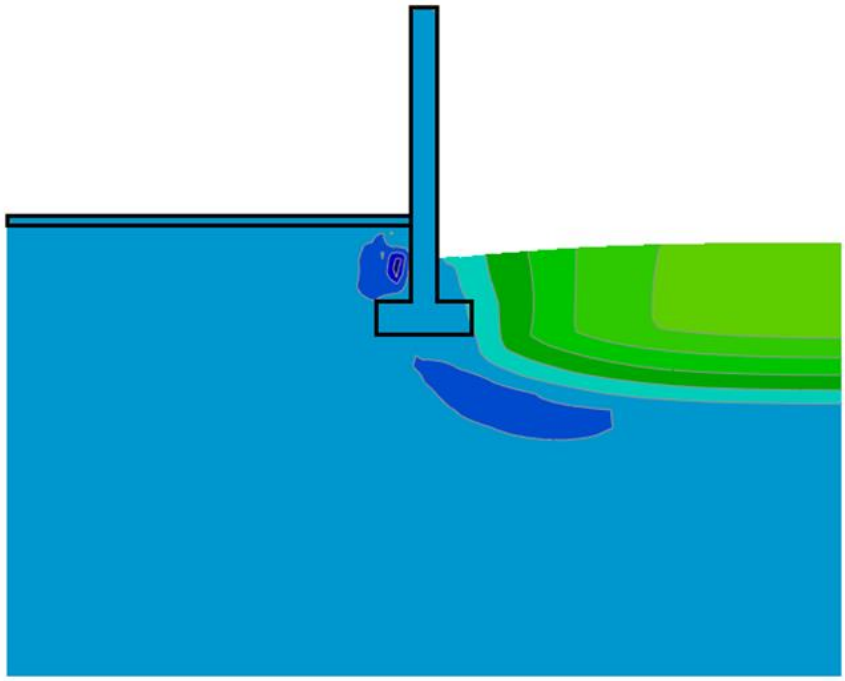

(c)

Figure 5.22 Distribution of vertical displacement (in meters): (a) t = 60 days, (b) t = 136 days, (c) t = 173 days (deformation exaggerated by a factor of 3)

Vertical displacements at two locations (points A and B in Figure 5.19(b)) are compared in Figure 5.23. Point A is selected far away from the wall on the ground surface to monitor the displacement on the ground not disturbed by the presence of the structure, whereas point B is 0.3 m from the wall, to explore the influence of the presence of the structure. Large differential displacement occurs on the ground surface, and the difference was as much as 6 cm. Since this difference persists till t = 200 days, even though the ground temperature is well above zero, the water from precipitation may flow toward the structure during long periods of the freeze-thaw cycle.

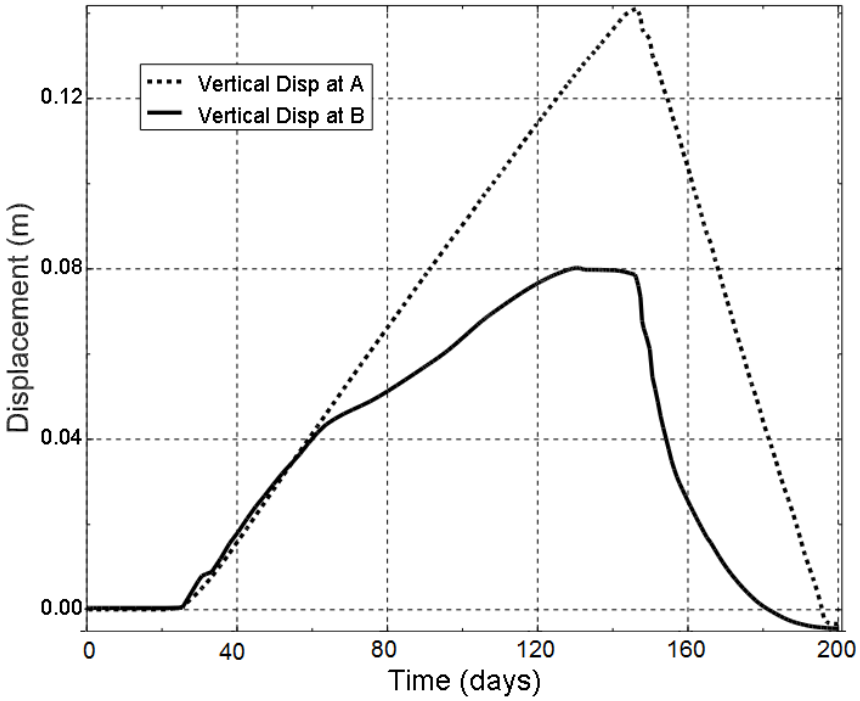

Figure 5.23 Vertical displacement at locations A and B (marked in Figure 5.19(b))

5.8 Remarks

The thermal-hydro-mechanical model with a porosity rate function was used successfully in the simulation of frost heave and thaw settlement of frost-susceptible soils. Calibration and validation of the porosity rate model reveals its good capability of reproducing heave and heave rate in a THM framework. A simulation of a footing placed over frost-susceptible soil, subjected to a freeze-thaw cycle, revealed the model's capability of solving complex boundary value problems related to engineering practice.

CHAPTER 6

APPLICATION OF THE MODEL

The THM model including the elastic-plastic constitutive relationship and the porosity rate function has been calibrated and validated using test data. The implementation of the model makes it possible to solve practical boundary value problems with complex geometries and boundary conditions. An example simulation of a warehouse footing was conducted to demonstrate the usefulness of the model. The simulation showed that the model is capable of predicting frost heave and thaw settlement, while at the same time capturing the changes in thermal and hydraulic fields in the process. More applications of the model in simulating realistic engineering problems are shown in this chapter. The chapter begins with a simulation of one-dimensional 8-meter soil column subjected to freezing and thawing air temperature measured in Aniak, Alaska. A comparison simulation using an approximate piece-wise linear change in measured ambient temperature is also shown to indicate consequences of simplifying the thermal boundary conditions. This simplification of the thermal boundary condition was attempted to reduce the computational cost and overcome convergence issues. Simulations of practical problems are shown next, including freezing and thawing of soils around a steel culvert, freezing and thawing of backfill behind a concrete retaining wall, and frost heave caused by a chilled gas pipeline. The application of thermal insulation in each case is also simulated and its usefulness in

reducing the frost damage to infrastructure is discussed. Each section concludes with final remarks.

6.1 1-D Simulation with Daily Air Temperature Changes

The daily temperature varies significantly, and so does the average daily temperature over the course of a year. In winter, the air temperature could be as low as -40°C, but it is commonly seen that the air temperature can suddenly rise to above 0°C for a few days and then drop again. It is interesting to explore whether or not such sudden changes in air temperature significantly affect the temperature profile in the soil.

In this section, a one-dimensional soil column experiencing freeze-thaw cycle will be simulated using daily air temperature changes. The interfacial effect between soil and air will be investigated. Meanwhile, a simplified (linearized) air temperature change corresponding to the average daily air temperature change will be used in a comparison simulation. The purpose is to find a reasonably simplified temperature boundary condition which could significantly lower the computational cost, avoid the difficulty in reaching convergence and, at the same time, give acceptable results compared to the real daily variable temperature boundary condition.

6.1.1 Air Temperature

The data of daily averaged air temperature in Aniak, AK, from year 1961 to 1962 was obtained from the National Climate Data Center (NCDC). The plot of the temperature data is shown in Figure 6.1. The highest temperature of the year is around 20°C in August whereas and the lowest temperature is around -40°C in January. The daily averaged temperature changes with the change of the seasons, but the general trend each year is quite regular (periodic).

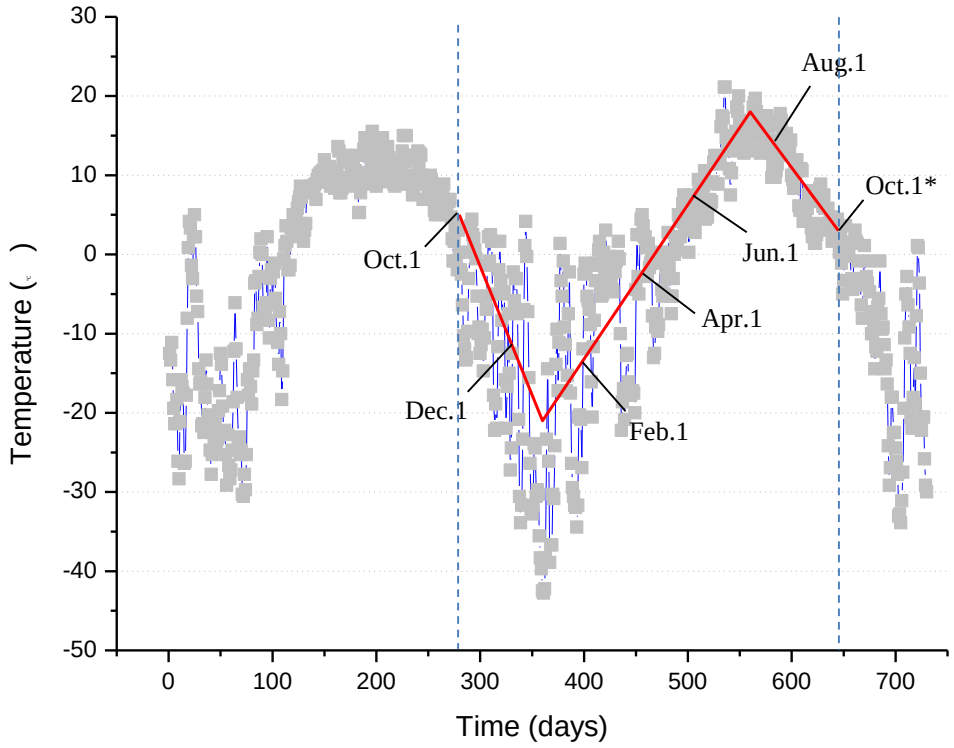

Figure 6.1 Daily air temperature variation in Aniak, AK (NCDC)

An overall trend of the yearly air temperature change can be described as a rotated "S". When freezing starts in mid-October, the air temperature drops down quickly from above zero to about -30°C in 3 months. After that, the air temperature tends to increase and reaches thawing in May. The freezing temperature in this area lasts for about 2/3 of a year. The air temperature then continues to increase thereafter to reach the maximum in August and then drops down again. The mean daily air temperature amplitude (defined as the difference between the peak and the mean daily value) is large in winter, which could reach about 20°C, and is relatively small in summer, about 5°C.

A portion of the temperature function from October 1st, 1961 to October 1st, 1962, a full year of 365 days (shown in between the dashed lines in Figure 6.1) will be used in the following simulations.

6.1.2 Ground Temperature Profile

The ground temperature in Alaska was monitored by researchers from U.S. Army Cold Regions Research and Engineering during the year 1947 to 1958 at several locations. The ground temperature in Aniak, AK, was reported and the temperature profile below the ground surface is shown in Figure 6.2 from the end of freezing season in 1952 until the middle of the freezing season in 1953 (Aitken and Fulwider, 1962).

Comparing the air temperature shown in Figure 6.1 and the temperature on the ground surface in Figure 6.2, one can tell that the range for the air temperature change (about -40°C to 20°C) is larger than the range for the ground surface temperature change (about -15°C to 15°C). Although the two were measured in different years, they were not reported as measured in an extreme weather year. Therefore, it is believed these measurements reflect the usual temperature range in this region. The difference between the two is due to interfacial effect between the soil and the air and the influence of the temperature in the ground.

Below the ground surface, the temperature distribution changes along with the change of air temperature. However, below certain depth, the variation in temperature is very small. The profile in Figure 6.2 indicates that the temperature becomes nearly constant of about 3°C (37°F) at the depth of about 7 m (22 ft). The temperature distribution indicates no permafrost exists in this area, and the thickness of the active layer (upper crust layer where active freezing-thawing cycles occur) is about 1.2 m.

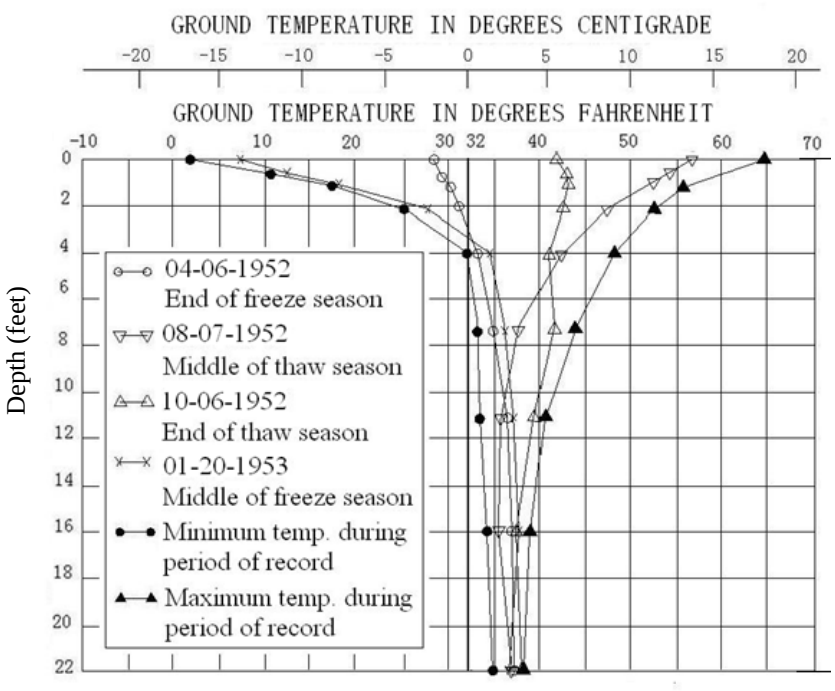

Figure 6.2 Below-ground temperature in Aniak, AK (after Aitken and Fulwider, 1962)

6.1.3 1-D Freeze-Thaw Cycle Simulation

A one-dimensional soil column under a freeze-thaw cycle was simulated, using both the measured daily averaged temperatures (data points) and the average piece-wise linear temperatures (red line in Figure 6.1). These temperature functions are used as the thermal boundary conditions at the top of an 8-meter soil column in the 1-D simulation. The bottom boundary of the column is set to a constant temperature of 3°C (shown in Figure 6.3). The 8-node trilinear displacement, pore pressure, and temperature elements (type C3D8PT in ABAQUS) are used in the column model. The total number of elements is 100 and the total number of nodes is 404.

The initial temperature distribution for the 1-D column is taken as steady state, with the temperature at the top to be 5°C and bottom 3°C. The side walls of the column are set to be adiabatic.

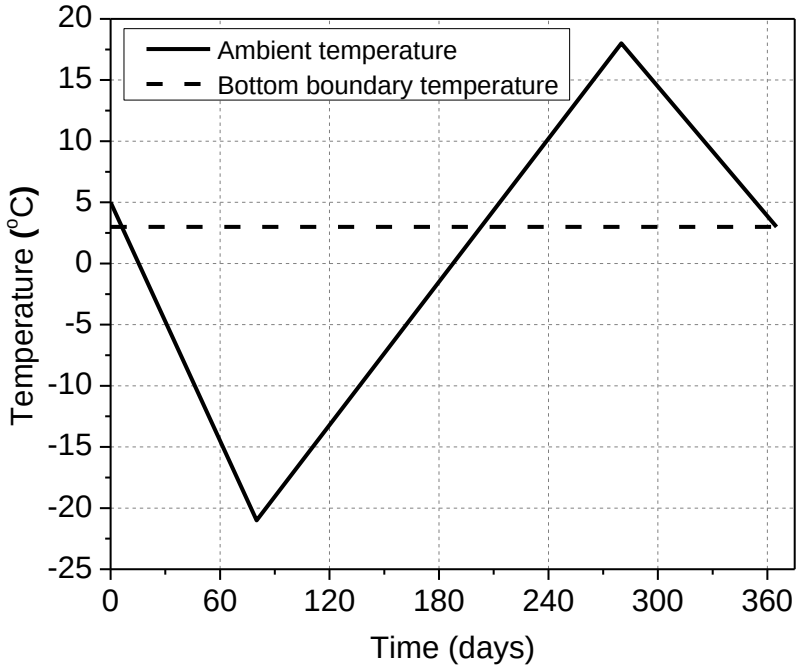

Figure 6.3 Thermal boundary conditions

To take into account this interfacial effect between soil and air, the Fourier boundary (also known as mixed boundary) condition is used. The function is expressed as

$$\lambda_m \nabla T = h_c (T_{air} - T) \tag{6.1}$$

where λ_m and h_c are the heat conductivity and convective heat transfer coefficient of soil mixture, T is soil temperature and T_{air} is the ambient air temperature.

As to the mechanical boundary conditions, the top boundary is free to move while the bottom boundary is fixed in both horizontal and vertical directions. Horizontal displacements are not allowed along vertical boundaries.

The hydraulic boundary condition on the top boundary allows drainage, but not intake of water, whereas the bottom boundary is set to be able to drain and intake water, with a hydraulic conductivity of $1.0 \cdot 10^{-7}$ m/s. The side boundaries are impermeable.

The parameters of the soil used in the simulation are: (1) for unfrozen water content, $w^* = 0.058$, $w_0 = 0.285$, $T_0 = 0$ ℃, and $a = 0.16$ °C^{-1}; (2) for elastic-plastic constitutive model, $\lambda = 0.35$, $\kappa = 0.07$, $p_0 = 80$ kPa, $M = 0.8$, $\alpha_1 = 0.2$, $\alpha_2 = 0.4$, $\alpha_3 = 0.6$, $p^r = 10$ kPa, $\beta = 0.18$, $p_t = -1.0$ MPa; (3) the parameters in the porosity rate function were taken from the calibration and validation section, the maximum porosity growth rate was reduced to 8% ($\dot{n}_m = 1.58 \cdot 10^{-6}$) to make the soil less frost-susceptible. The values of thermal properties for soil particles, water and ice in the simulation are the same as is shown in Table 5.2. The hydraulic conductivity for was taken as $1.0 \cdot 10^{-7}$ m/s for unfrozen soil and $1.0 \cdot 10^{-12}$ m/s for frozen soil with temperature below - 5 ℃; linear interpolation was used for temperatures between 0 ℃ and -5 ℃.

The simulated temperature of soil at the ground surface for both of the cases with ambient air temperature as the true measured temperature (“T” for short) and the piece-wise linear temperature (“L” for short) are shown in Figure 6.4. The surface temperature under the linearized boundary condition is close to the mean value of the true boundary condition. The ranges for the yearly surface temperature are about -30 ℃ to 15 ℃ for “T” and -15 ℃ to 15 ℃ for “L”, respectively. The “kinks” shown in the circles on the curve of the “L” case result from the release of latent heat.

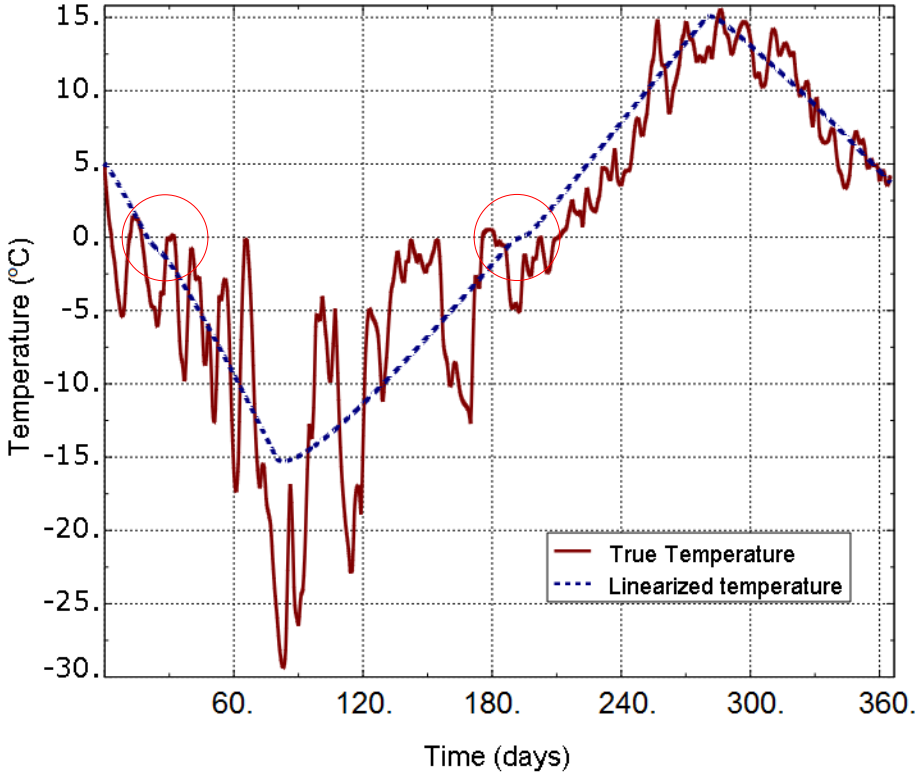

Figure 6.4 Temperature of soil at the ground surface

The frost heave and thaw settlement (vertical displacement) on the ground surface (top of the column) were compared in Figure 6.5. In the freezing process, the maximum frost heave is about 20 cm for the "L" case and about 17.5 cm for the "T" case, respectively. The heave rate for the "T" case is close but slightly smaller than that of the "L" case in the first part of the heaving, then drops quickly at the end of the heaving. The settlement for the "T" case starts a little later than for the "L" case, and the rate of settling for the "T" case is slightly larger than the "L" case. Both of the two cases show further thaw-settlements beneath the pre-freezing level after the freeze-thaw cycle, and the values are nearly identical at 2 cm. The extra settlement is caused by the suction-induced consolidation during the freezing process. This phenomenon for normally

consolidated soil upon freezing and thawing was reported earlier by Chamberlain and Gow (1978).

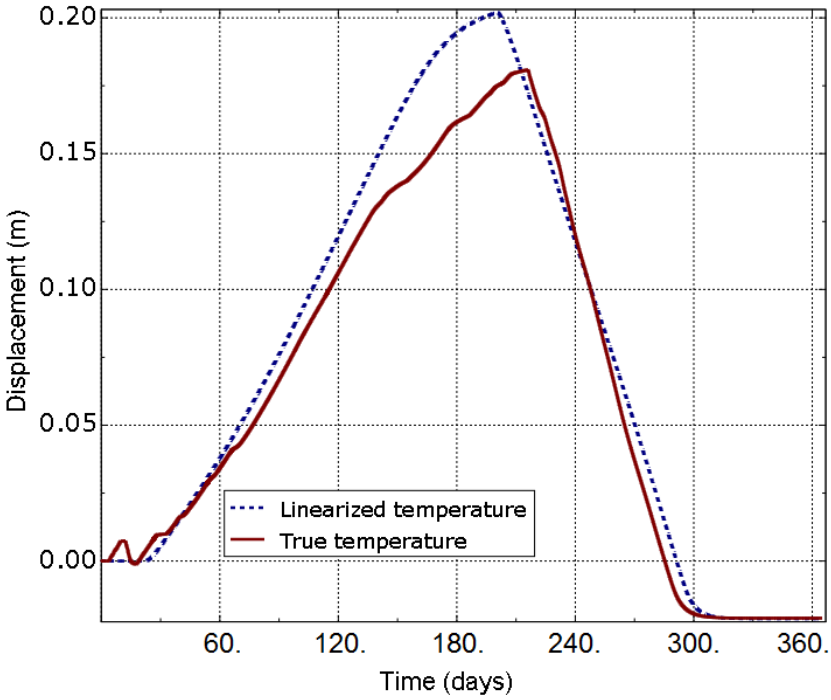

Figure 6.5 The frost heave and thaw settlement (displacement on the top surface)

The simulated change in ground temperature with depth for both of the cases are shown in Figure 6.6 (the solid line represents the “T” case and the dashed line represents the “L” case). The simulated temperature distribution and the freezing front propagation for the two cases are very close to each other below 2 m but have some difference above. However, the differences are reasonably small and both of them are in good agreement with the reported record.

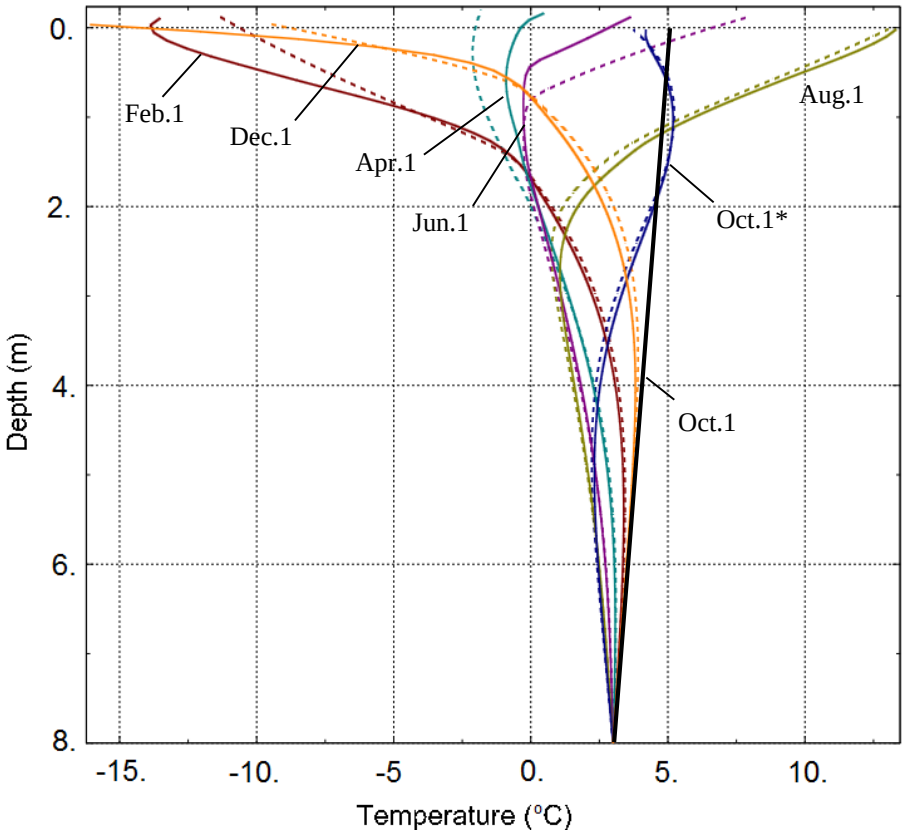

Figure 6.6 Change in ground temperature profile (dates are marked in Figure 6.1)

As the freezing front is propagating, the pore water turns into pore ice, which serves as a natural "cementation" in the soil and induces an increase in the soil strength. The volumetric fraction of ice and porosity are increasing in the frozen fringe according to the porosity rate function representing the ice lens growth. The strength and deformation parameters in the simulations were monitored and compared to investigate the influence of replacing the true boundary temperature with the piece-wise linear one.

The distribution of the pore ice ratio e_{ip} and the corresponding pseudo pre-consolidation stress are compared in Figure 6.7 and Figure 6.8.

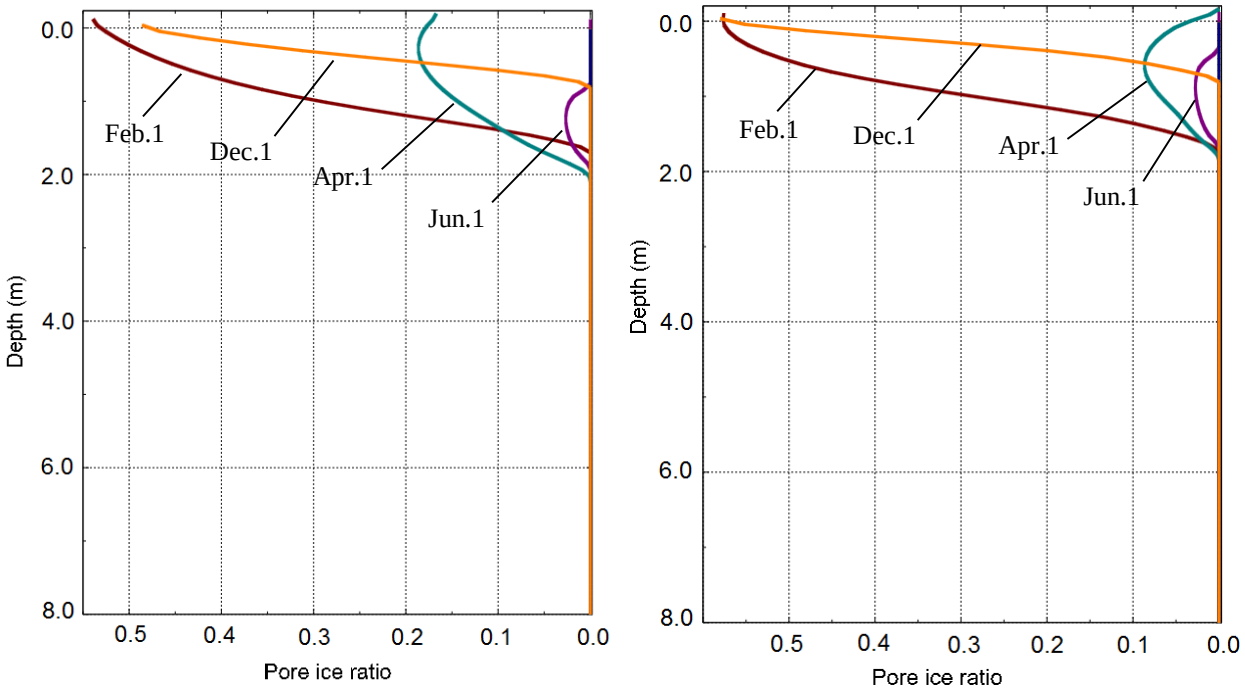

Figure 6.7 Distribution of pore ice ratio

The pore ice ratio increases as the temperature drops below freezing. The soil strength (the pseudo pre-consolidation stress) increases according to the proposed evolution law (Equation (4.19)). As initial condition, the soil near the ground surface (to 0.6 m in depth) is assumed to be over-consolidated due to drying, with the pre-consolidation stress to be 10.0 kPa, whereas the soil below is normally consolidated. During the freeze-thaw cycle, some portion of the soil consolidated due to increase in effective stress caused by suction (the effective stress exceeded the pseudo pre-consolidation stress). This explains further settlement after freeze-thaw cycle in Figure 6.5.

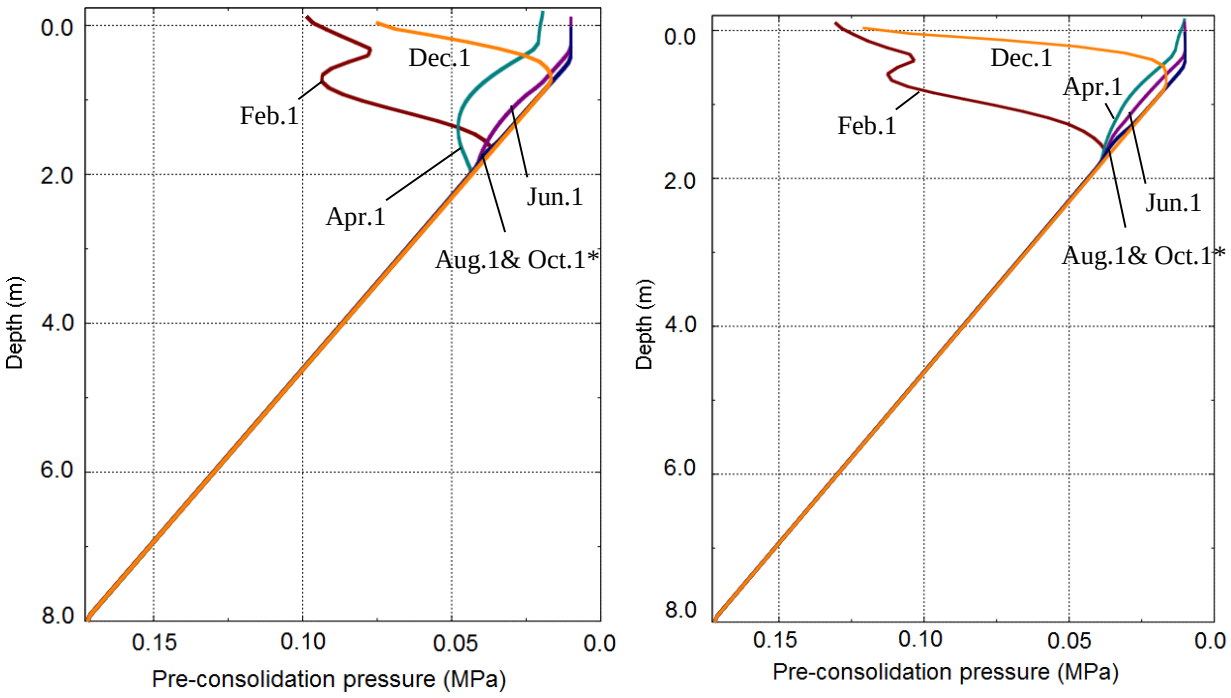

Figure 6.8 Distribution of "pseudo-pre-consolidation pressure"

The distribution of the excess pore pressure for the two cases are similar as compared in Figure 6.9. The suction (negative pore pressure) in the soil was generated from October through April or May indicating the ice lens formation was on going in this period, whereas from June to August or September, the positive pore pressure was generated because of the thaw consolidation. In the following October, the excess pore pressure in the soil profile went back to zero, indicating the consolidation process completed and the melted water had drained out.

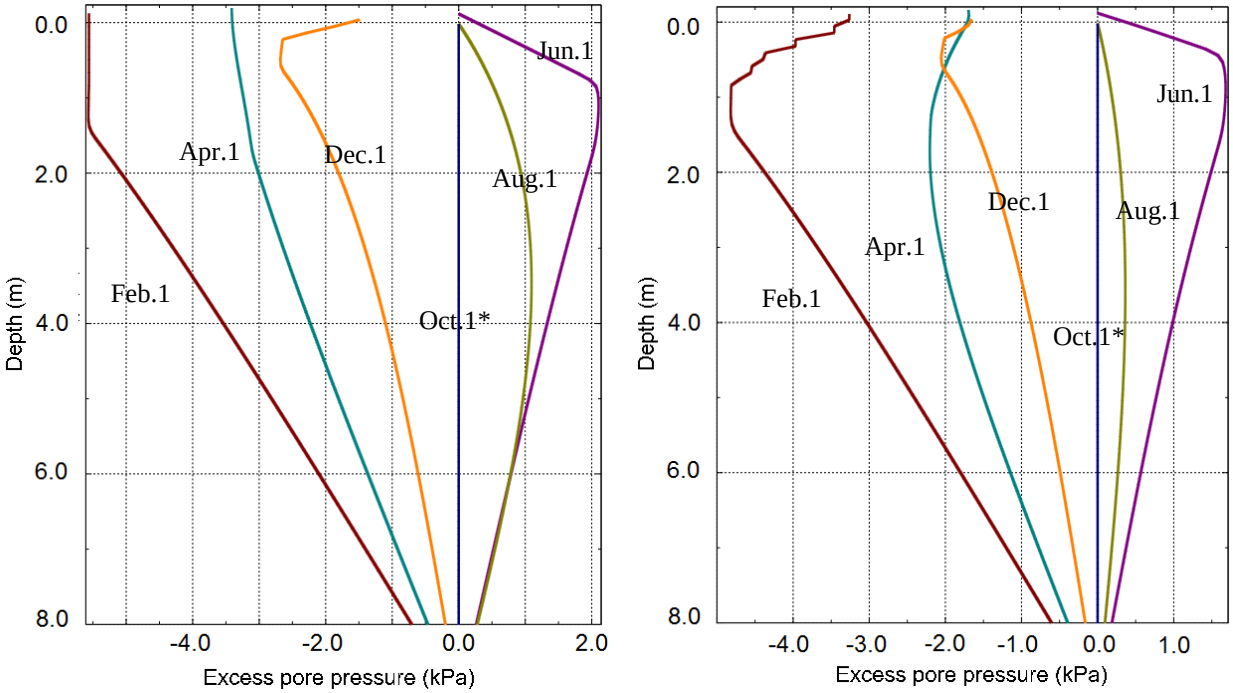

Figure 6.9 Distribution of excess pore pressure

The proposed model describes the growth of ice lenses as an increase in porosity and the porosity profiles are shown in Figure 6.10. Take the profile of Feb. 1 for "L" in Figure 6.10 as an example, the porosity growth of ice lenses dominates in the frozen region (above 1.6 m in depth), although the increased effective stress due to suction compresses the soil at the same time. In the area below the freezing front (1.6 m depth), the porosity decreases as a result of the consolidation caused by suction. At the end of the freeze-thaw cycle, a residual decrease in porosity occurs. This is again due to the yielding of soil by the increased effective stress, which exceeds the (pseudo) pre-consolidation stress. The distribution of volumetric ice content is compared in Figure 6.11.

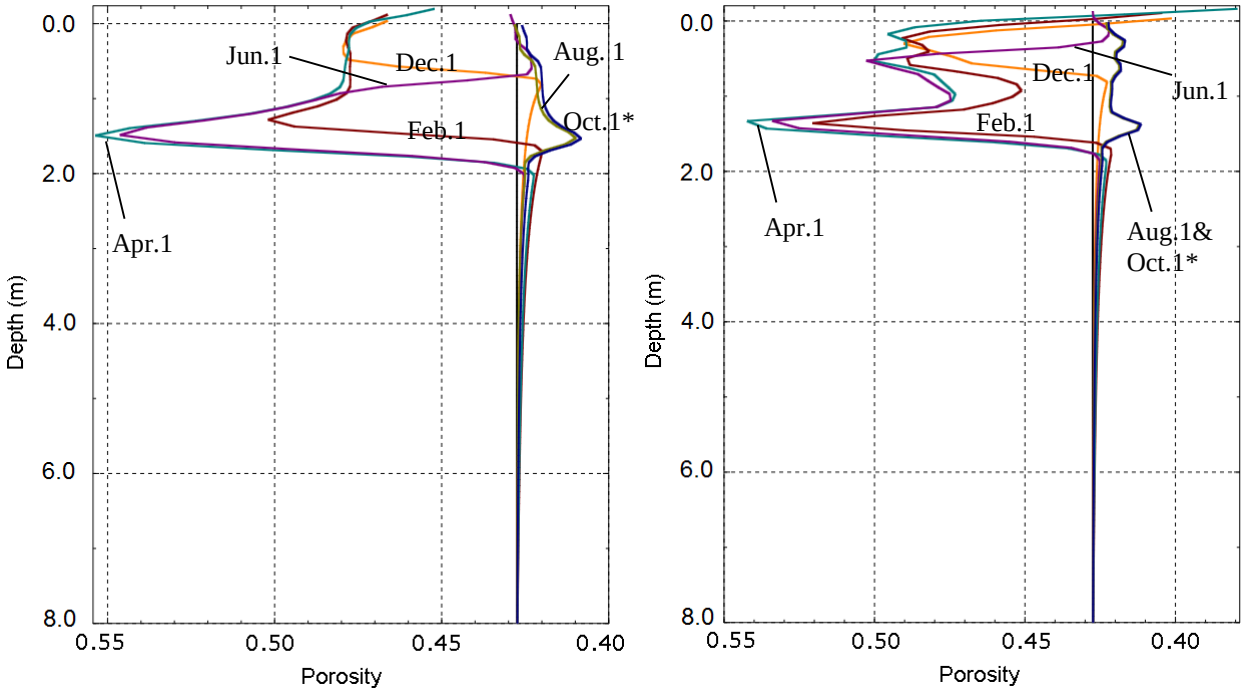

"L" "T"

Figure 6.10 Distribution of total void ratio

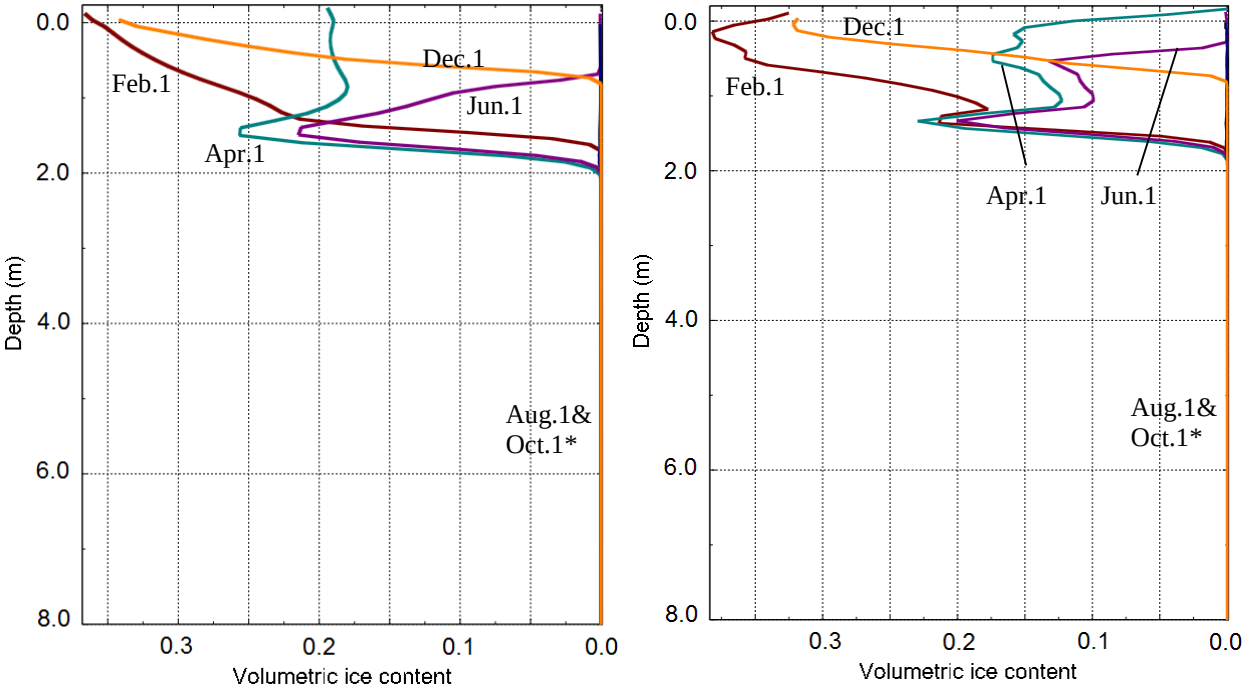

"L" "T"

Figure 6.11 Distribution of volumetric ice content

6.1.4 Remarks

The simulations of a 1-D soil column subjected to both measured and linearized temperature freeze-thaw cycle were conducted. By comparing the results, the 1-D frost heave and thaw settlement simulated using the linearized air temperature are very close to that from simulation with the true air temperature. Therefore, the linearized temperature change will be used as the thermal boundary condition in solving more practical boundary value problems. This will give reasonable results while significantly reducing the computational cost and avoiding convergence issues.

6.2 Frost Heave and Thaw Settlement around a Culvert

Culverts are conduits used in transportation infrastructure to convey water from one side of the road to the other. Figure 6.12 shows a set of culverts in the state of Alaska on the Richardson Highway to Valdez. In spring and summer, culverts are important infrastructure elements helping to channel water and they can alleviate the impact of sudden water flush. Culverts also play a key role in preventing soil erosion. In winter, however, they may become a source of maintenance problems and even damage to roads. Therefore, when designing and constructing culverts in cold regions, special attention should be paid to issues caused by extreme temperature.

Figure 6.12 Culverts in cold region (photograph by the author)

Because the inside of a culvert is exposed to open air flow, the temperature inside a culvert is expected to be very close to the outside air temperature. This will produce a significant impact on the temperature profile in the soil around a culvert. In summer, the soil properties do not change a lot with respect to the temperature and the influence of varied temperature is negligible. However, big issue may occur in winter, as the soil properties vary dramatically with temperature below freezing. For instance, differential frost heave and thaw settlement could result on the ground surface (road surface); the culvert itself could be damaged due to uneven displacement. Simulations were performed using the THM model developed to reveal possible response of ground surface above a culvert to freezing and thawing.

6.2.1 Problem Description

Simulations of freezing of an unpaved road above a culvert in frost susceptible soil were performed using ABAQUS. The geometry of the model for the culvert and the surrounding soil as well as the boundary conditions for the finite element analysis are shown in Figure 6.13. The top of the culvert in this model is located 1.0 m below the ground surface. The external diameter of the culvert is 1.0 m and its wall thickness is 10.0 mm. The material of the culvert is steel. Between the culvert and the soil, perfect bonding (ad-frozen interface) is assumed. The simulations will be performed for the air temperature that is consistent with Alaskan climate at Aniak, AK. Vertical displacement at two locations marked A and B (Figure 6.13) will be monitored to investigate the impact of the culvert to the heave on the ground surface.

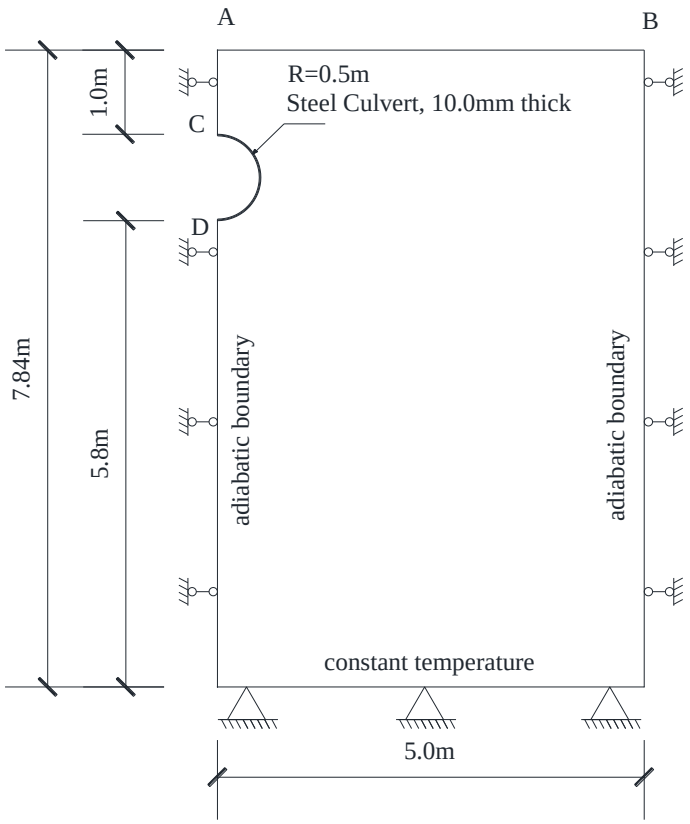

Figure 6.13 Geometry of the culvert and surrounding soil

As to the boundary conditions, the vertical sides are not allowed to move sideways, the bottom is fixed in both the horizontal and vertical directions, while the top surface and the culvert inside surface are free to move. The heat is not allowed to flow across the two vertical boundaries. Temperature consistent with the Alaskan climate at Aniak, AK will be used in the simulations: the simplified air temperature shown in Figure 6.14 will be used. The temperature at the bottom is set to a constant of 3°C. The Fourier boundary condition (Equation (6.1)) is used at both the top boundary and the culvert surface to simulate the interface between air and solid medium. The vertical boundaries and the culvert are impermeable. The bottom boundary is able to drain and intake water, with a hydraulic conductivity of $1.0 \cdot 10^{-7}$ m/s, whereas the ground

surface allows only drainage, but not intake of water. The simulation results at the moments marked in Figure 6.14 will be shown in the next sub-section.

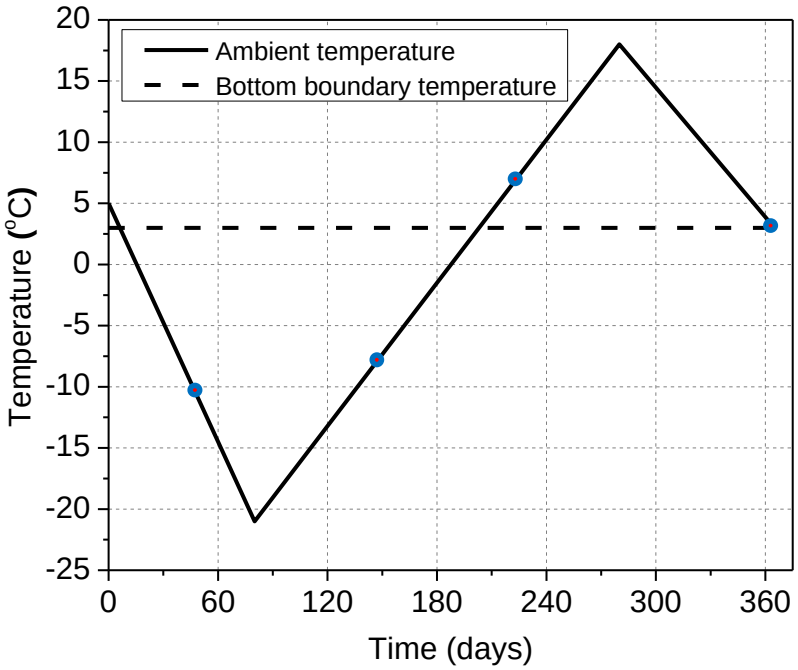

Figure 6.14 Thermal boundary conditions

The finite element mesh is shown in Figure 6.15. The model is discretized using 8-node solid elements, with only one element layer in the third direction (in plane y-direction). The boundary condition for the in-plane surfaces are adiabatic and not allowed to move along in-plane direction, therefore the model simulates a plane strain problem. The 8-node trilinear displacement and temperature elements (element type C3D8T in ABAQUS) are used for the culverts, whereas 8-node trilinear displacement, pore pressure, and temperature elements (type C3D8PT in ABAQUS) are used for the surrounding soil. The total number of elements is 2131 and the total number of nodes is 4470.

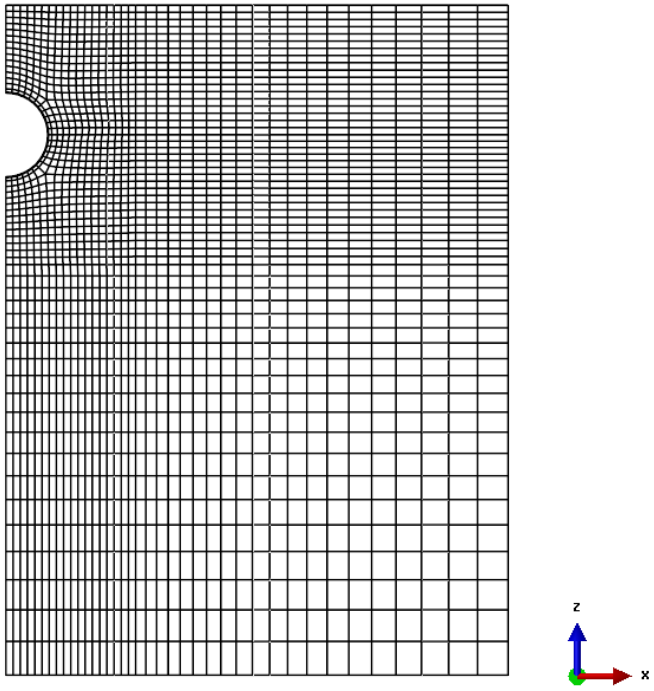

Figure 6.15 Finite element mesh

The initial temperature distribution shown in Figure 6.16 is obtained from running heat transfer simulation for three years under the thermal boundary condition shown in Figure 6.14. The soil temperature is above the freezing point everywhere (not the permafrost region).

The initial stress state of the soil affects both the elastic-plastic constitutive relationship and the porosity rate function. Therefore, before starting the simulation of the thermal problem, the steady-state geo-static stress distribution under self-weight was calculated. The stress state at each nodal point was calculated by ABAQUS and stored in a file. The file was then read into ABAQUS again to prescribe the initial stress field for the simulation. Figure 6.17 shows the initial geo-static vertical stress in the soil profile.

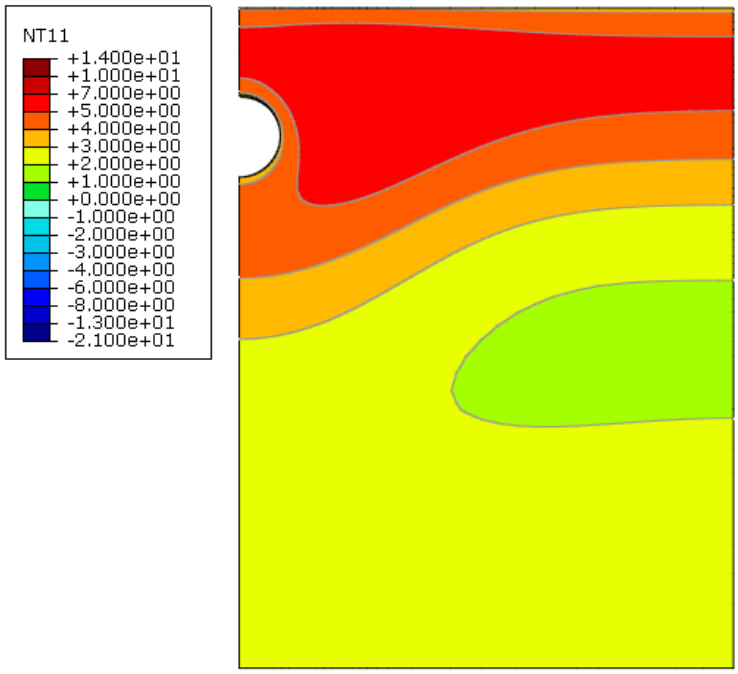

Figure 6.16 Initial temperature distribution (℃) at t = 0

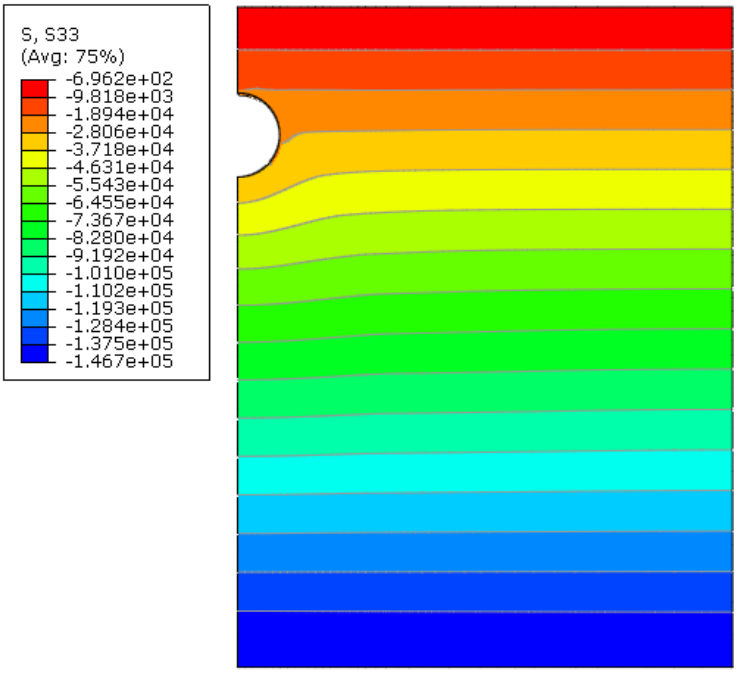

Figure 6.17 Distribution of geo-static vertical stress (Pa) at t = 0

The parameters of the soil used in the simulation are: (1) for unfrozen water content, $w^* = 0.058$, $w_0 = 0.285$, $T_0 = 0$ ℃, and $a = 0.16$ °C^{-1}; (2) for elastic-plastic constitutive model, $\lambda = 0.35$, $\kappa = 0.07$, $p_0 = 80$ kPa, $M = 0.8$, $\alpha_1 = 0.2$, $\alpha_2 = 0.4$, $\alpha_3 = 0.6$, $p^r = 10$ kPa, $\beta = 0.18$, $p_t = -1.0$ MPa; (3) for porosity rate function, $\dot{n}_m = 5.94 \cdot 10^{-}7\ s^{-1}$ (less frost susceptible soil, 3% of calibration value from Fukuda's tests), $T_m = -0.82$ ℃, $g_T = 100$ ℃/*m*, and $\zeta = 0.73$ MPa; the hydraulic conductivity for freezing soils was taken as $1.0 \cdot 10^{-7}$ m/s for unfrozen soil and $1.0 \cdot 10^{-12}$ m/s for frozen soil with temperature below -5 ℃; linear interpolation was used for temperatures between 0 ℃ and -5 ℃; the initial void ratio is 0.747.

In addition to simulating the boundary value problem defined in Figure 6.13, an influence of using culvert insulation on the frost heave resulting from the same thermal boundary conditions was studied. A 10 mm thick layer of insulation was simulated around the outside perimeter of the culvert. The material properties of the culvert (steel) and the insulation layer are shown in Table 6.1.

Table 6.1. Material properties of culvert and insulation

	Density ρ kg/m^3	Mass heat capacity c J/(kg· ℃)	Thermal Conductivity λ W/(m· ℃)	Convective coefficient h_c W/(m^2 ℃)	Young's modulus E Pa	Poisson's ratio
Steel	7800	480	1.60	700	$2.0 \cdot 10^{11}$	0.30
Insulation	50	2000	0.02	-	$1.0 \cdot 10^{7}$	0.30

6.2.2 Freezing and Thawing of Ground with a Culvert

The contours of temperature distribution for the soil around the culvert with and without insulation are compared in Figure 6.18 through Figure 6.21 at times t = 45, 150, 220 and 365 days. Deformations are exaggerated by a factor of 3 in all figures that follow.

In the first 45 days, the freezing front propagates to about 0.7 m below the ground surface in the area far from the culvert for both cases. In the area around the culvert, however, the insulation helps delay the freezing temperature from moving in. The freezing front around the culvert with insulation penetrates about half the distance of the one without insulation. At about t = 45 days, the freezing front moving from the ground surface down meets the front moving from the non-insulated culvert up.

At t = 150 days, the ambient temperature is increasing but still below the freezing point. The freezing front below the culvert propagates a distance of 1.8 m and 1.1 m for the non-insulated and insulated cases, respectively. In the ground far from the culvert, the freezing front is about 2.0 m below the ground surface.

At t = 200 days, the ambient temperature is about 7℃ and the ground is thawing. The freezing front below the culvert is about 2.0 m for non-insulated case and 1.5 m for insulated case, respectively. In the ground far from the culvert, the freezing front is about 2.5 m below the ground surface.

After t = 365 days, the ground has completely thawed. The temperature profiles for both of the cases are close to the initial temperature distribution shown in Figure 6.16, which is an expected outcome.

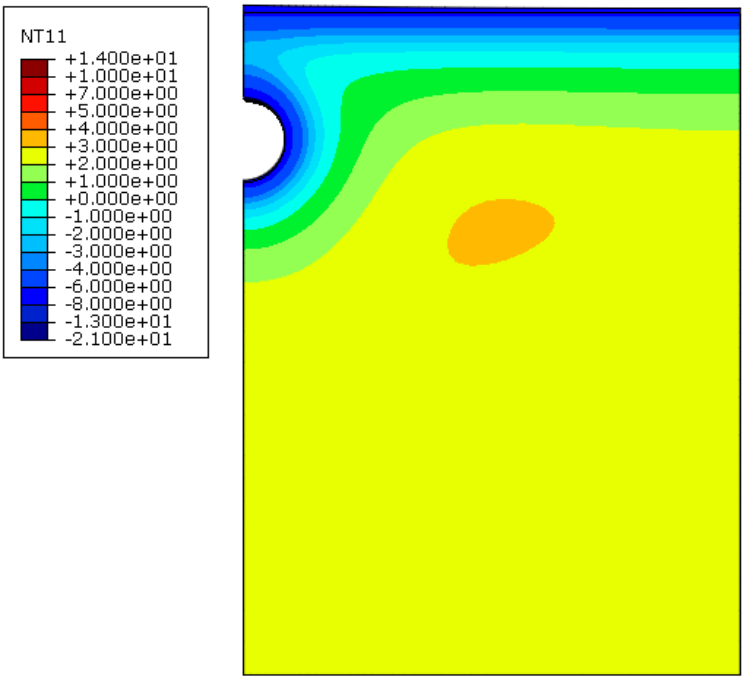

(a) Without insulation

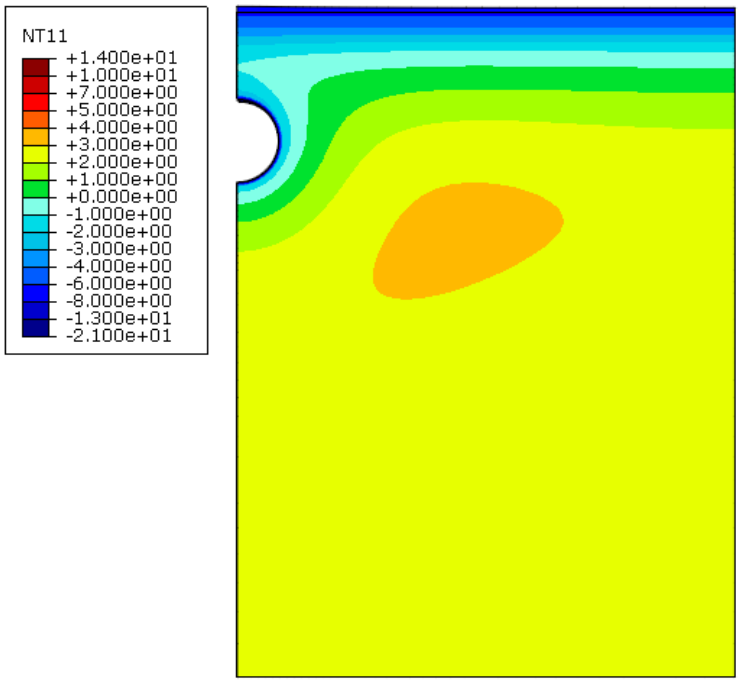

(b) With insulation

Figure 6.18 Temperature distribution (℃) at t = 45 days

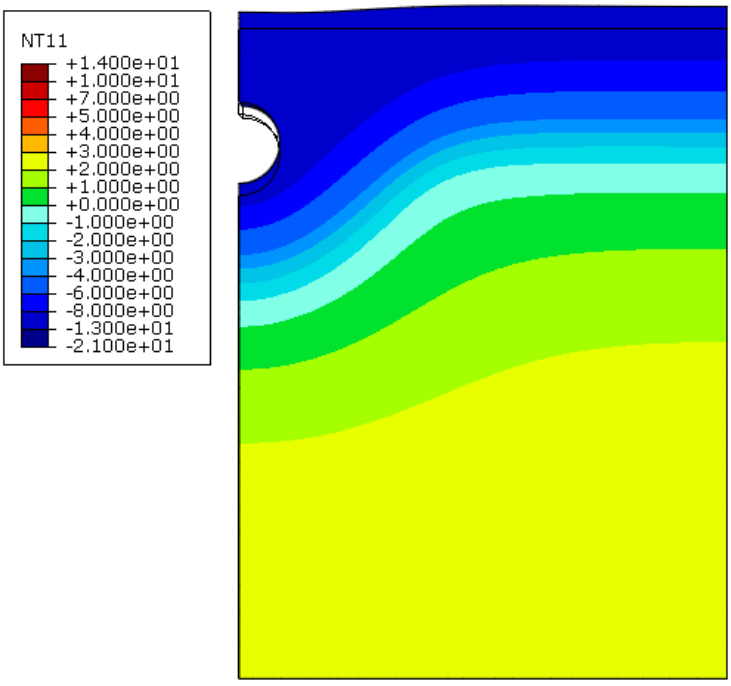

(a) Without insulation

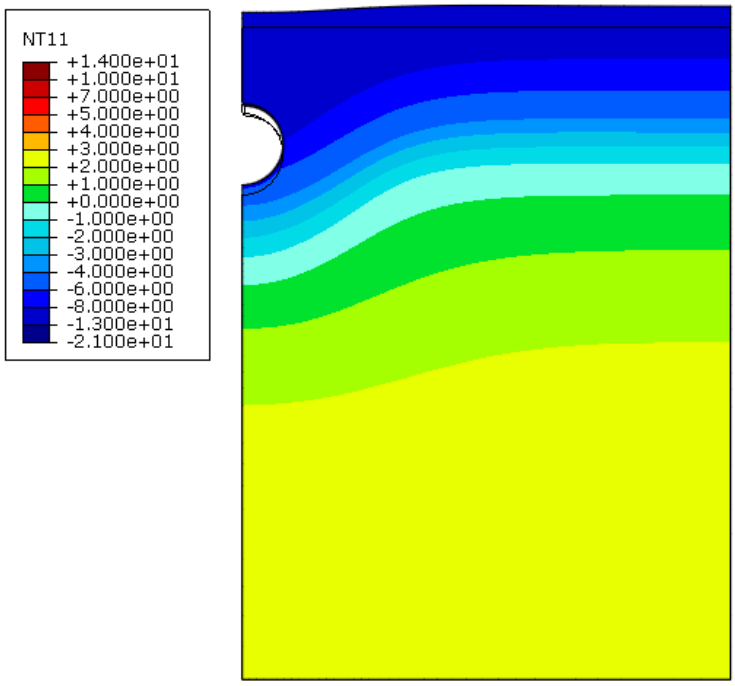

(b) With insulation

Figure 6.19 Temperature distribution (℃) at t = 150 days

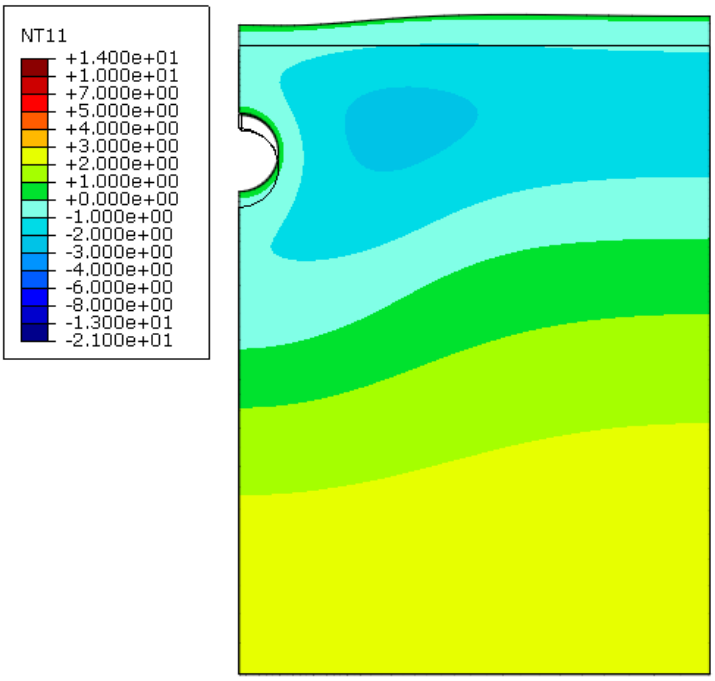

(a) Without insulation

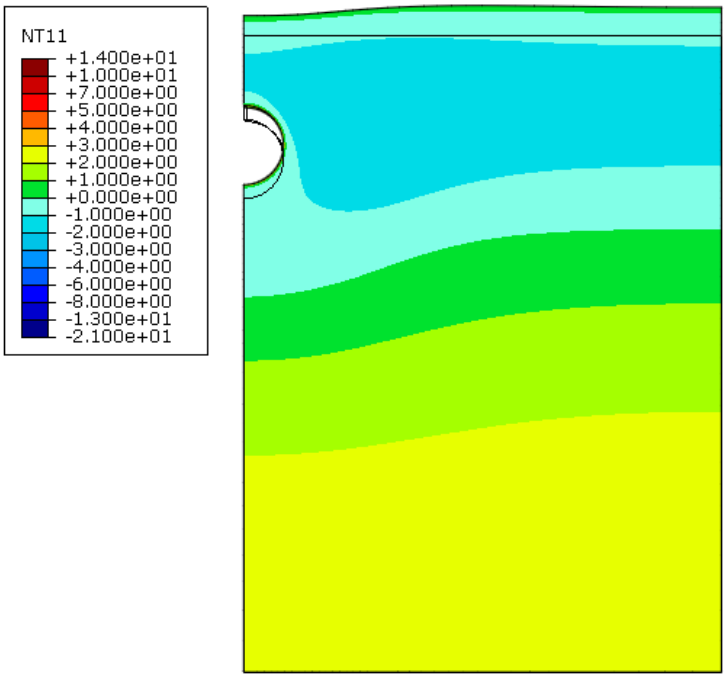

(b) With insulation

Figure 6.20 Temperature distribution (℃) at t = 220 days

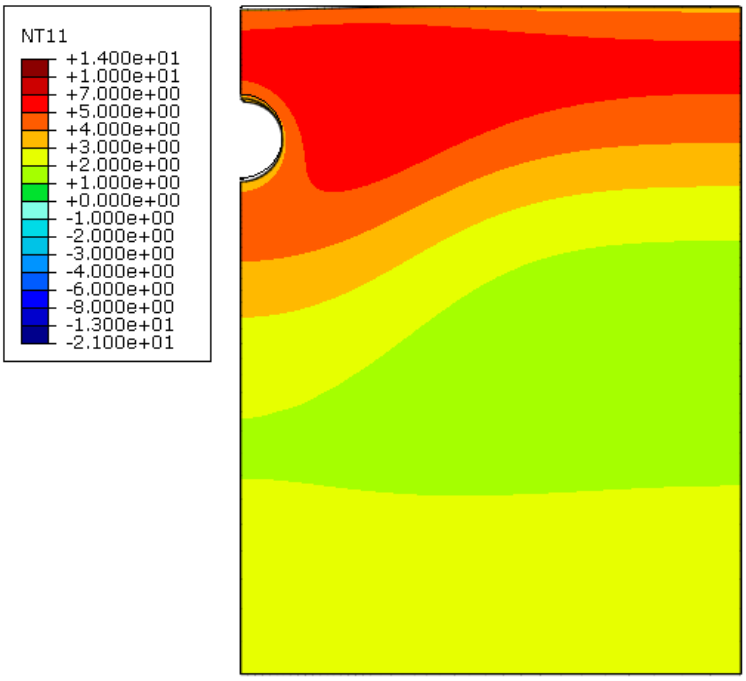

(a) Without insulation

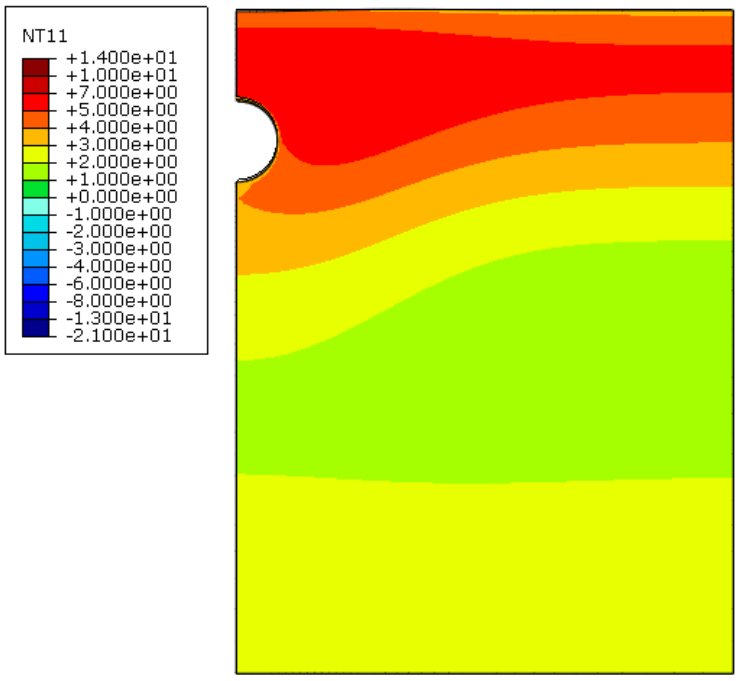

(b) With insulation

Figure 6.21 Temperature distribution (℃) at t = 365 days

The vertical displacement of the ground surface at location A (above the culvert) and B (away from the culvert) in Figure 6.13 are shown in Figure 6.22. The rates of frost heave and thaw settlement at location B are almost constant for both of the insulated and non-insulated cases, with the insulated one slightly lower than the other. The heave at location A is higher than at B from the beginning till about 45 days, and then it becomes opposite. This figure reveals that depending on the stage of the freeze-thaw cycle, the ground surface may have a "bump" or a "dip".

When the air temperature starts to drop below zero in winter, the freezing front propagates into the soil downward from the road surface and upward from the culvert. If the soil happens to be frost-susceptible, the heave process (growth of ice lenses) will occur in the soil beneath the road and in the soil immediately above the culvert. The resulting outcome is a more intensive heave, thus a bump on the road surface develops. If the freezing temperature continues, the bump will grow until all the soil area above the culvert becomes frozen (at about t = 45 days for this case). After that time, the heave of the area above the culvert ceases, but the heave in regions further away from the culvert continues, which may result in a "dip" in the road surface above the culvert. Then in the thawing process, there are two thawing fronts in the soil above the culvert, leading to a higher settling rate at location A. Then the settlement rate at A slows down, but the "dip" at the surface remains.

The usefulness of the insulation can be evaluated from Figure 6.22. At the beginning of the freezing process, it is effective to reduce the "bump" by slowing down the penetration of the freezing front from the culvert. However, it provides no help to reduce the "dip" on the ground surface. The residual differential displacement at the two locations is reduced, though it is primarily dependent on the soil properties and the suction generated in the freezing process.

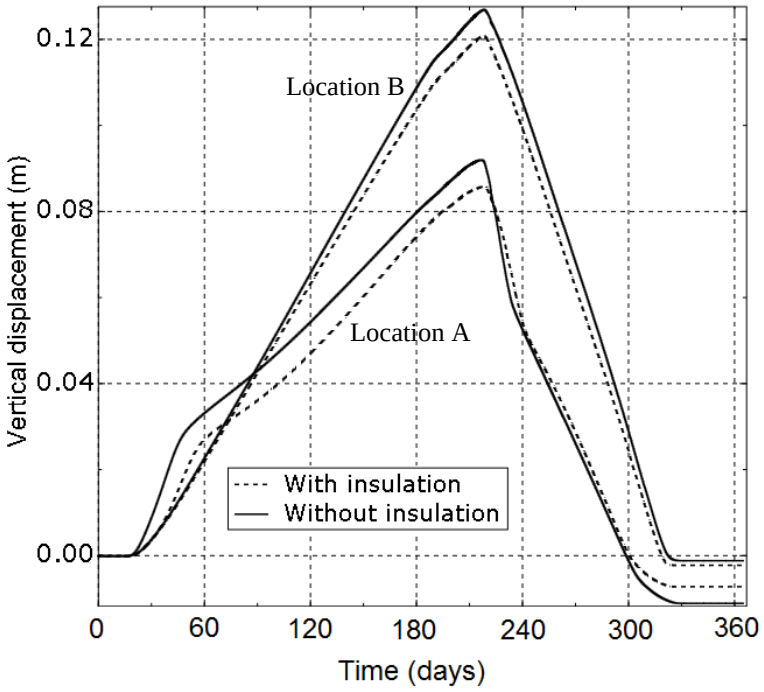

Figure 6.22 Vertical displacement at locations A and B in Figure 6.13

Therefore, the key factor that determines the profile of the surface above the culvert is the boundary condition. If the freezing temperature continues only for a short period, a "bump" will form on the ground surface, whereas if the freezing temperature persists for a long time, a "depression" is likely to occur. While the former is confirmed by observations (Andersland and Ladanyi 2004) the latter is a hypothetical long-term outcome. The contours of the vertical displacements caused by frost action and thaw settlement are shown in Figure 6.23 at times t = 45, 150, 220 and 365 days. The settlement slightly beneath the original ground level is caused by the suction during the freezing phase of the process.

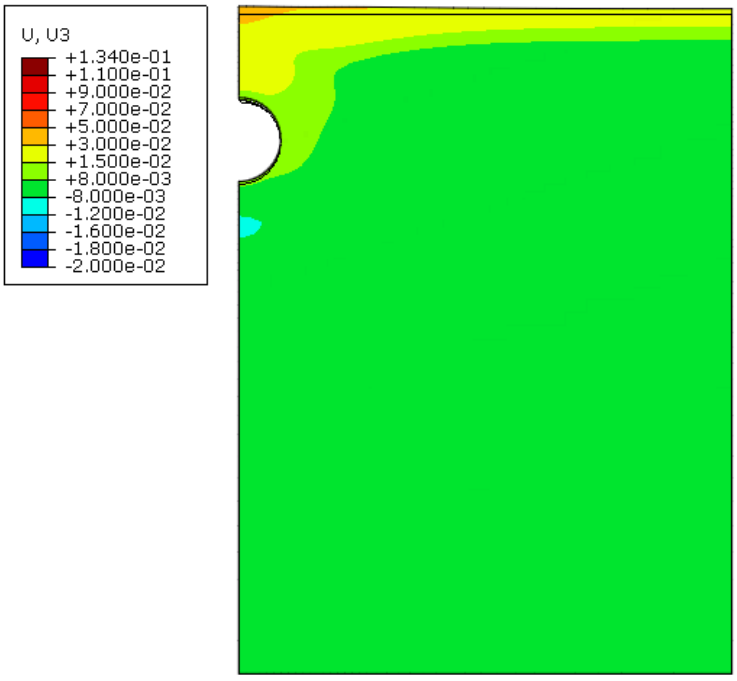

(a) t = 45 days

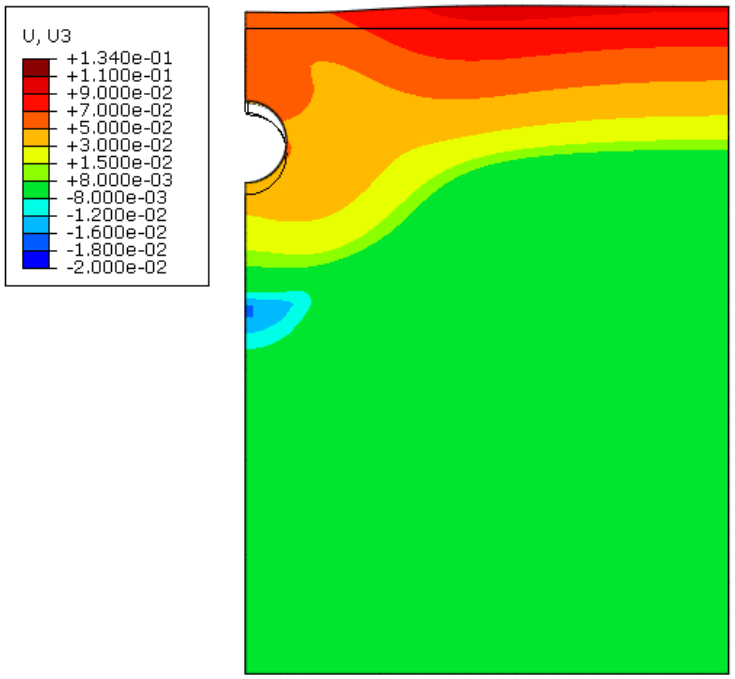

(b) t = 150 days

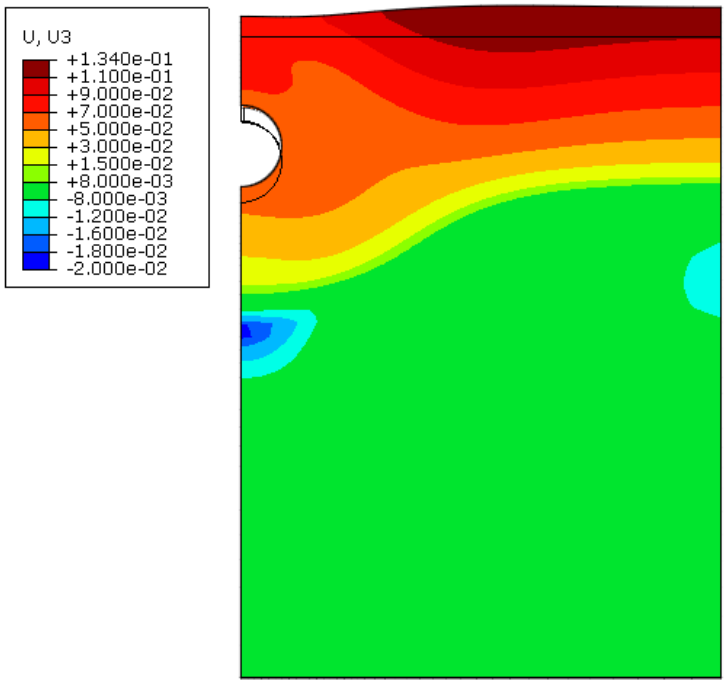

(c) t = 220 days

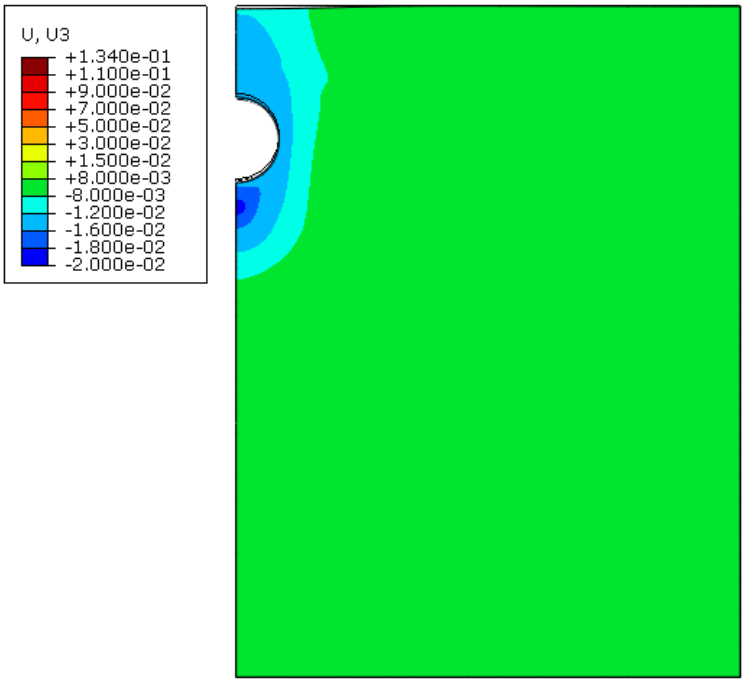

(d) t = 365 days

Figure 6.23 Vertical displacement (in meters): (a) t = 45 days, (b) t = 150 days, (c) t = 220 days, (d) t = 365 days

Figure 6.24 shows the change in excess pore pressure (suction negative) in the freeze-thaw cycle. After t = 45 days, negative pore pressure is induced, indicating water transport into the freezing zone and frost heaving. After 150 days, the negative pore pressure reaches a maximum to the upper right of the culvert. After 220 days, positive pore water pressure occurs indicating the thaw consolidation is taking place. The maximum value is around the culvert due to an intensive thawing and the impermeable pipe. After 365 days, the excess pore pressure is nearly zero, indicating that the consolidation in most of the area is completed.

The contours of porosity distribution are shown in Figure 6.25. These contours show the change in porosity caused both by the ice volume growth and the growth of effective stress (due to suction). The soil in the model was assumed to be uniform, with an initial porosity of 0.427. In the figures showing t = 45, 150 and 220 days, the porosity is increasing in the freezing area repressing the formation of ice lenses. At t = 220 days, the porosity reaches maximum value at the location close to and behind the freezing front. This is because the maximum rate $\dot{n}_m$ occurs at the isothermal line with temperature of -0.82 ℃, and the line stays long before thawing starts. After 365 days, some residual decrease in porosity remains, which is caused by the consolidation due to suction in freezing process.

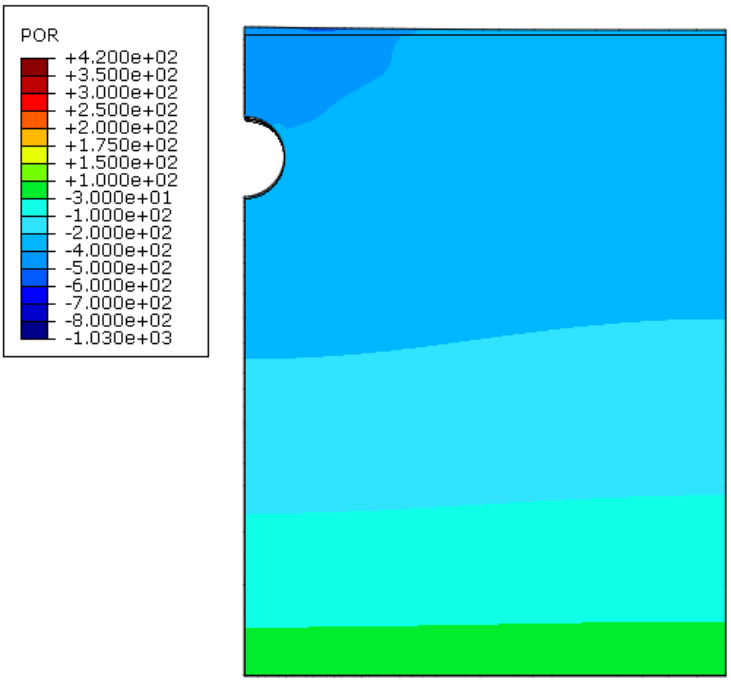

(a) t = 45 days

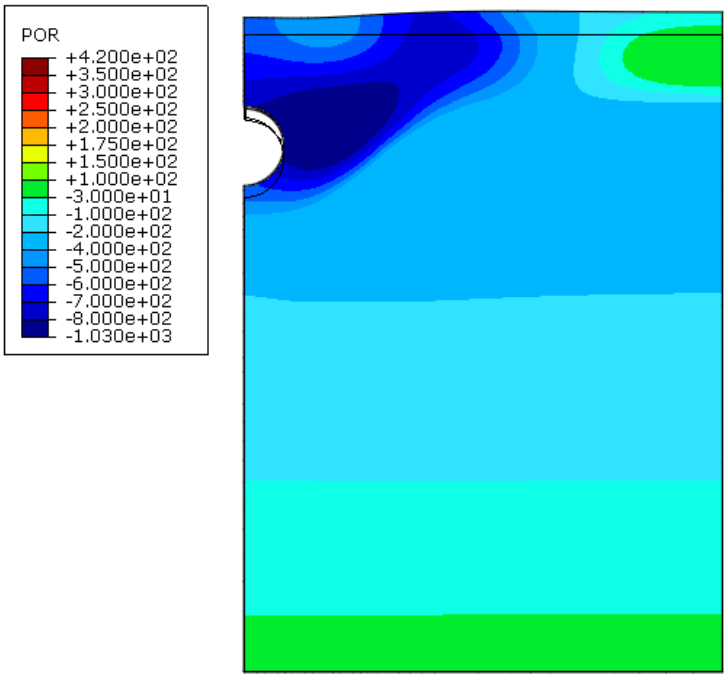

(b) t = 150 days

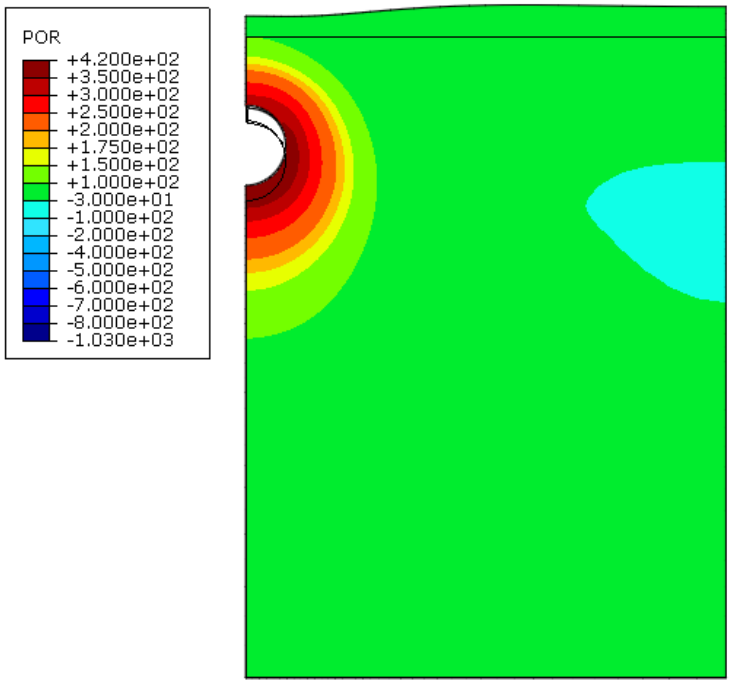

(c) t = 220 days

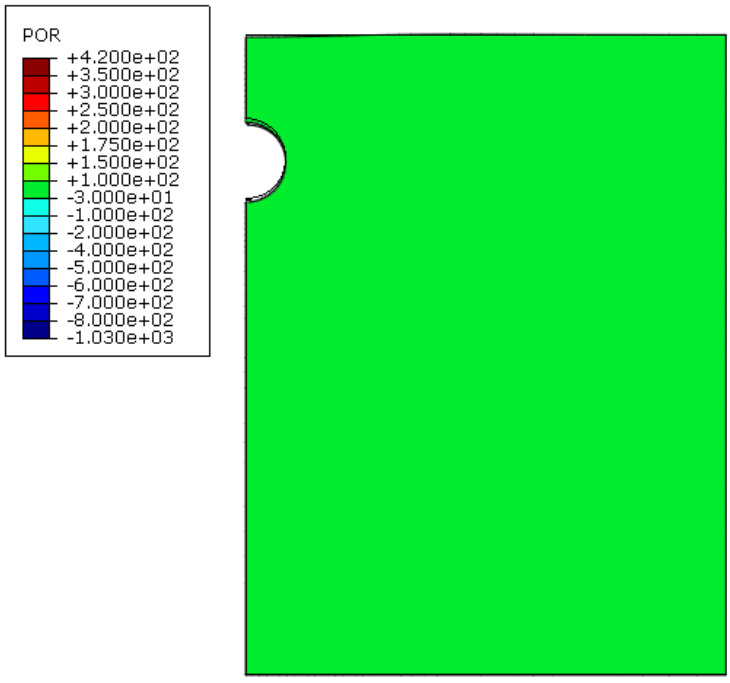

(d) t = 365 days

Figure 6.24 Excess pore pressure distribution (Pa): (a) t = 45 days, (b) t = 150 days, (c) t = 220 days, (d) t = 365 days

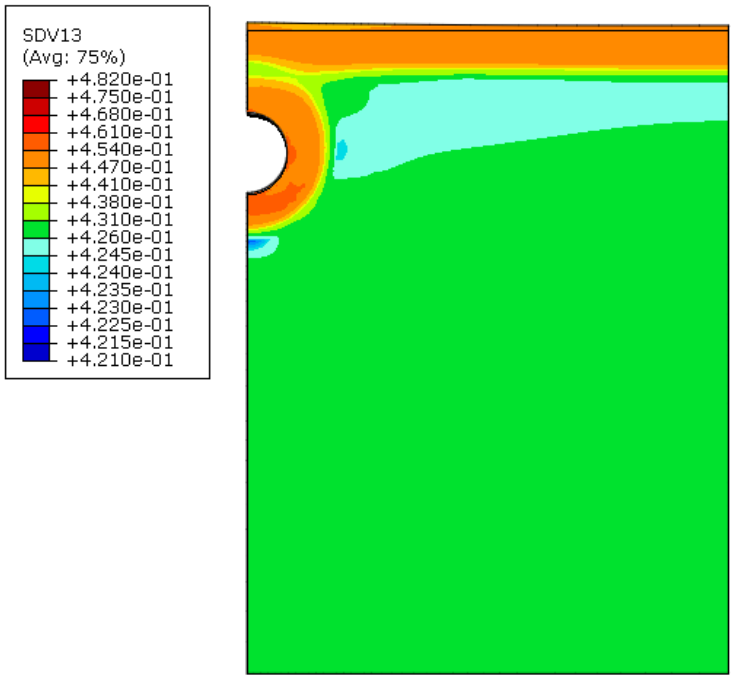

(a) t = 45 days

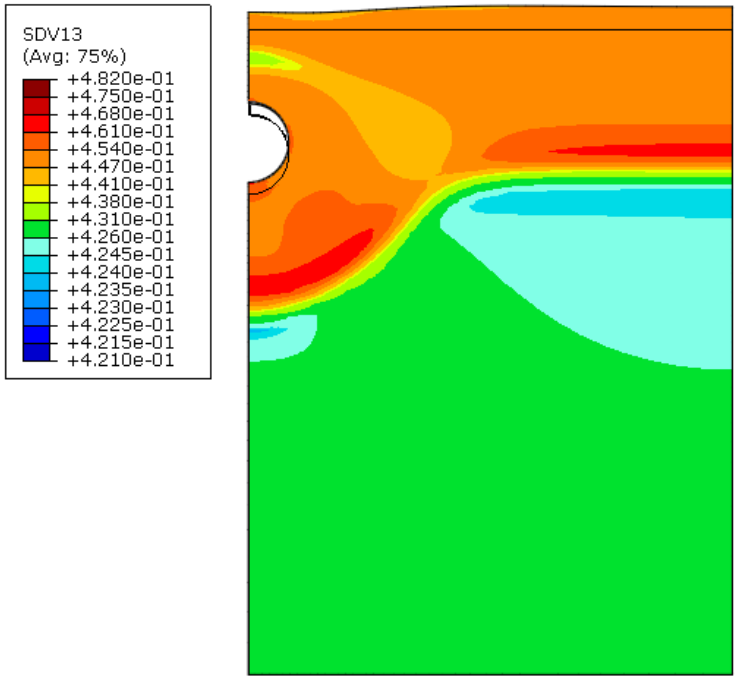

(b) t = 150 days

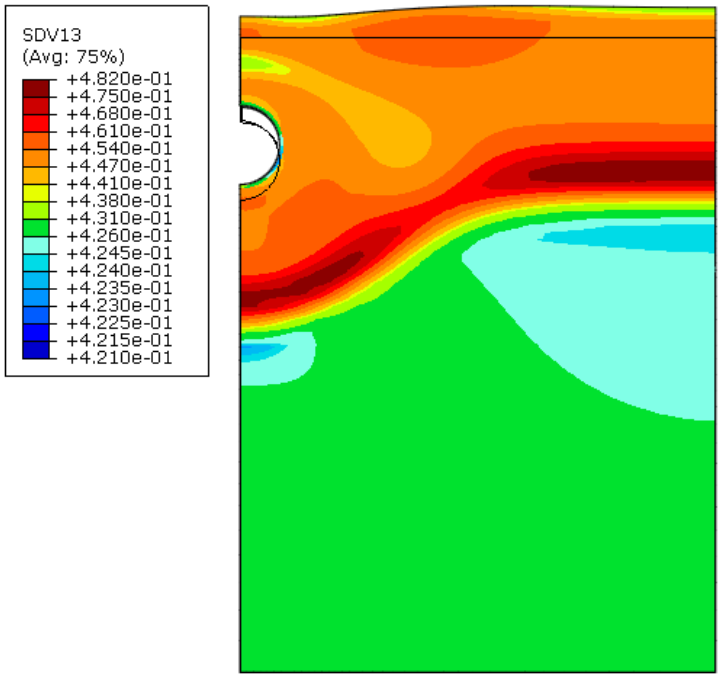

(c) t = 220 days

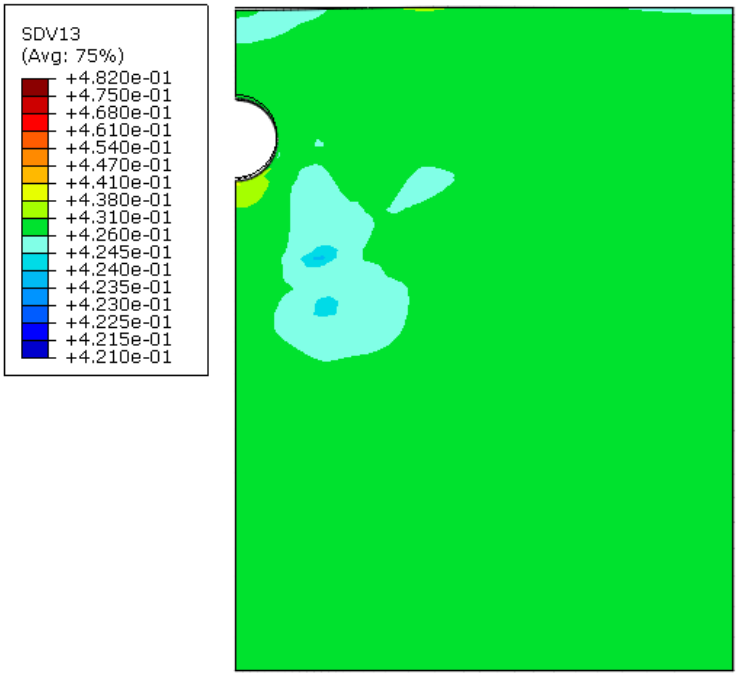

(d) t = 365 days

Figure 6.25 Porosity distribution (a) t = 45 days, (b) t = 150 days, (c) t = 220 days, (d) t = 365 days

6.2.3 Remarks

The freezing and thawing of soils around a culvert has been successfully simulated using the developed model. A differential displacement caused by frost heave and thaw settlement of the ground surface was observed. A “bump” or a “dip” may occur at the surface above the culvert depending on the duration of freezing. If the freezing temperature exists for only a short period, a “bump” will form on the ground surface, whereas if the freezing temperature persists for a long time, a “depression” is likely to occur.

The usefulness of insulation around a culvert in mitigating the differential displacement on the road surface was also evaluated. The simulation results show that insulation is effective at reducing the “bump” by slowing down the penetration of the freezing front from the culvert for shot freezing duration. However, the insulation provides no help in reducing the “dip” on the road surface.

6.3 Frost Heave and Thaw Settlement behind a Retaining Wall

Retaining walls built in cold regions are vulnerable to frost damage. This is because ice lenses will form behind the wall, and the wall will have a tendency to tilt due to frost heave.

Limited field testing was carried out in the past on retaining walls subjected to freezing and thawing in order to find the frost pressures against the walls as well as the resulting horizontal movements. However, less effort has been made to perform model based simulations to predict the potential frost damage to retaining structures. The THM model developed in this study will be used as a tool to simulate a retaining wall under frost action of soils behind and below the wall. The effectiveness of insulation behind the wall in reducing the horizontal movement is also investigated.

6.3.1 Problem Description

The geometry of the retaining wall and the surrounding soil profile are shown in Figure 6.26. The total height of the wall is 6.5 m, and the footing is 0.7 m. The ground surface in front of the wall is 1.5 m above the bottom of the footing. The thickness of the wall increases from 0.3 m at the top to 0.7 m at the bottom. The width of the footing is 4.0 m and the minimum thickness of the footing is 0.5 m. The retaining wall and the footing are made of concrete. A 0.1 m thick thermal insulation layer is used behind the wall. The total width of the model is 15.0 m and the total height is 12.0 m.

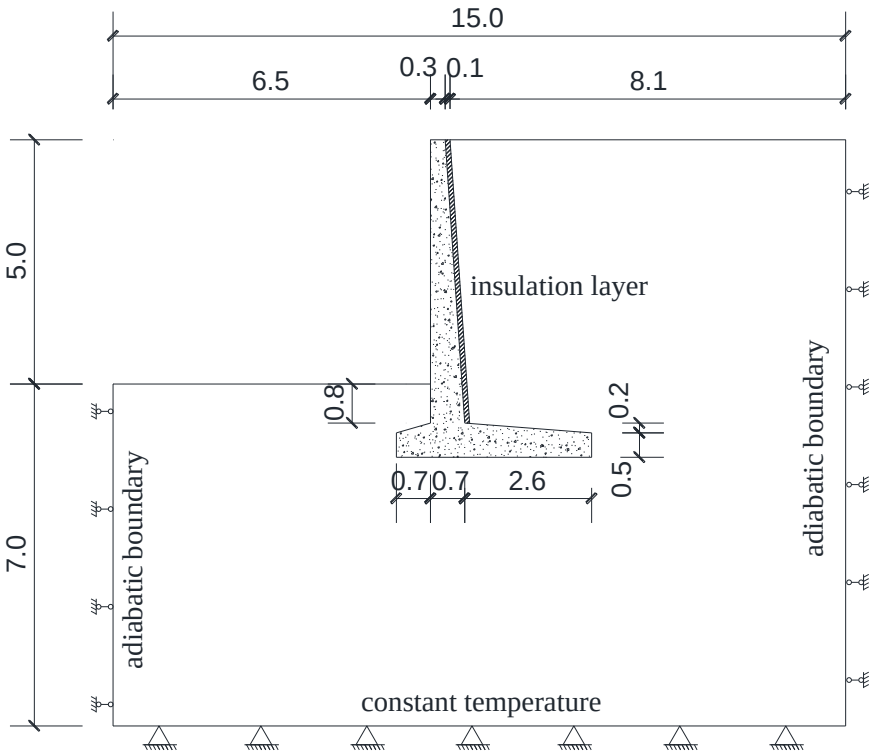

Figure 6.26 Geometry of retaining wall (in meters)

As for the boundary conditions, the vertical sides are not allowed to move sideways, the bottom is fixed in both horizontal and vertical directions. Heat is not allowed to flow across the two vertical boundaries. The other boundary temperatures used in the simulation are: the temperature at the bottom is set to be constant at 3°C; the ambient temperature at the top and on the wall surface is the simplified linear temperature according to the data measured in Aniak, AK (shown in Figure 6.14). The Fourier boundary condition in Equation (6.1) is used for both the ground surface and retaining wall surface that is exposed to the air. The hydraulic boundary condition for the vertical boundaries is impermeable. The bottom boundary is set to be able to drain and intake water, with a hydraulic conductivity to be $1.0 \cdot 10^{-7}$ m/s, whereas the ground

surface allows only drainage, but not intake of water. The simulation results at the moments marked in Figure 6.27 will be shown next.

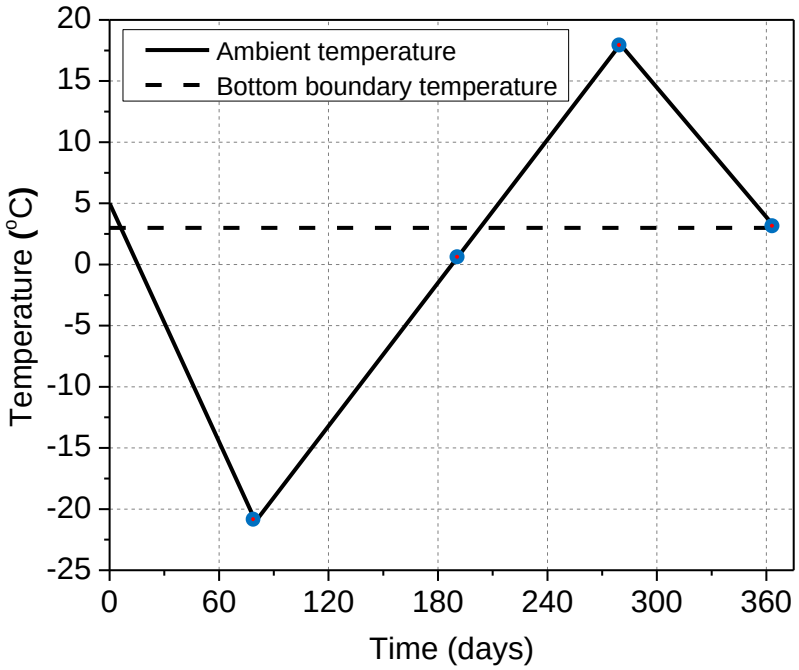

Figure 6.27 Thermal boundary conditions

The finite element mesh is shown in Figure 6.28. The model is discretized using 8-node solid elements, with one element layer in the direction perpendicular to the plane of deformation. The 8-node trilinear displacement and temperature elements (type C3D8T in ABAQUS) are used for the culverts and the insulation layer, whereas 8-node trilinear displacement, pore pressure, and temperature elements (type C3D8PT in ABAQUS) are used for the surrounding soil. The total number of elements is 999 and the total number of nodes is 2170.

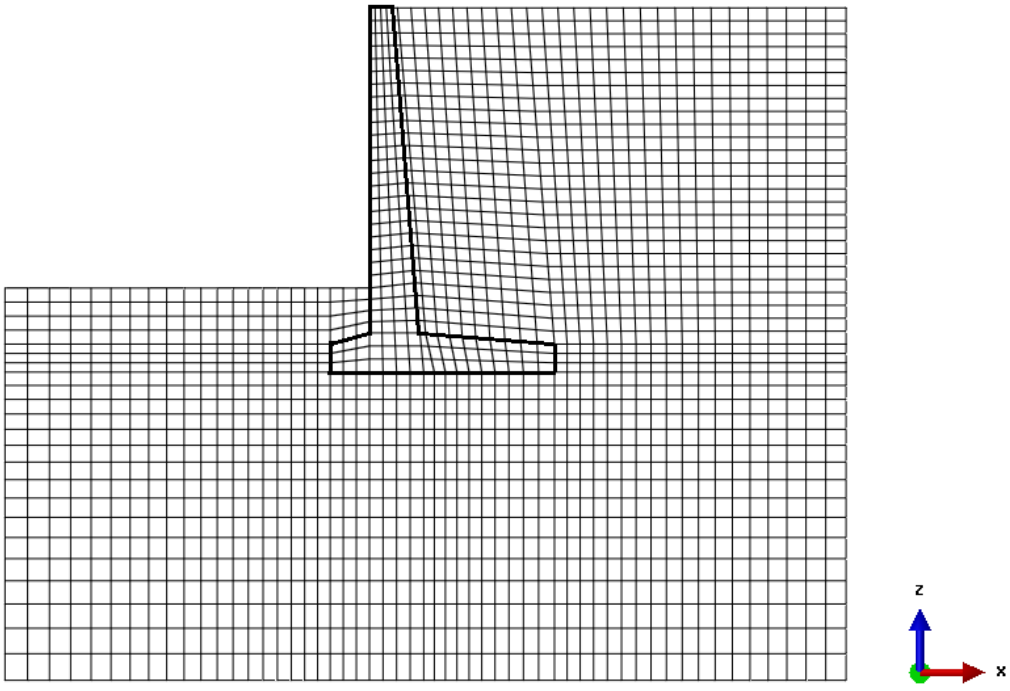

Figure 6.28 Finite element mesh

The initial temperature distribution is shown in Figure 6.29, which is a steady-state distribution associated with the constant temperatures at boundaries: top 5 ℃, bottom 3 ℃.

The initial stress state of the soil affects both elastic-plastic constitutive relationship and the porosity rate function. Therefore, before starting the simulation of the thermal problem, the steady-state geo-static stress distribution under self-weight was calculated. The stress state at each nodal point was calculated by ABAQUS and stored. The file was then read into ABAQUS again to prescribe the initial stress field for the simulations. Figure 6.30 shows the initial geo-static vertical stress in the soil. The initial deviatoric stress in the retaining wall is shown in Figure 6.31.

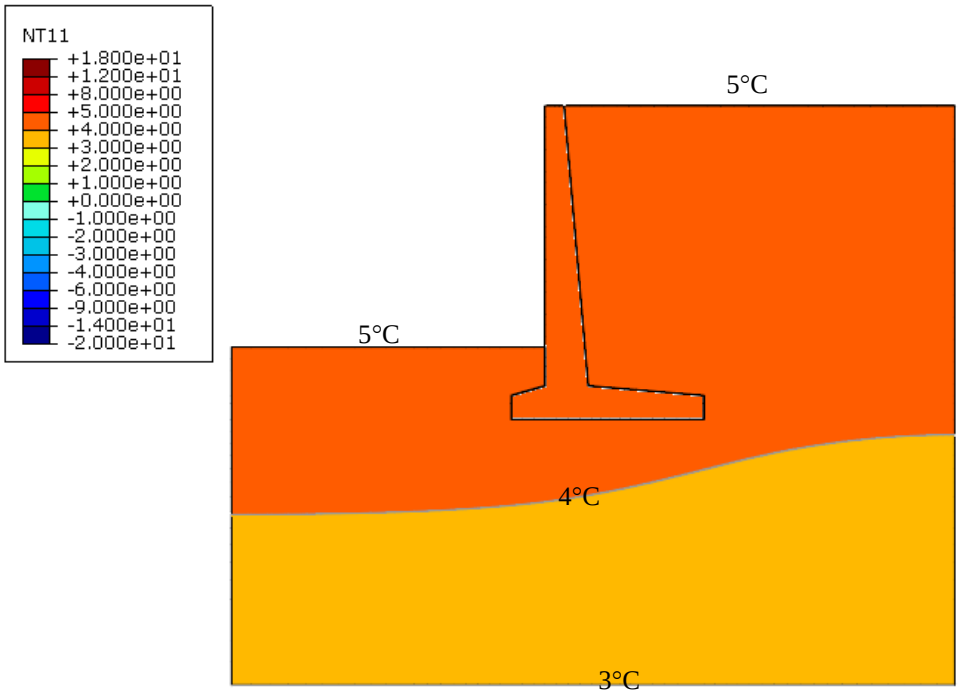

Figure 6.29 Steady-state temperature distribution (℃) at $t = 0$

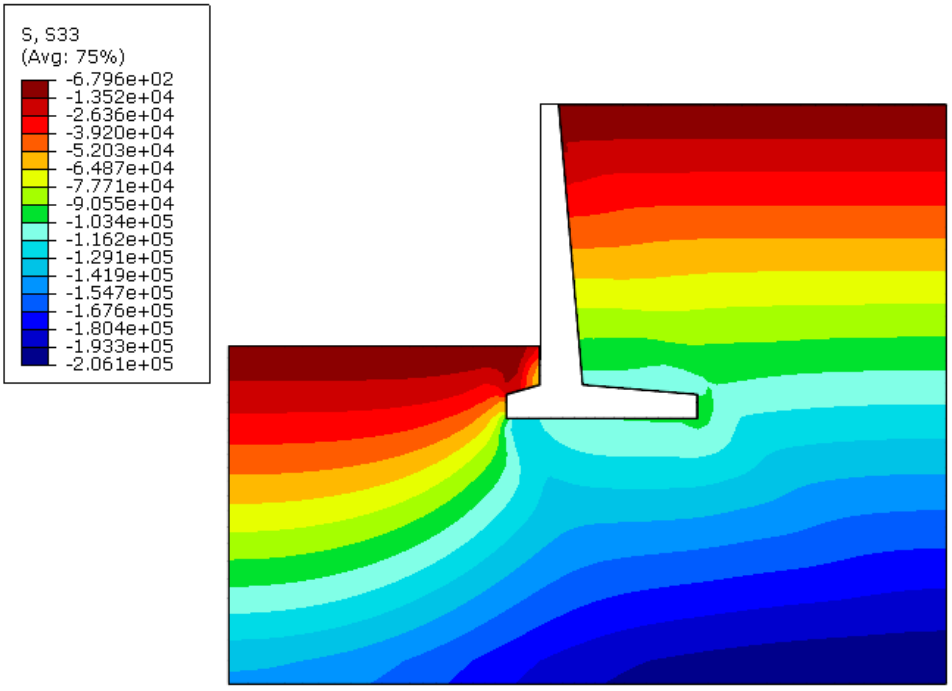

Figure 6.30 Distribution of geo-static vertical stress (Pa) in soil at $t = 0$

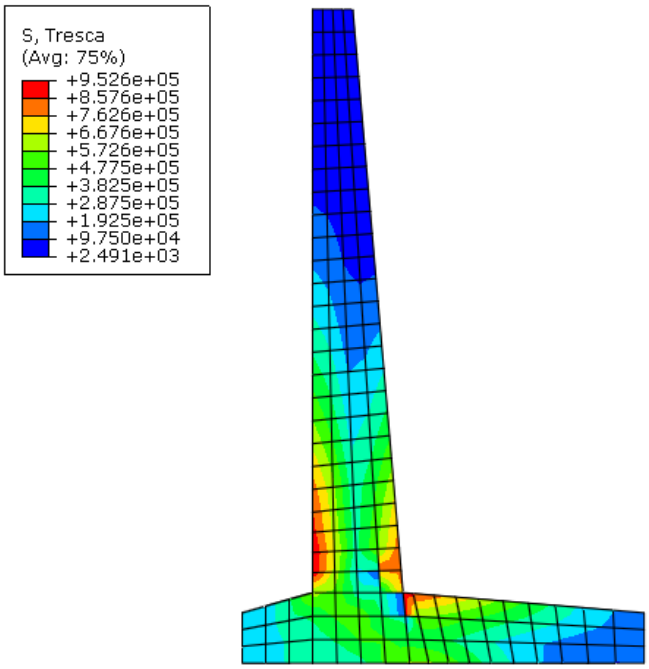

Figure 6.31 Deviatoric stress distribution (Pa) in retaining wall at $t = 0$

The parameters of the soil used in the simulation are listed in the following: (1) unfrozen water content: $w^* = 0.058$, $w_0 = 0.285$, $T_0 = 0$ ℃, and $a = 0.16$ °C^{-1}; (2) elastic-plastic constitutive model: $\lambda = 0.35$, $\kappa = 0.07$, $p_0 = 80$ kPa, $M = 0.8$, $\alpha_1 = 0.2$, $\alpha_2 = 0.4$, $\alpha_3 = 0.6$, $p^r = 10$ kPa, $\beta = 0.18$, $p_t = -1.0$ MPa; (3) porosity rate function: $\dot{n}_m = 5.94 \cdot 10^{-7}$ s^{-1} (less frost susceptible soil, 3% of calibrated value from Fukuda's tests), $T_m = -0.82$ ℃, $g_T = 100$ ℃/*m*, and $\zeta = 0.73$ MPa. The hydraulic conductivity for soils was taken as $1.0 \cdot 10^{-7}$ m/s for unfrozen soil and $1.0 \cdot 10^{-12}$ m/s for frozen soil with temperature below -5 ℃; linear interpolation was used for temperatures between 0 ℃ and -5 ℃; the initial void ratio is 0.747. A 0.1 m thick layer of insulation was simulated behind the retaining wall. The material properties of concrete retaining wall and the insulation layer are shown in Table 6.2.

Table 6.2. Material properties of retaining wall and insulation

	Density ρ kg/m^3	Mass heat capacity c J/(kg· ℃)	Thermal Conductivity λ W/m· ℃	Convective coefficient h_c W/(m^2 ℃)	Young's modulus E Pa	Poisson's ratio
Concrete	2240	970	1.60	90	$2.0 \cdot 10^{10}$	0.25
Insulation	50	2000	0.03	-	$1.0 \cdot 10^{7}$	0.30

6.3.2 Freezing and Thawing of Soil Retaining System

The contours of temperature distribution for the soil in front and behind the retaining wall with and without insulation are compared in Figure 6.32 through Figure 6.35 at times t = 80, 195, 280 and 365 days. Deformations are exaggerated by a factor of 3 in all the figures that follow.

In the first 80 days, the air temperature drops to its lowest value and the freezing front propagates to about 1.0 m below the surface in the open ground. The freezing front also penetrates into the soil from the wall side, with the isotherms parallel to the wall surface. For the case without insulation layer, this freezing front propagates to about 0.7 m into the backfill, whereas for the insulated wall, the freezing front moves just past the insulation layer.

At t = 195 days, the ambient temperature is increasing and reaches about the freezing point of water. The freezing front propagates further to about 2.0 m below the surface in the open ground. Behind the wall, the freezing front moves into the soil about half of the distance for the insulated system compared to the non-insulated wall. From the displacements shown in Figure 6.33, it is clear that the retaining wall with insulation tilted less than the one without insulation. The heave in the open ground is about the same for the two cases.

At t = 280 days, the ambient temperature reaches its highest value. However, for both of the cases with and without insulation, there is a small portion of still frozen soil behind the wall. The tilted non-insulated wall recovers to some extent compared to its position before thawing. The insulation layer under such circumstances plays a role in delaying the increase in temperature in the backfill. After t = 365 days, the ground has completely thawed.

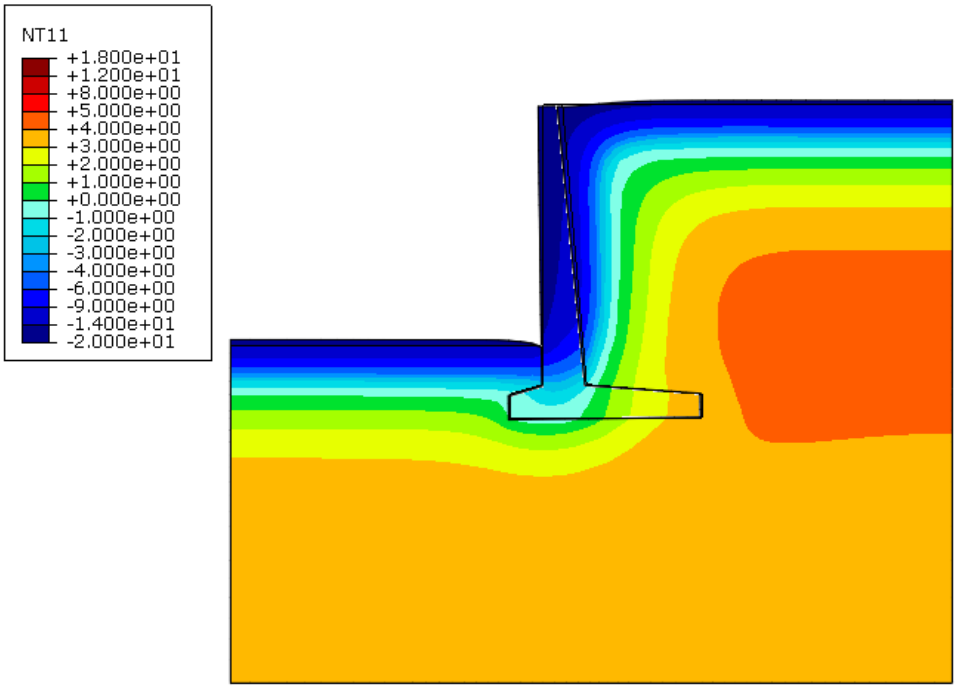

(a) Without insulation

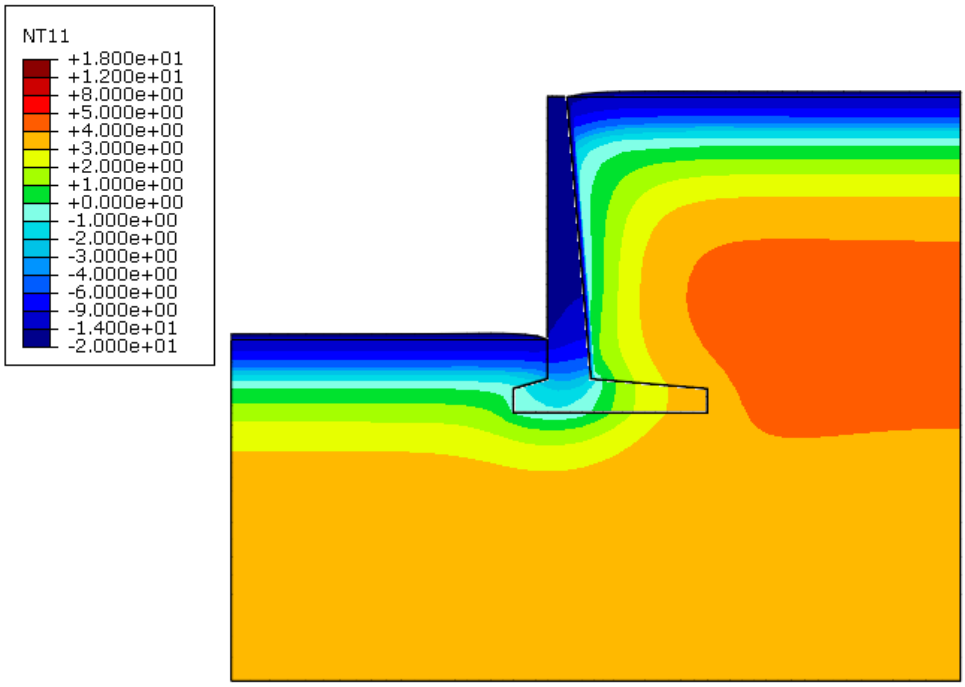

(b) With insulation

Figure 6.32 Temperature distribution (℃) at t = 80 days

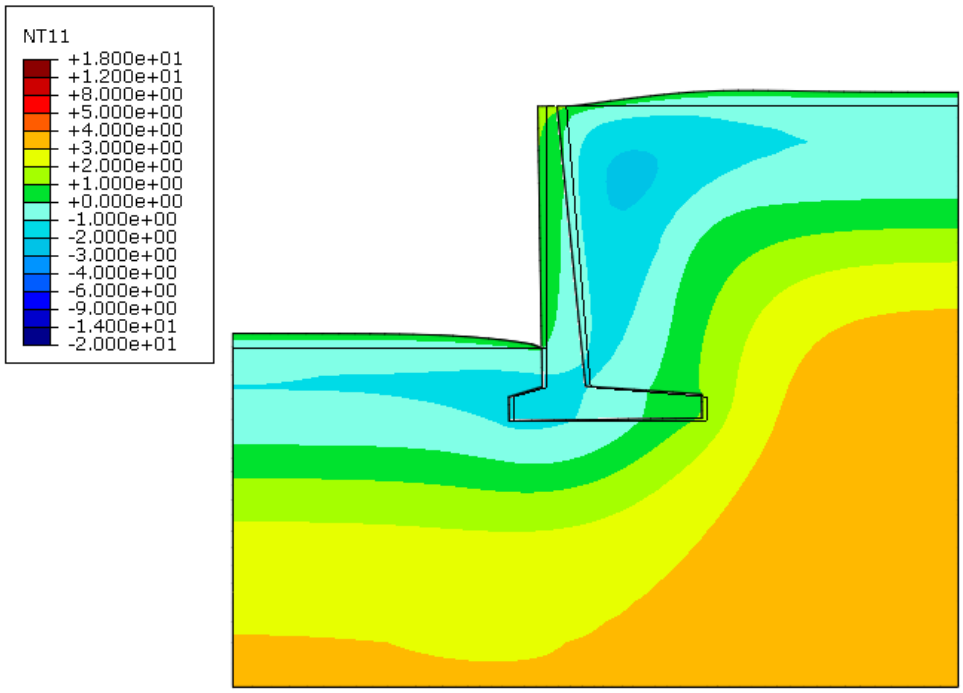

(a) Without insulation

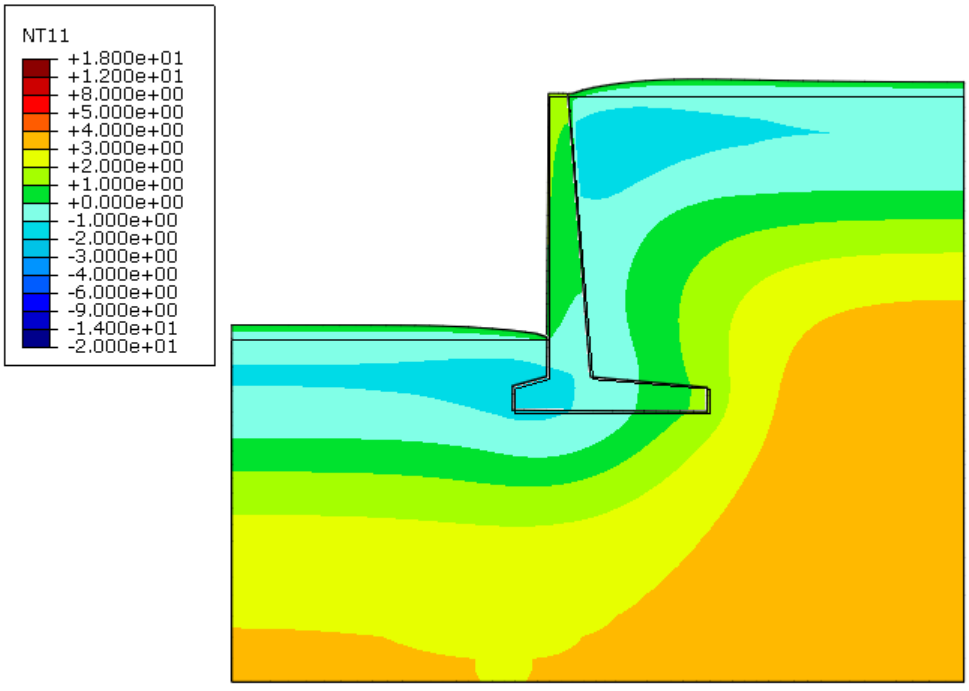

(b) With insulation

Figure 6.33 Temperature distribution (℃) at t = 195 days

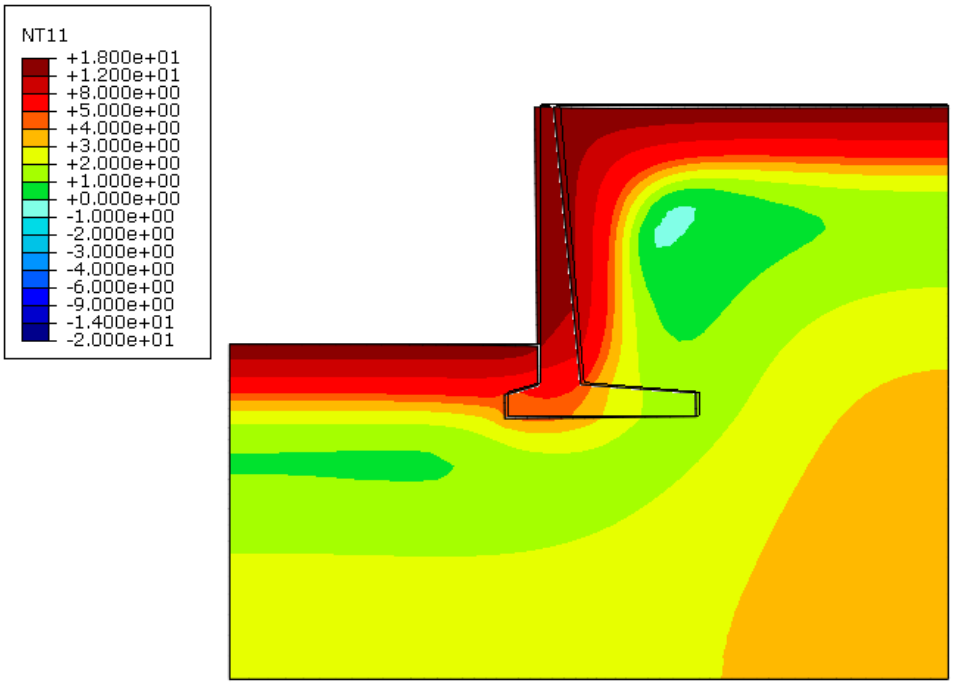

(a) Without insulation

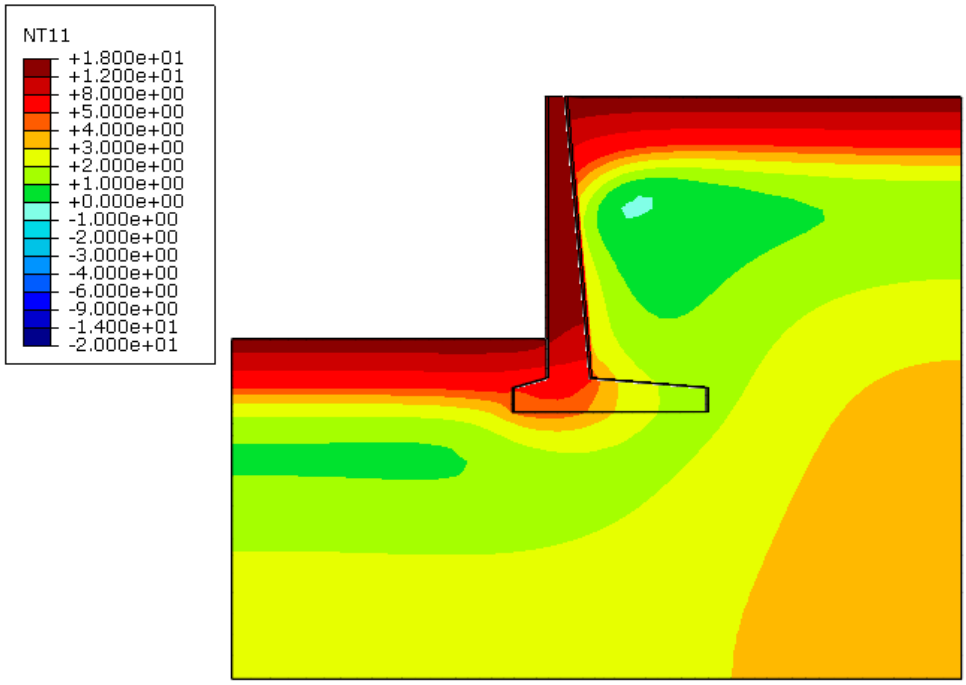

(b) With insulation

Figure 6.34 Temperature distribution (℃) at t = 280 days

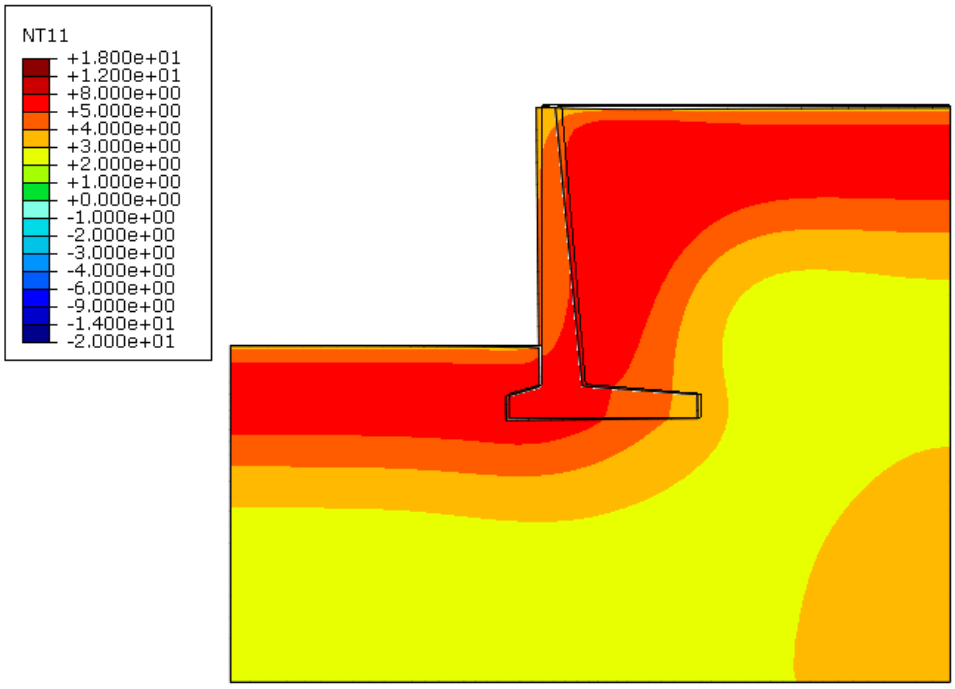

(a) Without insulation

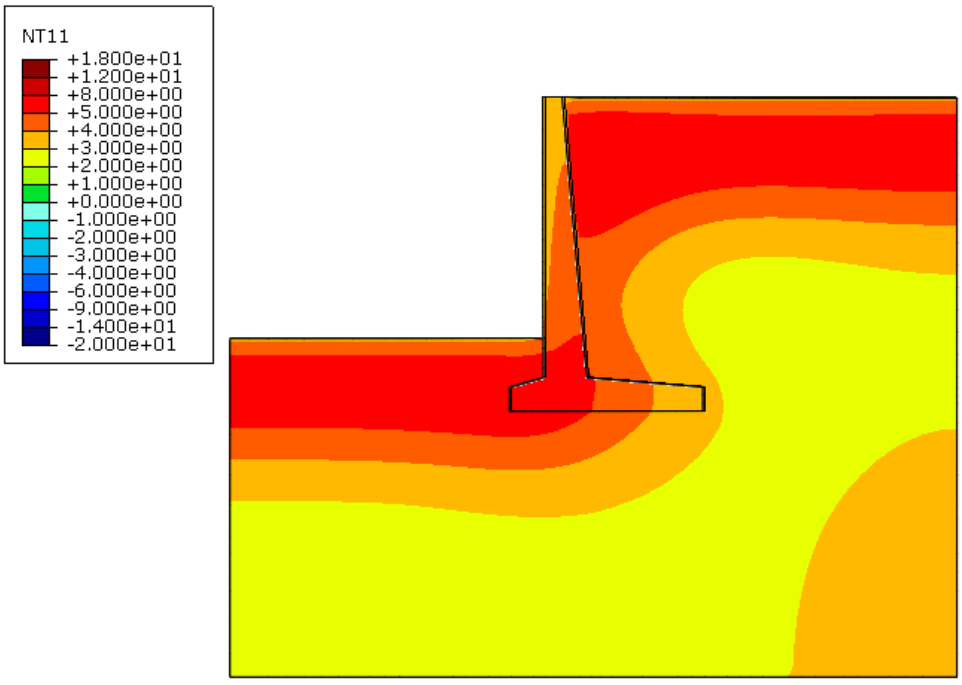

(b) With insulation

Figure 6.35 Temperature distribution (℃) at t = 365 days

The contours of excess pore pressure distribution (suction negative) in the freezing and thawing process for the non-insulated system are shown in Figure 6.36. After $t = 80$ days, negative pore pressure is generated and the maximum value occurs near the top and behind the wall. After 195 days, the negative pore pressure drops to lower magnitude behind the wall, indicating a lower rate of ice lenses growth. The soil in front of the wall starts thawing and positive pore pressure is generated. At $t = 280$ days, only a small portion of the soil behind the wall is still frozen. A high positive pore water pressure indicates rapid thawing and consolidation. After 365 days, the excess pore pressure is zero (Fig. 6.36d), indicating that the consolidation is completed.

The vertical displacements for the non-insulated system are shown in Figure 6.37. At $t = 80$ and $t = 195$ days, the heave is clearly visible and the wall is tilting. The soil beneath the toe of the wall is compressed by the wall. After $t = 365$ days, the soil is completely thawed.

The horizontal displacements for the non-insulated system are shown in Figure 6.38. At $t = 195$ days the horizontal heaving of the soil pushes the wall leftward and compresses the soil to the right. Residual leftward displacement of the wall occurs after the freeze-thaw cycle.

The contours of porosity distribution are shown in Figure 6.39. The figure for $t = 45$ days shows that the porosity growth occurs beneath the toe of the wall. At $t = 365$ days, the porosity behind wall is not significantly reduced.

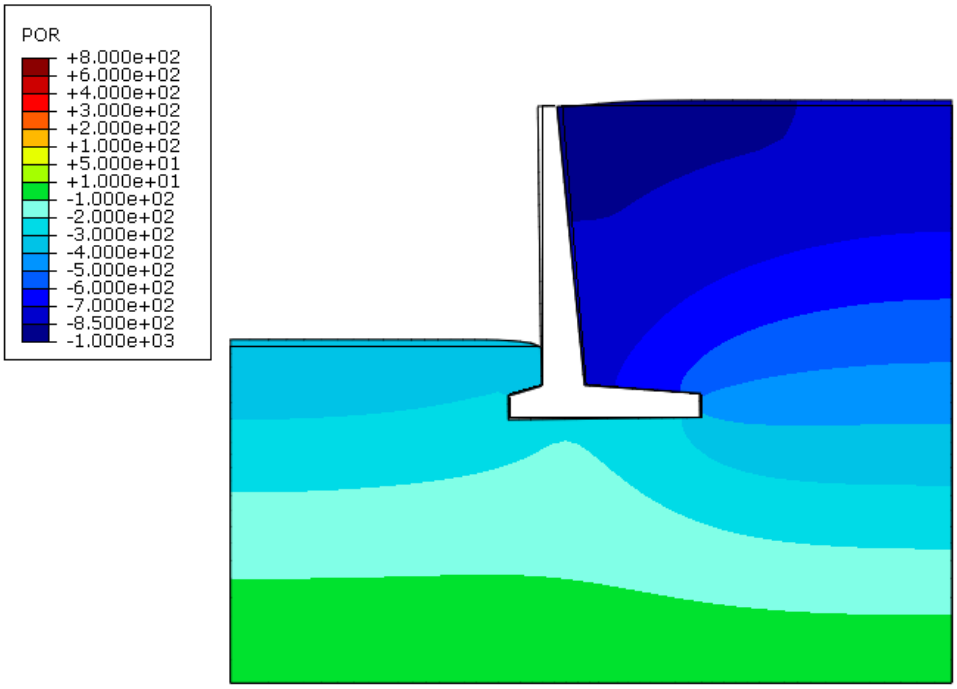

(a) t = 80 days

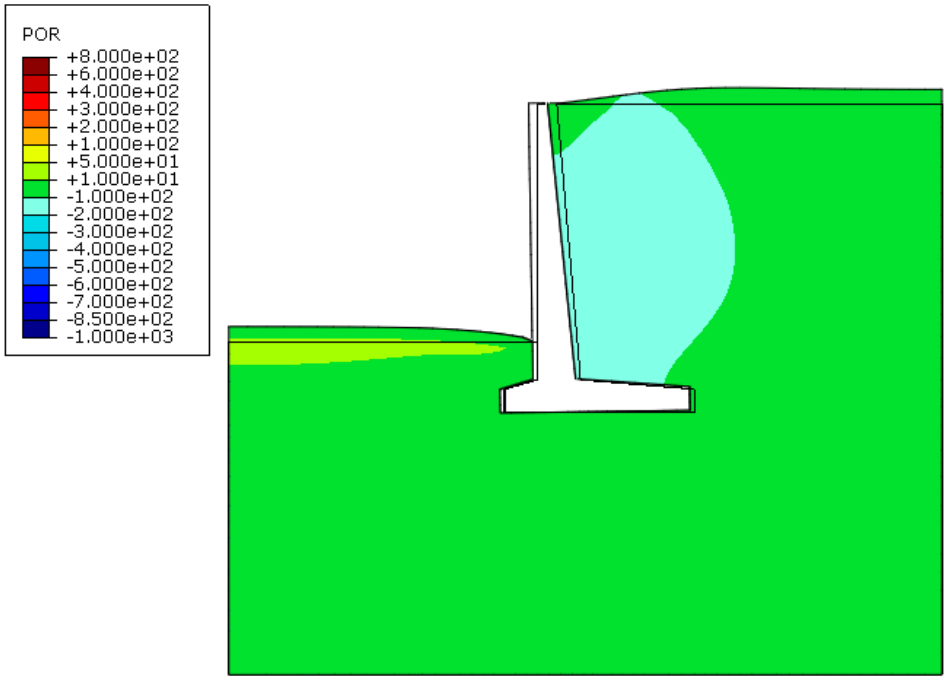

(b) t = 195 days

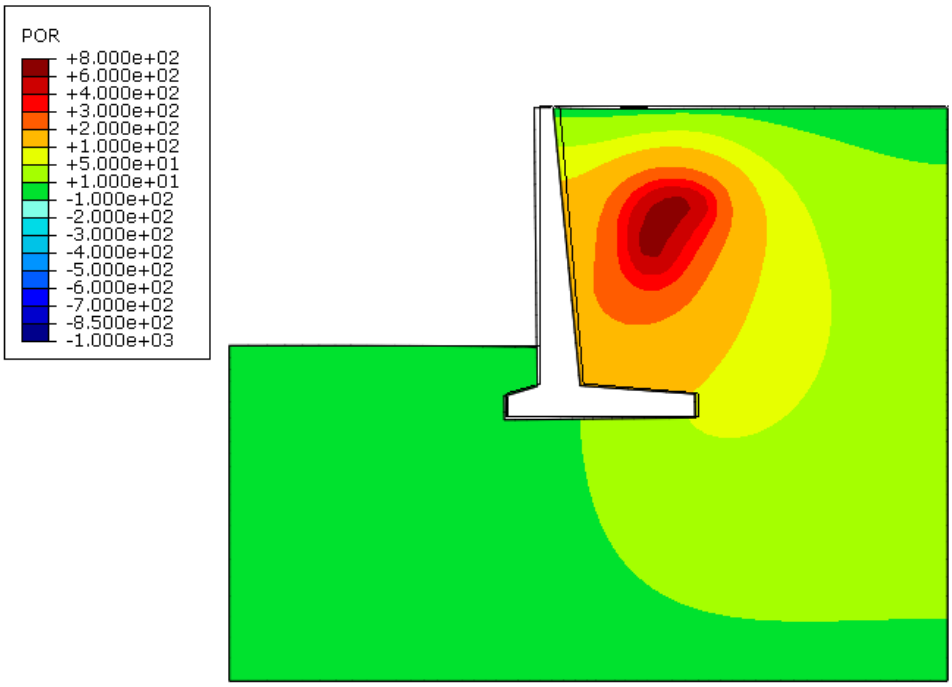

(c) t = 280 days

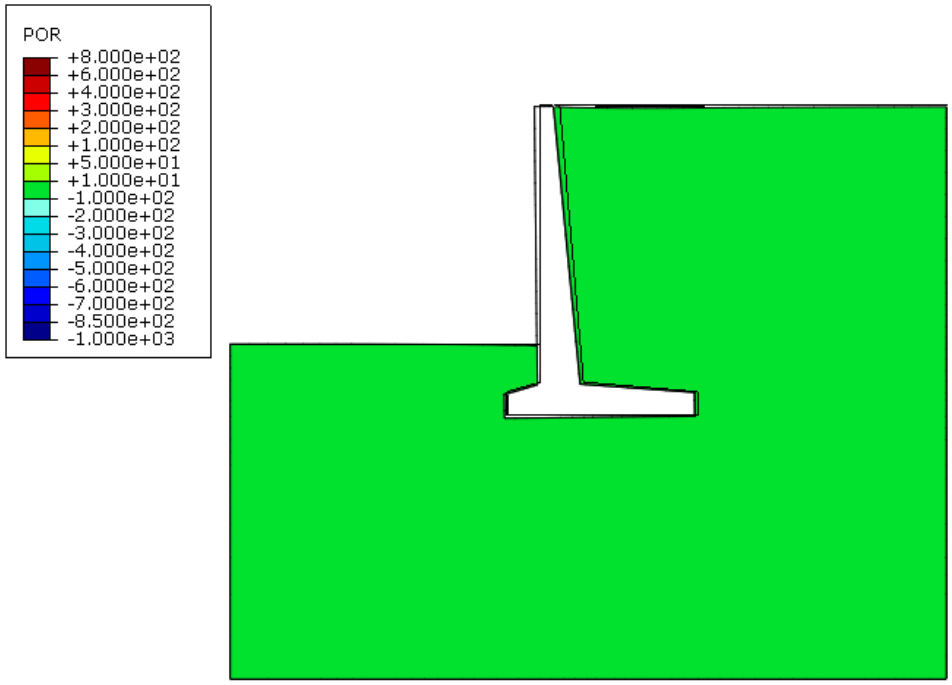

(d) t = 365 days

Figure 6.36 Excess pore pressure distribution (Pa): (a) t = 80 days, (b) t = 195 days, (c) t = 280 days, (d) t = 365 days

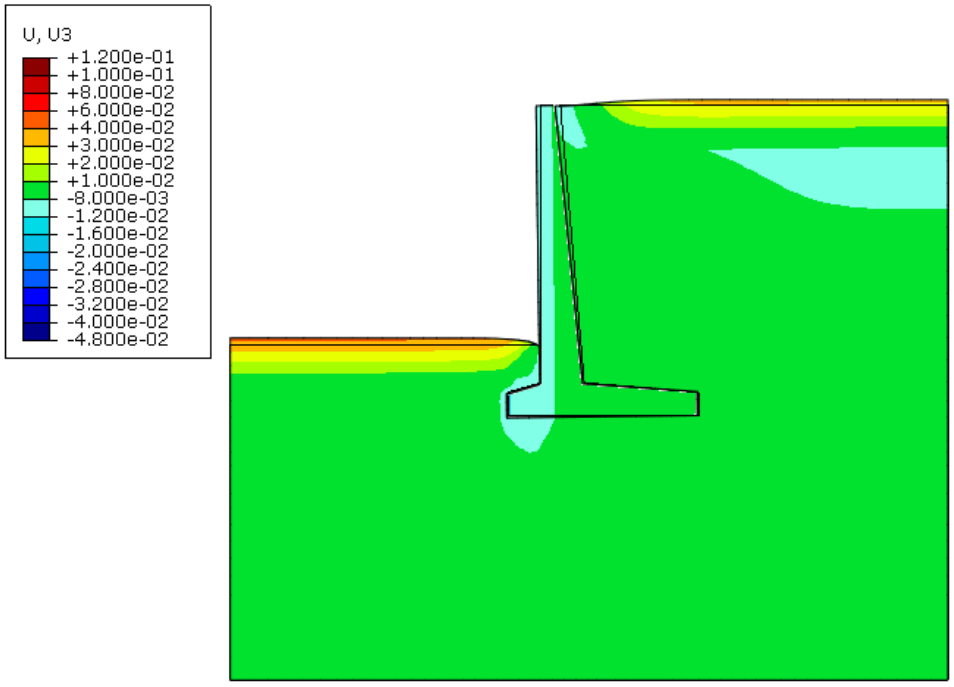

(a) t = 80 days

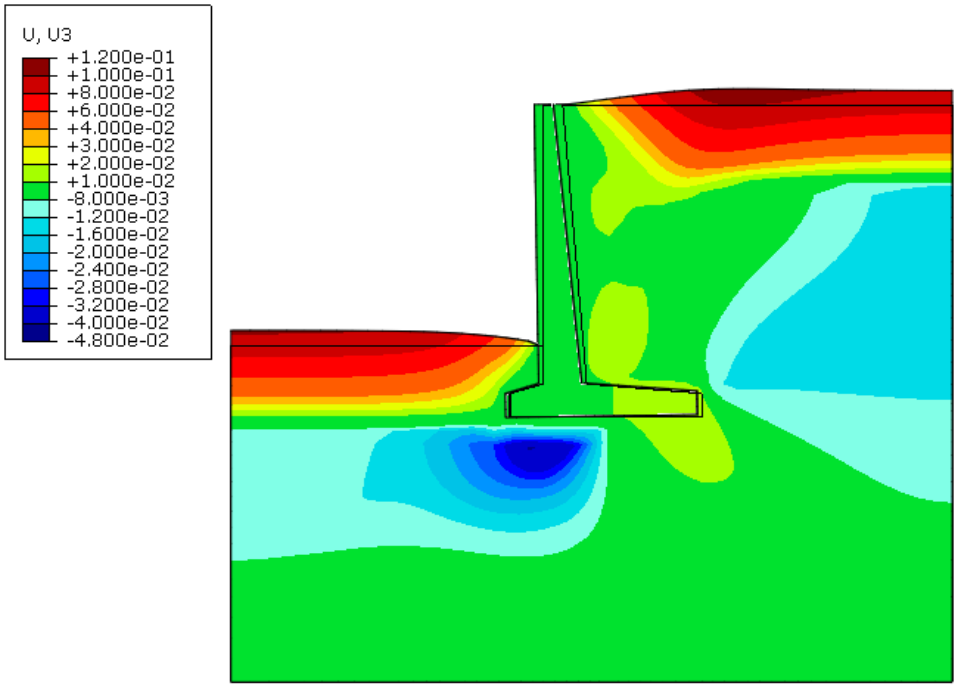

(b) t = 195 days

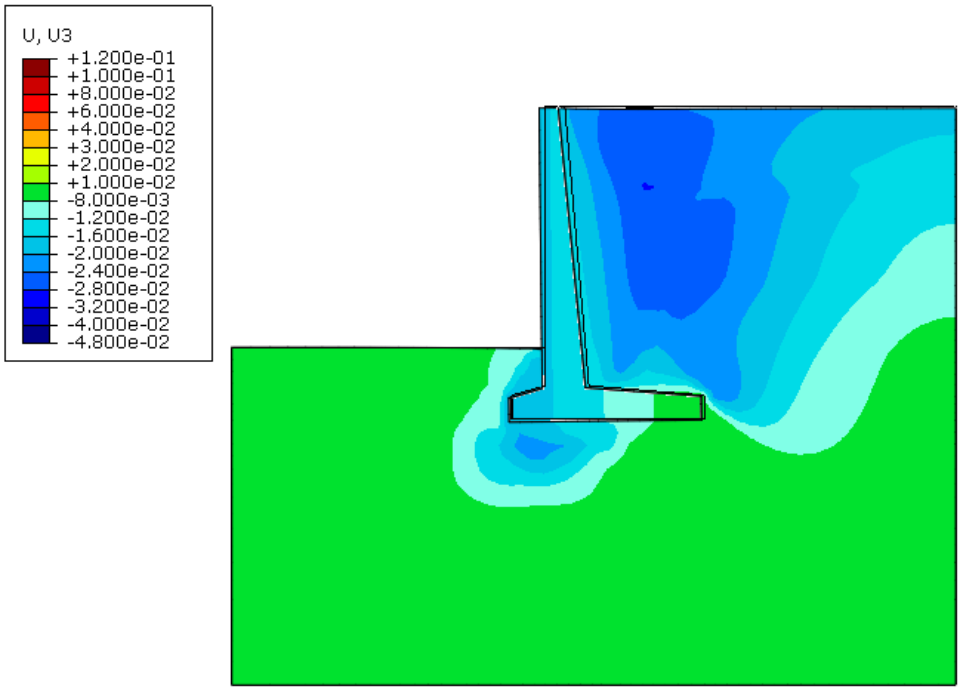

(c) t = 280 days

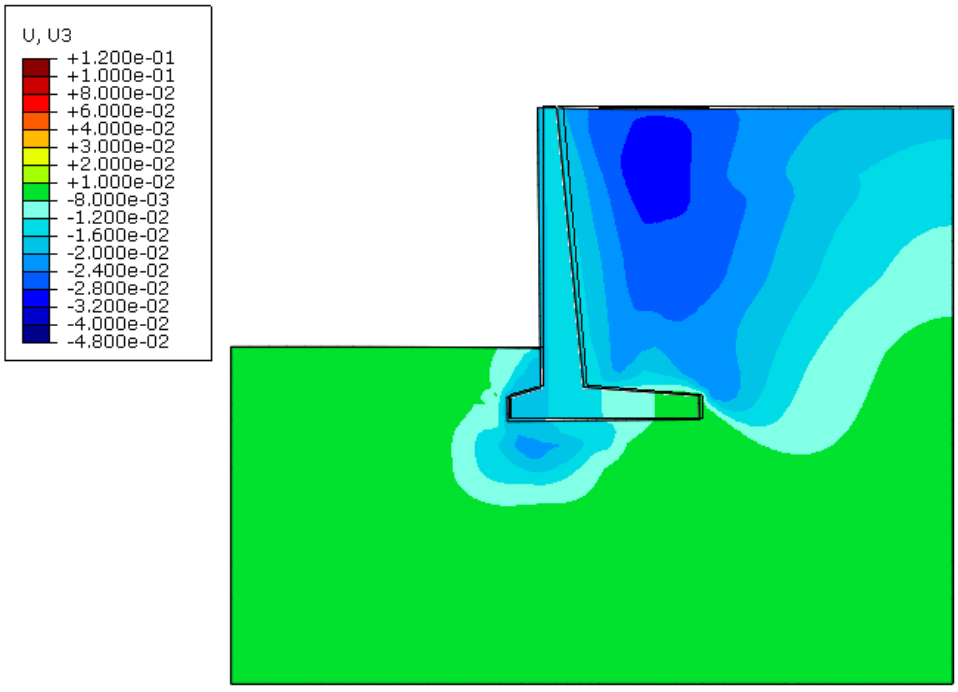

(d) t = 365 days

Figure 6.37 Vertical displacement (in meters): (a) t = 80 days, (b) t = 195 days, (c) t = 280 days, (d) t = 365 days

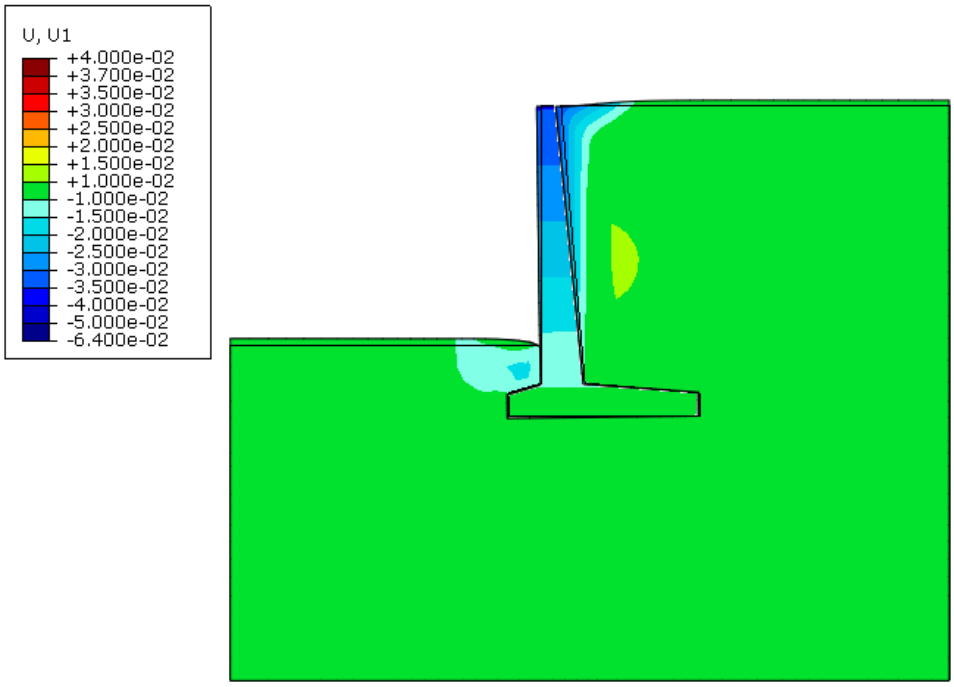

(a) t = 80 days

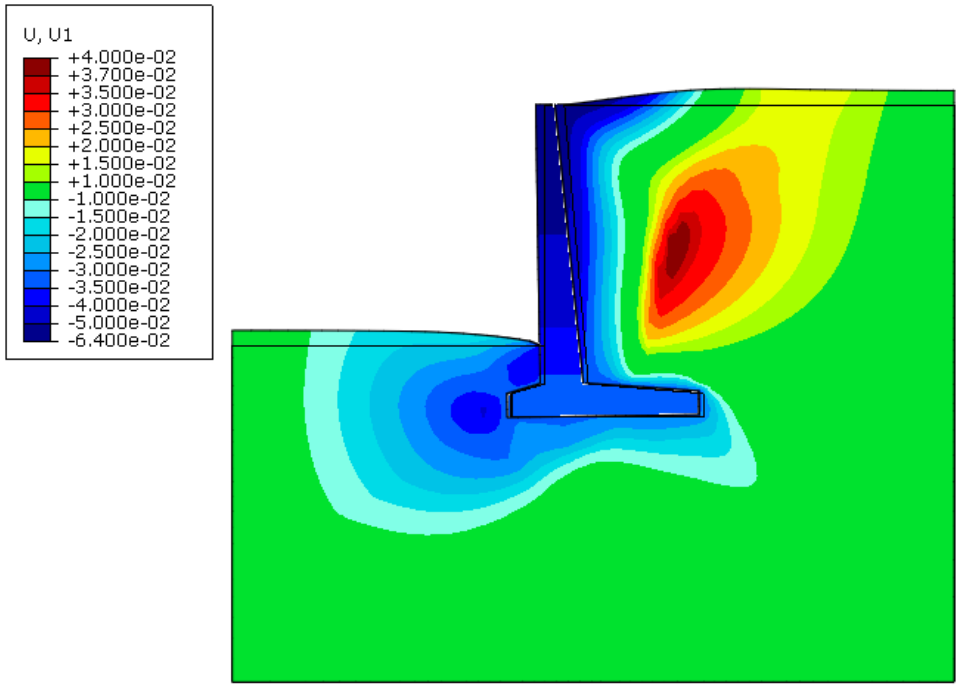

(b) t = 195 days

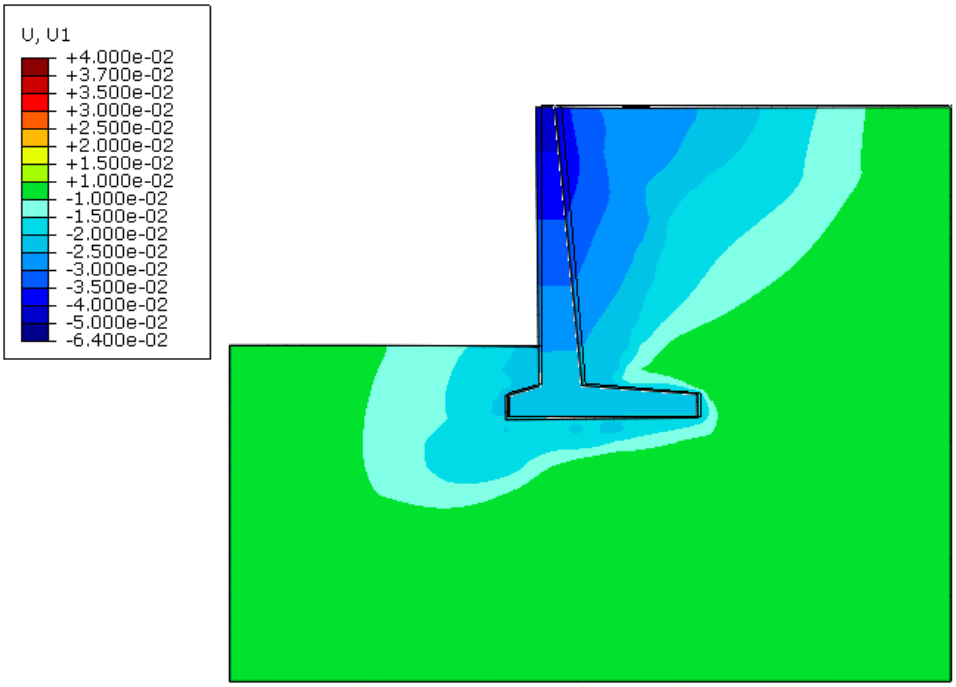

(c) t = 280 days

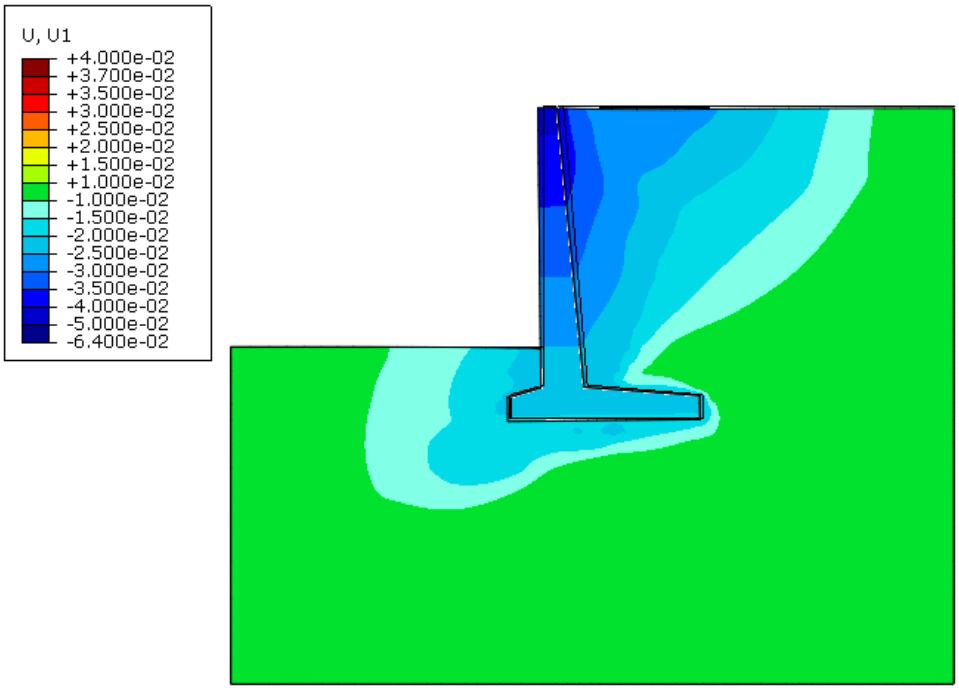

(d) t = 365 days

Figure 6.38 Horizontal displacement (in meters): (a) t = 80 days, (b) t = 195 days, (c) t = 280 days, (d) t = 365 days

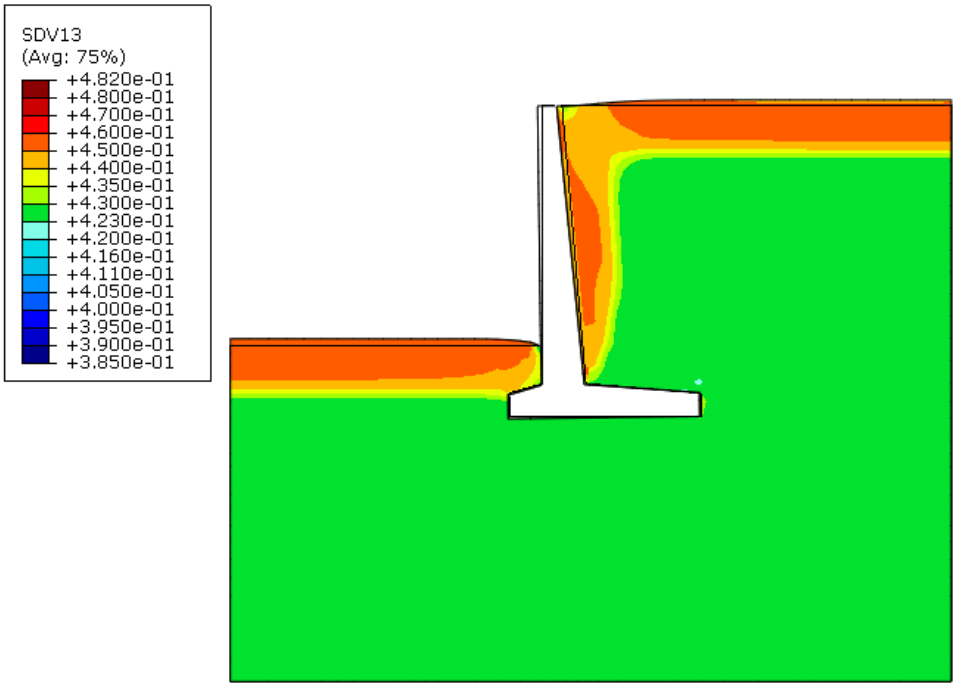

(a) t = 80 days

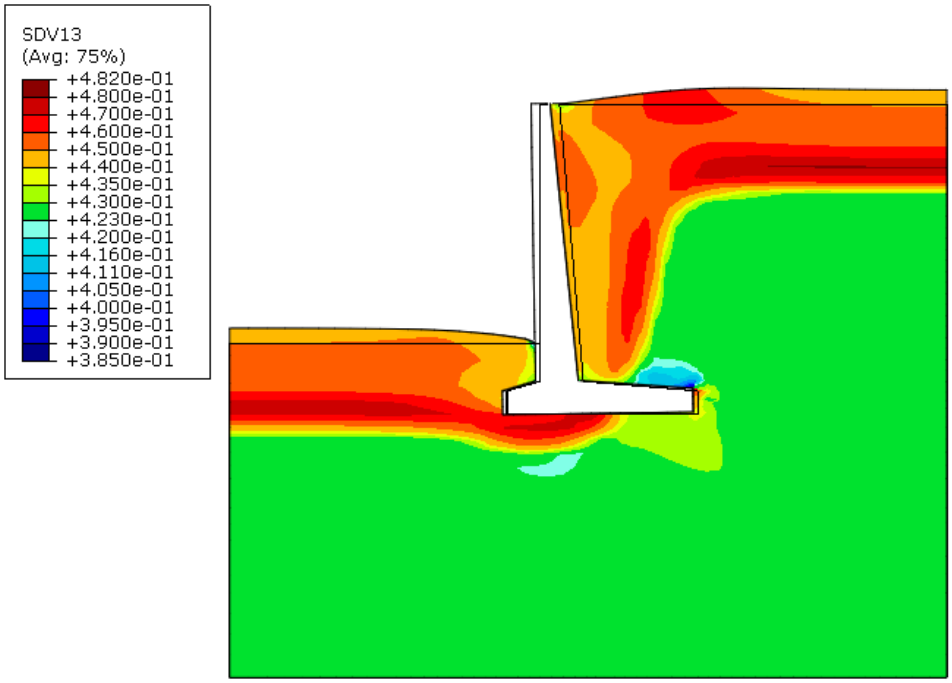

(b) t = 195 days

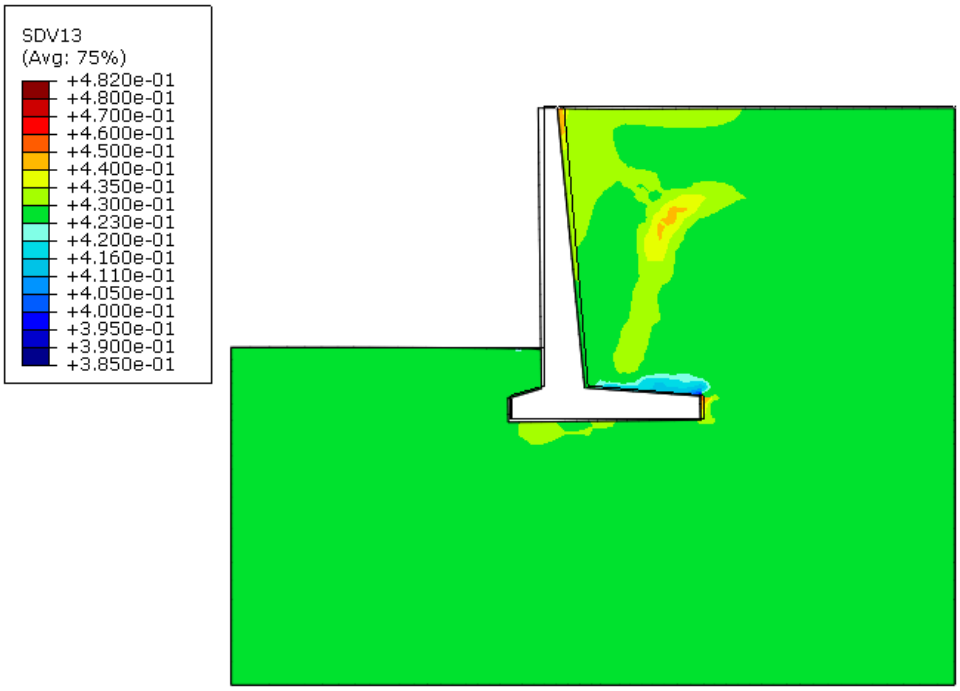

(c) t = 280 days

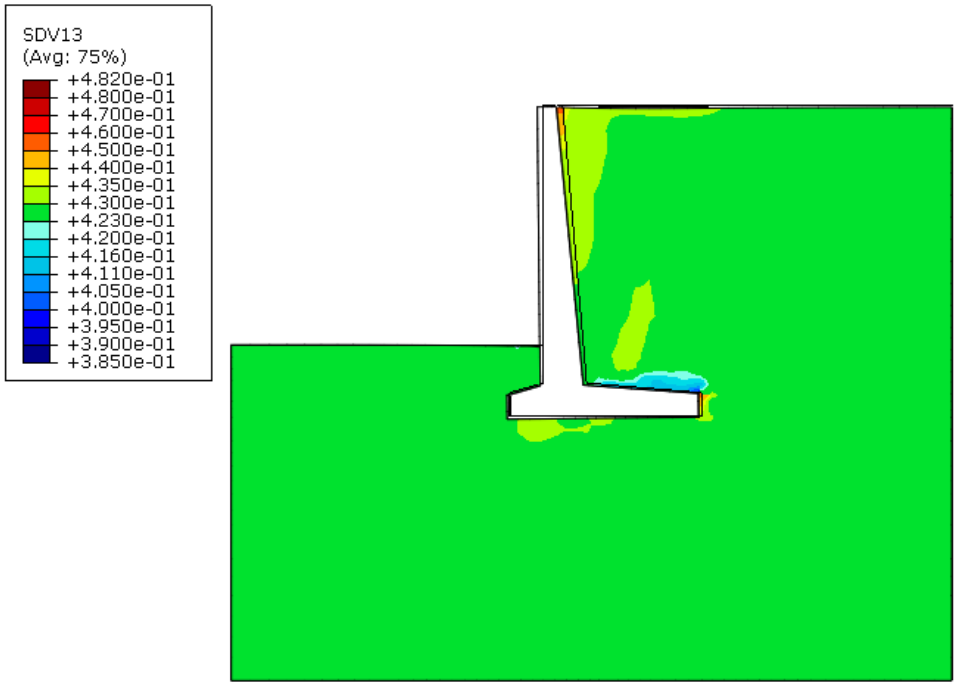

(d) t = 365 days

Figure 6.39 Porosity distribution (a) t = 80 days, (b) t = 195 days, (c) t = 280 days, (d) t = 365 days

The horizontal displacements at the top of the wall for the insulated and non-insulated retaining wall are compared in Figure 6.40. The insulation is proved to be very effective in reducing the movement of the wall caused by frost action. With the insulation, the peak and the residual horizontal movement of the wall does not vary a lot. Both are about 2 cm. For the non-insulated wall, the maximum outward movement is about 6 cm and the residual is about 4 cm. An interesting phenomenon is the kink of the curve marked as A-B-C-D in the figure. In process A-B, the top of the wall is moving back right because of the thawing of soil behind the wall. However, in the process of B-C, the frozen area beneath the left toe of the wall (see Figure 6.39(b)) starts thawing, leading to the top of the wall moving left again. Then, as the soil behind the wall continue thawing, the frost pressure on the wall keeps decreasing and the wall moves back to the right, to its final position.

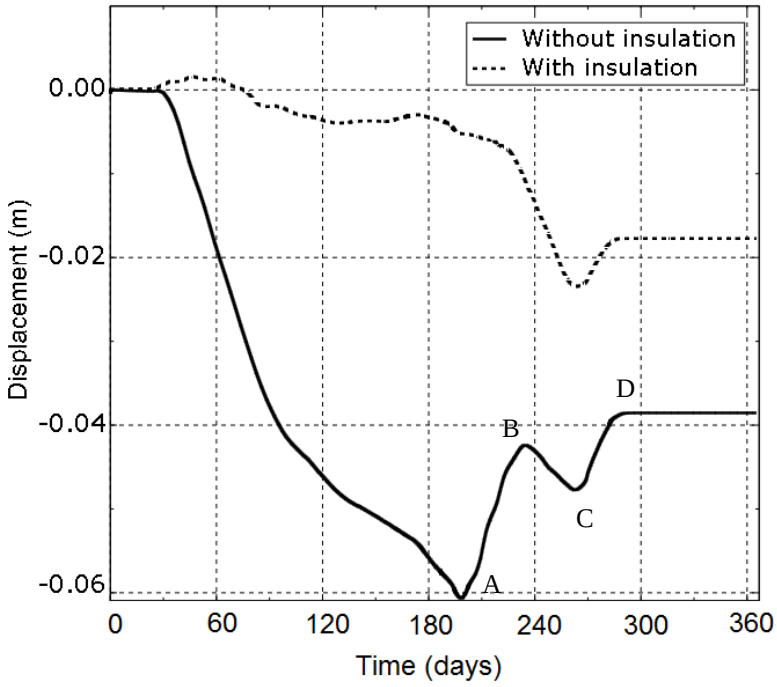

Figure 6.40 Horizontal displacement on top of the wall (negative is to the left)

6.3.3 Remarks

The freezing and thawing of soils in a retaining structure system has been successfully simulated using the developed model. The vertical displacements of the ground surface, as well as the horizontal displacement of the wall, caused by the frost heave and thaw settlement were tracked. The usefulness of insulation behind the retaining wall in mitigating the displacements caused by the freeze-thaw cycle was demonstrated. The simulation result shows that the insulation is effective at reducing the wall movement; therefore, the use of thermal insulation reduces the potential for frost damage.

6.4 Frost Heave and Thaw Settlement around Chilled Gas Pipeline

Large natural gas reserves were discovered in Prudhoe Bay in Alaska in 1967. Gas pipelines are used to transport natural gas from the reserves to the consumers. The Federal Power Commission proposed to construct a natural gas pipeline starting from Prudhoe Bay. Because part of the pipeline will run through permafrost, the gas in the pipe will be chilled to prevent thaw of the permafrost. Since 1980's, test sites were built at seven locations close to the Trans-Alaska oil pipeline over a 600 mile range with pipes buried in the ground to study the effects on the ground and the pipeline itself. Other field and laboratory testing were also performed in 1990's and 2000's before the construction of the pipeline.

In 2009, TransCanada and ExxonMobil began working together to develop the Alaska Pipeline Project. The project is designed to connect Alaska's North Slope natural gas resources to the U.S. Midwest. Permafrost areas are not expected to cause big issues to chilled pipelines. Of most concern are the seasonal freezing areas, where both the air temperature change and the chilled gas would result in frost heave and thaw settlement of the surrounding ground. Particular issues to the pipeline are the damages that might be caused by the potential differential heave when the pipeline goes through transition zones containing soils with diverse frost-susceptibilities.

In this section, a 3-D simulation of a chilled gas pipeline buried in a transition zone with frost-susceptible and non-frost-susceptible soils in seasonal freezing area will be performed using the model developed.

6.4.1 Problem Description

The geometry of the chilled gas pipeline system is shown in Figure 6.41. The pipeline is 0.8 m in diameter, 10.0 mm thick and is buried 1.0 m below the ground surface. A 50.0 mm insulation layer is placed around the pipeline. The length of the model is 20.0 m. The pipeline is simulated to transvers in a transition zone from non-frost-susceptible soil to frost-susceptible soil.

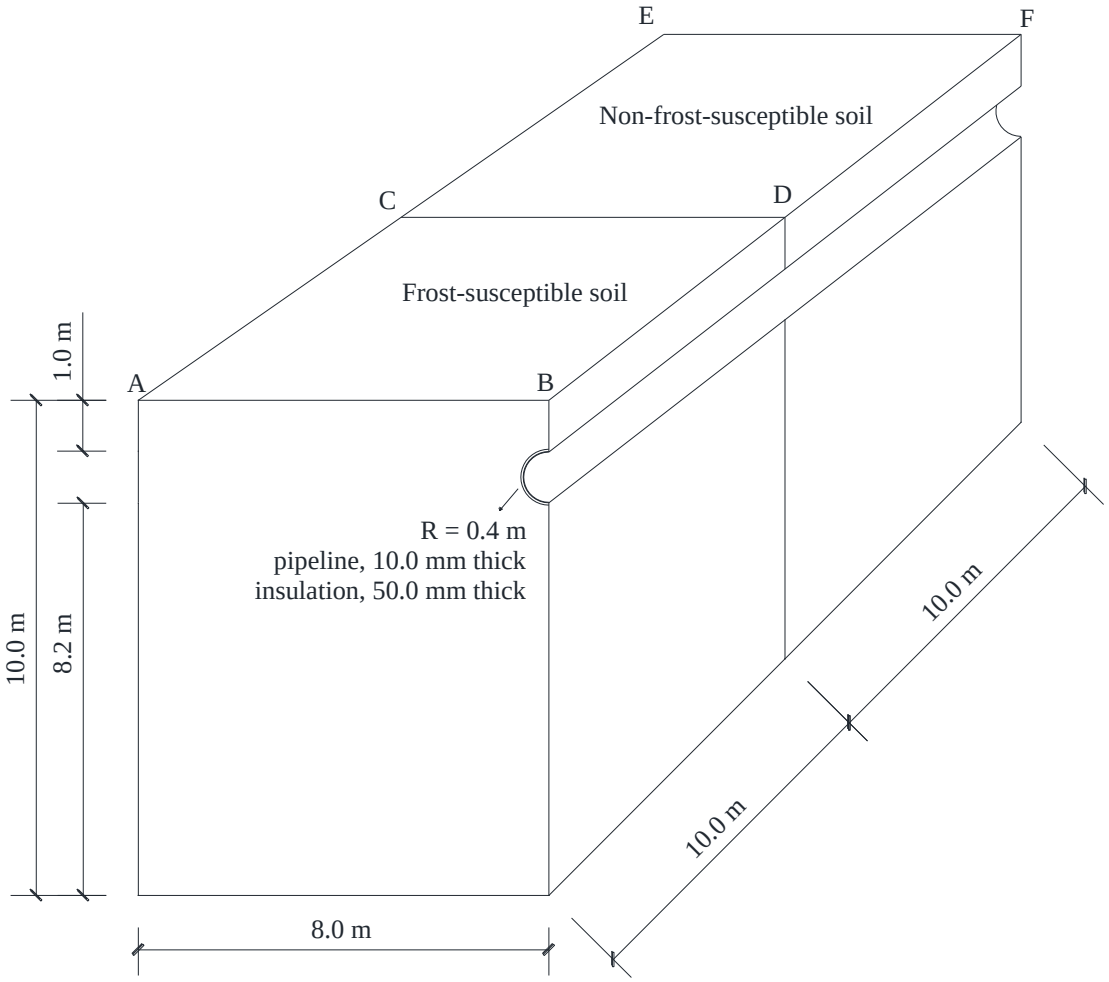

Figure 6.41 Geometry of chilled gas pipeline

Displacement boundary conditions: vertical boundaries are not allowed to move inward/outward, and the bottom is fixed in all the three directions. Heat is not allowed to flow across the vertical boundaries (adiabatic). Figure 6.42 shows the boundary temperatures. The temperature at the bottom boundary is set to be constant at 3°C. The simplified linear temperature according to the air temperature data in Aniak, AK is used as the ambient air temperature (shown in Figure 6.14) on the ground surface. The chilled gas temperature inside the pipeline is set to be constant at -12 ℃. The Fourier boundary condition in Equation (6.1) is used for both the ground surface and the pipe surface. The hydraulic boundary conditions for the vertical boundaries are impermeable. The bottom boundary is set to be able to drain and intake of water, with a hydraulic conductivity to be $1.0 \cdot 10^{-7}$ m/s, whereas the ground surface allows only drainage, but not intake of water.

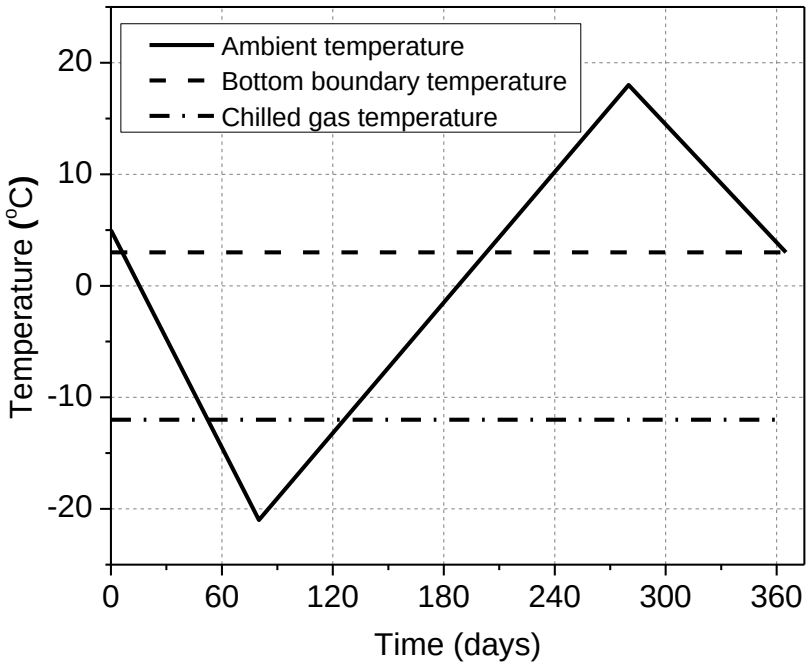

Figure 6.42 Thermal boundary conditions

The finite element mesh and initial temperature distribution are shown in Figure 6.43. The temperature distribution is a steady-state distribution associated with the constant temperatures at boundaries: top 5 ℃, bottom 3 ℃. Figure 6.44 shows the initial geo-static vertical stress in the soil profile.

The model is discretized using 8-node solid elements. The 8-node trilinear displacement and temperature elements (element type C3D8T in ABAQUS) are used for the pipeline and the insulation layer, whereas 8-node trilinear displacement, pore pressure, and temperature elements (type C3D8PT in ABAQUS) are used for the surrounding soil. The total number of elements is 13200 and the total number of nodes is 14679.

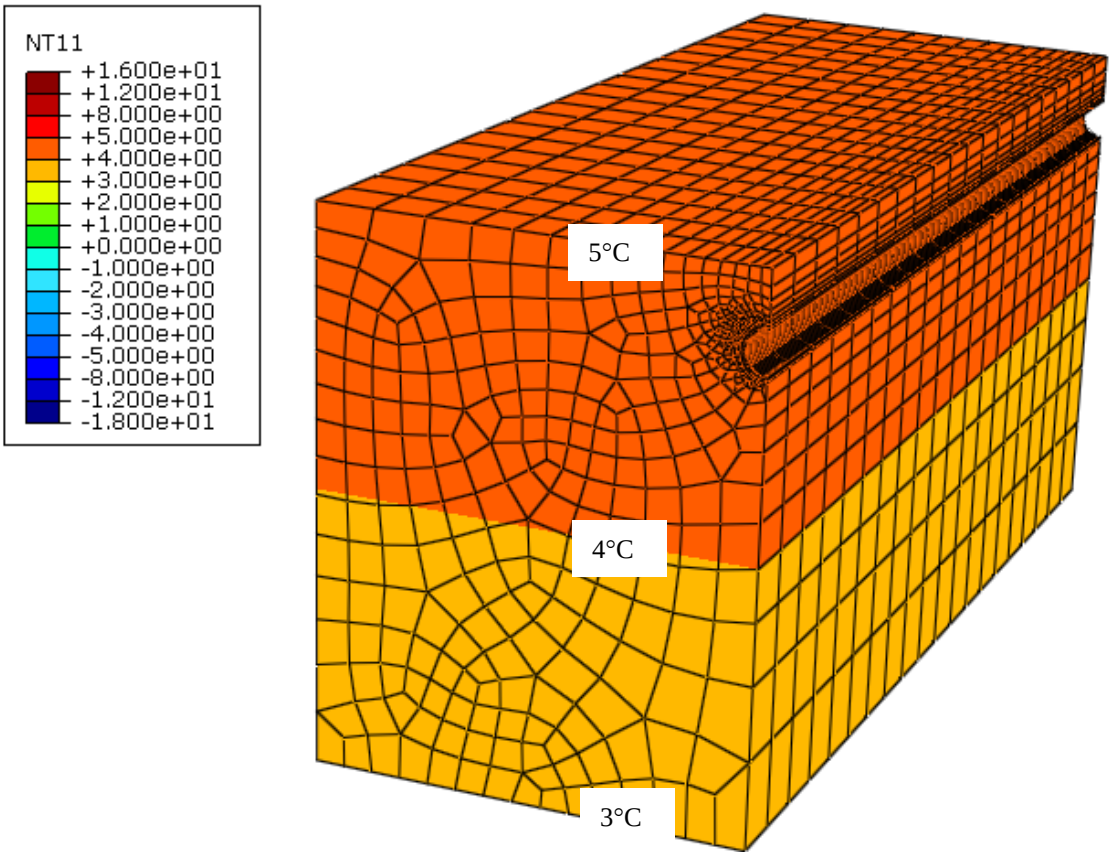

Figure 6.43 Finite element mesh and initial temperature distribution

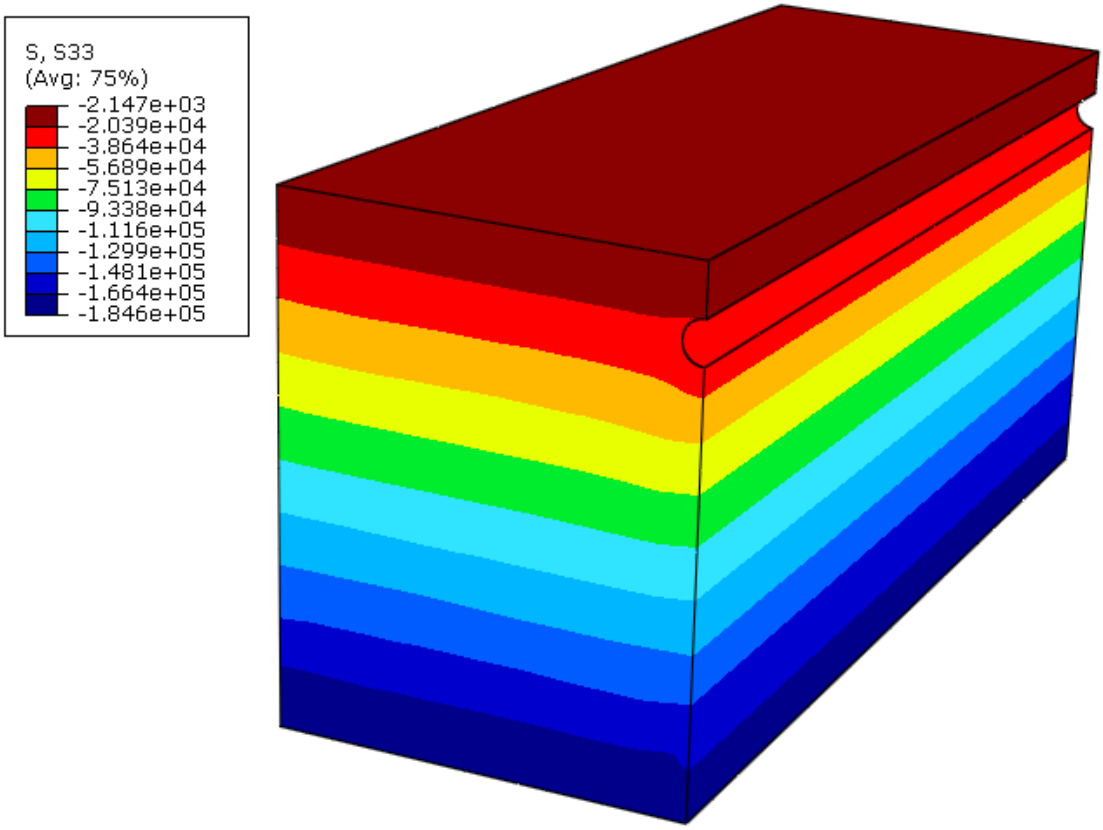

Figure 6.44 Distribution of geo-static vertical stress (Pa) in soil at $t = 0$

The parameters of the soil used in the simulation are listed below: (1) unfrozen water content: $w^* = 0.058$, $w_0 = 0.285$, $T_0 = 0$ ℃, and $a = 0.16$ °C^{-1} (2) elastic-plastic constitutive model: $\lambda = 0.35$, $\kappa = 0.07$, $p_0 = 80$ kPa, $M = 0.8$, $\alpha_1 = 0.2$, $\alpha_2 = 0.4$, $\alpha_3 = 0.6$, $p^r = 10$ kPa, $\beta = 0.18$, $p_t = -1.0$ MPa, (3) porosity rate function: $\dot{n}_m = 5.94 \cdot 10^{-7}$ s^{-1} (less frost susceptible soil, 3% of calibration value from Fukuda's tests), $T_m = -0.82$ ℃, $g_T = 100$ ℃/*m*, and $\zeta = 0.73$ MPa; the hydraulic conductivity for soils was taken as $1.0 \cdot 10^{-7}$ m/s for unfrozen soil and $1.0 \cdot 10^{-12}$ m/s for frozen soil with temperature below -5 ℃; linear interpolation was used for temperatures between 0 ℃ and -5 ℃; the initial void ratio is 0.747. A 50 mm thick insulation layer was

simulated around the pipe. The material properties of the pipeline and insulation layer are shown in Table 6.3.

Table 6.3. Material properties of pipeline and insulation

	Density ρ kg/m^3	Mass heat capacity c J/(kg· ℃)	Thermal Conductivity λ W/(m· ℃)	Convective coefficient h_c W/(m^2 ℃)	Young's modulus E Pa	Poisson's ratio
Steel	7800	480	1.60	700	$2.0 \cdot 10^{11}$	0.30
Insulation	50	2000	0.02	-	$1.0 \cdot 10^{7}$	0.30

6.4.2 Frost Action around a Chilled Gas Pipeline in Seasonal Freezing Area

The contours of temperature from the simulation are shown in Figure 6.45 at times t = 29, 200, 280 and 365 days. Deformations are exaggerated by a factor of 5 in all the figures that follow.

In the first 29 days, the air temperature drops to about -5 ℃ and the freezing fronts propagating from the ground surface and from the pipe meet each other right above the pipe. In the soil far away from the pipeline, the freezing front propagates a distance about 0.3 m.

At t = 200 days, the ambient temperature is slightly about 0 ℃. The temperature at the ground surface away from the pipeline just reaches 0 ℃, whereas at the ground surface right above the pipeline, the temperature is still below freezing. The freezing front under the pipeline propagates to 2.0 m below.

At t = 280 days, the ambient temperature reaches its highest value 18 ℃. The ground away from the pipeline is thawed off. After t = 365 days, most of ground has completely thawed, leaving a small bulb shaped frozen area around the pipe.

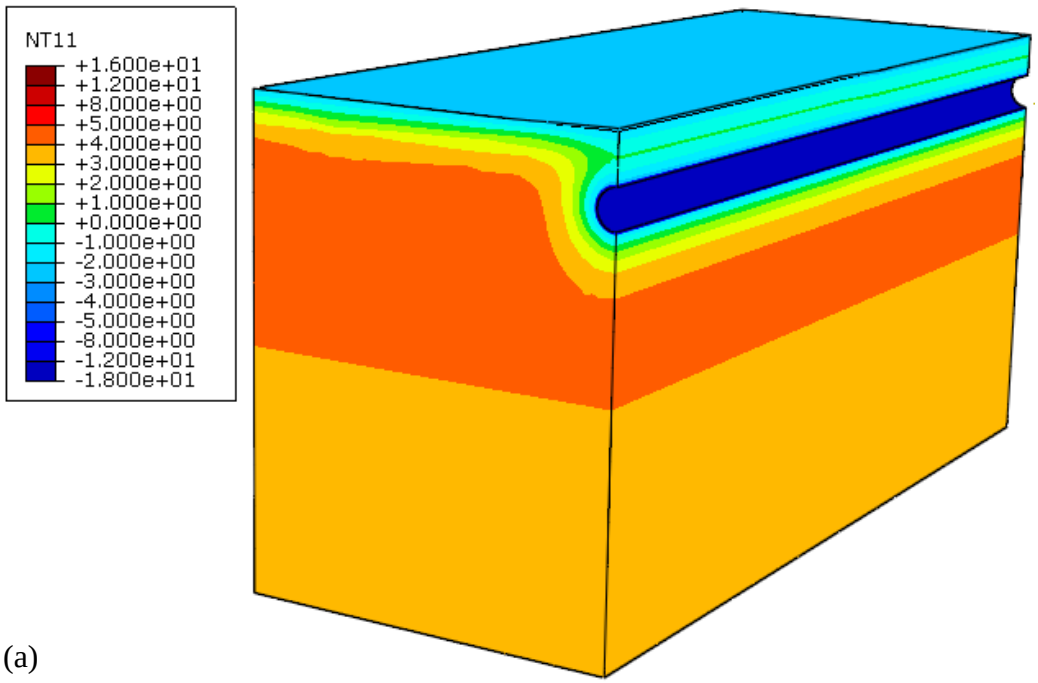
NT11
+1.600e+01
+1.200e+01
+8.000e+00
+5.000e+00
+4.000e+00
+3.000e+00
+2.000e+00
+1.000e+00
+0.000e+00
-1.000e+00
-2.000e+00
-3.000e+00
-4.000e+00
-5.000e+00
-8.000e+00
-1.200e+01
-1.800e+01

(a)

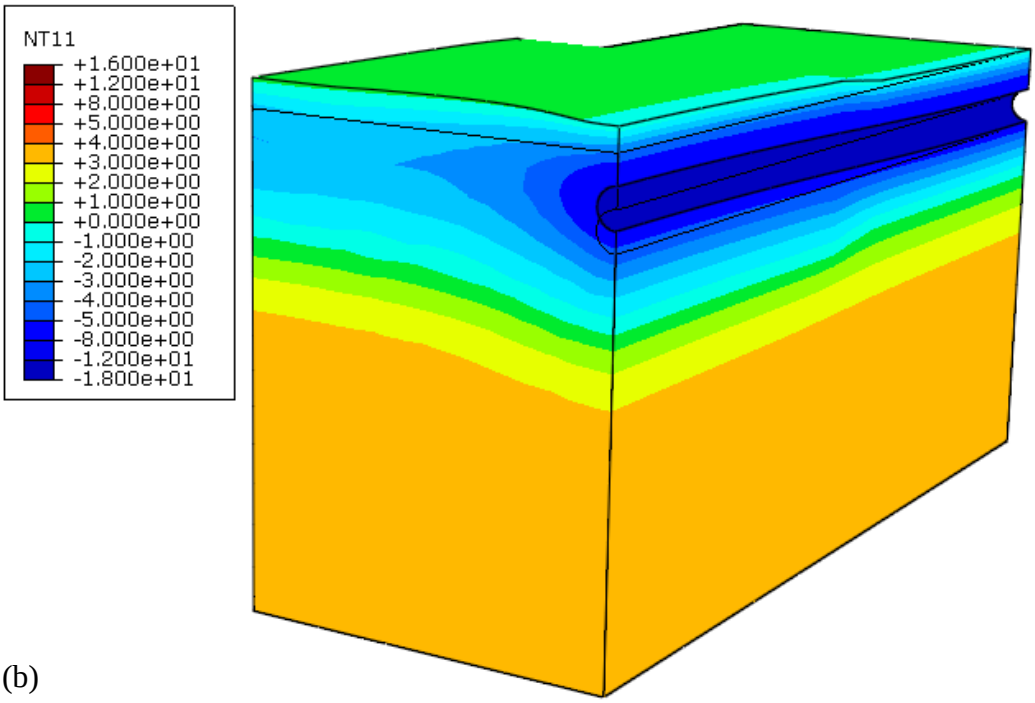
NT11
+1.600e+01
+1.200e+01
+8.000e+00
+5.000e+00
+4.000e+00
+3.000e+00
+2.000e+00
+1.000e+00
+0.000e+00
-1.000e+00
-2.000e+00
-3.000e+00
-4.000e+00
-5.000e+00
-8.000e+00
-1.200e+01
-1.800e+01

(b)

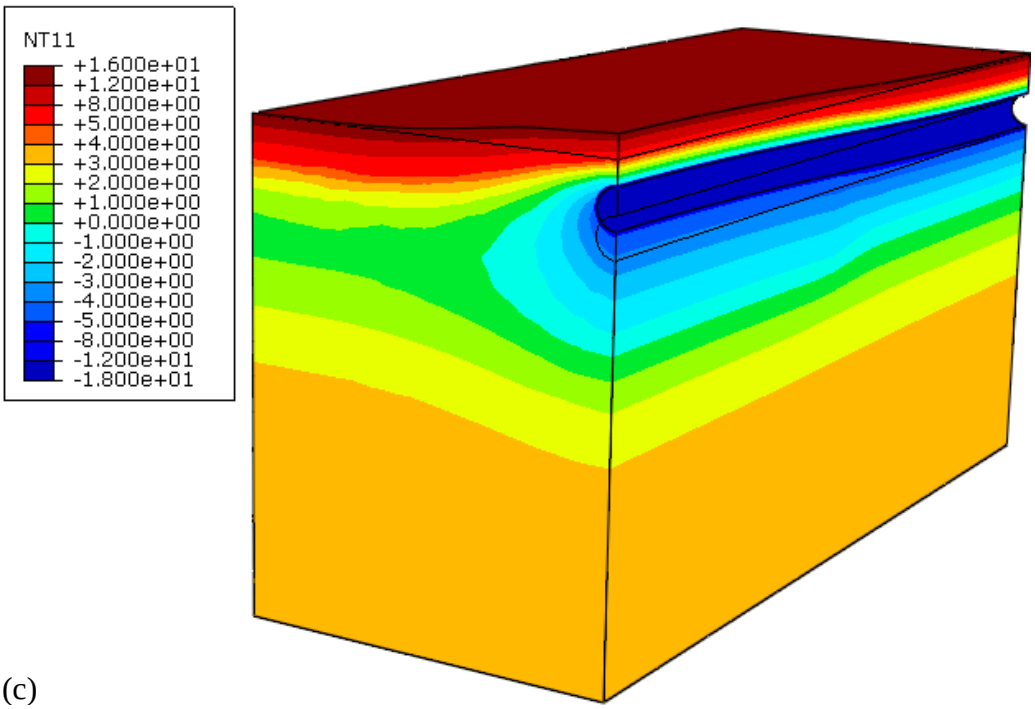

(c)

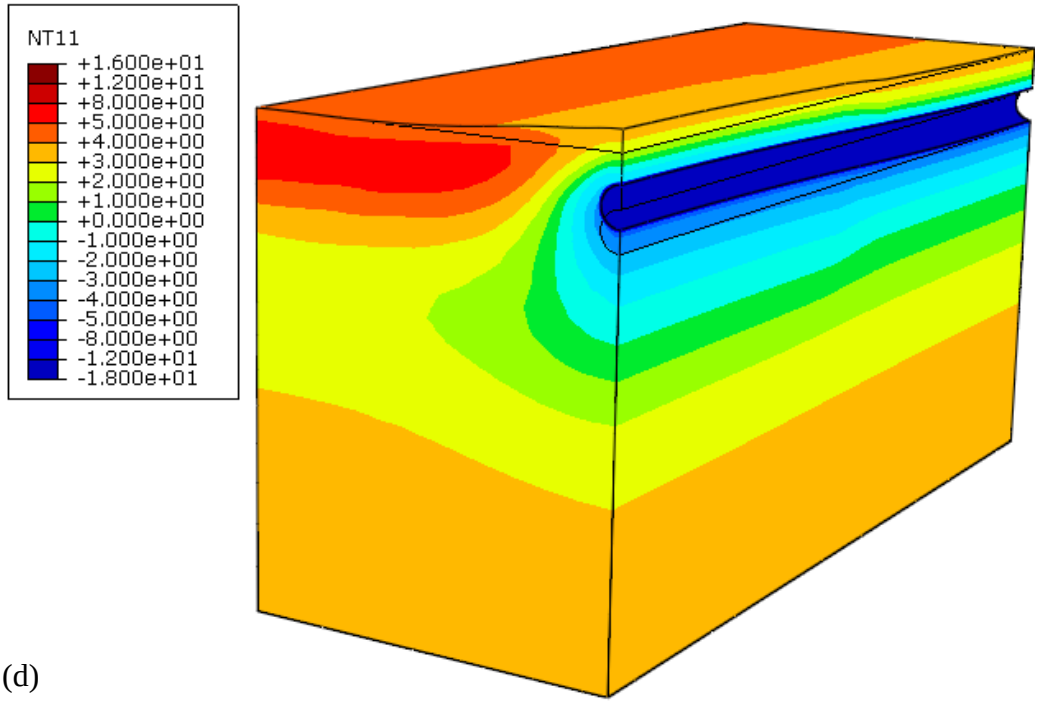

(d)

Figure 6.45 Temperature distribution (℃): (a) t = 29 days, (b) t = 200 days, (c) t = 280 days, (d) t = 365 days

The vertical displacements are shown in Figure 6.46. Before $t = 29$ days, the freezing front propagated from both the ground surface and from the pipe, and the heave of the ground surface above frost-susceptible soil above the pipe is faster than elsewhere. Thereafter, the freezing fronts join one another and the heave on the ground above the pipe slows down. At $t = 200$ days, the heave on the ground surface with frost-susceptible soil away from the pipe is larger than above the pipe. In the frost-susceptible soil, the pipe has been pushed up by the frost heave of soil below whereas in the non-frost-susceptible soil, the pipe is not moving. Therefore, the pipe is bending. At $t = 280$ and 365 days, the soil away from the pipe is thawing and the ground surface on top settles back. The ground surface on top of the pipe settles a little, but some of the heave remains because the soil around the pipe is still frozen.

The contours of excess pore pressure distribution (suction negative) are shown in Figure 6.47. At $t = 29$ and 200 days, negative pore pressure present and the frost heave is taking place. After 280 days, positive pore pressure dominates, although, portions of the soil around the pipe are still frozen. After 365 days, negative pore pressure is present in frost susceptible soil above the pipeline, indicating continued frost heaving.

The contours of porosity distribution are shown in Figure 6.48. In the figure for $t = 29$ days, it shows that the porosity growth occurs at both the ground surface and around the pipe. At $t = 200$ days, all the frozen area in the frost-susceptible soil from the ground surface to about 4 m below is experiencing porosity growth. The maximum increase in porosity is located beneath the pipe. Some decrease in porosity occurs below the pipe and on the interface between the frost-susceptible and non-susceptible soils. At $t = 280$ and 365 days, most of the excess porosity gained during freezing was reversed. In the area to the upper left of the pipe and below the pipe, a small decrease in porosity occurs.

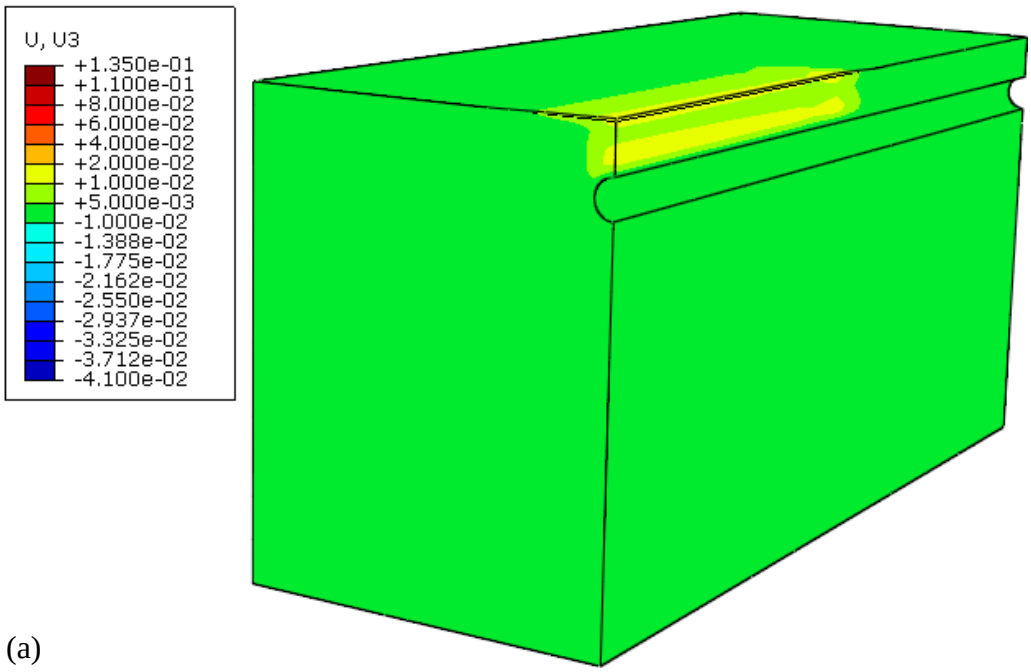
U, U3
+1.350e-01
+1.100e-01
+8.000e-02
+6.000e-02
+4.000e-02
+2.000e-02
+1.000e-02
+5.000e-03
-1.000e-02
-1.388e-02
-1.775e-02
-2.162e-02
-2.550e-02
-2.937e-02
-3.325e-02
-3.712e-02
-4.100e-02

(a)

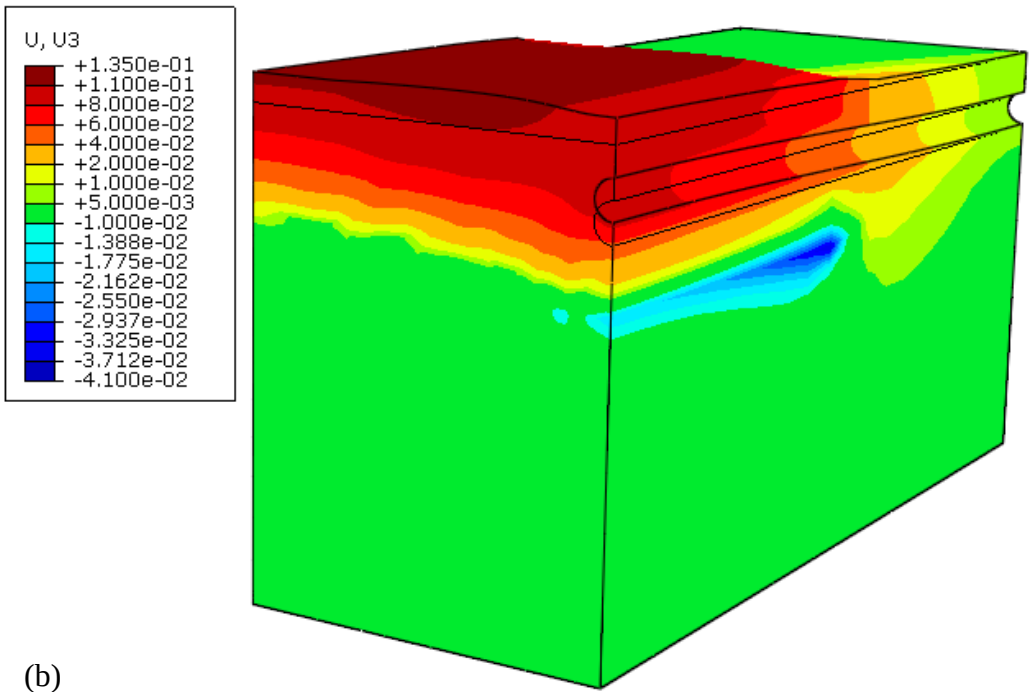
U, U3
+1.350e-01
+1.100e-01
+8.000e-02
+6.000e-02
+4.000e-02
+2.000e-02
+1.000e-02
+5.000e-03
-1.000e-02
-1.388e-02
-1.775e-02
-2.162e-02
-2.550e-02
-2.937e-02
-3.325e-02
-3.712e-02
-4.100e-02

(b)

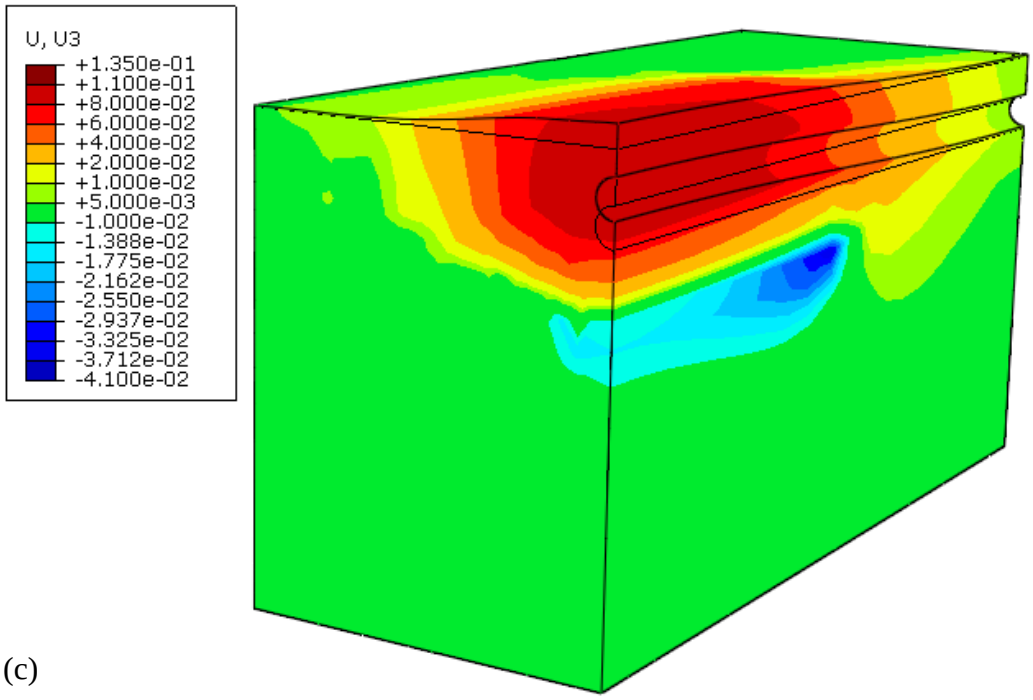

(c)

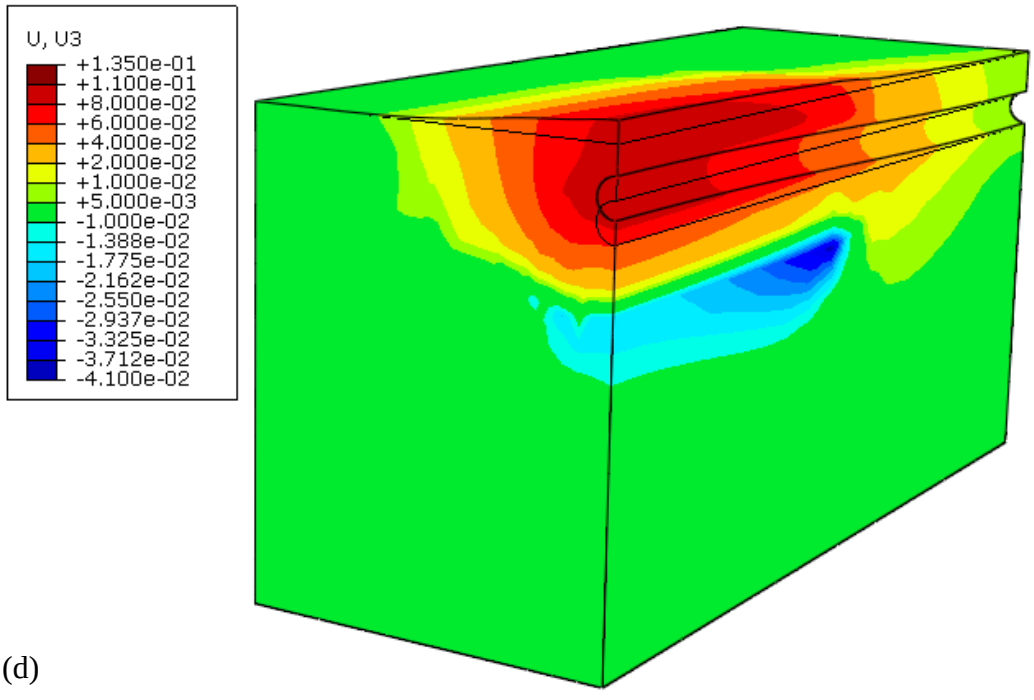

(d)

Figure 6.46 Vertical displacement distribution (in meters): (a) t = 29 days, (b) t = 200 days, (c) t = 280 days, (d) t = 365 days

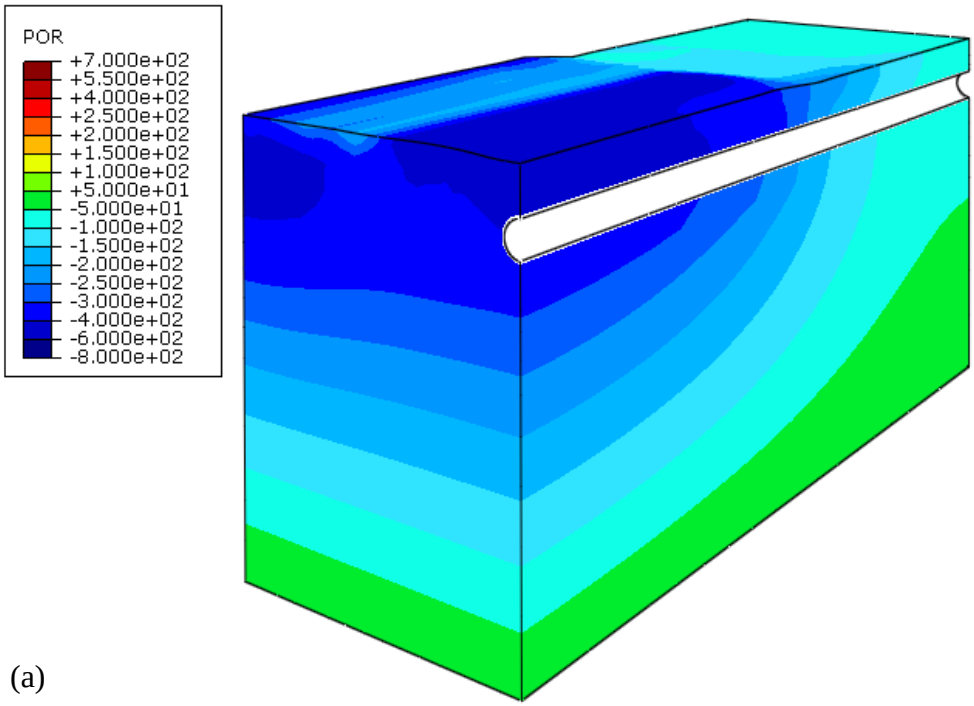
POR
+7.000e+02
+5.500e+02
+4.000e+02
+2.500e+02
+2.000e+02
+1.500e+02
+1.000e+02
+5.000e+01
-5.000e+01
-1.000e+02
-1.500e+02
-2.000e+02
-2.500e+02
-3.000e+02
-4.000e+02
-6.000e+02
-8.000e+02

(a)

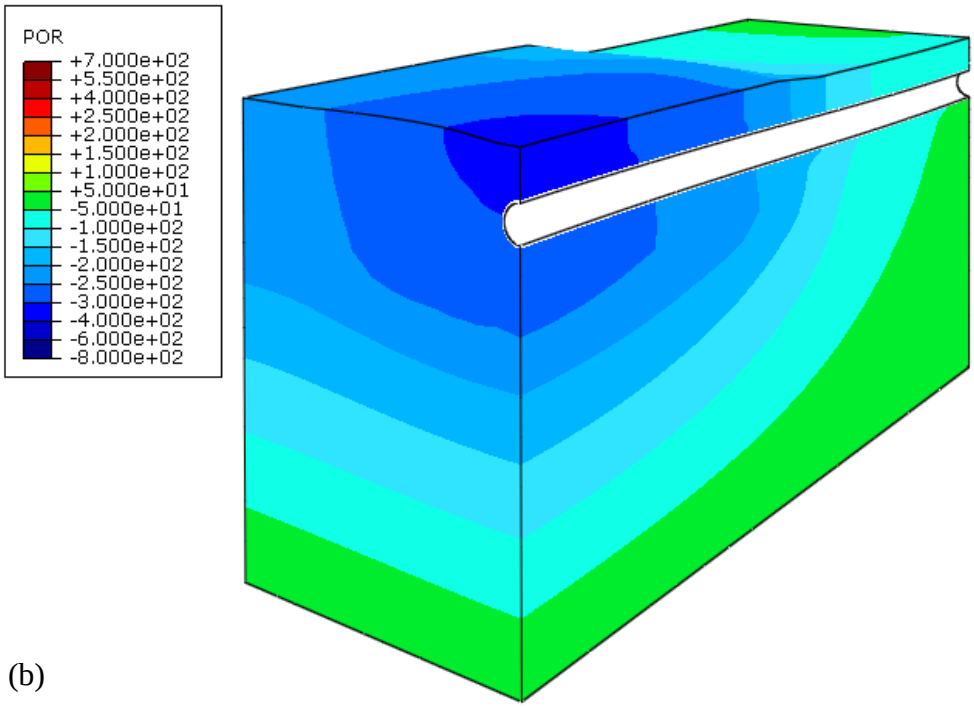
POR
+7.000e+02
+5.500e+02
+4.000e+02
+2.500e+02
+2.000e+02
+1.500e+02
+1.000e+02
+5.000e+01
-5.000e+01
-1.000e+02
-1.500e+02
-2.000e+02
-2.500e+02
-3.000e+02
-4.000e+02
-6.000e+02
-8.000e+02

(b)

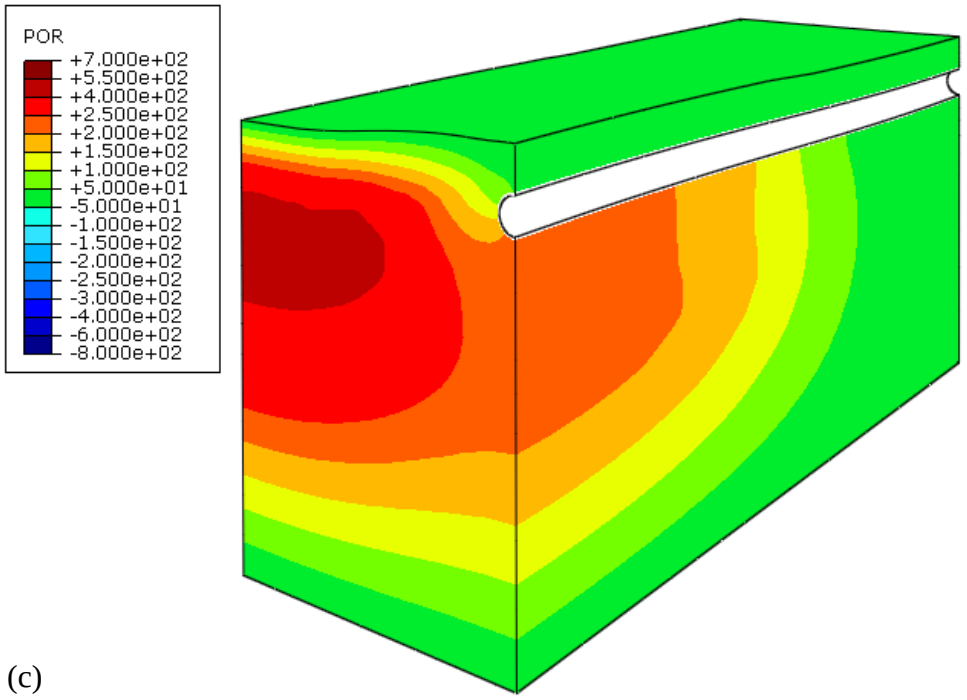

(c)

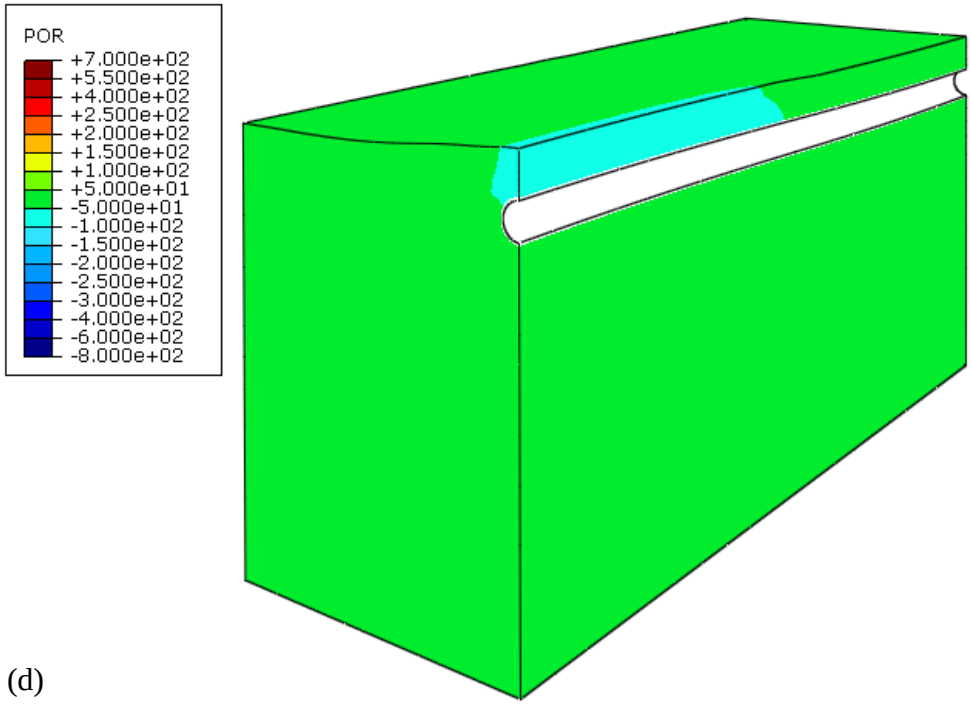

(d)

Figure 6.47 Excess pore pressure distribution (Pa): (a) t = 29 days, (b) t = 200 days, (c) t = 280 days, (d) t = 365 days

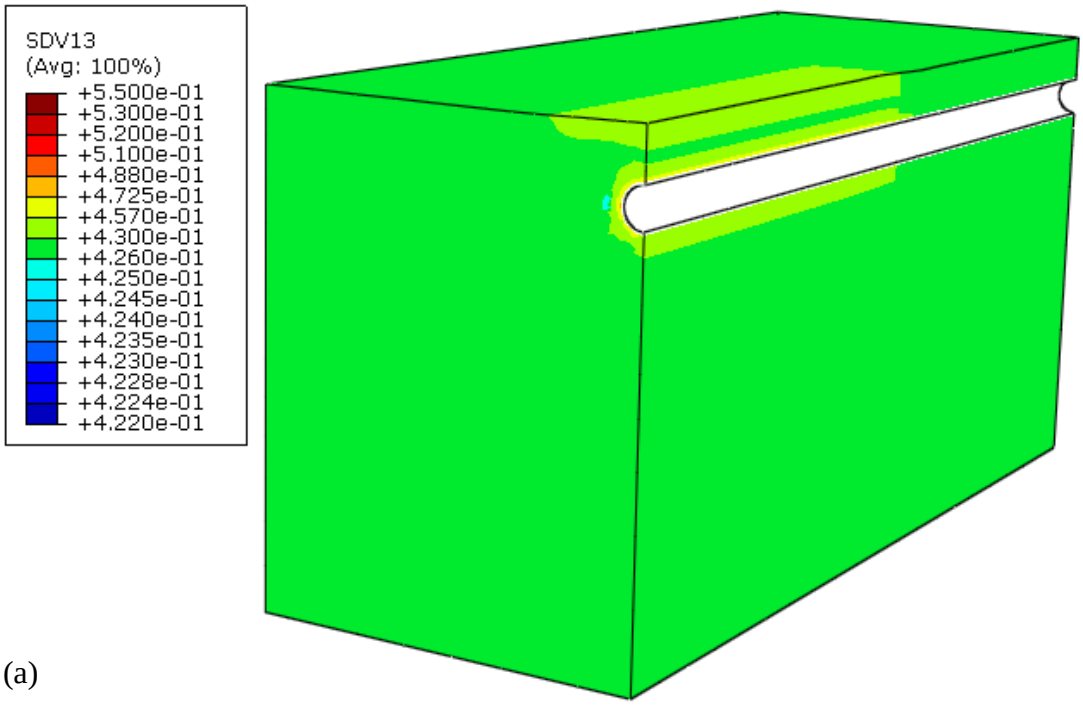
SDV13
(Avg: 100%)
+5.500e-01
+5.300e-01
+5.200e-01
+5.100e-01
+4.880e-01
+4.725e-01
+4.570e-01
+4.300e-01
+4.260e-01
+4.250e-01
+4.245e-01
+4.240e-01
+4.235e-01
+4.230e-01
+4.228e-01
+4.224e-01
+4.220e-01

(a)

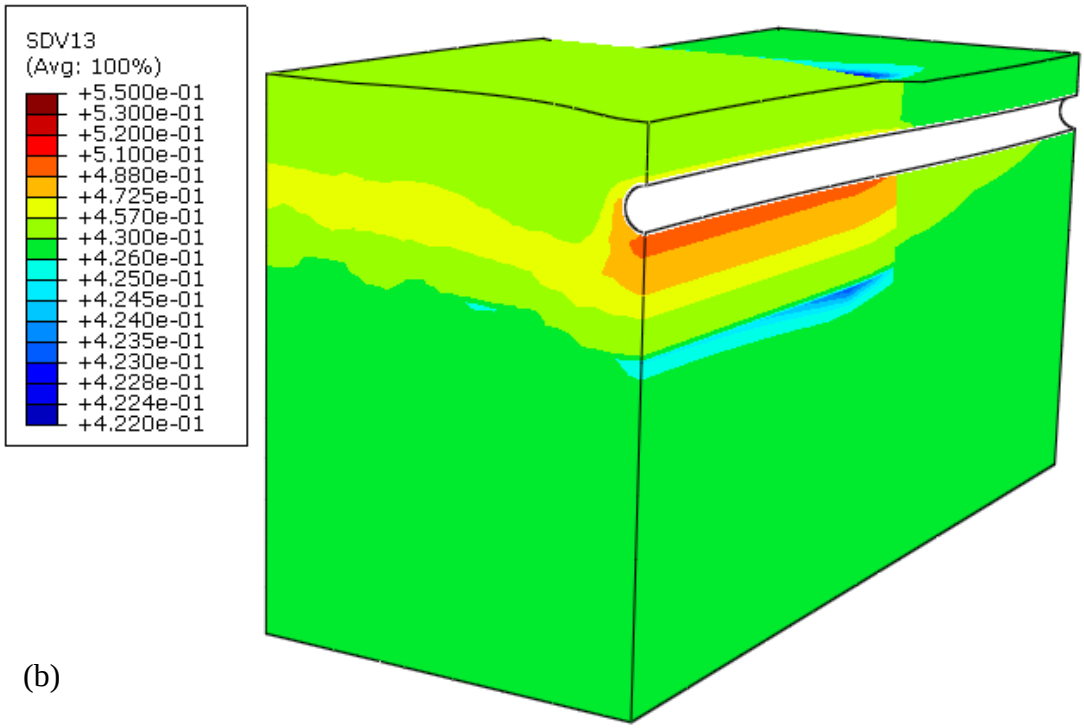
SDV13
(Avg: 100%)
+5.500e-01
+5.300e-01
+5.200e-01
+5.100e-01
+4.880e-01
+4.725e-01
+4.570e-01
+4.300e-01
+4.260e-01
+4.250e-01
+4.245e-01
+4.240e-01
+4.235e-01
+4.230e-01
+4.228e-01
+4.224e-01
+4.220e-01

(b)

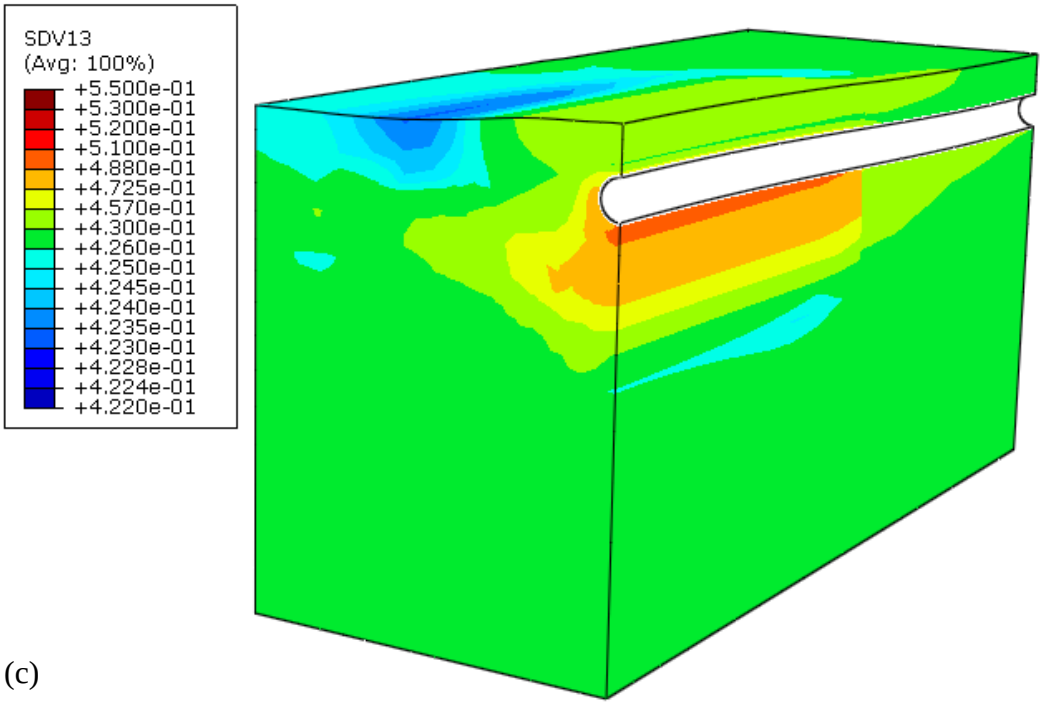

(c)

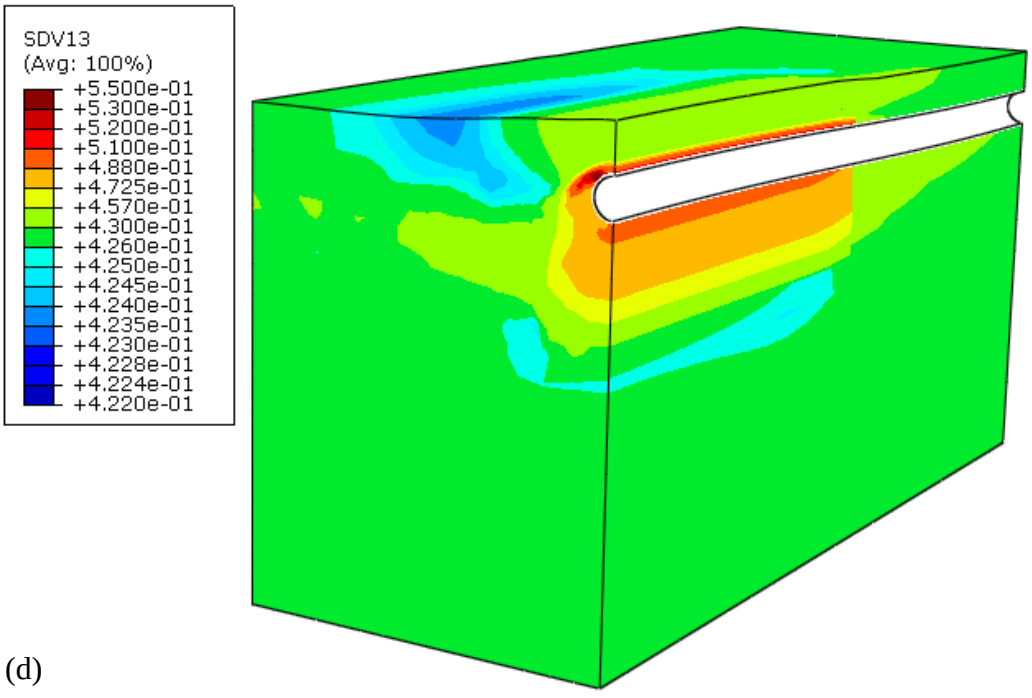

(d)

Figure 6.48 Porosity distribution: (a) t = 29 days, (b) t = 200 days, (c) t = 280 days, (d) t = 365 days

The vertical displacement of the pipeline is shown in Figure 6.49. The origin is set to be at the end of the modeled frost-susceptible soil zone. From 0 m to 10 m, the pipeline is in the frost-susceptible soil, whereas from 10 m to 20 m the pipeline is in the non-frost-susceptible soil. In the frost-susceptible soil, the pipeline has been pushed up about 10 cm after one year. The pipeline at the far end in the non-frost-susceptible zone is raised about 1 cm.

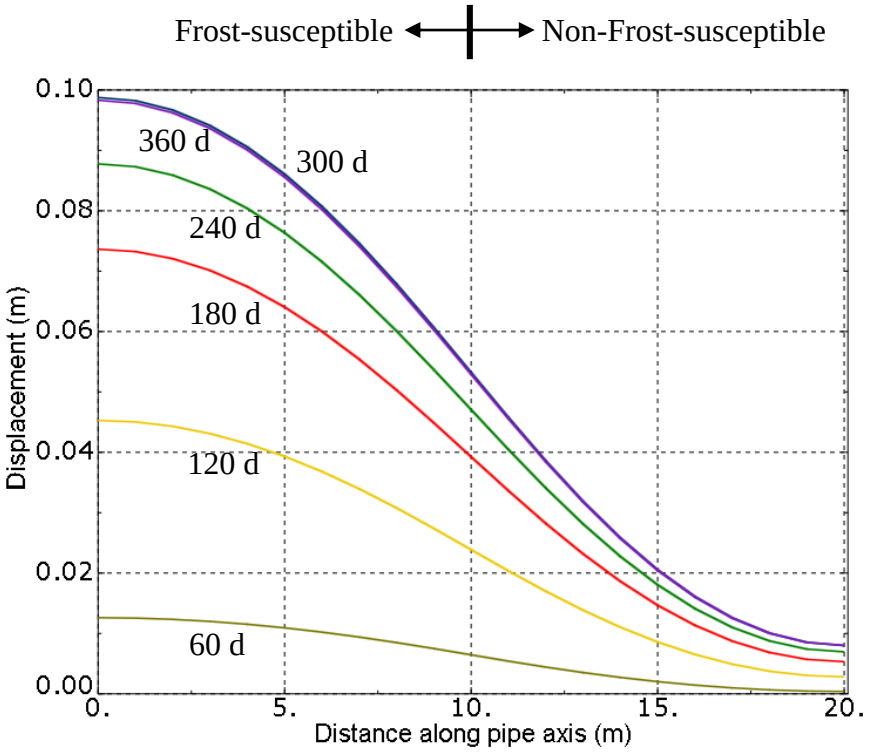

Figure 6.49 Vertical displacement of the pipeline

6.4.3 Remarks

The freezing and thawing of soils around a chilled gas pipeline going through a transition zone with both frost-susceptible and non-frost-susceptible soil was successfully simulated using a three-dimensional model. The differential displacements were clearly seen; they were caused by different frost-susceptibility and different thermal gradients in the soils in the transition region. The vertical displacement of the pipeline caused by the frost heave of the surrounding frost-susceptible soil was obtained from the simulation.

CHAPTER 7

FINAL REMARKS

This dissertation presented the research carried out in an effort to (a) develop a constitutive model describing the behavior of soils subjected to freezing and thawing, (b) implement the model into a finite element system with a thermal-hydro-mechanical framework to simulate the multi-physical processes during freeze-thaw cycles, and (c) use the model developed to solve boundary value problems with complex geometry and boundary conditions, important to engineering practice.

7.1 Dissertation Contributions

This research resulted in a mathematical description of freezing and thawing soils, and a numerical implementation for model-based simulations.

An elastic-plastic constitutive relationship was developed first. The model is based on hardening plasticity and the critical state framework, with the pore ice content and specific volume as the principal parameters responsible for hardening and softening of the soil. As the pore ice content is related to the unfrozen water content in frozen soil, the model developed is temperature dependent. The model describes the strengthening of soil upon freezing, and weakening upon thawing. The model was implemented into a finite element system and it was

calibrated using available test data. Isotropic and non-isotropic compression problems were simulated to demonstrate the capabilities of the model.

The porosity rate function was modified and implemented into the finite element system to simulate the ice lens growth in freezing frost-susceptible soils. The modified function took into account the reduction of the rate in ice lensing, produced by increasing ice volume in the soil (decaying growth effect). A thermal-hydro-mechanical framework was used to capture the multi-physical processes for freezing and thawing soils. Where discontinuities in ice content appeared due to phase change, a modified Heaviside function with a high gradient was used to make the ice content function differentiable.

The model was applied to three problems of practical importance: (a) freezing and thawing of soils around a culvert, (b) freezing and thawing of a retaining wall backfill, and (c) freezing and thawing around a chilled gas pipeline. The results of the simulations are encouraging and they indicate a very realistic response of the model to changing thermal boundary conditions.

7.2 Future Work

Future work will focus on:

1. Comprehensive testing of freezing and thawing for variety of frost susceptible soils, and calibration of the model for various soils;
2. The heat convection due to water flow is not taken into account in the model and should be included in the future to make the simulations even more realistic;
3. The current porosity rate function simulates the frost heave under the assumption that there is always sufficient supply of unfrozen water to move into the frozen fringe. The model

cannot address the situation with partially saturated soils, or permafrost, where the frozen soil beneath prevents the movement of water into the active layer. Future work will concentrate on applicability of the model to unsaturated soils;

4. The stress melting of ice and viscous behavior of ice are not considered in the model. These should be included, particularly if the model is to be used to simulate long-term problems.

REFERENCES

Abuel-Naga, H. M., Bergado, D. T. and Bouazza, A. (2007). "Thermally induced volume change and excess pore water pressure of soft Bangkok clay." *Eng. Geol.*, **89**, 144-154.

Abuel-Naga, H. M., Bergado, D. T., Bouazza, A. and Pender, M. (2009). "Thermo-mechanical model for saturated clays." *Géotechnique*, **59**(3), 273-278.

Aitken, G. W. and Fulwider, C. W. (1962). *Ground Temperature Observations, Aniak, Alaska*. U.S. Army Cold Region Research and Engineering Laboratory, Corps of Engineers, Hanover, New Hampshire, 10.

Akagawa, S. and Nishisato, K. (2009). "Tensile strength of frozen soil in the temperature range of the frozen fringe." *Cold Regions Science and Technology*, **57**, 13-22.

Alonso E. E., Gens A. and Josa A. (1990). "A constitutive model for partially saturated soils." *Géotechnique*, **40**(3), 405-430.

Andersland, O. B. and Ladanyi, B. (2004). *Frozen Ground Engineering.* Wiley, New Jersey, 102-119.

Chen, W., Tan, X., Yu, H., Wu, G. and Jia, S. (2009). "A fully coupled thermo-hydro-mechanical model for unsaturated porous media." *Journal of Rock Mechanics and Geotechnical Engineering*, **1**(1), 31-40.

Chijimatsu, M., Nguyen, T. S., Jing, L., De Jonge, J., Kohlmeier, M., Millard, A., Rejeb, A., Rutqvist, J., Souley, M. and Sugita, Y. (2005). "Numerical study of the THM effects on the near-field safety of a hypothetical nuclear waste repository-BMT1 of the DECOVALEX III project. Part 1: Conceptualization and characterization of the problems and summary of results." *Int. J. Rock Mech. Min. Sci.*, **42**, 720-730.

Chamberlain, E. J. (1981). "Overconsolidation effects of ground freezing." *Eng. Geol.*, **18**, 97-110.

Chamberlain, E.J. and Gow, A. J. (1979). "Effect of freezing and thawing on the permeability and structure of soils." *Eng. Geol.*, **13**, 73-92.

Corapcioglu, M. Y. and Panday, S. (1995). "Multiphase approach to thaw subsidence of unsaturated frozen soils: Equation development." *Journal of Engineering Mechanics*, **121**(3), 448-459.

Dumont, M., Taibi, S., Fleureau, J. M., Abou-Bekr, N. and Saouab, A. (2011). "A thermo-hydro-mechanical model for unsaturated soils based on the effective stress concept." *Int. J. Numer. Anal. Meth. Geomech.*, **35**, 1299-1317.

Eigenbrod, K. D. (1996). “Effects of cyclic freezing and thawing on volume changes and permeabilities of soft fine-grained soils.” *Can. Geotech. J.*, **33**, 529-537.

Eigenbrod, K. D., Knutsson, S., and Sheng, D. (1996). “Pore-water pressures in freezing and thawing fine-grained soils.” *Journal of Cold Regions Engineering*, **10**(2), 77-92.

Exadaktylos, G. E. (2006). “Freezing-thawing model for soils and rocks.” *Journal of Materials in Civil Engineering*, **18**(2), 241-249.

Foriero, A. and Ladanyi, B. (1995). “FEM assessment of large-strain thaw consolidation.” *Journal of Geotechnical Engineering*, **121**(2), 126-138.

Fossum, A. F. and Fredrich, J. T. (2000). “Cap plasticity models and compactive and pliant pre-failure deformation.” *Proc. of the 4th North American Rock Mechanics Symposium, NARMS2000, Seattle, Washington*, 1169-1176.

Fukuda, M., Kim H. and Kim Y. (1997). “Preliminary results of frost heave experiments using standard test sample provided by TC8.” *Proc. of the International Symposium on Ground Freezing and Frost Action in Soils, Luleå, Sweden*, 25 - 30.

Gallipoli, D., Gens, A. Sharma, R. and Vaunat, J. (2003). “An elasto-plastic model for unsaturated soil incorporating the effects of suction and degree of saturation on mechanical behavior.” *Géotechnique*, **53**(1), 123-135.

Gibson, R. E., Schiffman, R. L. and Cargill, K. W. (1981). “The theory of one-dimensional consolidation of saturated clays. II: Finite non-linear consolidation of thick homogeneous layers.” *Can. Geotech. J.*, **18**(2), 280-293.

Graham, J. and Au, V. C. S. (1985). "Effects of freeze-thaw and softening on a natural clay at low stresses." *Can. Geotech. J.*, **22**(1), 69-78.

Graham, J., Tanaka, N. Crilly, T. and Alfaro, M. (2001). “Modified Cam-Clay modelling of temperature effects in clays.” *Can. Geotech. J.*, **38**, 608-621.

Guymon, G. L., and J. N. Luthin. (1974). “A coupled heat and moisture transport model for arctic soils.” *Water Resour. Res.*, **10**(5), 995-1001.

Hansson, K., Simunek, J. Mizoguchi, M. Lundin, L. C. and Genuchten, M. T. (2004). “Water flow and heat transport in frozen soil: numerical solution and freeze-thaw applications.” *Vadose Zone Journal*, **3**, 693-704.

He, P., Zhu, Y. and Cheng, G. (2000). “Constitutive models of frozen soil.” *Can. Geotech. J.*, **37**, 811-816.

Hededal, O. (1994). *Object-oriented Structuring of Finite Elements.* PhD Thesis at Aalborg University.

Henry, K.S., Zhu, M. and Michalowski, R.L. (2005). “Evaluation of three frost heave models.” *Proc. of Bearing Capacity of Roads, Railways and Airfields, Trondheim, Norway,* 27-29.

Harlan, R. L. (1973). “Analysis of coupled heat-fluid transport in partially frozen soil.” *Water Resour. Res.*, **9**(5), 1314-1323.

Huang, S. L., Bray, M. T., Akagawa, S. and Fukuda, M. (2004). “Field investigation of soil heave by a large diameter chilled gas pipeline experiment, Fairbanks, Alaska.” *Journal of Cold Regions Engineering*, **18**(1), 2-34.

Hueckel, T., Francois, B. and Laloui, L. (2009). “Explaining thermal failure in saturated clays.” *Géotechnique*, **59**(3), 197-212.

Jame, Y. W. and Norum, D. I. (1980). “Heat and mass transfer in a freezing unsaturated porous medium.” *Water Resources Research*, **16**(4), 811-819.

Kang, Y., Liu, Q. and Huang, S. (2013). “A fully coupled thermo-hydro-mechanical model for rock mass under freezing/thawing condition.” *Cold Regions Science and Technology*, **95**, 19-26.

Konrad, J. M. (1989a). "Effect of freeze–thaw cycles on the freezing characteristics of a clayey silt at various overconsolidation ratios." *Can. Geotech. J.*, **26**(2), 217-226.

Konrad, J. M. (1989b). “Physical process during freeze-thaw cycles in clayey silts.” *Cold Regions Science and Technology*, **16**, 291-303.

Lai, Y., Long, J. and Chang, X. (2009). “Yield criterion and elasto-plastic damage constitutive model for frozen sandy soil.” *Int. J. Plasticity*, **25**, 1177-1205.

Lay, R. D. (2005). *Development of a Frost Heave Test Apparatus*. Brigham Young University Master of Science dissertation.

Lee, M. Y., Fossum, A., Costiin, L. S., Bronowski, D. and Jung, J. (2002). *Frozen Soil Material Testing and Constitutive Modeling*. Sandia National Laboratories, Albuquerque, NM and Livermore, CA.

Li, D., Fan, J. and Wang, R. (2011). “Research on visco-elastic-plastic creep model of artificially frozen soil under high confining pressures.” *Cold Regions Science and Technology*, **65** (2), 219-225.

Liu, M. D. and Carter, J. P. (1999). “Virgin compression of structured soils.” *Géotechnique*, **49**(1), 43-57.

Liu, M. D. and Carter, J. P. (2000). “Modelling the destructuring of soils during virgin compression.” *Géotechnique*, **50**(4), 479-483.

Liu, M. D. and Carter, J. P. (2002). "A structured cam clay model." *Canadian Geotechnical Journal*, **39**(6), 1313-1332.

Liu J. and Peng, L. (2009). "Experimental study on the unconfined compression of a thawing soil." *Cold Regions Science and Technology*, **58**, 92 – 96.

Michalowski, R. L. (1993). "A constitutive model of saturated soils for frost heave simulations." *Cold Regions Science and Technology*, **22**(1), 47-64.

Michalowski, R. L. and Zhu, M. (2006). "Frost heave modeling using porosity rate function." *International Journal for Numerical and Analytical Methods in Geomechanics*, **30**, 703-722.

Millard, A., Rejeb, A., Chijimatsu, M., Jing, L., De Jonge, J., Kohlmeier, M., Nguyen, T. S., Rutqvist, J., Souley, M. and Sugita, Y. (2005). "Numerical study of the THM effects on the near-field safety of a hypothetical nuclear waste repository-BMT1 of the DECOVALEX III project. Part 2: Effects of THM coupling in continuous and homogeneous rocks." *Int. J. Rock Mech. Min. Sci.*, **42**, 731-744.

Ming, F., Li, D. and Zhang, K. (2012). "Theoretical study on thaw settlement of saturated frozen soil." *Applied Mechanics and Materials*, **204**, 155-162.

Minkoff, S. E., Stone, C. M., Bryant, S., Peszynska, M., and Wheeler, M. F. (2003). "Coupled fluid flow and geomechanical deformation modeling." *J. Petrol. Sci. Engi.*, **38**, 37-56.

Missoum, H., Laredj, N., Bendani, K. and Maliki, M. (2011). "A fully-coupled thermo-hydro-mechanical model for the description of the behavior of swelling porous media." *Acta Polytechnica Hungarica*, **8**(4), 91-106.

Morgenstern, N. R. and Nixon, J. F. (1971). "One-dimensional consolidation of thawing soils." *Can. Geotech. J.*, **8**, 558-565.

Morgenstern, N. R., and Smith, L. B. (1973). "Thaw-consolidation tests on remoulded clays." *Can. Geotech. J.*, **10**, 25-40.

Neaupane, K. M. and Yamabe, T. (2001)."A fully coupled thermo-hydro-mechanical nonlinear model for a frozen medium." *Computer and Geotechnics*, **28**, 613-637.

Neaupane, K. M., Yamabe, T. and Yoshinaka, R. (1999). "Simulation of a fully coupled thermo-hydro-mechanical system in freezing and thawing rock." *International Journal of Rock Mechanics and Mining Sciences*, **36**, 563-580.

National Climate Data Center, Retrieved June 18, 2011, Record of Climatological Observations, from http://cdo.ncdc.noaa.gov/dly/DLY.

Ning, J. and Zhu, Z. (2007). "Constitutive model of frozen soil with damage and numerical simulation of the coupled problem." *Chinese Journal of Theoretical and Applied Mechanics*, **39**(1), 70-76.

Nishimura, S., Gens, A., Olivella, S. and Jardine, R. J. (2009). "THM-coupled finite element analysis of frozen soil: formulation and application." *Géotechnique*, **59**(3), 159-171.

Niu, Y., Miao, T., Zhang, C. and Zhang, J. (1998). "Damage model of frozen soil under multi-axial state stress." *Proc. of 7th International Conference on Permafrost*, 811-814.

Nixon, J. F. and Morgenstern, N. R. (1973). "The residual stress in thawing soils." *Canadian Geotechnical Journal*, **10**(4): 571-580.

Nixon, J. F. and Morgenstern, N. R. (1974). "Thaw-consolidation tests on undisturbed fine-grained permafrost." *Can. Geotech. J.*, **11**, 202-214.

Parameswaran, V.R. and Jones, S. J. (1981). "Triaxial testing of frozen sand." *Journal of Glaciology*, **27**(95), 148-155.

Penner, E. (1959). "The mechanism of frost heaving in soils." *Highway Research Board Bulletin*, **225**, 1-13.

Proskin, S., Sego, D. and Alostaz, M. (2010). "Freeze-thaw and consolidation tests on Suncor mature fine tailings." *Cold Regions Science and Technology*, **63**, 110-120.

Qi, J., Ma, W. and Song, C. (2007). "Influence of freeze-thaw on engineering properties of silty soil." *Cold Regions Science and Technology*, **53**, 397–404.

Qi, J., Hu, W. and Ma, W. (2010). "Experimental study of a pseudo-preconsolidation pressure in frozen soils." *Cold Regions Science and Technology*, **60**, 230-233.

Qi, J., Yao, X., Yu, F. and Liu, Y. (2012). "Study on thaw consolidation of permafrost under roadway embankment." *Cold Regions Science and Technology*, **81**, 48-54.

Qin, B., Chen, Z. H., Fang, Z. D., Sun, S. G., Fang, X. W., and Wang, J. (2010). "Analysis of coupled thermo-hydro-mechanical behavior of unsaturated soils based on theory of mixtures I." *Appl. Math. Mech. -Engl. Ed.*, **31**(12), 1561–1576.

Re, G. D., Germaine, J. T. and Ladd, C. C. (2003). "Triaxial testing of frozen sand: equipment and example results." *Journal of Cold Regions Engineering*, **17**(3), 90-118.

Robinet, J. C. Rahbaoui, A. Plas, F. and Lebon, P. (1996). "A constitutive thermomechanical model for saturated clays." *Engineering Geology*, **41**, 145-169.

Roscoe, K. H. and Burland, J. B. (1968). "On the generalized stress-strain behavior of 'wet' clay." *Engineering Plasticity* (eds Heyman, J. and Leckie, F. A.), Cambridge University Press, 535-609.

Roscoe, K. H. and Schofield, A. N. (1963). "Mechanical behavior of an idealized wet clay." *Proc. European Conf. Soil Mechs. Found. Engrg.*, 47-54.

Roscoe, K. H., Schofield, A. N. and Wroth, C. P. (1958). "On the yielding of soils." *Geotechnique*, **8**, 22-53.

Rutqvist, J., Börgesson, L., Chijimatsu, M., Nguyen, T. S., Jing, L., Noorishad, J. and Tsang, C. F. (2001a). "Thermohydromechanics of partially saturated geological media: governing equations and formulation of four finite element models." *Int. J. Rock Mech. Min. Sci.*, **38**, 105-127.

Rutqvist, J., Börgesson, L., Chijimatsu, M., Nguyen, T. S., Jing, L., Noorishad, J. and Tsang, C. F. (2001b). "Coupled thermo-hydro-mechanical analysis of a heater test in fractured rock and bentonite at Kamaishi mine-comparison of field results to predictions of four finite element codes." *Int. J. Rock Mech. Min. Sci.*, **38**, 129-142.

Rutqvist, J., Chijimatsu, M., Jing, L., Millard, A., Nguyen, T. S., De Jonge, J., Rejeb, A., Sugita, Y. and Tsang, C. F. (2005). "Numerical study of the THM effects on the near-field safety of a hypothetical nuclear waste repository-BMT1 of the DECOVALEX III project. Part 3: Effects of THM coupling in sparsely fractured rocks." *Int. J. Rock Mech. Min. Sci.*, **42**, 745-755.

Schofield, A. N. and Wroth, C. P. (1968). *Critical State Soil Mechanics*. McGraw-Hill, New York.

Selvadurai, A. P. S., Hu, J. and Konuk, I. (1999). "Computational modeling of frost heave induced soil-pipeline interaction, II. Modelling of experiments at the Caen test facility." *Cold Regions Science and Technology*, **29**, 229 - 257.

Sheng, J. C., Liu, J., Zhu, W. C., Elsworth, D. and Liu, J. X. (2008). "Stress analysis of a borehole in saturated rocks under in situ mechanical, hydrological and thermal interactions." *Energy Sources, Part A*, **30**, 157-169.

Shoop, S., Affeck, R., Haehnel, R., and Janoo, V. (2008). "Mechanical behavior modeling of thaw-weakened soil." *Cold Regions Science and Technology*, **52**, 191-206.

Suebsuk, J., Horpibulsuk, S. and Liu, M. D. (2010). "Modified Structured Cam Clay: A generalized critical state model for destructured, naturally structured and artificially structured clays." *Computers and Geotechnics*, **37**, 956–968.

Taber, S. (1929). "Frost heaving." *Journal of Geology*, **37**, 428 - 461.

Tao, Y., Xu, J., Liu, D. and Liang, Y. (2012). "Development and validation of THM coupling model of methane-containing coal." *International Journal of Mining Science and Technology*, **22**, 879–883.

Taylor, G. S. and Luthin, J. N. (1978). "A model for coupled heat and moisture transfer during soil freezing." *Can. Geotech. J.*, **15**, 548-555.

Tsytovich, N. A. (1960). "Bases and foundations on frozen soils." *Spec. Rep. 58*, Highway Research Board, National Academy of Sciences, Washington, D.C.

Yao, X., Qi, J. and Ma, W. (2009). "Influence of freeze-thaw on the stored free energy in soils." *Cold Regions Science and Technology*, **56**, 115–119.

Yao, X., Qi, J. and Wu, W. (2012). "Three dimensional analysis of large strain thaw consolidation in permafrost." *Acta Geotechnica*, **7**, 193–202

Viklander, P. (1998). "Permeability and volume changes in till due to cyclic freeze/thaw." *Can. Geotech. J.*, **35**, 471-477.

Wang, X. (2002). *Finite Element Method.* Tsinghua University Press, Beijing.

Wei, L., Hong, F. and He, W. (2011). "Research on visco-elastic-plastic creep model of artificially frozen soil under high confining pressures." *Cold Regions Science and Technology*, **65**(2), 219-225.

Williams, P. J. and Smith, M. W. (1989). *The Frozen Earth*: *Fundamentals of Geocryology*. Cambridge University Press, Cambridge.

Wood, M. D. (1990). *Soil Behavior and Critical State Soil Mechanics*. Cambridge University Press, Cambridge.

Zhang, Y. and Michalowski, R. L. (2013). "Constitutive model and simulation of non-segregation freezing and thawing in soils." *Proc. 18th International Conference on Soil Mechanics and Geotechnical Engineering*, Paris, 465-468.

Zhao, X., Zhou, G. and Chen G. (2013). "Triaxial compression strength for artificial frozen clay with thermal gradient." *J. Cent. South Univ.*, **20**, 218-225.

Zhou, J. and Li, D. (2012). "Numerical analysis of coupled water, heat and stress in saturated freezing soil." *Cold Regions Science and Technology*, **72**, 43-49.

Zhou, M. M. and Meschke, G. (2013). "A three-phase thermo-hydro-mechanical finite element model for freezing soils." *Int. J. Numer. Anal. Meth. Geomech*, **37**, 3173–3193.

Zhu, Y. Zhang, J. Peng, W. Sheng, Z. and Miao, L. (1992). "Constitutive relations of frozen soil in uniaxial compression." *Journal of Glaciology and Geocryology*, **14**(3), 210-217.

Zou Y. and Boley C. (2009). "Compressibility of fine-grained soils subjected to closed-system freezing and thaw consolidation." *Mining Science and Technology*, **19**, 631–635.